JAAVSO

Volume 51
Number 2
2023

The Journal of the American Association of Variable Star Observers

No Longer Eclipsing—The Strange Case of RS Crateris

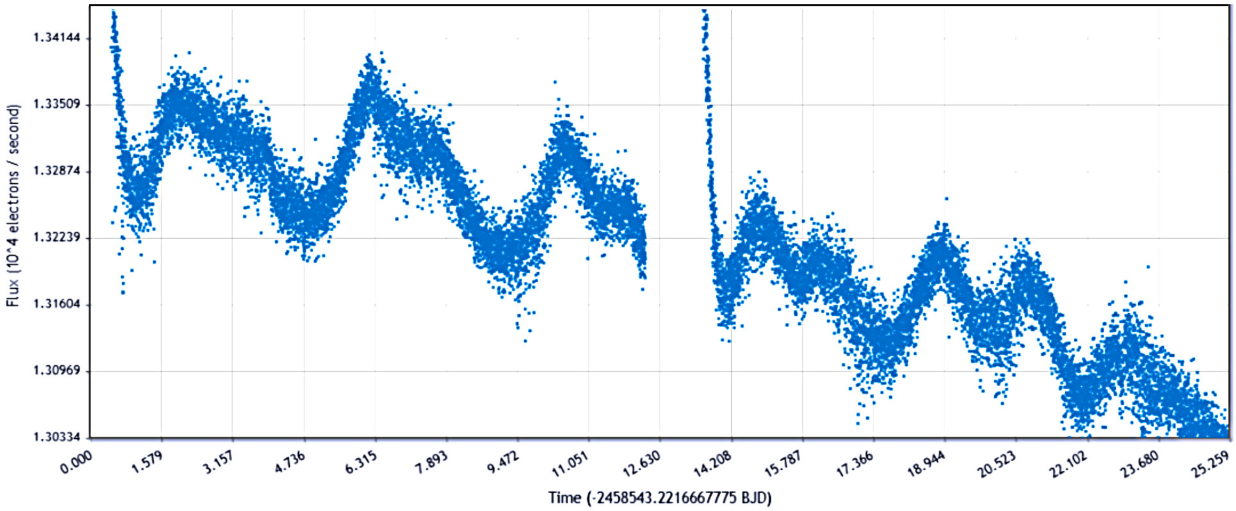

Recent light curve of RS Crt from TESS data.

Also in this issue...

- Spectroscopic and Photometric Study of the Asymptotic Giant Branch Star T Cephei
- The "Long Secondary Period (LSP) Variables": Overview and Some Analysis
- An Orbital Solution for WASP-12 b: Updated Ephemeris and Evidence for Decay Leveraging Citizen Science Data
- Ninety-Seven New Variable Stars in ω Centauri

Complete table of contents inside...

The American Association of Variable Star Observers
185 Alewife Brook Parkway, Suite 410, Cambridge, MA 02138, USA

The Journal of the American Association of Variable Star Observers

Editor-in-Chief
Nancy D. Morrison
Professor of Astronomy Emerita
Department of Physics
and Astronomy
The University of Toledo,
Toledo, Ohio

Associate Editor
Elizabeth O. Waagen

Production Editor
Michael Saladyga

Editorial Board
Geoffrey C. Clayton
Louisiana State University
Baton Rouge, Louisiana

Kosmas Gazeas
University of Athens
Athens, Greece

Laszlo L. Kiss
Konkoly Observatory
Budapest, Hungary

Katrien Kolenberg
Universities of Antwerp
and of Leuven, Belgium
and Harvard-Smithsonian Center
for Astrophysics
Cambridge, Massachusetts

Kristine Larsen
Department of Geological Sciences,
Central Connecticut
State University,
New Britain, Connecticut

Vanessa McBride
IAU Office of Astronomy for
Development; South African
Astronomical Observatory;
and University of Cape Town,
South Africa

Ulisse Munari
INAF/Astronomical Observatory
of Padua
Asiago, Italy

Karen Pollard
Director, Mt. John Observatory,
University of Canterbury,
Christchurch, New Zealand

Nikolaus Vogt
Universidad de Valparaiso
Valparaiso, Chile

The Board of the American Association of Variable Star Observers
2022–2023

Executive Director	Brian Kloppenborg
President	David Cowall
1st Vice President	Richard Berry
2nd Vice President	Sarah Austrin-Willis
Secretary	Kristine Larsen
Treasurer	Robert Stephens

Board Members
Martina Arndt
Peter Bealo
Pat Boyce
Robert Buchheim
Dennis Conti
Arne Henden
Ken Hudson
Thomas Maccarone
Antonella Nota

ISSN 0271-9053 (print)
ISSN 2380-3606 (online)

JAAVSO

The Journal of The American Association of Variable Star Observers

Volume 51
Number 2
2023

AAVSO
185 Alewife Brook Parkway,
Suite 410, Cambridge, MA 02138
USA

ISSN 0271-9053 (print)
ISSN 2380-3606 (online)

Publication Schedule

The Journal of the American Association of Variable Star Observers is published twice a year, June 15 (Number 1 of the volume) and December 15 (Number 2 of the volume). The submission window for inclusion in the next issue of JAAVSO closes six weeks before the publication date. A manuscript will be added to the table of contents for an issue when it has been fully accepted for publication upon successful completion of the referee process; these articles will be available online prior to the publication date. An author may not specify in which issue of JAAVSO a manuscript is to be published; accepted manuscripts will be published in the next available issue, except under extraordinary circumstances.

Page Charges

Page charges are waived for Members of the AAVSO. Publication of unsolicited manuscripts in JAAVSO requires a page charge of US $100/page for the final printed manuscript. Page charge waivers may be provided under certain circumstances.

Publication in *JAAVSO*

With the exception of abstracts of papers presented at AAVSO meetings, papers submitted to JAAVSO are peer-reviewed by individuals knowledgeable about the topic being discussed. We cannot guarantee that all submissions to JAAVSO will be published, but we encourage authors of all experience levels and in all fields related to variable star astronomy and the AAVSO to submit manuscripts. We especially encourage students and other mentees of researchers affiliated with the AAVSO to submit results of their completed research.

Subscriptions

Institutions and Libraries may subscribe to JAAVSO as part of the Complete Publications Package or as an individual subscription. Individuals may purchase printed copies of recent JAAVSO issues via Amazon KDP.

Instructions for Submissions

The *Journal of the AAVSO* welcomes papers from all persons concerned with the study of variable stars and topics specifically related to variability. All manuscripts should be written in a style designed to provide clear expositions of the topic. Contributors are encouraged to submit digitized text in MS WORD, LATEX+POSTSCRIPT, or plain-text format. Manuscripts should be submitted through the JAAVSO submission portal (https://www.aavso.org/apps/jaavso/submit/) or may be mailed electronically to journal@aavso.org or submitted by postal mail to JAAVSO, 185 Alewife Brook Parkway, Suite 410, Cambridge, MA 02138, USA.

Manuscripts must be submitted according to the following guidelines, or they will be returned to the author for correction:

Manuscripts must be:
  1) original, unpublished material;
  2) written in English;
  3) accompanied by an abstract of no more than 100 words.
  4) not more than 2,500–3,000 words in length (10–12 pages double-spaced).

Figures for publication must:
  1) be camera-ready or in a high-contrast, high-resolution, standard digitized image format;
  2) have all coordinates labeled with division marks on all four sides;
  3) be accompanied by a caption that clearly explains all symbols and significance, so that the reader can understand the figure without reference to the text.

Maximum published figure space is 4.5″ by 7″. When submitting original figures, be sure to allow for reduction in size by making all symbols, letters, and division marks sufficiently large.

Photographs and halftone images will be considered for publication if they directly illustrate the text.

Tables should be:
  1) provided separate from the main body of the text;
  2) numbered sequentially and referred to by Arabic number in the text, e.g., Table 1.

References:
  1) References should relate directly to the text.
  2) References should be keyed into the text with the author's last name and the year of publication, e.g., (Smith 1974; Jones 1974) or Smith (1974) and Jones (1974).
  3) In the case of three or more joint authors, the text reference should be written as follows: (Smith et al. 1976).
  4) All references must be listed at the end of the text in alphabetical order by the author's last name and the year of publication, according to the following format: Brown, J., and Green, E. B. 1974, *Astrophys. J.*, **200**, 765.
     Thomas, K. 1982, *Phys. Rep.*, **33**, 96.
  5) Abbreviations used in references should be based on recent issues of JAAVSO or the listing provided at the beginning of *Astronomy and Astrophysics Abstracts* (Springer-Verlag).

Miscellaneous:
  1) Equations should be written on a separate line and given a sequential Arabic number in parentheses near the right-hand margin. Equations should be referred to in the text as, e.g., equation (1).
  2) Magnitude will be assumed to be visual unless otherwise specified.
  3) Manuscripts may be submitted to referees for review without obligation of publication.

Online Access

Articles published in JAAVSO, and information for authors and referees may be found online at: https://www.aavso.org/apps/jaavso/

The Journal of the American Association of Variable Star Observers
Volume 51, Number 2, 2023

Editorial

Variable Star Research

Instruments, Methods, and Techniques

Table of Contents continued on next page

Variable Star Data

Editorial

Who are *JAAVSO*'s Authors?

Nancy D. Morrison
Editor-in-Chief, Journal of the AAVSO

Department of Physics and Astronomy and Ritter Observatory, MS 113, The University of Toledo, 2801 W. Bancroft Street, Toledo OH 43606; jaavso.editor@aavso.org

Received December 5, 2023

Among the AAVSO's goals are to foster communication and collaboration between amateur and professional astronomers and to further astronomy education. *JAAVSO* aims to support both roles by bringing amateurs' research results to the attention of professionals and by publishing the results of of students' research and of amateur-professional collaborations. One measure of the strength of that support is the composition of the ensemble of our authors, who are an interesting mix of astronomy enthusiasts. They include students, teachers, professors in higher education, and amateur astronomers, who may themselves be employed or retired professionals in other science fields.

Figure 1 gives the number of first authors (or corresponding authors, if they are different) in each of the most recent five volumes, across all our published articles on research, data, instruments/techniques, and education/outreach.

In making these counts, I inferred authors' status from the affiliation given with their articles. If the affiliation is a private observatory or a home address, I assumed the author to be an amateur astronomer unless I had information to the contrary. I considered a retired professional astronomer to be still a professional.

In the case of a university affiliation, I used the university website to identify faculty members. Most universities with graduate programs also list graduate students. If an author is affiliated with a university but not identified on the institutional website, I assumed that person to be an undergraduate. In a few cases, I know authors' status from their presentations at AAVSO meetings. Affiliation with a high school identifies the authors to be high school students or (in a couple of known cases) teachers. I classified the teachers as professionals. A few ambiguous cases may cause these counts to be randomly in error by one or two.

Our non-student authors are a roughly equal mix of amateurs and professionals. Inspection of Figure 1 shows the mix wandering back and forth, but the five-year averages are almost equal: 14.4 amateurs and 13.4 professionals per volume. Over the same time frame, the average number of papers per year with at least one amateur and one professional co-author is 5.4. These numbers are healthy for the AAVSO, although I would like to see the number of amateur-professional collaborations even larger.

Usually the first and the corresponding author are the same person. A straightforward reason for them not to be is that the submitting (and often corresponding) author must be an AAVSO member to avoid publication charges, but, for scientific/scholarly reasons, that person is not always the first author. Another case is that of student projects, where often the student author is listed first, but the faculty adviser

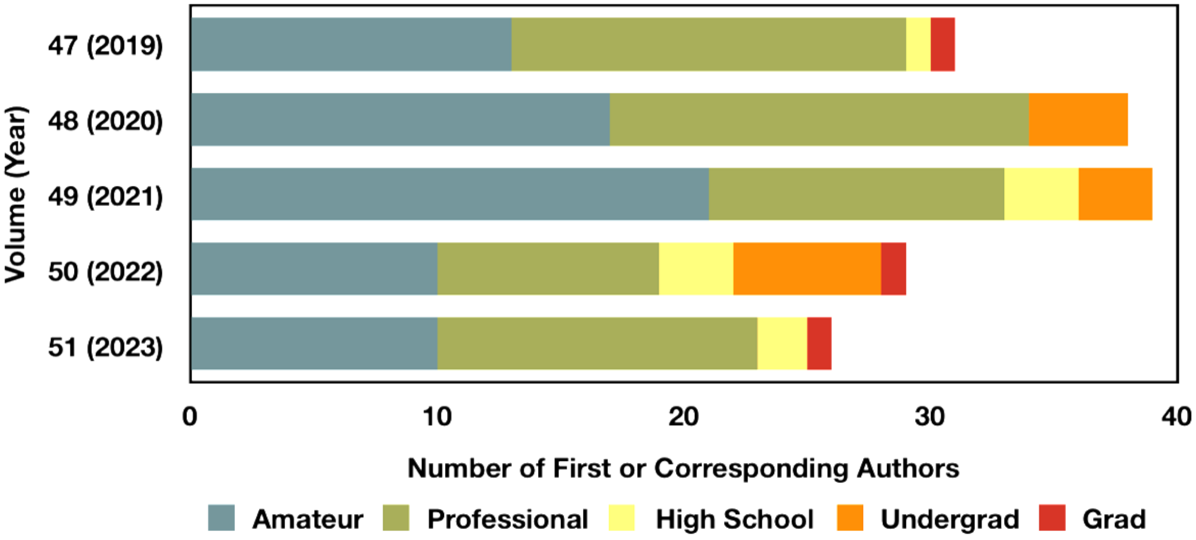

Figure 1. The number of first or corresponding authors in each of the most recent five volumes of *JAAVSO*, summed across all paper categories.

conducts correspondence with the journal because the student has graduated or otherwise moved on. Authors with whom I corresponded about a paper are included in the count, regardless of that person's place in the author list.

Some papers are authored by large groups of students; the total number of student authors (not just first authors) in the five-year period is about 100. However, I counted just first/corresponding authors because only those individuals acquire the educational experience of interacting directly with the editor and the referee.

When I took on this editorship, I promised then-Executive Director Dr. Stella Kafka that I would help students approach a professional level of paper construction while preserving as much of their personal styles as possible. This commitment reflects the importance of the publication process in science education. When authors figure out how to explain their ideas clearly, they think deeply through the issues in their research and go on to do better science.

The importance of this concept came through strongly in a hybrid workshop held at the 242nd meeting of the American Astronomical Society in Albuquerque, New Mexico, in June, 2023. Its organizers were Brian Kloppenborg (American Association of Variable Star Observers), Russell Genet (California Polytechnic State University), and Rachel Freed (Institute for Student Astronomical Research). Entitled, "Small Ground and Space Telescopes in the New Era of Big Telescope Surveys," the workshop included a full afternoon session (Session 3) on astronomy education via research with small telescopes. Most of the speakers' slides are available for download.[1] I attended portions of this workshop remotely. Several speakers (Russ Genet comes to mind in particular) emphasized the importance of publication as the culmination of a student research project, along with how rewarding it is to make the effort of advising a student on preparing a paper. Throughout my teaching and editorial careers, I have embraced this concept, and I will continue to do so.

I thank all our authors for their contributions, and I thank those who are advising students in research.

---

[1] https://www.aavso.org/workshops/aas-242-sky-surveys-and-small-telescopes

Tracking Spectroscopically Determined H-alpha and H-beta Indices for Two Emission-Line Objects

Tyler B. Harding
Eric G. Hintz
Department of Physics and Astronomy, Brigham Young University, Provo, UT 84602; hintz@byu.edu

Received July 29, 2022; revised February 16, May 11, July 5, 2023, accepted July 5, 2023

Abstract Spectroscopic methods were used to monitor the Hα and Hβ indices for two emission-line objects, X Persei and γ Cassiopeiae. The spectroscopic data covered a timeline from 2010 to 2020. The Hα index for X Per showed substantial variation, with the Hβ index changes being less pronounced. The shape of the Hα variations for X Per were a mirror image to archival V-magnitude observations. In the case of γ Cas only a slight rise in value for the Hα index was seen. To allow comparison to published observations, we determined a transformation from the two indices to equivalent width values. The values determined for X Per fill time gaps in the previously published equivalent width values. The γ Cas values provide no additional coverage.

1. Introduction

Joner and Hintz (2015) detail calibrated Hα and Hβ indices for a significant number of main sequence stars. The Hβ index is effectively the original photometric filter system designed by Crawford (1960) and often used in conjunction with the Strömgren filter set. The index is based on wide and narrow filters centered on the Hβ line. Although not stated in Joner and Hintz (2015), the development of a similar Hα index started with the creation of similar physical filters centered on the Hα line. To check the early results a set of spectroscopic observations was obtained. This allowed testing of a range of filter shapes since different functions could be convolved over the spectrum to obtain photometric values. The development of the new Hα index then became a photometric project based on spectroscopic observations. However, in the end scans of the original filters were used to determine the values that appear in Joner and Hintz (2015).

As part of the observing program that led to Joner and Hintz (2015), data were secured for a wide range of potentially variable objects such as pulsating variable stars Bugg and Hintz (2019), eclipsing binaries, active galaxies, and emission-line objects. This was in preparation for the potential long-term monitoring with physical filters. Two of the emission-line objects observed were X Persei (X Per) and γ Cassiopeiae (γ Cas). Here we will demonstrate the ability of the two indices to track temporal changes of spectral lines for these types of objects.

While the indices can be used to monitor changes in emission line strength on their own, we recognize the need to compare with published equivalent width measurements (EW hereafter). Therefore, we provide a calibrated conversion of the Hα and Hβ indices to EW values. For comparison we gathered EW values for X Per from a number of papers (Roche *et al.* 1993; Engin and Yuce 1998; Liu and Hang 2001; Grundstrom *et al.* 2007; Li *et al.* 2014; Reig *et al.* 2016; Zamanov *et al.* 2019). This provides nearly continuous coverage from 1979 to 2021 for at least the Hα line. A good summary of recent Hα EW measurements for γ Cas was found in Pollmann (2021).

While the original Joner and Hintz (2015) paper was based on scanned filter functions convolved over spectroscopic observations, the original intent of the system was to be a photometric system using filters like the original Hβ system. This paper demonstrates the future application of physical filters to monitor variable objects such as emission-line objects.

2. Observations

Spectroscopic data were collected using the 1.2-meter McKellar Telescope of the Dominion Astrophysical Observatory (DAO) operating in robotic mode. Since both targets are the brightest objects in their fields this mode works extremely well and allowed for the collection of a significant number of observations. The observations of X Per were collected from 2010 to 2020, providing 66 total nights of data. A total of 87 nights of data were collected for γ Cas from 2011 to 2020. In addition, spectroscopic observations of 15 other emission-line objects were secured during this same window of time. Each night also contained a sample of the standard stars from Joner and Hintz (2015).

The 3231 grating was used and provided 40.9 Å mm^{-1}. The spectra were imaged onto the Site4 CCD with 15 μm pixels that resulted in a spectral resolution of 0.614 Å $pixel^{-1}$. The Site4 CCD has 4096 pixels along the dispersion axis which provided approximately 2500 Å of total spectral coverage. This grating was aligned to provide a central wavelength of 5710 Å, thus covering a range from 4450 Å to 6970 Å. The selected range allowed for the simultaneous observation of both the Hα and the Hβ lines. All spectra were processed using a FeAr comparison lamp and compressed to 1D using the SPECRED packages in the IRAF reduction software. Figure 1 shows an example processed spectrum for X Per and Figure 2 for γ Cas.

For comparison purposes, V-filter observations of both targets were downloaded from the American Association of Variable Star Observers (hereafter AAVSO) website (Kafka (2021). The AAVSO archive provided 139 data points for X Per for the years 2010 through 2020 and 584 data points for γ Cas for the years 2011 through 2020. It should be noted that more data exist in the AAVSO archive, but we only selected the data which correspond to our timeline.

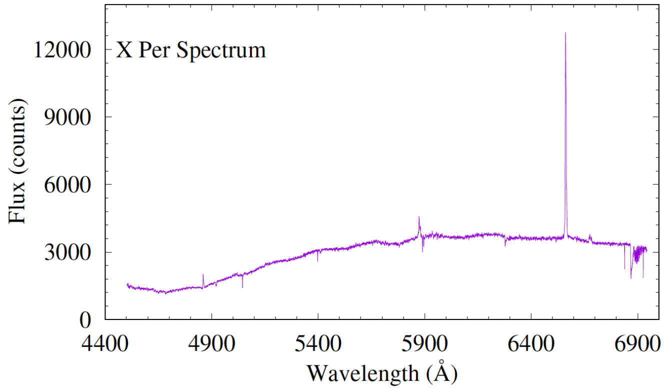

Figure 1. Typical spectrum for X Per collected from the DAO 1.2-m telescope.

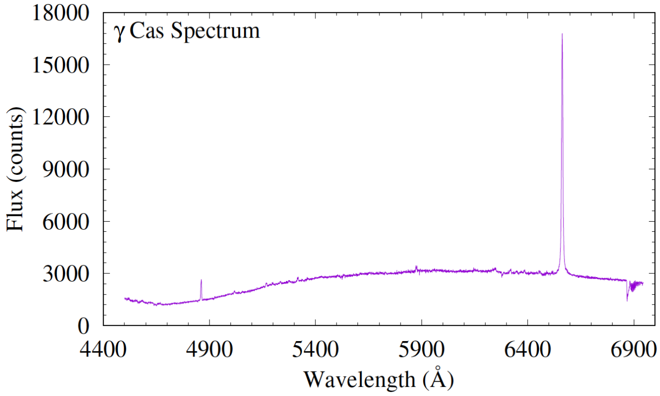

Figure 2. Typical spectrum for γ Cas collected from the DAO 1.2-m telescope.

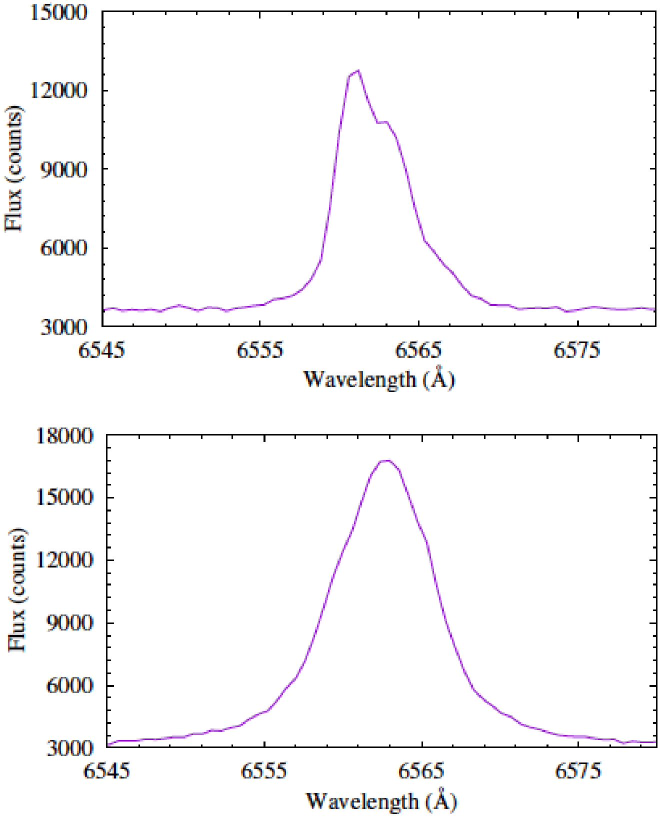

Figure 3. A zoomed in view of the Hα emission line for X Per (top) and γ Cas (bottom).

3. Analysis

After the data were processed to 1D wavelength calibrated spectra, we used the methods detailed in Joner and Hintz (2015) to provide calibrated Hα and Hβ index values for each observation. In other words, we convolved each filter function over the spectrum and formed each index by subtracting the wide magnitude from the narrow magnitude. That value was then calibrated against the standard stars from Joner and Hintz (2015) taken each night.

In Figure 3 we show detailed views of a typical Hα line for X Per and γ Cas. In total we obtained 161 spectra for X Per and 543 spectra for γ Cas. Given that both targets are bright, the error per observation is in the 0.003 to 0.006 range for index measurements. We do note that for some spectra the Hα line was saturated so that we could only determine an Hβ measurement from those spectra. In addition, a number of nights had very low signal in the blue region and the Hβ values were unreliable.

As has been stated before, the Hα and Hβ values were always meant to be done by imaging with physical filters. Since emission-line objects are most often tracked with changes to the EW, we developed a transformation from the index values to EW. To do this we used single observations for 16 emission-line objects mentioned earlier for which we had determined Hα and Hβ indices. Using the SPLOT command within IRAF we examined the EW values. We note that there are five different options for measuring EW with this command. We selected the option that provides the integration of pixel intensities between the marked points (the "e" keystroke). The limits were determined by finding the continuum level then marking the first point where the curve reached this level on each side of the line center. The values are reported in Table 1.

Figure 4 shows the comparison of the index values and the EW values for the Hα line. Both linear and second-order fits were determined. For Hα the coefficients on the second-order fit are clearly significant as shown in Equation 1. In Figure 4 we show the linear fit as a solid line and the second-order fit as a dashed line. The standard errors for the fits are found to be 1.40 Å for the linear fit and 0.60 Å for the second-order fit.

$$EW\alpha = -19.51(2.80)\times H\alpha^2 + 132.70(12.15)\times H\alpha - 211.69(12.99) \quad (1)$$

In Figure 5 the relation between EW and Hβ is displayed. We note that for the Hβ relation HD 31293 was clearly in absorption. Therefore HD 31293 was removed from the transformation discussed here. Again we checked both a linear fit and a second-order fit. A t-test on the second-order terms is right at the edge of significance and the difference in standard error is not significantly improved by inclusion of the second-order term. Therefore, the Hβ to EW transformation is done with a linear fit as given in Equation 2. The error for this transformation is 0.67 Å.

$$EW\beta = 40.07(2.01) \times H\beta - 100.81(4.97) \quad (2)$$

Equation 1 and Equation 2 were used to generate EW values for all our observations. To check the Hα EW values we gathered the published data from HJD 2455000 to HJD 2458500 to match

Table 1. Hα and Hβ versus equivalent width values for a sample of emission-line targets.

Object	*Hα*	*EWα Å*	*Hβ*	*EWβ Å*
κ Dra	2.165	–15.82	2.586	2.32
1H 1936+541	1.995	–23.81	2.493	–2.38
V1357 Cyg	2.549	–0.51	2.554	1.12
λ Cep	2.538	–0.14	2.545	1.25
AG Dra	1.737	–39.48	2.191	–13.95
1H 2202+501	1.770	–38.86	2.532	0.32
4U 2206+54	2.525	–0.76	2.552	1.12
52 Aql	2.405	–6.05	2.520	0.66
α Cam	2.496	–2.29	2.524	0.84
HD 229221	1.934	–27.86	2.424	–3.03
X Per	1.953	–26.93	2.400	–3.82
HD 31293	2.077	–21.43	2.780	14.03
RX J0440.9+4431	2.267	–11.08	2.480	–1.22
EXO 051910+3737.7	1.902	–30.54	2.414	–3.04
1A 0535+262	2.216	–12.48	2.456	–1.93
4U 0548+29	1.828	–33.77	2.466	–2.48

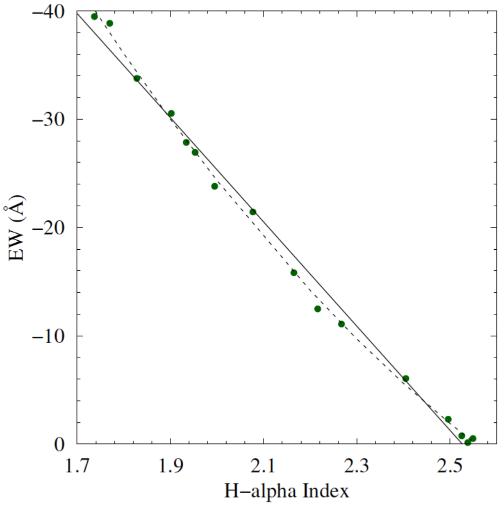

Figure 4. EW width versus Hα index values.

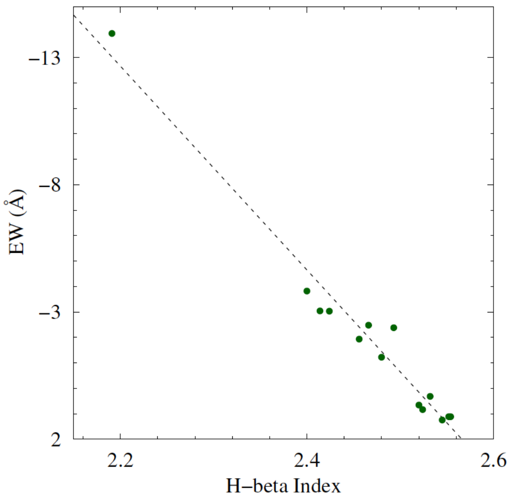

Figure 5. EW width versus Hβ index values.

Table 2. Sample table of Hα and Hβ and equivalent width values for X Per.

HJD	*Hα*	*EWα Å*	*Hβ*	*EWβ Å*
2455261.9115	1.886	–33.0	2.369	–5.9
2455461.9157	1.887	–33.0	2.368	–5.9
2455461.9199	1.886	–33.0	2.370	–5.8
2455548.7535	1.911	–31.5	2.383	–5.3
2455548.7562	1.914	–31.4	2.383	–5.3
2455548.7589	1.913	–31.4	2.382	–5.4
2455611.6519	1.967	–28.4	2.417	–4.0
2455611.6546	1.962	–28.6	2.416	–4.0
2455611.6574	1.958	–28.9	2.407	–4.4
2455612.6251	1.968	–28.3	2.415	–4.0

Note: The remainder of the table is published as a machine-readable table. This table will be web-archived and made available through the AAVSO ftp site at: ftp://ftp.aavso.org/public/datasets/3847-Harding-512-HardingTable2.txt.

Table 3. Sample table of Hα and Hβ and equivalent width values for γ Cas.

HJD	*Hα*	*EWα Å*	*Hβ*	*EWβ Å*
2455806.9621	1.964	–28.5	2.376	–5.6
2455806.9626	1.944	–29.7	2.387	–5.2
2455806.9630	1.905	–31.9	2.405	–4.4
2455828.8716	1.899	–32.2	2.458	–2.3
2455828.8721	1.881	–33.3	2.451	–2.6
2455828.8726	1.892	–32.7	2.429	–3.5
2455904.6018	1.900	–32.2	2.411	–4.2
2455904.6022	1.897	–32.4	2.418	–3.9
2455904.6026	1.901	–32.1	2.414	–4.1
2455904.6029	1.896	–32.4	2.418	–3.9

Note: The remainder of the table is published as a machine-readable table. This table will be web-archived and made available through the AAVSO ftp site at: ftp://ftp.aavso.org/public/datasets/3847-Harding-512-HardingTable3.txt.

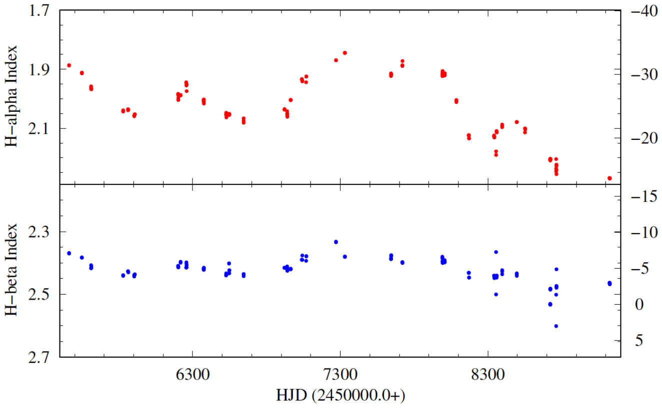

Figure 6. Hα and Hβ values in both index value and equivalent width for X Per. This data covers the time from 2010 to 2020.

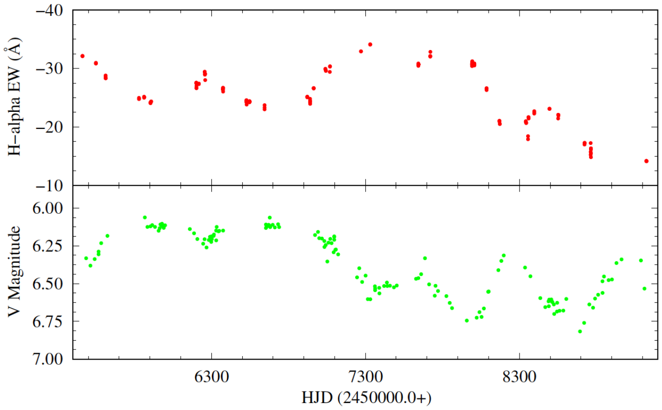

Figure 7. Hα Equivalent Width and V magnitude for X Per over the entire observing time.

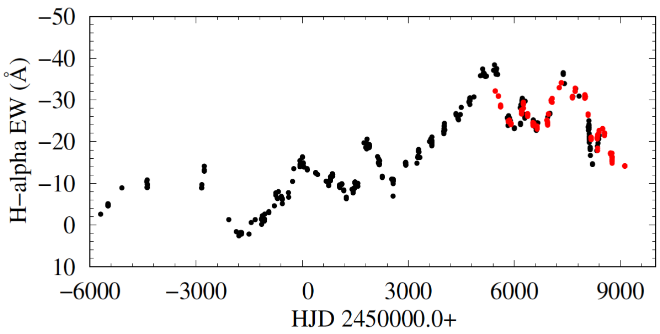

Figure 8. Hα Equivalent Width values with published data (black) and data from this paper (red) for X Persei.

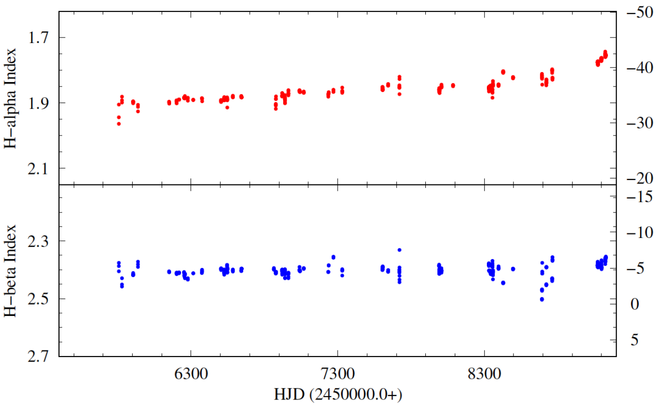

Figure 9. Collected data points of Hα strength of γ Cas during the years 2011 to 2020.

the time range of our data. Minimizing the offset between the two sets of data, at common epochs, we find a systematic shift of –2.2 Å between our values and the published values for the Hα EW. The shift likely comes from differences in how our EW values were determined compared to the published values, including determination of the continuum level. The additional shift is included in the Hα values detailed in Table 2 for X Per and Table 3 for γ Cas to bring them in line with the published values. The systematic shift has not been added to the Hα transformation equation.

3.1. X Persei

In Figure 6 we see the run of both the Hα and Hβ indices for X Per over the time of observation. The scale on the left of the figure is the index values defined by Joner and Hintz (2015) and the right side is the EW in Å. There is clearly a larger range in the Hα line, but the Hβ values do track roughly with the Hα. In all cases the lower, or more negative the value the stronger the hydrogen line. One can clearly see changes in X Per that at first glance might seem periodic in nature, although no periodic nature has ever been confirmed.

A comparison of the Hα values to the published V magnitudes is shown in Figure 7. It is interesting to note that the two curves are almost mirror images of each other: when the V magnitude goes up the strength of the Hα line tends to decrease, although there is not a perfect correspondence.

In Figure 8 we show the published EW values for X Per in black and our data in red. There are clearly a few epochs where our data fill gaps in the overall published curve. To examine the entire run of data for periodic behavior we used the Peranzo software package. Peranzo (Paunzen and Vanmunster 2016) is a package that brings together versions of many standard period search programs like PDM, ANOVA, etc. It includes seven versions of Fourier period searches and nine other methods. We used all 16 packages to examine the combined Hα data for periodic behavior. No clear periodicity was found in any package, as expected.

3.2. γ Cassiopeiae

Following a similar pattern to our X Per analysis, we examined the Hα and Hβ information gathered for γ Cas. In Figure 9 we show the Hα and Hβ variations in our line measurements. γ Cas shows smooth, slowly rising EW values in the Hα index from 2011 to 2020. This is also seen in the data from Pollmann (2021). Our data appear to be in reasonable agreement with the data displayed in that publication. Our Hβ data might show a very small rise over the entire data run, but it is not statistically significant.

4. Conclusions

Using the system detailed in Joner and Hintz (2015) we tracked Hα and Hβ index values over approximately 10 years for X Per and γ Cas. X Per showed significant variations in the Hα index and to a lesser degree in Hβ. γ Cas shows a steady strengthening in the Hα index, with no clear change in Hβ. From the observations of these two objects it is clear that the Hα and Hβ indices can be used to monitor emission-line objects. This is especially important when the indices are determined from the traditional physical filters.

While future photometric monitoring with the Hα and Hβ indices can be done, it is important to be able to convert to EW values in order to compare with the long range monitoring of these objects. Therefore we provide a conversion between the two indices and EW values. Once converted the EW values determined from the index values agree with published EW.

5. Acknowledgements

Based on observations obtained at the Dominion Astrophysical Observatory, NRC Herzberg, Programs in Astronomy and Astrophysics, National Research Council of Canada. We are especially thankful to David Bohlender and Dmitry Monin at DAO for help with the robotic operations mode. We acknowledge with thanks the variable star observations from the AAVSO International Database contributed by observers worldwide and used in this research. We acknowledge the Brigham Young University, Department of Physics and Astronomy for their continued support of our research efforts. Finally, we acknowledge the help of Maureen Hintz with editorial reviews of all manuscripts.

References

Bugg, A. G., and Hintz, E. G. 2019, *Res. Notes Amer. Astron. Soc.*, **3**, 63.

Crawford, D. L. 1960, *Astrophys. J.*, **132**, 66.

Engin, S., and Yuce, K. 1998, *Inf. Bull. Var. Stars*, No. 4648, 1.

Grundstrom, E. D., *et al.* 2007, *Astrophys. J.*, **660**, 1398.

Joner, M. D., and Hintz, E. G. 2015, *Astron. J.*, **150**, 204.

Kafka, S. 2021, Observations from the AAVSO International Database (https://www.aavso.org/data-download).

Li, H., Yan, J., Zhou, J., and Liu, Q. 2014, *Astron. J.*, **148**, 113.

Liu, Q.-Z. and Hang, H.-R. 2001, *Astrophys. Space Sci.*, **275**, 401.

Paunzen, E., and Vanmunster, T. 2016, *Astron. Nachr.*, **337**, 239.

Pollmann, E. 2021, *J. Amer. Assoc. Var. Star Obs.*, **49**, 77.

Reig, P., Nersesian, A., Zezas, A. 2016, Gkouvelis, L., and Coe, M. J. 2016, *Astron. Astrophys.*, **590A**, 122.

Roche, P., *et al.* 1993, *Astron. Astrophys.*, **270**, 122.

Zamanov, R., Stoyanov, K. A., Wolter, U., Marchev, D., and Petrov, N. I. 2019, *Astron. Astrophys.*, **622A**, 173.

Photometry and Transit Modeling of Exoplanet XO-1b

Simon Sikora
Adlai E. Stevenson High School, 1 Stevenson Drive, Lincolnshire, IL 60069

Timothy Banks
Department of Physical Science and Engineering, Harper College, 1200 W. Algonquin Road, Palatine, IL 60067, and Data Science, Nielsen, 200 W. Jackson, Chicago, IL 60606; tim.banks@nielsen.com

Received September 16, 2022; revised September 4, 2023; accepted September 6, 2023

Abstract CCD images of transits by the exoplanet XO-1b over the years 2018 to 2021 are analyzed. The data were collected by a MicroObservatory telescope in Arizona. These are supplemented by analysis of TESS space telescope data along with transits observed by amateur astronomers, leading to an investigation of the mid-transit times and the orbital period of the exoplanet. No evidence is found to support transit timing variations, with a period of 3.9415049 ± 0.0000008 days being sufficient to explain mid-transit times over 2006 to 2021. Using TESS data, the orbital radius is estimated to be some 11.10 ± 0.15 times the radius of the host star, and the planetary radius 0.1300 ± 0.0016 times the stellar radius. A simple transit model is combined with Bayesian sampling to provide estimates for the orbital inclination, radii, and limb darkening, however these estimates are not internally consistent. This is likely due to the application of the "small planet approximation," which neglects a radial gradient in the stellar flux obscured by the planet (due to the limb darkening effect), together with the model not accounting for variation in the stellar flux.

1. Introduction

The study of exoplanets, via transits, is an appealing field for students who can contribute to the rapidly growing scientific knowledge of such systems. Banks *et al.* (2020) outlined a research program involving undergraduate students analysing transit and radial velocity data for exoplanets, and commented that such programs are ideal for astronomical outreach projects. Not only were students able to conduct meaningful and publishable research, they were able to expand their skill sets such as in computer programming through building models from first principles and implementing optimization techniques. Such skills are marketable and valuable in the commercial world, with these projects building up not only the students' interest in, and support of, astronomy but also skills for the wider workplace. Banks *et al.* ended their paper suggesting that such programs could be possible for final year high school students. The current paper outlines such an extension. It describes work by a high school student analyzing archival data, both images and reduced data, investigating the exoplanet XO-1b. The project aim was to estimate parameters such as planetary radius and orbital inclination for the system as well as model the period of the system, searching for variations in the mid-transit timings that could indicate the gravitational effect of another currently unknown (and non-transiting) planet or planets. Such variations are known as TTVs, or Transit Timing Variations.

F. Sienkiewicz of the Harvard-Smithsonian Center for Astrophysics (CfA) suggested the study of the exoplanet XO-1b (orbiting the host star also known as BD+28 2507, which has ICRS (2000) coordinates α = 16:02:11.8, δ = +28:10:10.4), using imagery from the CfA's MicroObservatory (MObs) which he kindly supplied to the authors. This transiting exoplanet was discovered by the XO project (McCullough *et al.* 2006), with confirmation later that year by SuperWASP-North (Wilson *et al.* 2006). The planet's mass is estimated to be ~0.9 times that of Jupiter, completing an orbit in $3.9415160^{+0.0000230}_{-0.0000250}$ days (Patel and Espinoza 2022) at a distance of ~ 0.49 astronomical unit. "Surface" temperatures are estimated at around 1200 Celsius, leading to XO-1b being identified as an example of the "Hot Jupiter" class of exoplanets.

2. Data Analysis

2.1. MicroObservatory

The analyzed observations were taken by a 6-inch aperture MicroObservatory (MObs; Sadler *et al.* 2001) telescope. This automated telescope is located at Mount Hopkins in Arizona (latitude 31.675°, longitude –110.952°, and a 1,268-m altitude above sea level). 60-second long exposures were collected using a KAF-1403 ME CCD camera. The CCD has a pixel scale of 5.2 arcseconds. 2 × 2 binning was applied to the images to reduce noise. No filters were used in the observations, i.e., the images were in white light.

The software exotic (Zellem *et al.* 2020) was used to reduce the transit data. This is Python software developed by the Jet Propulsion Laboratory's "Exoplanet Watch" program. It can run on a variety of different operating systems (as a Python library) and is also available online inside Google's "Colaboratory" (This is how Google spells the name for this tool). exotic is intended for the analysis of individual transits, processing science frames through calibration and photometric measurement to the final fitting of a transit light curve model using Markov Chain Monte Carlo (MCMC) for optimization. exotic can be used to reduce the images collected during a transit after the event, or process science images as they are acquired during a transit. If calibration frames are available (such as flat field, dark, and bias images), exotic will automatically apply these to the science images as part of its data reduction before performing differential photometry. The user will select a number of possible comparison stars, which exotic evaluates for stability (excluding any "comparison" stars with observed variability). The software can also be used to model observed

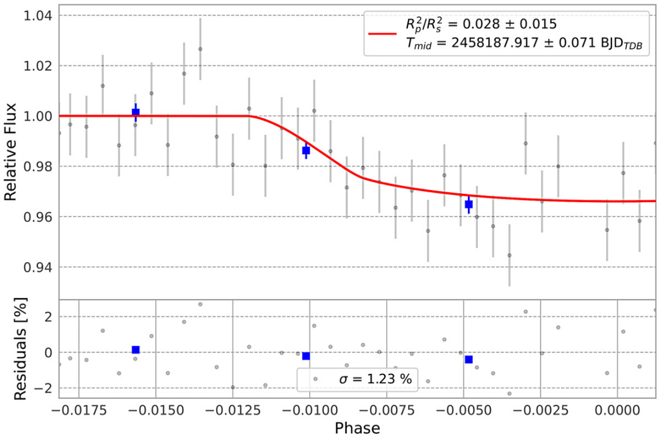

(a) 13 March 2018

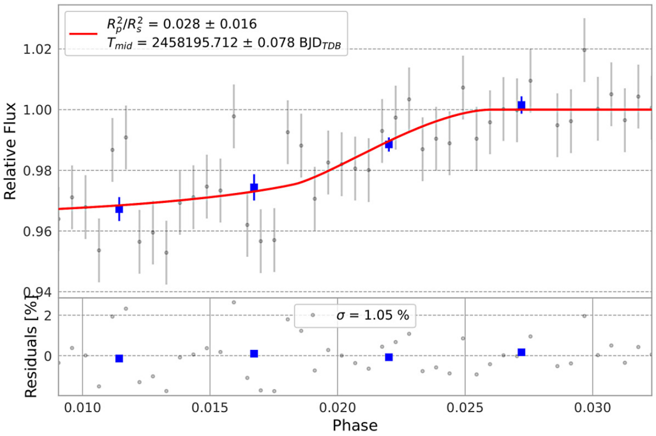

(b) 17 March 2018

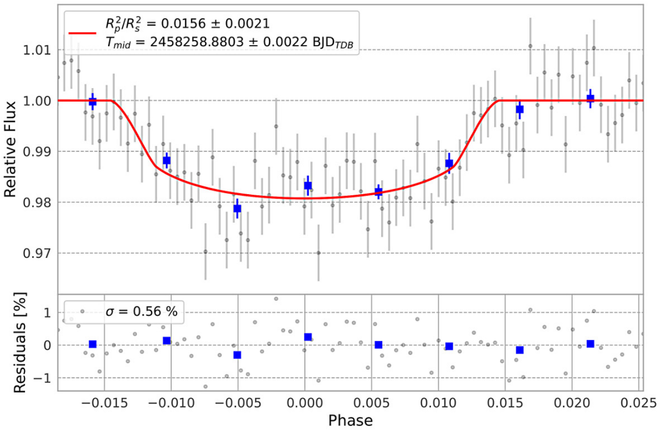

(c) 20 May 2018

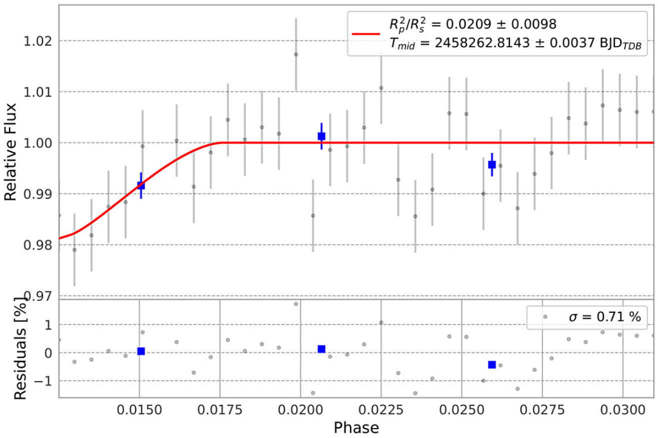

(d) 24 May 2018

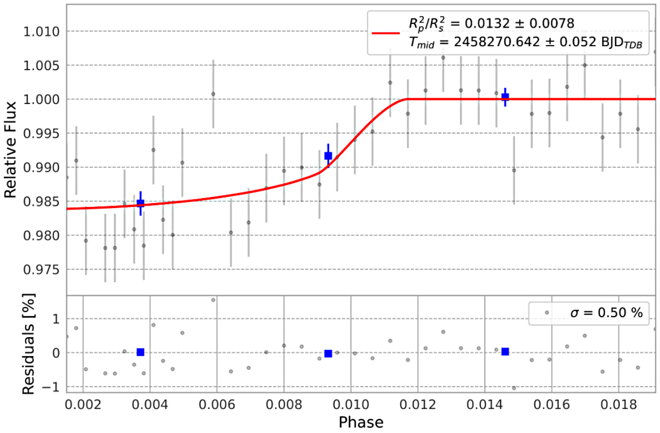

(e) 31 May 2018

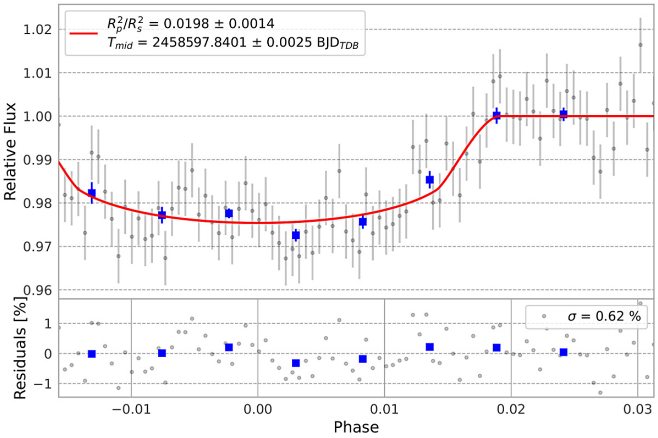

(f) 24 April 2019

Figure 1. MicroObservatory XO-1b transit data and models. The red lines show the expected variation based on the best fitting exotic model for each transit.

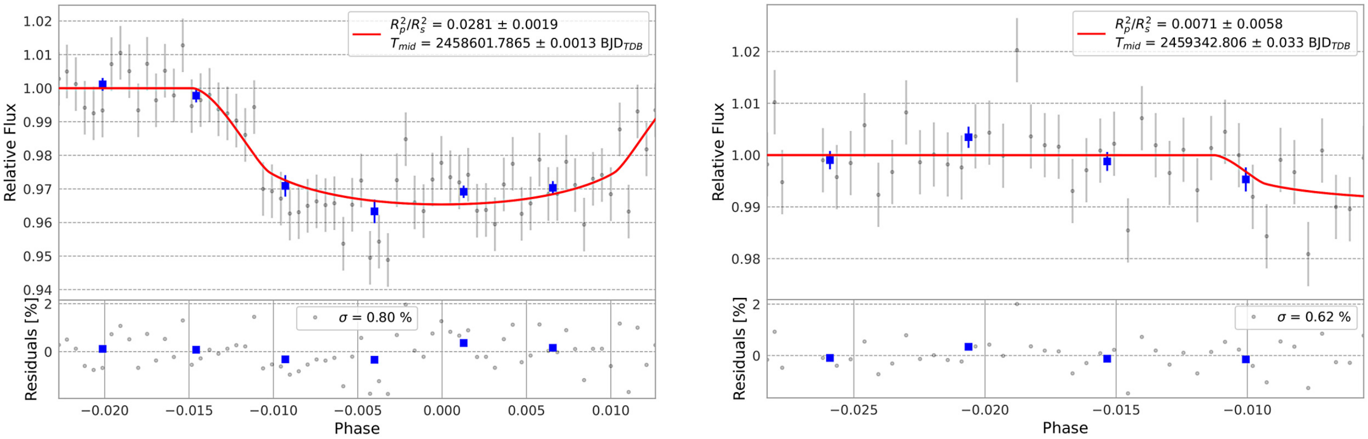

(g) 28 April 2019

(j) 12 May 2021

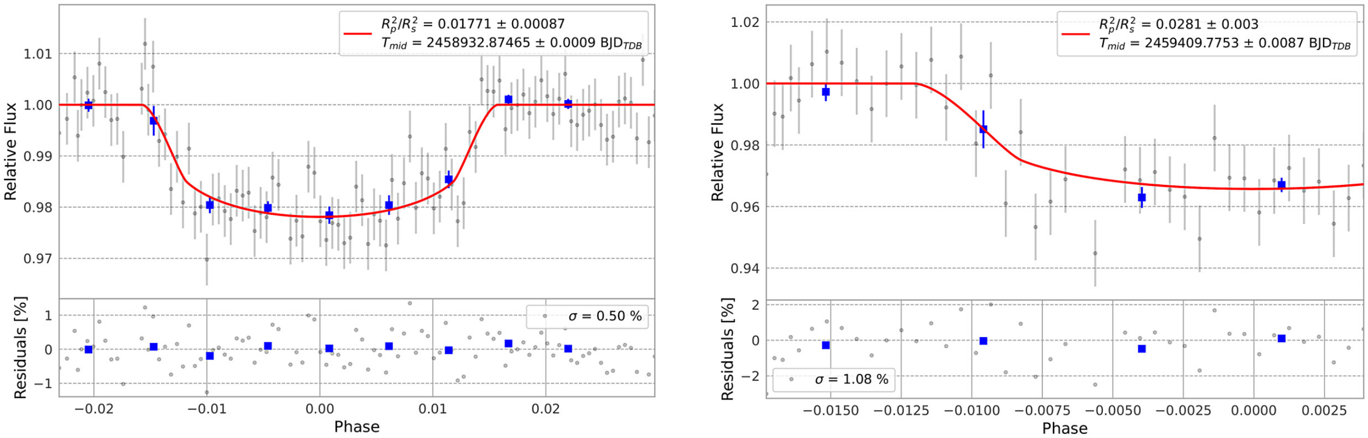

(h) 23 March 2020

(k) 18 July 2021

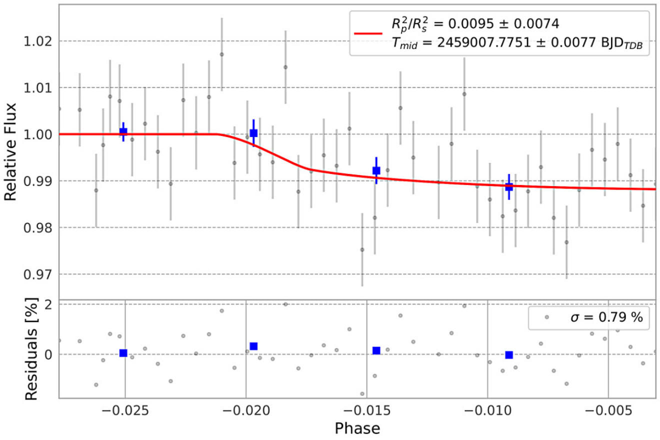

(i) 07 June 2020

Figure 1. MicroObservatory XO-1b transit data and models, cont.

Table 1. Fitted Parameters for XO-1b from the EXOTIC modelling.

Date	*Mid-transit*	a/r_s	r_s/a	r_p/r_s	*Quality*	*Source*
14 March 2006	2453808.9158 ± 0.0003	11.420 ± 0.084	0.0876 ± 0.0006	0.1296 ± 0.0012	Complete	Bruce Gary, Arizona
01 June 2006	2453887.74685 ± 0.00037	11.160 ± 0.081	0.0896 ± 0.0007	0.13223 ± 0.00096	Complete	Bruce Gary, Arizona
24 July 2007	2454214.89356 ± 0.00049	11.09 ± 0.11	0.0902 ± 0.0009	0.1346 ± 0.0010	Complete	Bruce Gary, Arizona
28 March 2008	2454553.85823 ± 0.00041	10.485 ± 0.085	0.0954 ± 0.0008	0.1314 ± 0.0011	Background uneven	Bruce Gary, Arizona
03 June 2008	2454620.86759 ± 0.00043	11.106 ± 0.087	0.0900 ± 0.0007	0.1342 ± 0.0009	Complete	Cindy Foote, Utah
07 June 2008	2454624.8118 ± 0.0009	11.76 ± 0.23	0.0850 ± 0.0017	0.1317 ± 0.0023	Complete	Cindy Foote, Utah
11 June 2008	2454628.7484 ± 0.0035	10.95 ± 0.60	0.0913 ± 0.0050	0.1307 ± 0.0014	Partial	Bruce Gary, Arizona
02 May 2009	2454963.7784 ± 0.0004	11.273 ± 0.082	0.0887 ± 0.0006	0.12550 ± 0.00077	Complete	Bruce Gary, Arizona
13 May 2009	2454983.4856 ± 0.0005	11.29 ± 0.12	0.0886 ± 0.0009	0.1315 ± 0.014	Complete	Jose Gregorio, Portugal
16 May 2009	2454967.71796 ± 0.00040	10.928 ± 0.095	0.0915 ± 0.0008	0.13295 ± 0.00098	Complete	Bruce Gary, Arizona
20 May 2009	2454971.65900 ± 0.00045	10.801 ± 0.005	0.09258 ± 0.00004	0.13576 ± 0.00093	Almost complete	Bill Norby, Missouri
13 March 2018	2458187.917 ± 0.061	14.88 ± 2.29	0.067 ± 0.010	0.167 ± 0.045	Partial	MObs
17 March 2018	2458195.712 ± 0.078	7.12 ± 1.56	0.140 ± 0.031	0.166 ± 0.047	Partial	MObs
20 May 2018	2458258.8803 ± 0.0022	11.99 ± 0.78	0.083 ± 0.005	0.1249 ± 0.0084	Complete	MObs
24 May 2018	2458262.8143 ± 0.0037	10.21 ± 1.77	0.098 ± 0.017	0.144 ± 0.034	Very partial	MObs
31 May 2018	2458270.642 ± 0.005	14.62 ± 2.26	0.068 ± 0.011	0.115 ± 0.034	Partial	MObs
24 April 2019	2458597.8401 ± 0.0025	9.42 ± 0.36	0.106 ± 0.004	0.1407 ± 0.0048	Almost complete	MObs
23 April 2019	2458601.7865 ± 0.0013	12.28 ± 0.38	0.081 ± 0.003	0.1677 ± 0.0056	Almost complete	MObs
23 March 2020	2458932.8746 ± 0.0009	11.23 ± 0.19	0.089 ± 0.002	0.1331 ± 0.0033	Complete	MObs
21 April 2020	2458960.46415 ± 0.00037	11.120 ± 0.076	0.0899 ± 0.0006	0.12896 ± 0.00081	Complete	TESS
24 April 2020	2458964.40590 ± 0.00036	11.118 ± 0.079	0.0899 ± 0.0006	0.13070 ± 0.00079	Complete	TESS
06 May 2020	2458976.22962 ± 0.00036	11.104 ± 0.075	0.0901 ± 0.0006	0.13030 ± 0.00079	Complete	TESS
10 May 2020	2458980.16968 ± 0.00035	11.062 ± 0.075	0.0904 ± 0.0006	0.13007 ± 0.00078	Complete	TESS
07 June 2020	2459007.7751 ± 0.0077	8.13 ± 1.97	0.123 ± 0.030	0.098 ± 0.038	Partial	MObs
12 May 2021	2459342.806 ± 0.033	14.17 ± 2.34	0.068 ± 0.011	0.084 ± 0.034	Very partial	MObs
18 July 2021	2459409.7753 ± 0.0087	14.89 ± 1.76	0.067 ± 0.008	0.1676 ± 0.0089	Partial	MObs

Notes: Mid-transit times are given in Barycentric Julian Dates (Barycentric Dynamical Time), the orbital semi-major axis (a) in terms of the stellar radius (r_s), and the planetary radius (r_p) relative to the stellar radius. exotic outputs a/r_s, so a column giving the inverse is given for convenience when comparing with a later model and the literature. Uncertainties are 1σ "MObs" indicates the source is the MicroObservatory telescope described in the text, "TESS" indicates this space telescope, and for amateur-contributed data the name of the observer and their general location is given. The amateur-contributed data were sourced from the NASA Exoplanet Archive.

fluxes, such as obtained through other reduction packages for photometry, and fit a transit model (as we will see below for data from the TESS space telescope). exotic automatically scrapes "priors" for the MCMC fitting from the online NASA Exoplanet Archive (NEA; Akeson *et al.* 2013). "Priors" are assumed probability distributions based on previous (prior) experience. Limb darkening values are taken from exofast (Eastman *et al.* 2013).

The MicroObservatory observations included only science frames and dark images. No flat fields were collected, while the dark frames were collected at the beginning and end of the observations each night. We followed the reduction process outlined by North and Banks (2022).

The results from the exotic fitting are given in Table 1. Figure 2 plots the observations for each fit together with the model estimated by exotic. There were only 2 complete transits observed out of the 11 clear nights. The other 9 attempts were partial transits, which led us to consider that perhaps XO-1b was subject to transit timing variations (TTV). We expected the telescope time to be scheduled such that the transit would be within the planned observation period. Partial transits lead to greater estimated uncertainties. Additional complete transits could lead to confirmation whether XO-1b was subject to TTVs, which could explain why so many of the MObs observation sessions were actually incomplete observations of the transits. To explore this idea further we sourced additional data, namely from the TESS space telescope and from the NASA Exoplanet Archive.

2.2. TESS

The Transiting Exoplanet Survey Satellite (TESS; Ricker *et al.* 2014) has been operational since 2018. XO-1 was observed with a two-minute cadence by TESS over the period 16 April 2020 to 12 May 2020. Four transits were selected from this period, having data to each side of a complete transit. TESS data are of high quality (see Figure 2). Results of the exotic fits can be found in Table 1. Taking arithmetic means across the four values, the planet radius (r_p) was estimated as 0.1300 ± 0.0016 times the radius of its host star (r_s), with the semi-major axis of the orbit (a) being 11.10 ± 0.15 times the stellar radius. By comparison, for the two complete MObs transits exotic estimated a planetary radius of 0.1249 ± 0.0064 and 0.1331 ± 0.0033 stellar radii, within error of the estimate based on the TESS data. The orbital radius estimates from these MObs transits were 11.99 ± 0.78 and 11.23 ± 0.19, again within formal error of the estimate from the TESS data.

We also applied the algebraic transit model of Mandel and Agol (2002) to two of the TESS transits, in order to estimate the orbital inclination of the planet and the limb darkening (which are not available from exotic). We prepared this in the R programming language and made use of the Hamiltonian Markov Chain Monte Carlo (MCMC) optimization method (hereafter abbreviated as HMC) as implemented in the Stan programming language (Carpenter *et al.* 2017; Stan Development Team 2022). Monte Carlo techniques are sampling methods. MCMC involves sampling from probability distributions using Markov chains. A Markov Chain is a

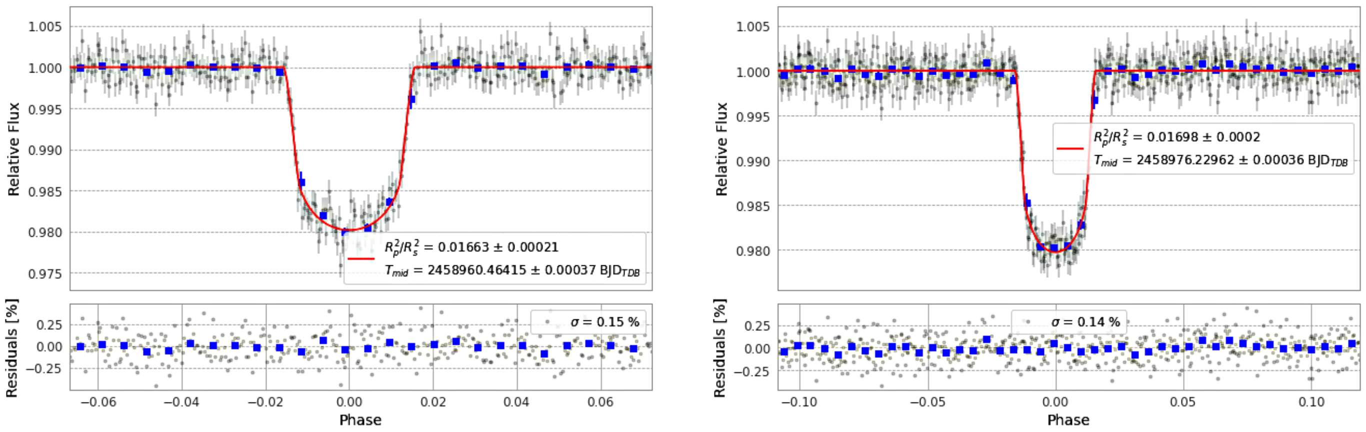

(a) 21 April 2020

(c) 06 May 2020

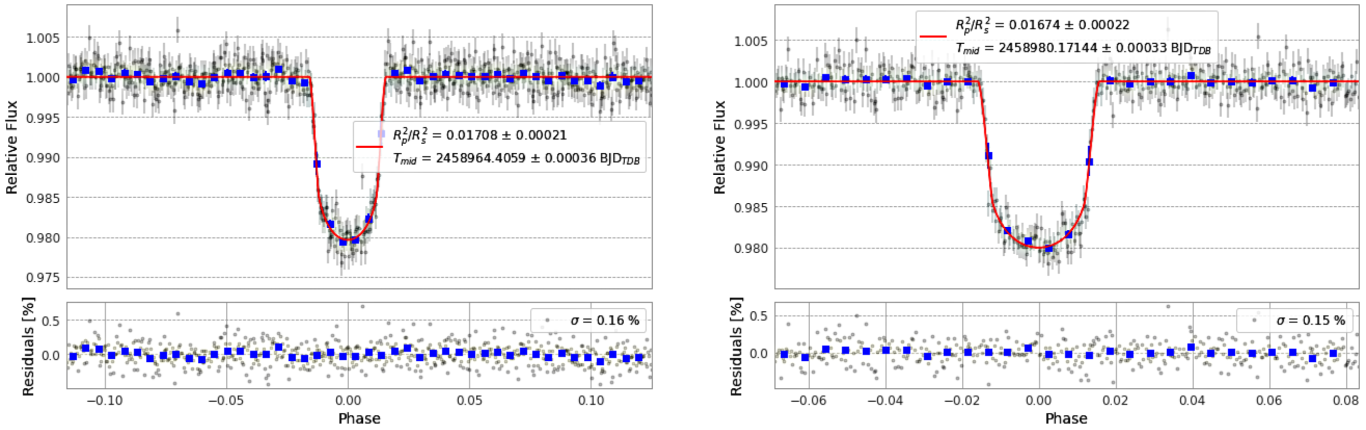

(b) 24 April 2020

(d) 10 May 2020

Figure 2. TESS XO-1b transit data for four dates and best fit transit models. We used a different way of running exotic to model the TESS data. Instead of using a GUI-based wrapper for EXOTIC, we directly called exotic as a library inside a PYTHON program. This allowed us to input zero airmasses for the TESS data since the space telescope is outside the Earth's atmosphere. A downside was that we had no control of where the information box, giving output parameters, was placed on the charts.

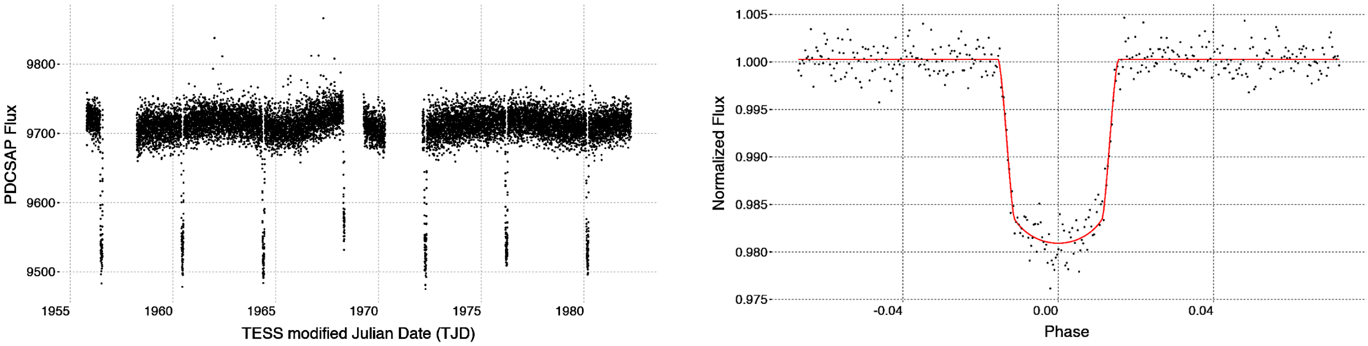

(a) TESS photometry

(b) 20 April 2020 transit

Figure 3. The figure on the left (a) shows the non-normalized Pre-search Data Conditioning Simple Aperture Photometry (PDC SAP) generated by the TESS team, which removed longstanding systematic trends and so provides better data quality than simple aperture photometry (also available from MAST). Exposures were 120-second and the data period covered 16 April 2020 to 12 May 2020. The relatively small variability of the host star is clearly visible. The figure on the right (b) shows one of these transits plus the optimal model generated by the HMC code. This transit is the first following the break in the data to the left of Figure 3a.

sequence of events, sampled from an unknown or target distribution, with each state depending only on the state of its immediate predecessor and not on earlier states. MCMC techniques allow the use of such chains to draw samples which are progressively more likely to represent the target distribution, explaining their use in optimization. A similar implementation was made by North and Banks (2022), where further details of the transit model and the MCMC technique can be found. We therefore refer the interested reader to that paper in *JAAVSO* for further details. MCMC takes a long time to run. Typically a single fit took several days to complete on the laptops we were using, explaining why we did not fit all of the available transits with this method.

The model of Mandel and Agol (2002) has the following parameters: r_p is the planetary radius relative to that of the host star (r_s), a is the orbital semi-major axis in terms of the stellar radius, u is the linear limb darkening co-efficient, cos i is the cosine of the orbital inclination, and L is the adjustment in normalized flux. The implementation of this model in HMC included the parameter σ, which is an estimate of the Gaussian noise, and "offset," which is the adjustment in phase.

Figure 3 displays the TESS photometry, together with one of the model transit fits to the TESS data. Figure 4 displays the "corner" or "pair" plot which was output by the HMC optimization. A pair plot like this allows comparisons between pairs of variables. The density plots in the upper left show the distribution of parameter estimates by the Markov chains for each of the pairs of variables, e.g., the sub-plot in the upper left corner plots the distribution of parameter estimates for the random noise σ (which is taken as a variable in the fitting model) and the planetary radius r_p. The color red indicates that many steps (or parameter estimates) were in this point, whereas green indicates that there were fewer steps at a point shaded with this color and is therefore a lower fit to the observed data. The histograms on the diagonal from lower left to upper right show the distributions of each of the fitting variables. Finally, the

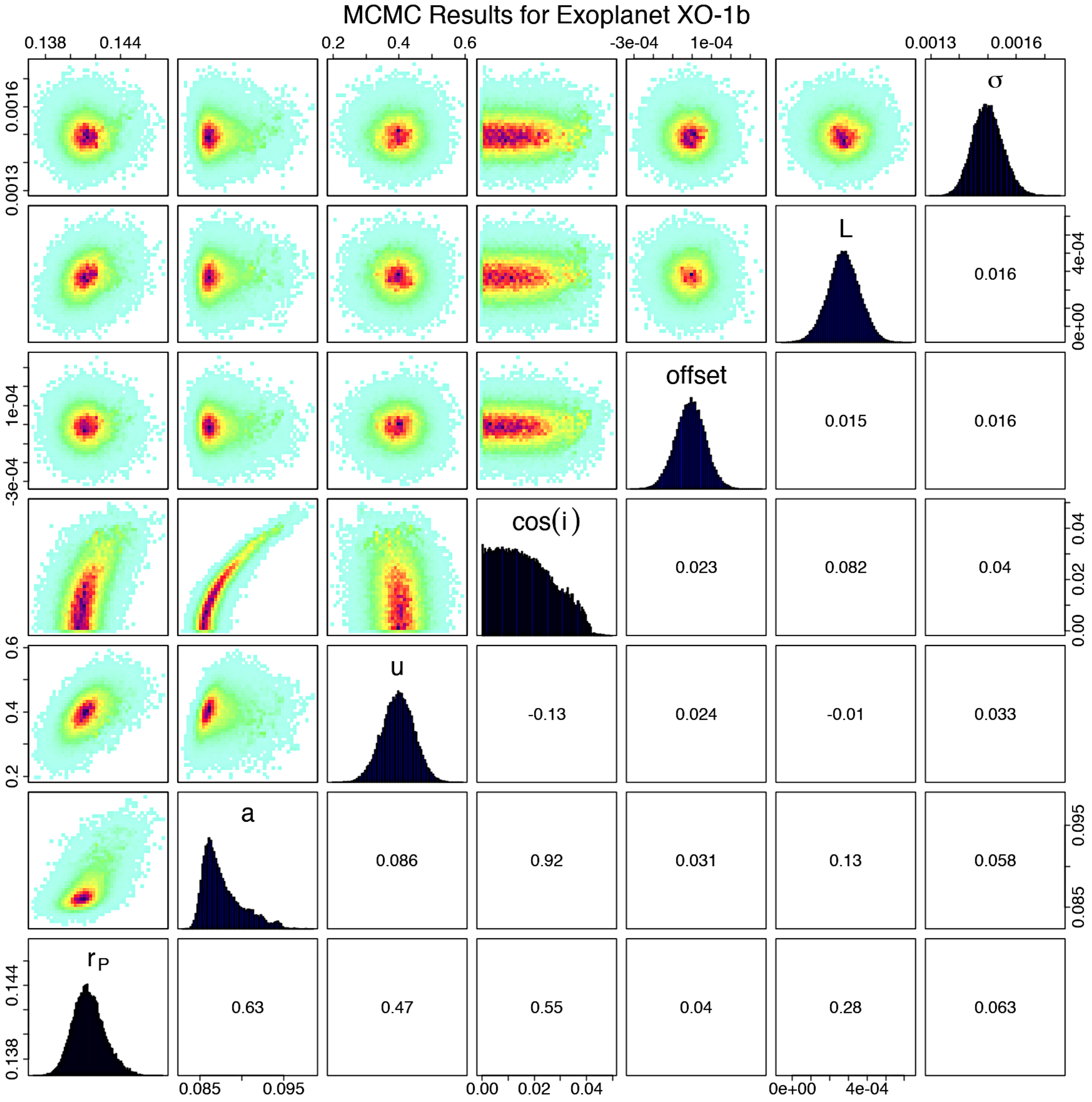

Figure 4. Pair-plot of the MCMC results for the 20 April 2020 transit of XO-1b. This represents 100,000 steps in each of the four Markov chains. An additional 50,000 steps (per chain) at the start of the optimization were excluded as "burn-in." The axes of the density plots are in the units of each parameter, as given in the text. The numbers in the lower right of the diagram are the Pearson correlation coefficients (R) for each pair of variables. This diagram was prepared using the base R programming language command "pairs."

correlations between the variables are given as the values in the boxes in the lower right. For example, we can see that the correlation between σ and the linear limb darkening u is close to zero (0.033), as we would expect. The figure is based on 100,000 steps by the chains, following the initial 50,000 steps of each chain being discarded. These initial steps are routinely discarded by MCMC practitioners since the starting parameters for the chains are likely to be far from the final optimal values. The parameter values therefore will trend as the optimizer steps towards the global minimum (best fitting values) and should be discarded from the error analysis.

Fitting the first modelled transit (second transit from the left in Figure 3a) resulted in r_p / r_s being estimated as 0.14161 ± 0.0006, $r_s / a = 0.0877 \pm 0.0007$, inclination i = 89.03 ± 0.04 degrees, and limb darkening u = 0.396 ± 0.001. Uncertainties are single sigma. The second transit (second from the right in Figure 3a) modelled using the HMC technique resulted in r_p / r_s being estimated as 0.14558 ± 0.0004, $r_s / a = 0.0922 \pm 0.0008$, inclination i = 88.26 ± 0.12 degrees, and limb darkening u = 0.451 ± 0.003. The formal uncertainties for the two sets of parameters do not, in general, overlap, suggesting that these formal one-sigma errors are under-estimates. This could partially be due to the stellar variations visible in Figure 3a, which was not accounted for in our modelling, together with a deficiency in the implemented model described below.

Our estimates for orbital inclination are in good agreement with the literature, e.g., 88.81 ± 0.50 degrees (Stassun *et al.* 2017), $88.81^{+0.70}_{-0.30}$ (Bonomo *et al.* 2017), 89.06 ± 0.84 (Southworth 2010), 88.8 ± 0.2 (Burke *et al.* 2010), $88.81^{+0.70}_{-0.30}$ (Torres *et al.* 2008), $89.31^{+0.46}_{-0.53}$ (Holman *et al.* 2006), 87.7 ± 1.2 (McCullough *et al.* 2006), and 88.92 ± 1.04 (Wilson *et al.* 2006). There is considerable variation in the literature estimates, in line with the HMC modeling.

Our HMC-based estimates for r_p are substantially larger than the literature, e.g., compared to 0.138 ± 0.020 (Wilson *et al.* 2006), 0.13102 ± 0.00064 (Holman *et al.* 2006), $0.1326^{+0.0004}_{-0.0005}$ (Torres *et al.* 2008), and $0.1315^{+0.0016}_{-0.0020}$ (Patel and Espinoza 2022) as well as our EXOTIC estimates. This leads to our estimates for r_p / r_s being correspondingly smaller than the literature and our EXOTIC estimates. We believe the problem lies in our use of the "small planet approximation," where we did not take into account the gradient of the limb darkening coefficient. Instead we took the limb darkening value corresponding to the centre of the planetary disc in front of the stellar disk, and applied this value across the entire obscured region. This appears to be too much of an approximation for XO-1b, which is a relatively large planet compared to its host star. Croll *et al.* (2007) noted that the small planet approximation is valid for $r_p = 0.1\ r_s$ and smaller. We therefore plan that future application of this simple model should be restricted to planets inside this limit, or the model be modified to account for the changing limb darkening values in the obscured regions. Despite this setback we have included the HMC analysis as a demonstration that motivated high school students can develop such analyses, as well as a "warning" for subsequent student research projects either to choose smaller planets relative to their stars or to integrate the limb-darkening flux to better account for the changes in limb darkening (particularly near the early ingress and late egress of the planet where limb darkening is at its greatest and so will impact estimates of the planetary radius). Modeling the stellar variation, such as through a Gaussian process (see Ng *et al.* 2021), would also be advisable.

2.3. NASA Exoplanet Archive

Light curves are available from the NASA Exoplanet Archive (NEA) which were collected by amateur astronomers and placed into the public domain. We examined the available data sets and selected those with complete or nearly complete transits, ignoring data sets that only partially covered the transits since we were primarily interested in as accurate as possible measurements of the mid-transit timings. Again, results from the EXOTIC fittings may be found in Table 1. Figure 5 presents the modelled data sets together with the light curves based on the best fitting models. The NEA fitted automatically a simple model to each dataset to estimate the mid-transit times (without a formal error being provided). The mean difference between the two methods (EXOTIC and NEA) was –49 ± 97 seconds, which is larger than we had hoped but reassuring that there is no significant difference from zero. We chose to model the period with the results from EXOTIC, as we believe this is a more complete transit model.

2.4. Period analysis

We performed regression analysis of the mid-transit times using R. A linear regression fitted the data well; no need for higher-order polynomial terms was required. We included the mid-transit timings of Bonomo *et al.* (2017), Patel and Espinoza (2022), and Kokori *et al.* (2022) to expand the data set. The period was estimated as 3.941498 ± 0.000008 days, using all available measurements. We subsequently restricted analysis to just complete and near complete transits, leading to a period estimate of 3.9415049 ± 0.0000008 days, which is outside the formal error range of the first estimate using all available data. Given the uncertainty of the fits to less complete data, we prefer the second period estimate. Our estimate is in good agreement with the literature values, e.g., $3.9415160^{+0.0000230}_{-0.0000250}$ days of Patel and Espinoza (2021), 3.941530 ± 0.000027 (Stassun *et al.* 2017), 3.9415128 ± 0.0000028 (Southworth 2010), etc.

Figure 6a shows the residuals from the linear fit to all available data, while Figure 6b shows the residuals from the fit to only complete or near complete transits. Figures 6c and 6d expand sections of the data shown in Figures 6a and 6b, respectively. There is no clear evidence for transit timing variations, with the formal uncertainties for the majority of residuals overlapping zero. However, there could be a bias introduced by our choice of only including complete transits for the earlier data. We therefore recommend that XO-1 continue to be monitored so that additional transits may be observed and timed. TTVs are therefore not the likely cause of the timing problems noted with the MObs data.

3. Discussion

We have presented reductions of 26 transit events for X0-1b, deriving an orbital period and finding no evidence for transit timing variations. Our estimates for the planetary and orbital

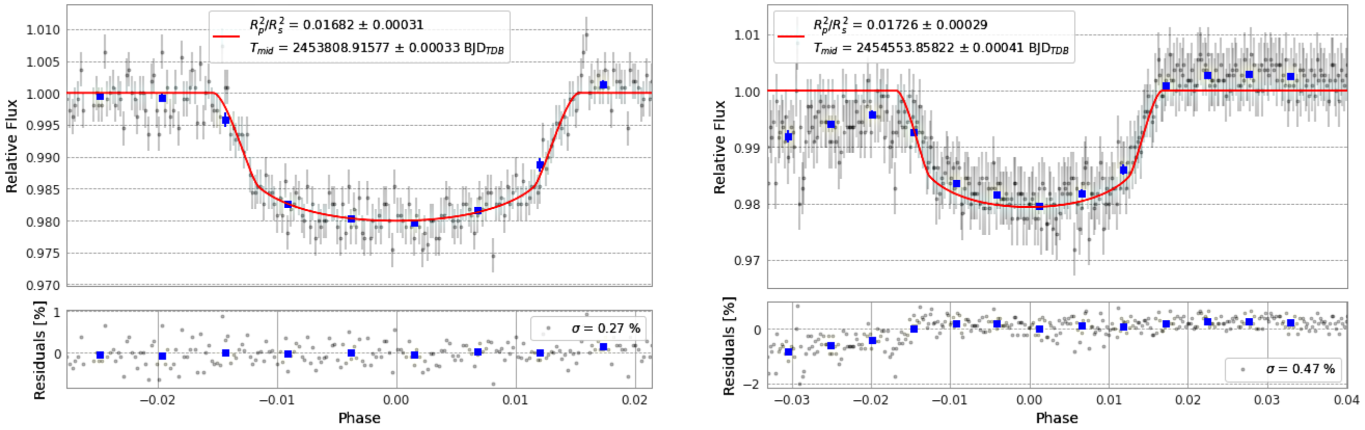

(a) 14 March 2006 (R)

(d) 28 March 2008 (R)

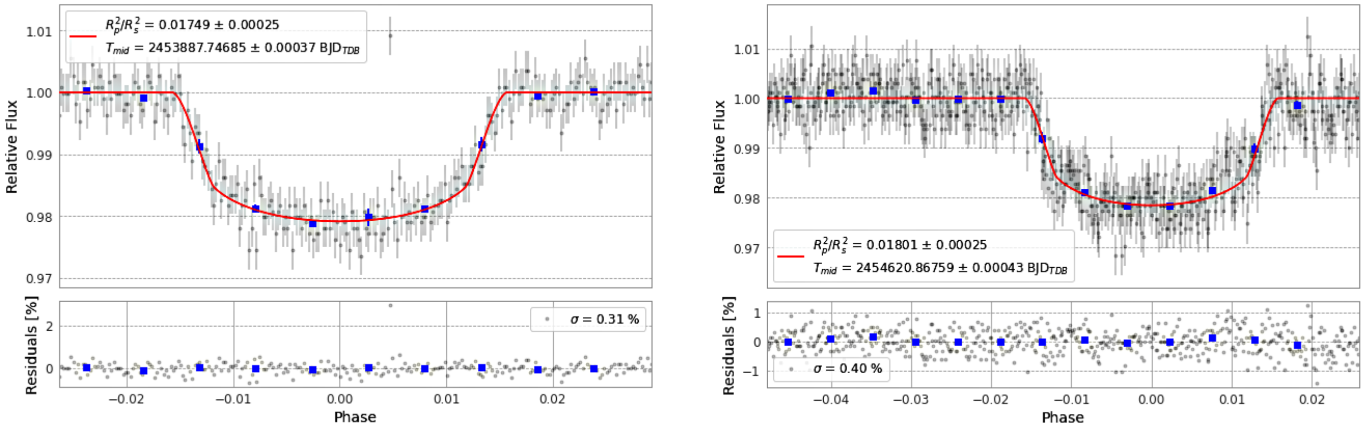

(b) 01 June 2006 (R)

(e) 03 June 2008 (R)

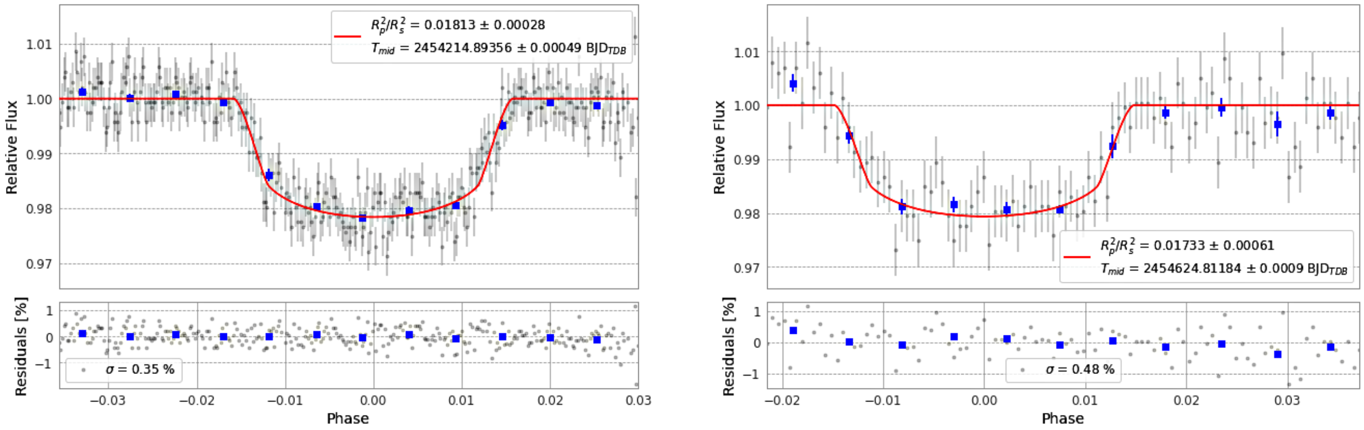

(c) 29 July 2007 (R)

(f) 07 June 2008 (R)

Figure 5. XO-1b amateur contributed transit data and models: The red lines show the expected light variation based on the best fitting exotic model for each transit. The filters used are indicated by the text in brackets in the sub-figure captions: “B” is Johnson B, “R” is Johnson R, and “Clear” is no filter.

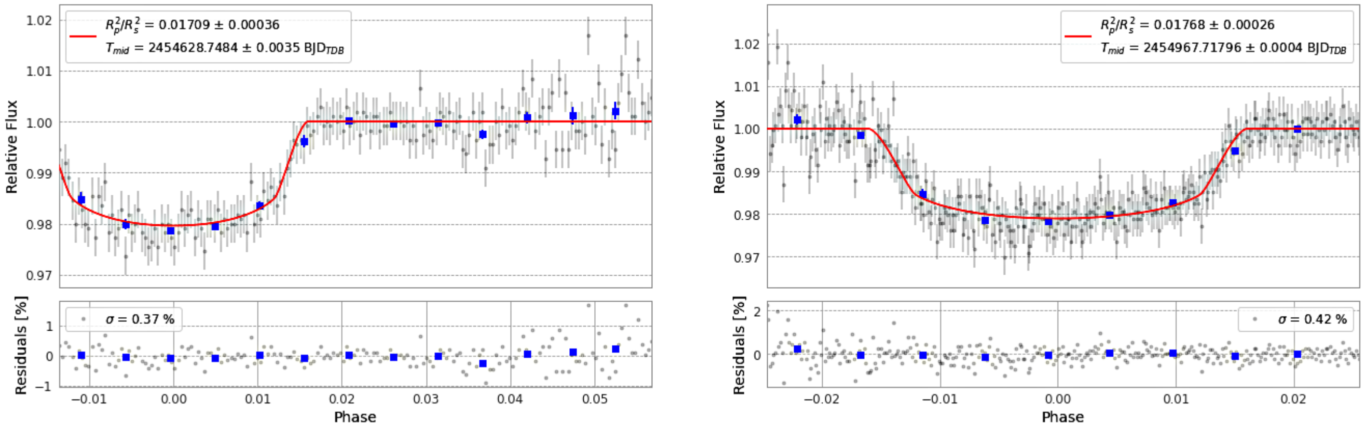

(g) 11 June 2008 (R)

(j) 16 May 2009 (R)

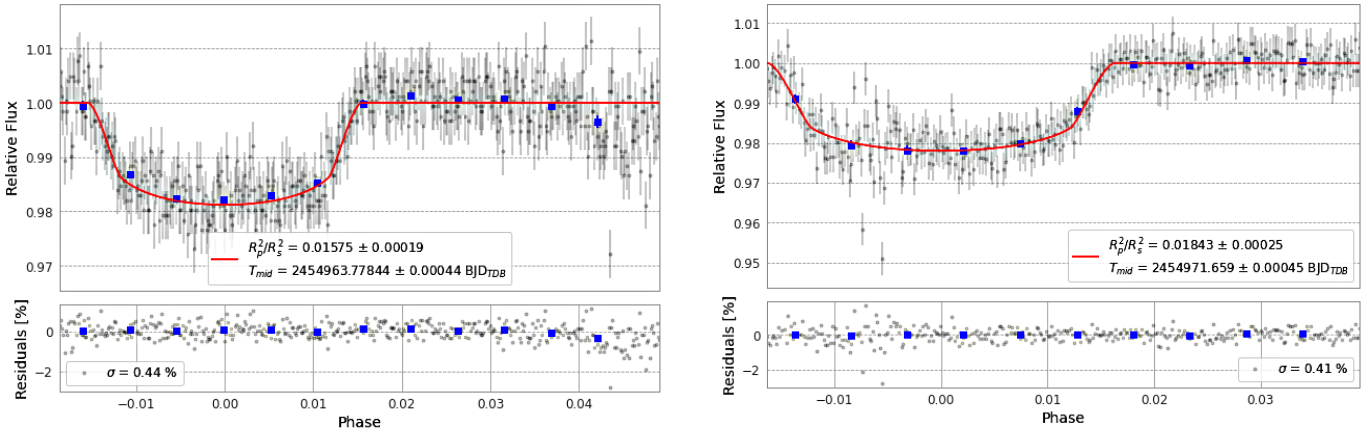

(h) 02 May 2009 (R)

(k) 20 May 2009 (R)

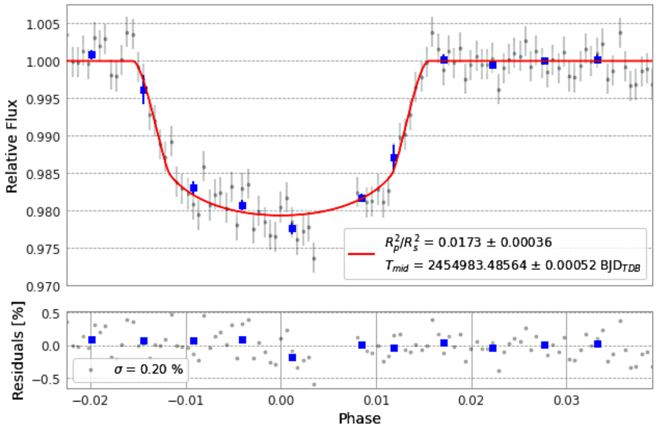

(i) 13 May 2009 (R)

Figure 5. XO-1b amateur contributed transit data and models, cont.

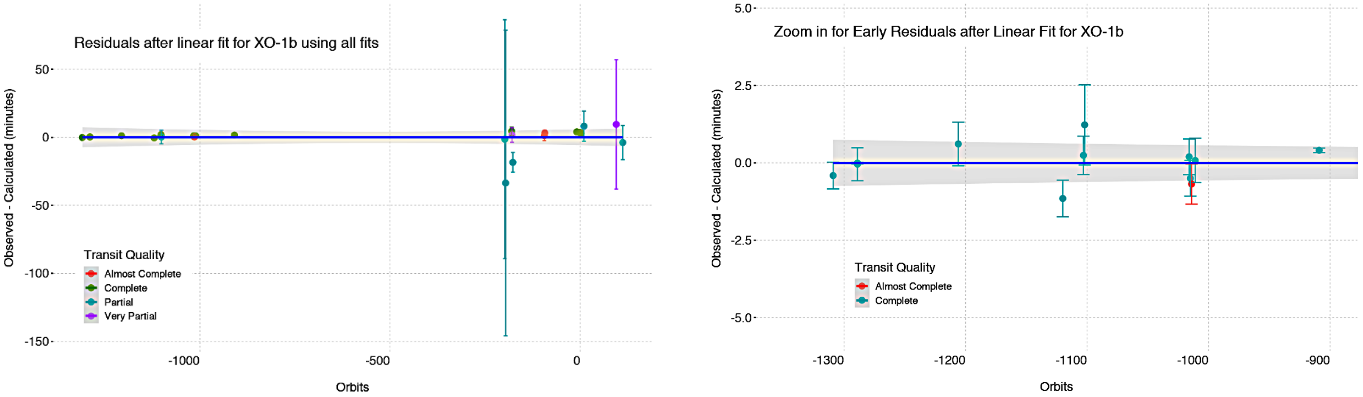

(a) All transits

(c) Fits to early complete and near-complete transits

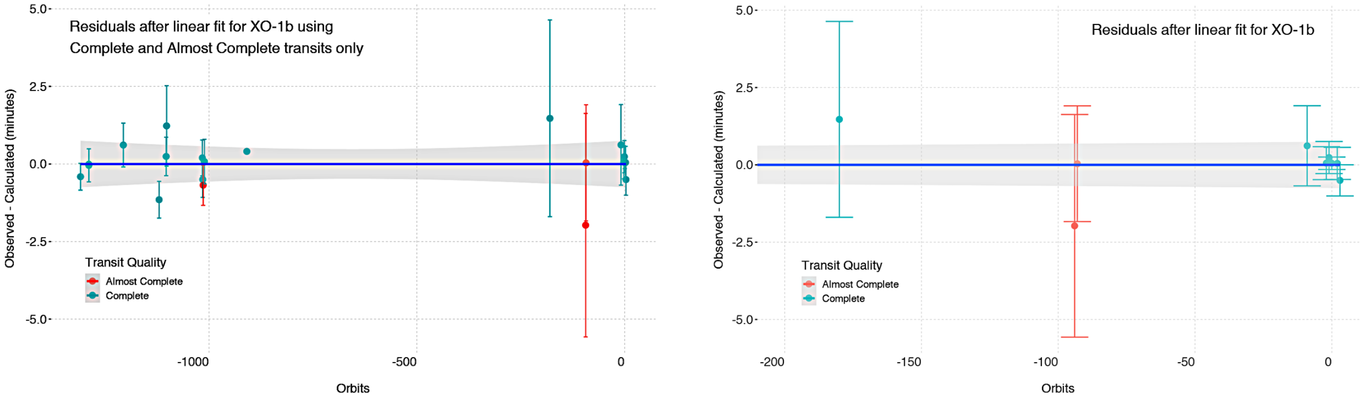

(b) Only complete and near-complete transits

(d) Fits to late complete and near-complete transits

Figure 6. Regression fits to the mid-transit times. Sub-figure 6a shows the the residuals are a linear fit to the mid-transit timings. The grey shaded area plots the 3σ confidence range of a linear regression to these residuals. Sub-figure 6b is similar, but using only transits that were considered complete or nearly complete (see Table 1). Sub-figures 6c zooms into the early data in Sub-figure 6b, while 6d zooms into the more recent data.

radii are in good agreement with the literature. We applied Bayesian Optimization together with a simple transit model in order to estimate the orbital inclination, limb darkening, and radii. However, the implementation was too simple for a planet of the relative size XO-1b has to its host star, leading to recommendations on how to improve the modeling for further work.

A possible extension for projects similar to the current one could be to investigate combining observations from several transits together. EXOTIC outputs processed photometry, allowing users of this tool to explore this idea. Data would be phased by the orbital period (such as derived from a regression analysis as in this paper). The combined "transit" could then be analysed to see if the parameter estimates are better defined than in the analyses of the individual transits. This would need to include careful examination of the transit data to see if there were any additional variations in the data, such as might be caused by "star spots," and keeping to the same band passes across the data set.

This project is part of a wider effort, initially involving final year undergraduate (Honors) students in statistics at the National University of Singapore since 2012. Students found the exoplanet and variable star projects to be interesting and challenging, giving them the opportunity to develop an understanding of the scientific method, scientific programming skills (such as R, PYTHON, JULIA, AND FORTRAN), and documentation skills (including scientific publishing and LaTeX). The program was extended to a community college in the US, with similarly favorable results (see, e.g., Parker *et al.* 2021). Banks *et al.* (2020, and references therein) discussed the overall project and its benefits, which hopefully include increasing student interest in astronomy and science in general. They encouraged possible extension to high school students, leading to this particular project as a test case. We believe it confirms that such efforts are worthwhile, both at high school and undergraduate levels—which is supported by the success of other programs reported in this journal such as Stanford Online High School led by Kalée Tock (see, e.g., Bansal *et al.* 2022), the RR Lyrae star clusters project (see, e.g., Soper *et al.*, 2022) led by Dr. M. Fitzgerald (Edith Cowan University, Australia), and papers such as Kim and Percy (2022). There are sufficient astronomical databases and imagery available (or partnerships with active amateur astronomers could lead to interesting photometry or radial velocity based analysis projects), together with easy-to-run analysis tools such as EXOTIC, to create interesting and "bite sized" projects for such students. The workload of a project is an important consideration given that high school students must balance the research project with their high school studies, sporting activities, and college applications. Based on our experience, we strongly recommend projects such as the current one as both interesting for the students, regardless of whether they advance to tertiary study in astronomy, and good for the future support of astronomy.

4. Acknowledgements

This publication makes use of the EXOTIC data reduction package from Exoplanet Watch (also known as Exowatch), a citizen science project managed by NASA's Jet Propulsion Laboratory (JPL) on behalf of NASA's Universe of Learning and which is supported by NASA under award number NNX16AC65A to the Space Telescope Science Institute. We thank the Harvard-Smithsonian Center for Astrophysics for the MicroObservatory (MObs) data kindly made available by Frank Sienkiewicz for this project. These data would be available on reasonable request to him. MObs data for individual transits can also be requested from the Exoplanet Watch website (https://exoplanets.nasa.gov/exoplanet-watch/how-to-contribute/data-checkout/). This research has made use of the NASA Exoplanet Archive, which is operated by the California Institute of Technology, under contract with the National Aeronautics and Space Administration under the Exoplanet Exploration Program. We thank the University of Queensland for collaboration software. This paper includes data collected by the TESS mission and obtained from the MAST data archive at the Space Telescope Science Institute (STScI). STScI is operated by the Association of Universities for Research in Astronomy, Inc., under NASA contract NAS 5-26555. We are grateful to the amateur astronomers who kindly placed their transit observations into the NEA for public access. We thank the anonymous referee for their comments and guidance which improved the paper.

References

Akeson, R. L., *et al.* 2013, *Publ. Astron. Soc. Pacific.*, **125**, 989.

Banks, T., Rhodes, M. D., and Budding, E. 2020, *South. Stars*, **59**, 17.

Bansal, A., Hamrick, P., and Tock, K. 2022, *J. Amer. Assoc. Var. Star Obs.*, **50**, 34.

Bonomo, A. S., *et al.* 2017, *Astron. Astrophys.*, **602**, 107.

Burke, C. J., *et al.* 2010, *Astrophys. J.*, **719**, 1796.

Carpenter, B., *et al.* 2017, *J. Statistical Software*, **76**, 1.

Croll B., *et al.* 2007, *Astrophys. J.*, **658**, 1328.

Eastman, J., Gaudi, B. S., and Agol, E. 2013, *Publ. Astron. Soc. Pacific*, **125**, 83.

Holman, M. J., *et al.* 2006, *Astrophys. J.*, **652**, 1715.

Kim, J. V. E., and Percy, J. R. 2022, *J. Amer. Assoc. Var. Star Obs.*, **50**, 178.

Kokori, A., *et al.* 2022, *Astrophys. J., Suppl. Ser.*, **258**, 40.

Mandel, K., and Agol, E. 2002, *Astrophys. J., Lett.*, **580L**, 171.

McCullough, P. R., *et al.* 2006, *Astrophys. J.*, **648**, 1228.

Ng, S. Y., Jiadi, Z., Püsküllü, Ç, Banks, T., Budding, E., and Rhodes, M. D. 2021, *J. Astrophys. Astron.*, **42**, 110.

North, A., and Banks, T. 2022, *J. Amer. Assoc. Var. Star Obs.*, **50**, 184.

Parker, R., Parker, L., Parker, H, Uddin, F., and Banks, T. 2021, *J. Amer. Assoc. Var. Star Obs.*, **49**, 178.

Patel, J. A., and Espinoza, N. 2022, *Astron. J.*, **163**, 228.

Ricker, G. R., *et al.* 2014, *Proc. SPIE*, **9143**, 914320 (DOI: 10.1117/12.2063489).

Sadler, P. M., *et al.* 2001, *J. Sci. Education Technol.*, **10**, 39 (DOI: 10.1023/A:1016668526933).

Soper, C., Tenenbaum, C., Lounsbery, A., Rheiner, J., and Klassen, D. 2022, *J. Amer. Assoc. Var. Star Obs.*, **50**, 28.

Southworth, J., 2010, *Mon. Not. Roy. Astron. Soc.*, **408**, 1689.

Stan Development Team. 2022, RStan: the R interface to Stan (http://mc-stan.org).

Stassun, K. G., Collins, K. A., and Gaudi, B. S. 2017, *Astron. J.*, **153**, 136.

Torres, G., Winn, J. N., and Holman, M. J. 2008, *Astophys. J.*, **677**, 1324.

Wilson, D. M., *et al.* 2006, *Publ. Astron. Soc. Pacific*, **118**, 1245.

Zellem, R. T., *et al.* 2020, *Publ. Astron. Soc. Pacific*, **132**, 054401 (DOI: 10.1088/1538-3873/ab7ee7).

Investigation of the Variable Star CH Camelopardalis in the Planetary Nebula NGC 1501

Trent Mosher
Aisha Randhawa
Carolina Noviello
Adela Horsting
Kalée Tock
Stanford Online High School, Academy Hall Floor 2 8853, 415 Broadway, Redwood City, CA 94063; kaleeg@stanford.edu

Received October 26, 2022; revised June 13, 2023; accepted June 19, 2023

Abstract Time series images of the planetary nebula NGC 1501 were taken over several nights from the Las Cumbres Observatory robotic telescope network. Light curves of the central variable pre-white dwarf of NGC 1501, CH Cam, were derived using three different aperture photometry methods: image stacking on AstroImageJ, a custom Python program that used Source Extractor photometry, and a point spread photometry method. The light curves resulting from these photometric reductions were period-folded with multiple software routines including Skynet plotting, Astrosource, Period04, and Peranso. Approximately 30 prospective periods, ranging from 3 minutes to 110 minutes, were found. Some of these were similar to periods identified in previously-published literature, while others were not. Because CH Cam has been shown to have several pulsation modes, two pre-whitening methods—Period04 software and a custom Python sine-subtraction program—were also employed. Inconsistencies between periodograms resulting from the different photometric and analytic methods employed here, together with the low amplitude of the pulsations relative to the light of the background nebula and the expectation that these may vary with time, prevent us from drawing a firm conclusion about the pulsations of CH Cam.

1. Introduction

Commonly known as the Oyster Nebula, NGC 1501 (TIC 084306468) was discovered by William Herschel in 1787. It is characterized by its tetra-lobed ellipsoid shape (Sabbadin *et al.* 2000). Its central star, CH Camelopardalis (CH Cam), has coordinates 61.747487°, 60.920610° and parallax 0.5789 milliarcseconds, implying that it is a little over 1720 parsecs from Earth (Gaia Collab. *et al.* 2016; Babusiaux *et al.* 2023).

CH Cam is found in the instability strip on the Hertzsprung-Russell Diagram, to the left and above where white dwarf stars are found. It is classified as a GW Vir pulsating pre-white dwarf (pre-WD). GW Vir stars are recognized as having multi-periodic variations in luminosity with periods ranging from 300 to 6000 seconds, and are known to exhibit non-radial g modes (Córsico *et al.* 2019). Within CH Cam's classification as a pre-white dwarf, it is further described as a planetary nebula nucleus variable (PNNV) and a WCE or early-WC, which is a pulsating Wolf-Rayet with a dominant carbon line visual spectrum (Córsico *et al.* 2021; Ciardullo and Bond 1996). Specifically, it is classified as a WC4 star. CH Cam has $\log(T_{\mathrm{eff}}) = 4.91 \pm 0.03$ and a surface chemical composition rich in helium, carbon, and oxygen (Bond *et al.* 1996).

Past research suggests that because of the current evolutionary stage of CH Cam, its pulsations likely change over a time scale of months. Not only is there is some expected variation in the magnitude and frequency with which the periods show up, but also, there is a possibility that some periodicities sometimes may not be present at all (Bond *et al.* 1996). Because of this variable star's location in the center of a planetary nebula, its small expected variations, and the fact that these may be changing with time, this target is particularly challenging.

CH Cam's variations were first detected by Ciardullo and Bond (1996), who found 10 periodicities between 1154 and 2000 seconds with low power spectrum amplitudes. Those authors used a software program called CLEAN (Roberts *et al.* 1987) to analyze the power spectrum, which demonstrated various low-frequency pulsation modes, as well as large variations in amplitude from one run to the next. These periods can be found in Table 1 (Bond *et al.* 1996). Later observations using 2019 TESS data detected 16 periods ranging between 1254 and 2077 seconds with amplitudes between 0.55 and 1.77 ppt (Córsico *et al.* 2021). This research used Fourier transforms and a customized pre-whitening tool with a 0.1% significance threshold to derive their variations.

Since the pixel size of the TESS telescope is large, it is useful to follow up TESS observations with images from ground-based telescopes that have smaller pixels, as is done in this work. Specifically, 218 images were taken across 7 different nights in late February and early March 2022 according to the target's window of visibility and our telescope time allotment. Each image was taken with a 150-second exposure time and a Johnson B filter. We did not have access to information on the characteristics of each night that images were taken, but the images we used were free of defects. Listed in Table 2 are the coordinates of CH Cam, and the comparison stars used in our research, which were chosen using the AAVSO's Variable Star Plotter (AAVSO 2022). The chosen comparison stars were the closest in the field in distance and in magnitude to the target star. Images for which the stars were blurry or the target was not centered were removed from the series.

This study employed three different photometries: AstroImageJ (AIJ; Collins *et al.* 2017), a Source Extractor module called via custom code written in Python (Bertin

Table 1. Bond *et al.* (1996) periods of CH Cam.

Period (s)	*Period (minutes)*	*Amplitude (of Power Spectrum)*
1154.36 ± 0.06	19.24	5.00 ± 0.37
1168.90 ± 0.18*	19.48	1.84 ± 0.37
1251.91 ± 0.13	20.87	2.66 ± 0.36
1251.91 ± 0.13	21.98	5.05 ± 0.36
1372.94 ± 0.22	22.89	1.87 ± 0.35
1431.53 ± 0.25	23.86	1.80 ± 0.36
1512.66 ± 0.28	25.21	1.77 ± 0.36
1760.73 ± 0.22	29.35	3.15 ± 0.36
1892.95 ± 0.32	31.55	2.55 ± 0.36
1999.16 ± 0.46	33.32	1.92 ± 0.36
5234.81 ± 1.62	87.25	3.73 ± 0.36

* *Possible alias (Bone* et al. *1996).*

Table 2. Target and comparison stars magnitudes and coordinates.

Name/Title	*R.A. h m s*	*Dec. ° ' "*	*Mag. V*	*AAVSO AUID*
CH Cam	04 06 59.2	60 55 15.6	14.4	000-BDH-360
Comp 1	04 07 31.35	60 57 38.8	14.081	000-BKG-698
Comp 2	04 07 07.12	60 59 48.3	14.314	000-BKG-699
Comp 3	04 07 39.90	60 57 48.7	14.758	000-BKG-700

and Arnouts 1996), and point spread photometry, which used processed images from Our Solar Siblings pipeline. The five methods of analysis employed in this paper are as follows:

1. 1-term Lomb Scargle Afterglow software Skynet plotting with the AIJ and SExtractor photometries.
2. Prewhitening with the AIJ and SExtractor photometry through a custom code and Period04 (Vanmunster 2004–2021).
3. Phase Dispersion Minimization with the psx photometry.
4. Astrosource's various algorithms including Lomb Scargle with the psx photometry.
5. Peranso's CLEANest algorithm, which simultaneously searches for multiple periods, with the psx photometry.

In addition, we confirmed the results found in Córsico *et al.* (2021) for the 2019 TESS data, which used the Period04 software.

1.1. Nyquist, Aliasing, and Spectral Window

Each of the 7 nights of data was sampled for a few hours at a cadence of about 162 seconds, or 2.7 minutes. Since these were sampled across multiple nights separated by random time intervals, our data count as nonuniform. As described in section 4.1 of VanderPlas (2018), such non-uniformity problematizes the application of the Nyquist frequency. Notably, "For unevenly sampled data, the truth is that the 'Nyquist limit' might or might not exist, and even in cases where it does exist, it tends to be far larger (and thus far less relevant) than in the evenly sampled case" (VanderPlas 2018). For this reason, we do not consider our data to be compromised by the Nyquist limit.

Aside from Nyquist, other aliasing artifacts can arise. Peranso's Spectral Window eliminates periods that are likely artifacts of sampling, which provides validation of the periods that it finds. In order to confirm our results, we used several period-finding methods such as Persanso and others on our data.

2. Instrumentation

The target star was imaged using 0.4-meter SBIG telescopes in Haleakala, Hawaii; MacDonald, Texas; and Teide, Spain, from the Las Cumbres Observatory Global Telescope network (Brown *et al.* 2013). The LCO network has standardized telescopes and cameras across all locations. The 218 images were taken with a SBIG STL 6303 camera. The camera has a format of 3K × 2K 9-micron, and a Field of View of 29.2 × 19.5 arcminutes. The pixel size used is 0.571 arcsecond/pixel. The files use 1 × 1 binning. The read noise is 14.5 e-, the gain is 1.6 ADU/e, and the dark current is 0.03 at 100° C.

3. AstroImageJ photometry

3.1. Description

A light curve showing all data from the AstroImageJ (AIJ) analysis was rendered using the Python library called bokeh. plotting and is shown in Figure 1. AIJ performs differential aperture photometry, which involves measuring the flux of a target star relative to the combined flux of one or more comparison stars (Collins *et al.* 2017). The target star's relative flux is then calculated by dividing the target star's net integrated counts by the sum of the net integrated counts of all comparison stars. Net integrated counts represent the sum of all ADU counts within the aperture (after subtracting the average background flux between inner and outer annulus). The aperture size of 6 pixels (px), which was used for each reduction, was chosen manually because it enclosed the target while limiting the inclusion of the peripheral light of the nebula. The inner and outer radii of background annulus were set at 14 and 21 units,

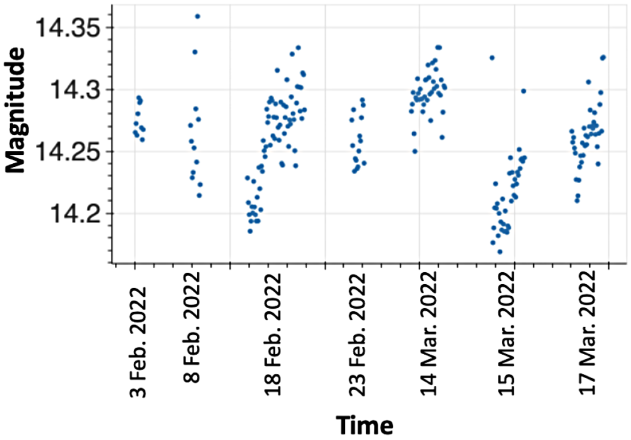

Figure 1. AIJ light curves for all 218 images used in this analysis.

respectively. The settings used on AIJ were accessed from the plot menu under seeing profile → multiple-aperture settings, and included default values of 1.5 for CCD gain, 9.5 for CCD readout noise, and 0.0 for CCD dark current per second.

Aperture photometry data for seven nights of images, totaling 218 images, were downloaded from AIJ into a spreadsheet. The following equation was used to convert the flux to calibrated magnitude:

$$\mathrm{Mag} = -2.5\mathrm{Log10}\ (\mathrm{Flux}) \qquad (1)$$

The instrumental magnitude was then added to the zero point for the telescope, resulting in the calibrated magnitude. Table 3 demonstrates the calculations to obtain calibrated magnitudes for CH Cam and comparison stars 1, 2, and 3 in the first image of Image Set 1.

The calibrated magnitude values for all 218 images and the corresponding Julian Dates were entered into the Skynet plotting software for variable stars, Afterglow (Reichart 2021). The three Afterglow periodograms generated from separate calibration with each comparison star yielded five closely-matching prospective periods. Because the variation between periods found with each of the three comparison stars were negligible but Comp 3 showed the clearest peaks, only the five periods found using Comp 3 as seen in the periodogram in Figure 2 were inputted into the Skynet period-folding algorithm. As shown in Figure 5, all five period folds demonstrated a subtle dip in magnitude and a sine wave-like form. Using Desmos online graphing software, a sine wave was visually fitted to the calibrated target photometry and folded over a period of 89.84 minutes. This yielded an estimated amplitude of 0.037 magnitude, and is shown in Figure 3.

Because the form of the underlying sine wave from Figure 3 was difficult to approximate accurately, the average between each adjacent data point was calculated and plotted. This process was repeated three more times, which resulted in the more pronounced sine wave shown in Figure 4. A sine curve was then manually fitted to the data with more precision, resulting in a changed estimated amplitude of 0.0311 (in contrast with 0.037 as estimated with the non-averaged data). This suggests that the 89.84-minute period of CH Cam fluctuates 0.0311 in magnitude, mirroring data from the literature that detected similar low-amplitude pulsations.

This analysis suggests that the star CH Cam has five periods ranging from 84.56 to 110.54 minutes, shown in Figure 5. Of these periods, 84.56 and 89.61 minutes most closely correspond with the previous published period of 87.23 minutes. A list of these periods and their comparison to the periods found in the literature is shown in Table 4.

Table 3. Sample calculation of calibrated magnitude: first image.

Image 1 Set 1	*Netint Counts*	*Mag.*	*Zero Point*	*Calibrated Mag.*
CH Cam	84006	–6.87	22.75	15.88
Comp 1	80307	–6.82	22.75	15.93
Comp 2	97501	–7.03	22.75	15.72
Comp 3	52657	–6.36	22.75	16.39

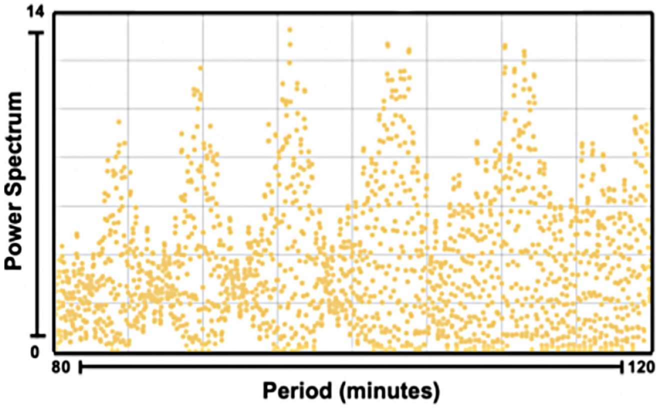

Figure 2. AIJ periodogram from 0 to 120 minutes.

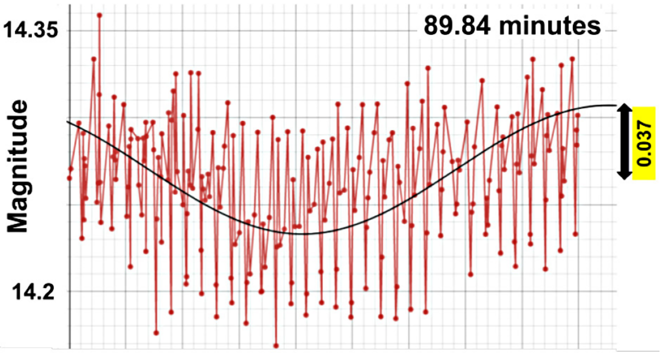

Figure 3. AIJ data period folded over 89.84 minutes and manually fitted with a sine curve. Estimated amplitude = 0.037.

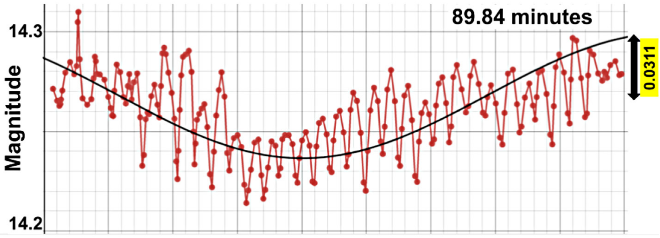

Figure 4. AIJ data period folded over 89.84 minutes with adjacent points averaged four times. Estimated amplitude = 0.0311.

4. Source Extractor method

4.1. Data collection

To confirm the findings from AIJ, a second analysis was employed using Source Extractor (Bertin and Arnouts 1996), accessed through Google Colab and plotted using the Bokeh plotting library. The same 218 images were used in this method. In this process, it was found that Source Extractor was less dependent on aperture size than AstroImageJ was, as there was no difference in the periods found when the aperture size was adjusted. An aperture size of 6 pixels was used to match the previous analysis. In addition, to minimize variation by the comparison star chosen, the data points from each image for each comparison star were averaged. One outlier was identified and removed using lower and upper bounds as in Equation 2, which is sometimes called the Interquartile Range Method.

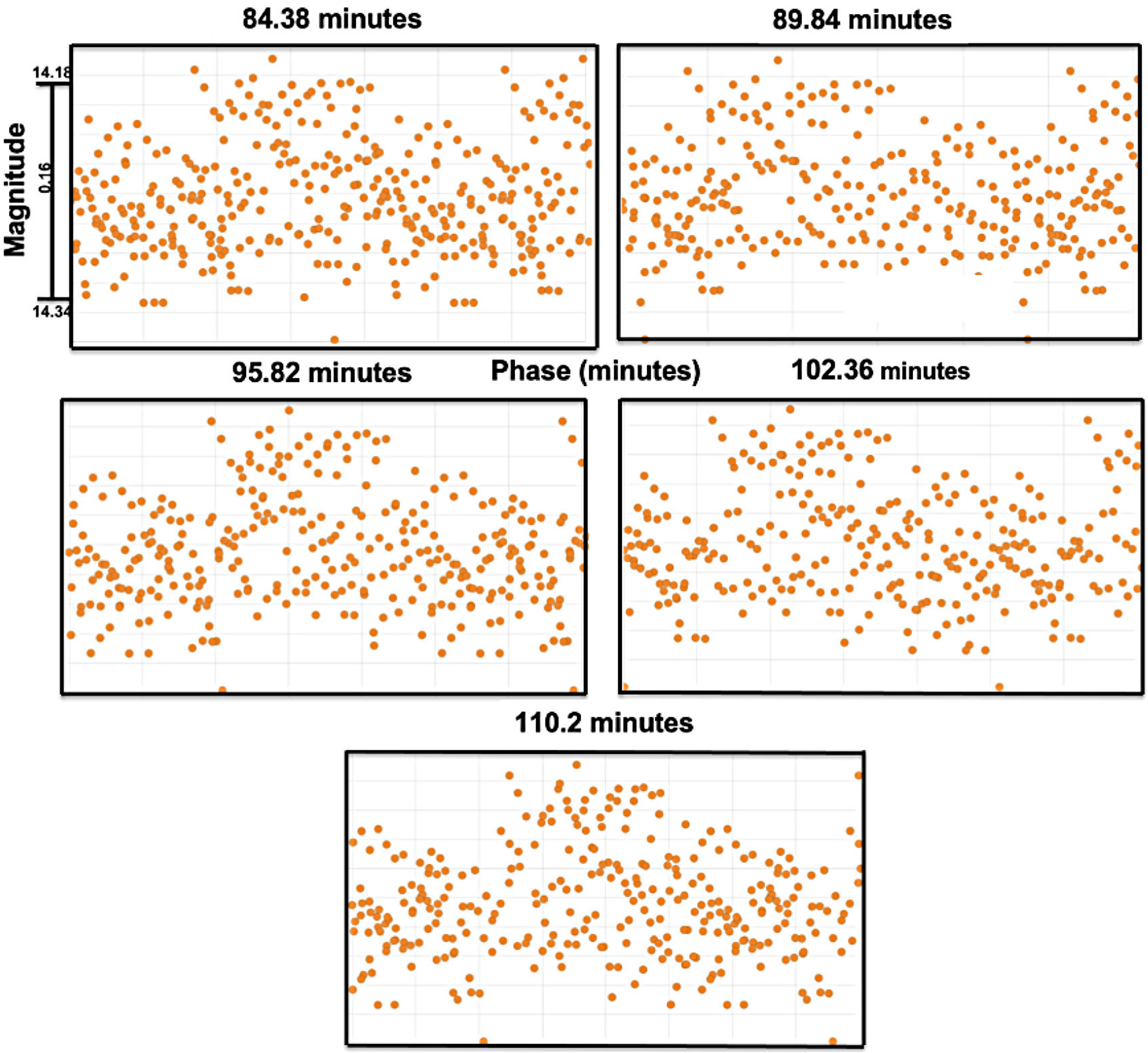

Figure 5. Period folded light curves using AstroImageJ Data. Five prospective periods (in minutes) from the first comparison star. As shown along the y-axis of the first graph, the curves displayed a variation in magnitude of about 0.16. Outliers were not excluded, as they made a negligible difference.

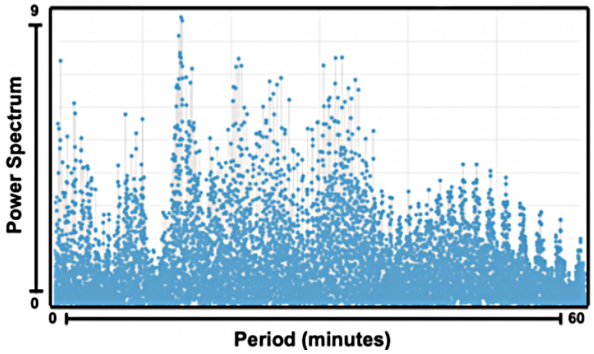

Figure 6. Skynet plotting Source Extractor periodogram from 0 to 60 minutes.

In this equation, Q_1 is the mean of the lower 50% of the data, Q_3 is the mean of the upper 50%, and R is the difference of Q3 – Q_1. Any data points that fell outside this bound were not included in the analysis.

$$B_{\text{Lower}} = Q_1 - 1.5\,R,\ B_{\text{Upper}} = Q_3 + 1.5\,R \qquad (2)$$

4.2. Periodograms

The calibrated SExtractor photometric measurements were folded through the "Variable" and "Pulsar" tabs of Skynet Plotting. The period-finding method employed by both these tabs is the one-term Lomb-Scargle periodogram as described by VanderPlas (2018). Although Lomb-Scargle is also cited as AIJ's period-folding method, the Skynet periodogram of the

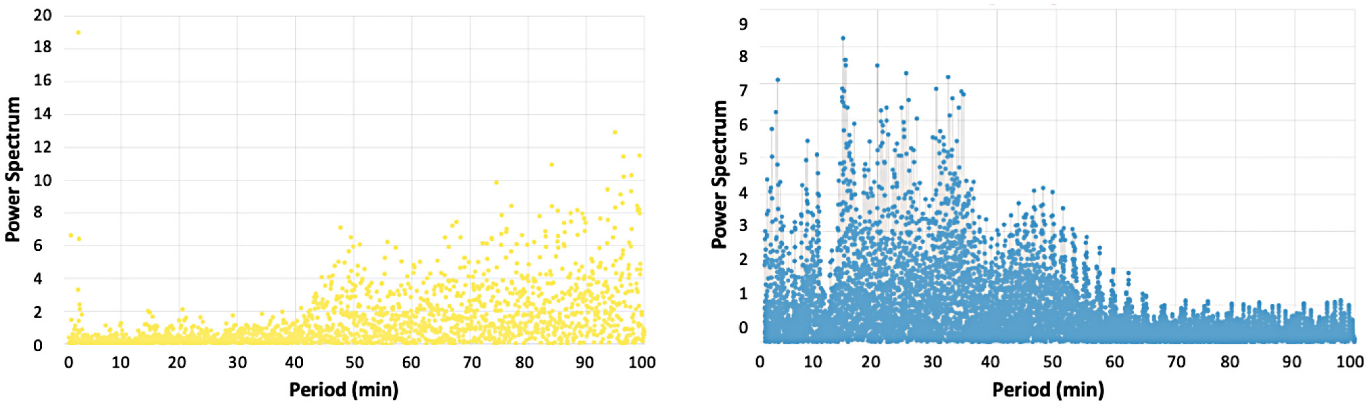

Figure 7. Skynet plotting source extractor period folds for variable tab in Skynet (left) and pulsar tab in Skynet (right).

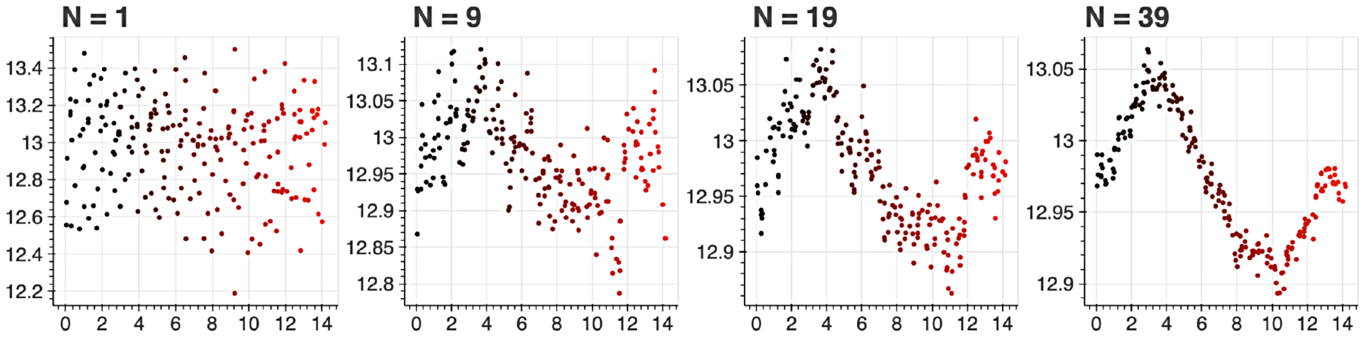

Figure 8. Different period folding graphs at period of 14.2029 by averaging adjacent points with different number of points N. Colormap: black to red, beginning of pulse to end.

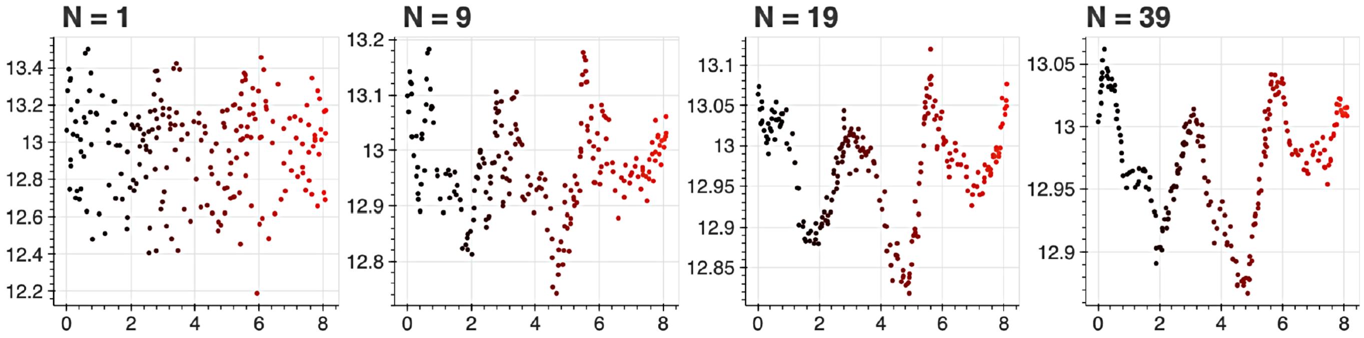

Figure 9. Different period folding graphs at period of 8.1264 by averaging adjacent points with different number of points N. Colormap: black to red, beginning of pulse to end.

SExtractor data did not resemble the AIJ periodogram. As shown in Figure 6, the AIJ periodogram peaks all occurred at periods longer than 80 minutes, while the SExtractor periodogram generated by the Skynet pulsar tab showed peaks that all occurred at periods under 50 minutes. Note that to generate a variable star periodogram in the Pulsar section, it was necessary to subtract the timestamp of the first image from that of all subsequent images, convert the time of each data point into units of minutes, and specify the use of 0 bins, since data binning is a feature relevant to pulsars. In addition, calibration was set to 1.

When the Source Extractor photometry was initially folded in the respective "Variable" and "Pulsar" tabs, the periodograms made were rather different; see Figure 7 for this comparison. The "Variable" tab showed no noticeable peaks under 40 minutes and only noise above 40 minutes. The "Pulsar" tab did show many peaks, similar to those found in Bond *et al.* (1996). When the means of the data set from each of the seven nights were subtracted from each corresponding set, the Skynet variable star tab's results became similar to those of the pulsar tab. This suggests that the pulsar tab's medium background subtraction algorithm, which is what differentiates the pulsar tab from the variable tab, might be optimal for variable stars with small periods, such as CH Cam.

4.3. Calculating amplitudes

Python code was written to approximate the amplitudes of the pulsations found from the SExtractor photometry, smoothing the data by arithmetically averaging adjacent values. The value

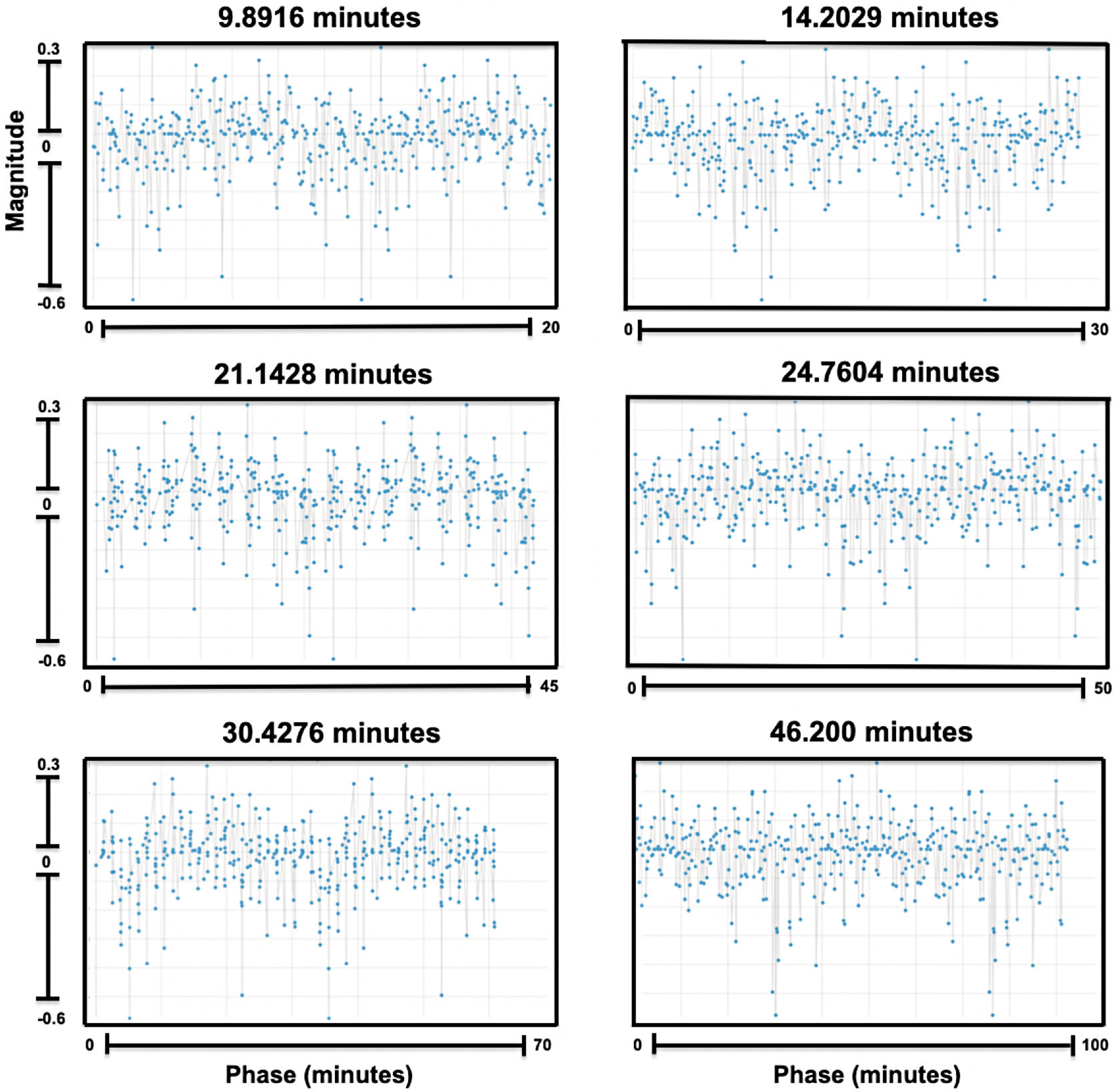

Figure 10. SExtractor period folds.

N represents the number of adjacent points averaged. Using the method that will be described in section 5, the magnitudes of these newly muted pulsations were then corrected. Figures 8 and 9 show the use of this averaging technique. However, these pulsations were spurious because the overlap of the points used in adjacent averages causes the adjacent averages to be artificially similar to one another. This was confirmed by shuffling the data randomly and observing similar spurious pulsations. Therefore, this technique was only used to approximate amplitudes but not used to find periods.

4.4. Findings

Up to 16 different possible periods using the SExtractor data, which aligned between the pulsar tab and variable star tab, were identified and are listed in full in Table 4. Examples of period folds can be found in Figure 10. Some periods were found to be close to half the value of some periods in Bond *et al.* (1996). Due to the properties of the Fourier transform, this is expected; the different period values that are a factor of 2 apart probably refer to the same pulsation.

5. Analyzing the effects of exposure time on magnitude

After finding a possible period of 2.878 minutes, it was necessary to see how much the magnitude found from period-folding was affected by the very close 2.5-minute exposure time. To model this, a simulation was coded on an online graphing calculator, Desmos. The simulation can be found at this url:

https://www.desmos.com/calculator/vlizyqjuvx.

To begin, assume that a star fluctuates with period T and amplitude A_{real}, over time x. This implies that the magnitude of the star can be modeled as in Equation 3:

$$F(x) = A_{real} \sin\left(\frac{2\pi}{T} x\right) \tag{3}$$

We can allow the star to have an average magnitude of 0 for purposes of the simulation. Then assume that the images taken have an exposure of length E. Accordingly, the magnitude found in any photo from time x – E/2 to x + E/2 will be the average magnitude of F(x), which is $F_{found}(x)$ in Equation 4:

$$F_{found}(x) = \frac{1}{E} \int_{x-E/2}^{x+E/2} F(t)\,dt \tag{4}$$

Computing $F_{found}(x)$ from the integral in Equation 4 and the definition of F(x) in Equation 3 we find Equation 5:

$$F_{found}(x) = \frac{A_{real}T}{E\pi} \sin\left(\frac{\pi E}{T}\right) \sin\left(\frac{2\pi}{T}\right). \tag{5}$$

After imaging with exposure E, the period will not have changed, we can take the amplitude of $F_{found}(x)$ and find Equation 6:

$$A_{imaged} = \frac{A_{real}T}{\pi E} \sin\left(\frac{\pi E}{T}\right). \tag{6}$$

From this equation one can use A_{imaged} to approximate the true amplitude of the star's variations. If T >> E or when E tends to 0, it is not necessary to use this approximation. By using this equation, the amplitudes of high-frequency pulsations are sometimes found to be slightly higher then when they are estimated by folding the data.

6. Prewhitening

6.1. Introduction

Prewhitening is a method for finding more pulsations of a variable star, if the star has more than one simultaneous pulsation. The method is performed by finding the most likely pulsation, fitting a curve to that pulsation (usually a sine curve), and then using the parameters of that sine curve to subtract that found pulsation out of the data. This new data set is then analyzed again in the same manner, finding pulsations, subtracting them such that the data become cleaner every time a pulsation is subtracted. The goal in performing this analysis is to try to decrease the error in the periods found, and possibly find more periods as the data set becomes clearer.

6.2. PERIOD04

PERIOD04 software is a prewhitening tool, performing the same prewhitening algorithm described above, and is adapted to work with time series containing gaps (Lenz and Breger 2005). It employs three different tabs to perform a prewhitening analysis: Time String (to record periods), Fit (to calculate the statistical significance of periods), and Fourier (to get a periodogram). Both the ASTROIMAGEJ photometry and Source Extractor photometry were input into the PERIOD04 software.

The frequencies were extracted using the procedure outlined under the "Tutorial 2: Least-Squares fitting of data including a periodic time shift" (page 58 of the PERIOD04 User Guide). Eight periods were found with the ASTROIMAGEJ photometry and 14 were found with the Source Extractor photometry. Most periods found in each method were rather similar to those found earlier, except for a few periods ranging from 50 to 75 minutes. The fits were obtained by simultaneously fitting the periods to the data. See Table 4 for a list of these periods. The significance of these periods was calculated by the software. Most significances for the ASTROIMAGEJ photometry were around 0.002 and those of the Source Extractor photometry were around 10^{-6}. We stopped running the software when it recommended that the periods it found were no longer significant (which was around 0.005 σ).

6.3. PYTHON PREWHITENING code

In an attempt to ascertain greater confidence in the periods found by Source Extractor, we also wrote a code that would subtract the sine curves out of the dataset, which was used as part of a pre-whitening method in tandem with the periodogram by SKYNET.

The code first folded the data around the period found by SKYNET. Then, to attain a more confident sine fit, it averaged each data point with the 49 that surrounded it (centered around each data point). Then, because this is analogous to taking an exposure, the correction derived in section 5 was used to better approximate the amplitude. In addition, instead of just using the period that was suggested by SKYNET, four more periods at ± 0.0006% and ± 0.0012% the suggested period were tried. An example is shown in Figure 11. These percentages were chosen based on some testing which showed that these numbers made slightly better fits in some cases, while staying within the peaks in the periodograms from SKYNET. Then, the PYTHON library called SCIPY was used to determine the best fit of a sine curve across all the five total averaged period folds.

After the parameters of this sine curve were found, we subtracted the sine curves out of the original, un-averaged data set, and then confirmed through testing that the corresponding period was absent from the periodogram.

This method found many more periods than Source Extractor, as after more and more periods were subtracted out of the data set, more would appear. Most of the periods that arose were below the periodogram amplitude of spurious periods that arose by randomly shuffling the Source Extractor data around and running them through SKYNET. Therefore, no periods found by this method are reported here.

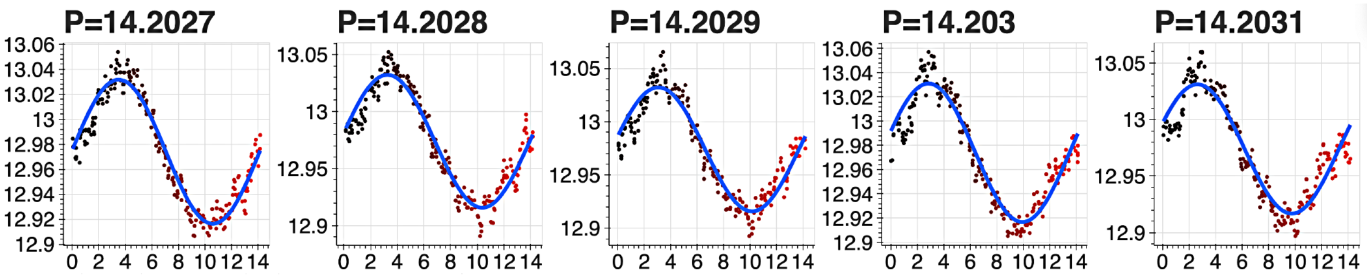

Figure 11. Five different sine fits for small differences in periods P.

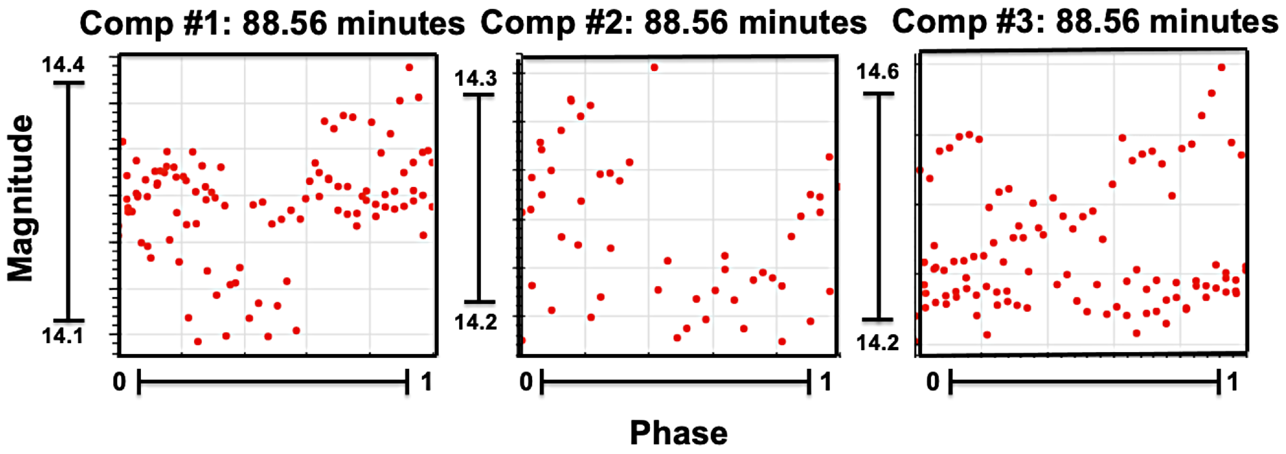

Figure 12. psx Photometry: The different period folds for each comparison star at a period of 88.56 minutes.

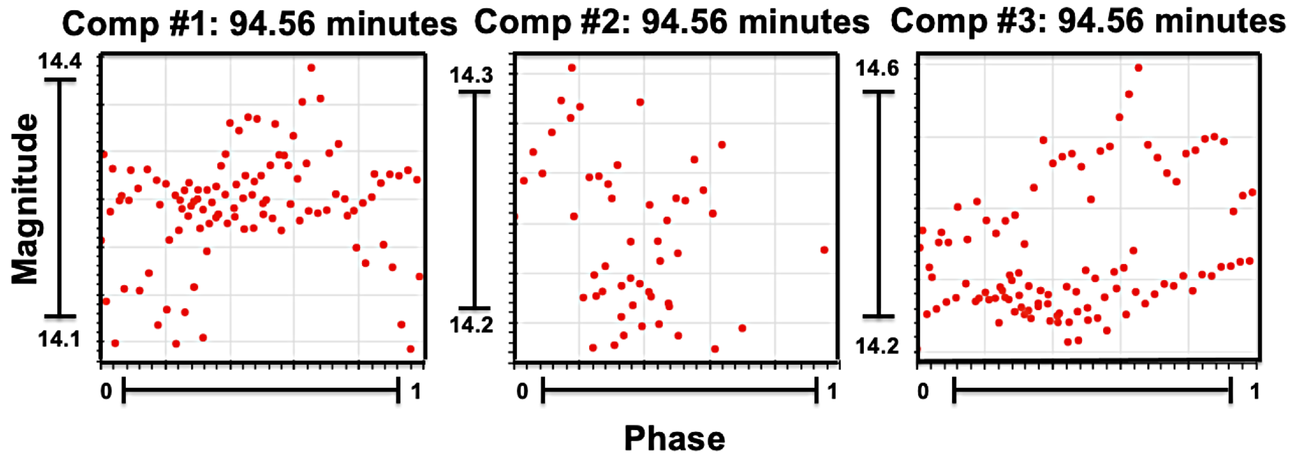

Figure 13. psx Photometry: The different period folds for each comparison star at a period of 94.56 minutes.

7. psx method

Another attempted method of analysis was psx photometry (Bertin and Arnouts 1996). This method uses a point spread function to identify stars and measure their magnitudes. Using this photometry, we were unable to confirm any of the periods found in the literature, nor any of the periods we had found using the AstroImageJ method or the Source Extractor method. We wrote a Python code to use the data returned by the Our Solar Siblings pipeline and period-fold for any period of input. Our 218 images were used for this method in addition to some archival data from previous LCO observations of this nebula. No conclusive periods were found from this method.

In the end, this method ended up containing messier data than those derived from the AIJ and Source Extractor methods; both Figures 12 and 13 show how different the period folds for two sample periods looked between each of the three comparison stars. The second comp star was not found in all the images, which explains why there are visually fewer data points for that plot. The dissimilarity of the plots renders this method inconclusive and in need of further investigation.

8. PERANSO

Peranso (Vanmunster 2004–2021) is a light curve and period analysis software that is able to run CLEANest (Foster 1995)

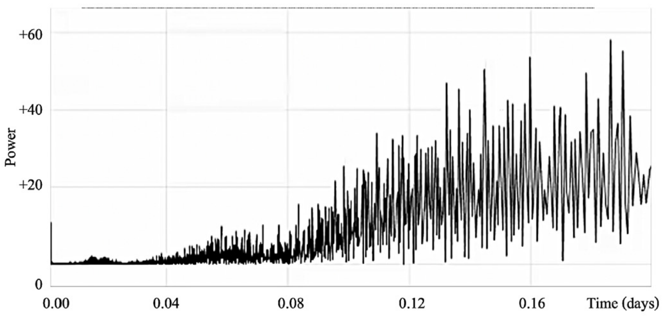

Figure 14. Peranso CLEANest periodogram on this study's data and a few other points from the LCO archive.

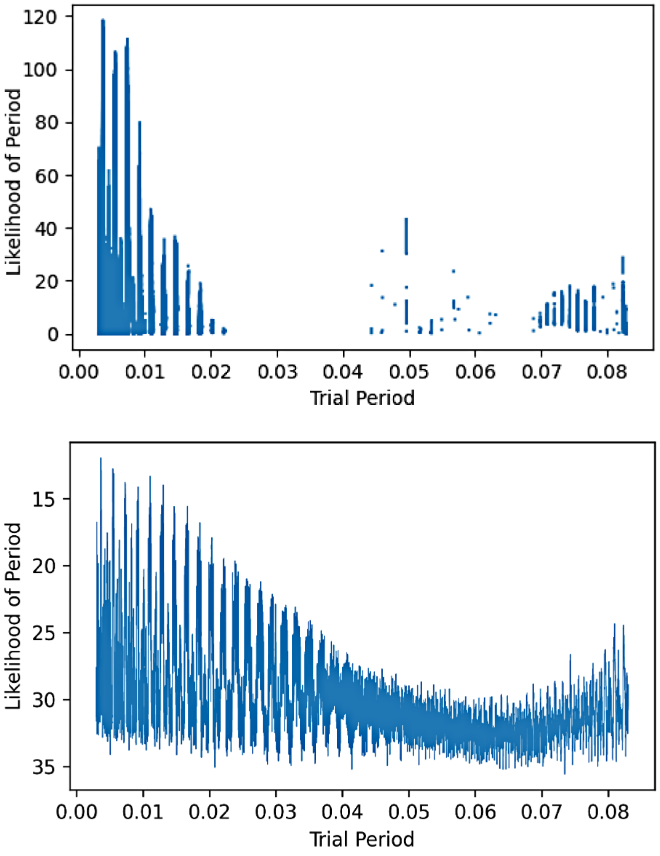

Figure 15. (Upper) ANOVA periodogram. (Lower) String PDM Periodogram.

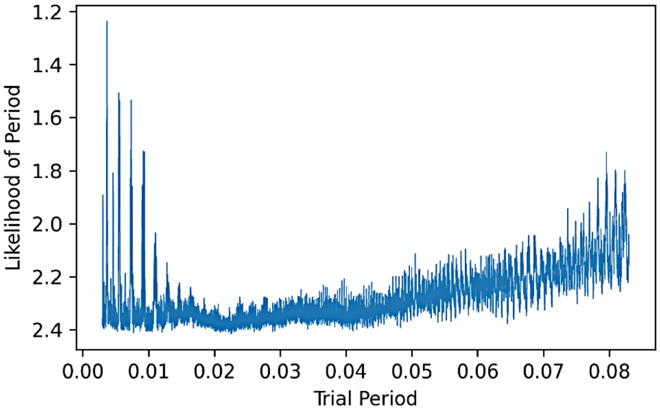

Figure 16. PDM periodogram.

analysis. This software was used with the assistance of Michael Fitzgerald to see whether CLEANest would be able to more accurately find the many pulsations of CH Cam. However, the main periods found were much larger than expected for this type of star. The data used were a compilation of our 218 images data collected from Las Cumbres Observatory, along with a few other data points from the past ten years that had used the same filter and captured CH Cam. As shown in Figure 14, the clearest peak in the periodogram was close to the sampling frequency, suggesting an alias.

9. ASTROSOURCE

For further analysis of the psx method, we used Astrosource, a software developed by Michael Fitzgerald (Fitzgerald *et al.* 2021). To use the software, the psx photometry from the OSS Pipeline was used as the input. To search for comparison stars, the code first uses the list of stars and compares the variance of each star's flux, as the standard deviation, to each other star. Then it eliminates the stars that had higher variance. This repeats until the optimal comparison stars are found. After calibrating with those comps, it uses various methods to compute the most probable periods, including ANOVA, harmonic ANOVA, Phase Dispersion Minimization (PDM), and Lomb Scargle (VanderPlas 2018; Dworetsky 1983). PDM and String are similar, in that they both attempt to minimize the distribution of a binned data, either by calculating the distance between the points in flux-phase space or by their standard deviation. Figures 15 and 16 show the likelihood plots for ANOVA, String, and PDM. The archival LCO images along with our 218 images were used in this method.

For Lomb Scargle, up to six summations of sine curves were output by the software, as shown in Figure 17. However, including more than three terms is not justified given the constraints of the system, and from visual inspection, additional terms do not improve the fit. In addition, the one-term Lomb-Scargle did not find a good fit. The two- and three-term Lomb-Scargle fits looked better, but these used almost negligible second and third sinusoidal terms. Given that they fitted the data to essentially one sine curve, this pulsation should have been found by the one-term fit. In addition, the period listed by the two-term and three-term Lomb-Scargle fits was around 5.37 minutes, which is almost exactly twice as long as the sampling frequency, suggesting a possible alias. The hypothesis that this is an alias is substantiated by the fact that Peranso did not find a period of that length, and Peranso takes into account the Spectral Window, as described in the Introduction; see section 1.1

10. TESS data analysis

As part of our process to verify the results of our analysis methods, we tried to replicate the analysis and results found in the 2019 paper using the same TESS data (Córsico *et al.* 2021). A complete download of the TESS data for NGC 1501, released in 2018, was found in the MAST observatory portal. In the 2019 paper, the analysis was done using pre-whitening that was done through the authors' customized tool (Córsico

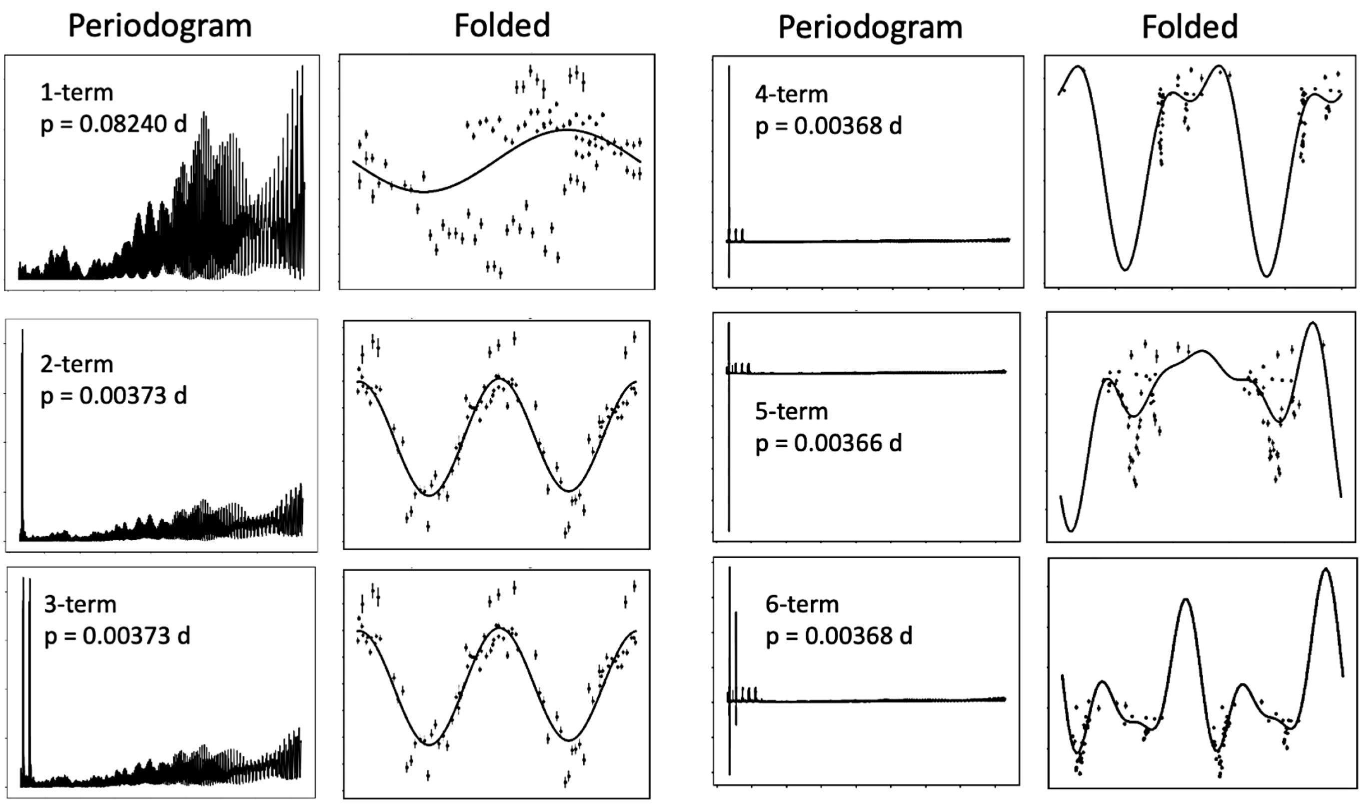

Figure 17. The different period folds for each comparison star at a period of 94.56 minutes.

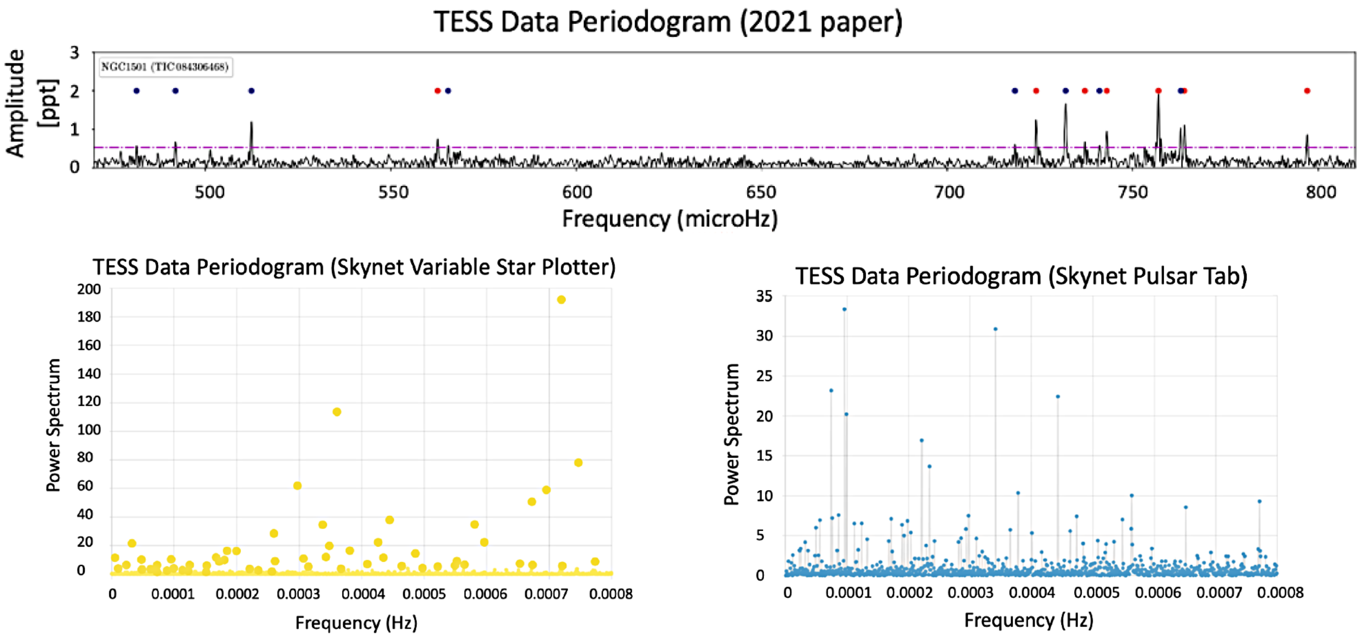

Figure 18. Comparison of TESS data periodograms.

et al. 2021). We ran these data through Skynet plotting—both the Pulsar and Variable Star tabs (see section 4.2)—as well as through Period04 (see section 6.2).

10.1. Skynet plotting

In applying the TESS data to both Skynet's variable star plotter and its Pulsar tool, the initial light curve of the data aligned with that of Figure 2 in Córsico *et al.* (2021). Neither periodogram from the Skynet Pulsar or Variable Star tabs confidently matched the periodogram given in Córsico *et al.* (2021); see Figure 18. However, some similarities were found. Peaks were found around 650–800 µHz in the Skynet Variable Star tab, which could align with the periods found in that same range by Córsico *et al.* (2021). It is likely that the discrepancies that arose were due to the differences in our methods of analysis using Skynet and the customized method used in Córsico *et al.* (2021). Further investigation would be helpful to verify the validity of the analysis of our own results and of past results.

10.2. Period04

The same TESS data were run in Period04, and were able to reproduce 10 of 11 periods that were found in Córsico *et al.* (2021) within about ± 0.1 second in all cases; see column 5 in Table 4. This suggests that the results from Period04 discussed in section 6.2 were valid. Four additional periods were found. It is likely that any of the small discrepancies in results are due to the custom nature of their tool.

11. **Conclusion**

After performing several different methods—AstroImageJ, Source Extractor, psx, Astrosource, Prewhitening, and Peranso—about 30 periods were found, shown in Table 4. Six of the periods found using the AstroImageJ and SExtractor methods are rather close to historical periods, while about three are close to the half values of historical periods. Reduction of our data via psx, Astrosource, and Peranso did not confirm pulsations in CH Cam, while Prewhitening with the Period04 software and our custom code both confirmed these periods and found additional ones. In accordance with the expectation that this phase in stellar evolution of pre-white dwarfs is expected to change over short time periods, it is possible that in the time since some of the historical periods were calculated, particularly those in the Bond paper, the periods of CH Cam have changed. Some inconsistencies among the results of the various period finding methods employed here as well as the complexity of CH Cam suggest that further research would be helpful in the investigation of this star.

12. Acknowledgements

We thank our referee for a very thorough and helpful review.

This work has made use of data from the European Space Agency (ESA) mission *Gaia* (https://www.cosmos.esa.int/gaia), processed by the *Gaia* Data Processing and Analysis Consortium (https://www.cosmos.esa.int/web/gaia/dpac/consortium); funding for which has been provided by national institutions, in particular the institutions participating in the *Gaia* Multilateral Agreement.

The team was grateful for the advice and assistance of Michael Fitzgerald, who processed our images using the OSS pipeline and helped us to run Peranso on them.

Credit is due to the developers of the principal software, as well as the databases that provided valuable information about NGC 1501:

- Fabien Chéreau: Stellarium Sky Atlas
- Karen Collins and John Kielkopf: AstroImageJ processing and reduction software
- Las Cumbres Observatory Global Telescope Network
- American Association of Variable Star Observers International Database
- Guido Van Rossum: Python Colab
- The Our Solar Siblings Pipeline
- Mulsiki Archive for Space Telescopes
- Astrosource

Thank you to Michael Fitzgerald for giving counsel to many of the questions raised by this project.

References

AAVSO. 2022, Variable Star Plotter (https://www.aavso.org/apps/vsp/).

Babusiaux, C., *et al.* 2023, *Astron. Astrophys.*, **674A**, 32 (DOI: 10.1051/0004-6361/202243790, arXiv:2206.05989).

Bertin, E., and Arnouts, S. 1996, *Astron. Astrophys., Suppl. Ser.*, **117**, 393 (DOI: 10.1051/aas:1996164).

Bond, H. E., *et al.* 1996, *Astron. J.*, **112**, 2699 (DOI: 10.1086/118214).

Brown, T. M., *et al.* 2013, *Publ. Astron. Soc. Pacific*, **125**, 1031 (DOI: 10.1086/673168).

Córsico, A. H., Althaus, L. G., Miller Bertolami, M. M., and Kepler, S. O. 2019, *Astron. Astrophys. Rev.*, **27**, 7 (DOI: 10.1007/s00159-019-0118-4).

Córsico, A. H., *et al.* 2021, *Astron. Astrophys.*, **645A**, 117 (DOI: 10.1051/0004-6361/202039202).

Ciardullo, R., and Bond, H. E. 1996, *Astron. J.*, **111**, 2332 (DOI: 10.1086/117967).

Collins, K. A., Kielkopf, J. F., Stassun, K. G., and Hessman, F. V. 2017, *Astron. J.*, **153**, 77 (DOI: 10.3847/1538-3881/153/2/77).

Dworetsky, M. M. 1983, *Mon. Not. Roy. Astron. Soc.*, **203**, 917 (DOI: 10.1093/mnras/203.4.917).

Fitzgerald, M. T., Gomez, E., Salimpour, S., Singleton, J., and Wibowo, R. W. 2021, *J. Open Source Software*, **6**, 2641 (DOI: 10.21105/joss.02641).

Foster, G. 1995, *Astron. J.*, **109**, 1889.

Gaia Collaboration, *et al.* 2016, *Astron. Astrophys.*, **595A**, 1 (DOI: 10.1051/0004-6361/201629272).

Lenz, P., and Breger, M. 2005, *Comun. Asteroseismology*, **146**, 53 (DOI: 10.1553/cia146s53).

Reichart, D. E. 2021, *Phys. Teacher*, **59**, 728 (DOI: 10.48550/arXiv.2103.09895).

Roberts, D. H., Lehar, J., and Dreher, J. W. 1987, *Astron. J.*, **93**, 968.

Sabbadin, F., Benetti, S., Cappellaro, E., and Turatto, M. 2000, *Astron. Astrophys.*, **361**, 1112 (DOI: 10.48550/arXiv.astro-ph/0007039).

VanderPlas, J. T. 2018, *Astrophys. J., Suppl. Ser.*, **236**, 16 (DOI: 10.3847/1538-4365/aab766).

Vanmunster, T. 2004–2021, Peranso v.2.50 light curve and period analysis software (http://www.cbabelgium.com/peranso).

No Longer Eclipsing—The Strange Case of RS Crateris

Stephen P. Cook
910 Oak Terrace Drive, Prescott, AZ 86301; scook@projectworldview.org

Received December 7, 2022; revised May 26, June 14, 2023; accepted June 15, 2023

Abstract For decades mistakenly classified as a solar (spectral class G0) Algol-type eclipsing binary with 0.7-magnitude amplitude, RS Crt is now listed as constant at V magnitude 10.62 in the AAVSO's International Variable Star Index (VSX). The author's 2020 differential photometry supports this reclassification, showing RS Crt to be constant (with 0.042 V mag. scatter). Investigating when its light variation ceased, the author analyzes data (including his own) from several observers obtained between 1972 and 1995 and concludes none show periodic variation. Citing the poor quality of the 1930–1944 data upon which its previous classification was based, one could argue RS Crt never was an eclipsing binary. Finding eight new minima (from 1929 to 1948) in the digitized Harvard Plate Collection/DASCH—and deriving a period of 0.8272 day that fits the early data better than the older period of 0.8168 day—the author seemingly refutes that contention. Four additional minima (from 1964 to 1971) gleaned from the APPLAUSE archive strengthen his contentions including that the period drastically shortened before eclipses ceased. Confirming it quit eclipsing—and admitting it to a tiny, select group of objects—would require spectroscopic confirmation of its binary nature. If such much-needed future observation fails to show that, speculations—of its compact binary past with spiral death march ending with coalescence into a single object, or of a history marked by a collision with a high-speed interloper—might be strengthened. Despite its recent constant classification, TESS data show RS Crt varies with amplitude <0.01 magnitude in a roughly four-day periodic fashion. Study of the beats, overtones, and damping in this light curve might lead to portraying its past in terms of pulsations, not eclipses.

1. Introduction

1.1. RS Crt may be a very unusual object—what this paper tries to do

There are at least two reasons why RS Crt deserves attention. First, it may belong in the short list of eclipsing binary stars that have been firmly established as having quit eclipsing—along with objects like V907 Sco and HS Hya. Second, prior to having ceased exhibiting eclipses in the early 1970s, it appears that the orbital period of RS Crt decayed over two or three decades at a rate seldom, if ever, seen among compact eclipsing binary systems. Like another extraordinary object, V1309 Sco, had this "spiral death" march continued, it might have ended in a dramatic outburst. Apparently that never happened. What did happen is that the eclipses ceased.

Out of the huge (approaching 100,000?) number of catalogued eclipsing binaries, up until recently only six had been convincingly established to have stopped eclipsing: QX Cas, SV Cen, SV Gem, SS Lac, AY Mus, and V907 Sco (Guinan 2012). Recently HS Hya has been added to that list. For V907 Sco, Lacy *et al.* (1999) reported: "The earliest observations of the system in the year 1899 show eclipses; the eclipses stopped around 1918, started again around 1963, and stopped again in about 1986." As a recent paper (Zasche *et al.* 2023) notes—and strives to make sense of—its eclipses have started up again a bit sooner than expected. For HS Hya, Davenport *et al.* (2021) report: "With a total baseline of over 125 yr, this unique combination of data sets—from photographic plates to precision space-based photometry—allows us to trace the emergence and decay of eclipses from HS Hydrae.... Recent TESS observations...confirm that eclipses have ceased, ...we estimate they will begin again in 2195."

While these binaries' eclipses typically ceased gradually due to system orbital inclination changes caused by a third star—something conceivably at work for RS Crt—V1309 Sco's ended after catastrophic binary interactions as part of a "common envelope" evolution. This general process has been described (Pejcha *et al.* 2017) as "short-lived and poorly understood" with an outcome having "crucial implications for all stages of stellar evolution." Prior to its coalescing into a single object, V1309 Sco, over thousands of orbital cycles of decaying period, had a light curve that "gradually morphed from a double-hump profile (typical for contact binaries) to single-hump shape...." Chiefly based on visual estimates in 1944 that poorly determined five times of minima with large scatter, RS Crt was listed as having completely different Algol-type eclipses. Yet now, having a much more complete picture of its observational history, one can argue that linking RS Crt to V1390 Sco rather than Algol might help us better understand it.

This paper takes the limited observational data—from visual estimates, from old photographic plates, all with large uncertainties—and pushes them to the limit in making the case for the reality of the assertions in this section's initial paragraph. Few, if any, who read it completely will doubt that decades ago RS Crt ceased exhibiting periodic light variations in the 0.5-magnitude range. More readers will fail to be convinced that periodic light variations once seen were caused by eclipses; a few may even dispute that RS Crt's light output varied periodically at all, but instead attribute all reports to the contrary as in error. As for RS Crt's supposed dramatic period changes, this paper challenges those who don't accept the author's admittedly highly speculative sketch of this object's history over the last century to back up their skepticism by pointing to where the observational foundation simply won't support demands made on it and/or where the analysis breaks down.

1.2. RS Crt observational history

RS Crt was discovered in 1930 and initially observed by European and Soviet observers. On 36 photographic plates taken between March 1929 and April 1934, RS Crt stayed more or less constant at photographic magnitude 10.8, with typical plus or minus 0.2-magnitude uncertainty. But one taken on April 23, 1930, recorded it had seemingly dimmed to magnitude 11.5. This (singular?) observation of a 0.7-magnitude drop would be linked with RS Crt's eclipse amplitude for the next nine decades. Based on what was also reported with that first time of minimum (Sandig 1948), had skeptics prevailed from the start, this dimming might have been dismissed as being recorded on an old and worn plate.

Lange (1935) reported two times of minima and an amplitude of 0.4 magnitude. From 51 visual estimates made in 1944, V. P. Tsesevich (1947) determined three times of minima and reported an amplitude of 0.5 magnitude. This was noted in the University of Pennsylvania—later University of Florida—Eclipsing Binary (EB) Card Catalogue and subsequent editions of "A Finding List for Observers of Interacting Binary Stars" (Wood *et al.* 1980). There, along with noting that Tsesevich provided a light curve and Algol-type classification, RS Crt was said to vary from visual magnitude 10.0 to 10.5 with period of 0.8168 day, and six-hour long eclipses. In a later publication, Tsesevich (1954) provided two additional times of minima, also based on 1944 visual observations. Table 1 lists times of minima for RS Crt.

Table 1. Times of minima for RS Crt used to determine Equation 1.

Minimum No.	*TOM (JD)*	*Method*	*N*	*O–C (d)*	*Source*
1	2426090.336	pg	–6269.5	–0.1264	Sandig (1948)
2	2427842.25	vis	–4125	0.16	Lange (1935)
3	2427890.23	vis	–4066	–0.0512	Lange (1935)
4	2431211.35	vis	0	–0.04	Tsesevich (1954)
5	2431212.27	vis	1	0.0632	Tsesevich (1954)
6	2431252.2	vis	50	–0.03	Tsesevich (1954)
7	2431256.25	vis	55	–0.064	Tsesevich (1954)
8	2431266.19	vis	67	0.0744	Tsesevich (1954)

The 0.8168-day period was most likely a provisional value derived from times of minima. Combined with some initial epoch, the period goes into an equation for computing times of minima for future eclipses:

$$\text{JD TOM} = 2431211.39 + 0.8168\,N, \qquad (1)$$

where N = number of eclipse cycle. The period can be refined using such an equation to compute time of eclipse, and O–C, the observed time of minimum minus the computed time. The fifth column in Table 1 provides these. They can be plotted vs. number N of eclipse cycle as in Figure 1, along with the line defined by Equation 1. The distance above or below the line provides a measure of how good the period is. (Note: the plot also includes a point for the mathematically determined initial epoch.)

The first minimum listed in Table 1 only fits nicely into the Figure 1 plot if it is assumed to have a one-half whole number N (= –6269.5) commonly associated with a secondary minimum—even though its associated amplitude (0.7-magnitude drop) is the greatest of the eight. Accepting this implies RS Crt exhibited noticeable brightness changes not every 0.8168 day = about twenty hours, but every ten hours. That, combined with the roughly six-hour eclipse duration—apparently from Tsesevich's light curve—implies that much of the time RS Crt will not be at maximum brightness. It is very difficult to reconcile that with Sandig's report that RS Crt was constant on 36 of 37 plates in the 1929 to 1934 era.

V. P. Tsesevich was born in 1907 and died in 1983. According to Nikolai Samus, the man in charge of recent editions of the *General Catalogue of Variable Stars* (GCVS), Tsesevich was "a famous man" in the top tier of renown amongst Russian variable star observers (Samus 2007). One suspects Tsesevich was responsible for the characterization of RS Crt in the third (1968) edition of the GCVS. Photometrically it listed RS Crt as an Algol type eclipsing binary, with primary amplitude 0.7 magnitude, and eclipses lasting six hours. Astrometrically, the position it provided was believed accurate to better than 1 second in R.A., and 0.1 arc minute in Dec. Spectroscopically, RS Crt was assigned spectral class G0. We now know the information in all three areas was wrong to some extent.

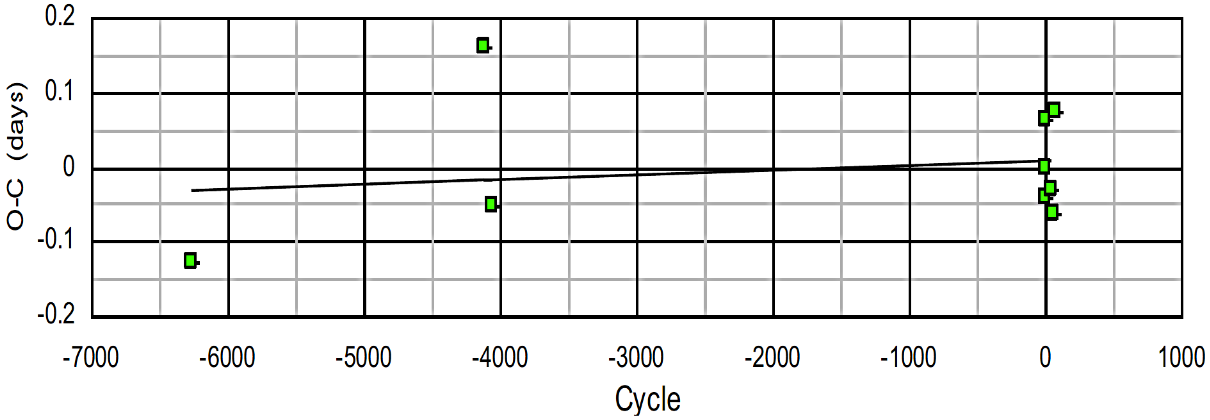

Figure 1. Observed minus Computed (O–C) diagram for RS Crt (from Nelson 2016).

Early on, RS Crt's reported six-hour eclipse duration, representing 30% of its 20-hour = (0.8168 day) period, should have raised suspicions as being too long for an Algol-type eclipser. Algol itself has an eclipse duration that is 14% of its period. Back then, V Crt—another eclipsing star with a short (0.7020 day) period, and 0.6-magnitude amplitude—was similarly listed as having five-hour eclipses. (Decades later that was revised to three hours.)

By the 1970s observers began reporting they were not seeing eclipses. Based on three nights of observing in 1972–1973, DuMont (Popper and DuMont 1977) reported it as constant at 10.67 V magnitude (with 0.01 error) and having B–V = +0.54. In March 1976, Swiss visual observer Kurt Locher (Locher 1976) reported: "The results of my survey at all phases during the past 13 months show [constant magnitude and]…estimated brightnesses scatter (RMS) less than [0.1 magnitude]." Locher used two comparison stars differing by 0.8 magnitude in brightness—the brighter one most likely GSC 005520-00393. Over a decade later, then-AAVSO Eclipsing Binary Committee Chair Marvin Baldwin likewise made visual observations of RS Crt. Unfortunately, no record exists of the comparison stars he used. After devising his own step sequence, he made 151 observations on thirty-six nights between March 1987 and May 1988—with variation ranging from a brightest of 27 on his scale to faintest of 46. His data can be found in the AAVSO International Database (AID; Kloppenborg 2023). Baldwin told the author 0.03 magnitude might be a good estimate for the value of each of these steps. Despite large scatter—discussed in section 5— no evidence for eclipses was found.

The 1990s brought spectroscopic data that challenged RS Crt's previous classification (based on low-resolution objective prism spectra) as a solar-type, spectral class G0 star. After getting three high-resolution spectra of it at Lick Observatory, in 1996 Dan Popper both reclassified it (based on sodium D lines) as a late F (F5—F8) star and, based on its narrow lines, ruled out its published short period (Popper 1996). His three spectra showed no variation in radial velocity—the current accepted value (Gaia Collab. *et al.* (DR2) 2016, 2018) is –3.66 km/sec ± 0.40.

Astrometrically, in 2004 Shawn Dvorak noted that the (2000 epoch) position of RS Crt in the 1968 GCVS (Kukarkin and Parenago 1968) as R.A. 11^{h} 49^{m} 06^{s}, Dec. –10° 37' 12" was slightly off; more accurately it is R.A. 11h 49m 03.13s, Dec. –10° 37' 14.9" (Dvorak 2004). Note that the GCVS editors admit that R.A. "error may reach + or – 3 sec" (Kholopov 1985). Finally, in 2020, based on Gaia space observatory data gathered in the 2014–2017 era, a highly accurate parallax for RS Crt of 5.8463 milliarcsec ± 0.0268 was published (Gaia Collab. *et al.* (DR3) 2022,) along with proper motion data: –25.429 milliarcsec/yr in R.A., and 0.428 milliarcsec/yr in Dec. (Its parallax tells us that RS Crt is 171 parsecs distant.)

Despite all of these observations—astrometric, photometric, spectral, and radial velocity data—there are insufficient data to say with 100% certainty that it's not a member of a binary star system.

2. The author's work on RS Crt—observations and data mining

2.1. Photometry

The author first observed RS Crt on two nights in 1995 using an ST6 CCD imager attached to a small (50-mm diameter) wide-angle lens. Fifteen data points—put together from 42 images obtained on two nights in April 1995—showed roughly constant V magnitude of 10.65 with no variation beyond 0.082 mag. (standard deviation-based) scatter. The comparison "star" used was actually an average of stars A and B in Table 2. See the AID for these observations. Although he failed to see the eclipse predicted by Equation 1, given poor signal/noise ratio for this nearly 11th-magnitude object, he decided a more capable system was needed.

Table 2. Comparison stars used for the author's differential CCD photometry of RS Crt.

Star	*GSC No.*	*R.A. (2000)* *h m s*	*Dec. (2000)* *° ' "*	*V Mag.* *Tycho 2*	*V Mag.* *APASS DR3*	*B–V*
A	5520–0303	11 47 19	–10 45 57	10.075	9.998	+0.655
B	5520–0628	11 48 32.40	–10 43 06	10.383	10.361	+0.41
C	5520–0393	11 48 42.30	–10 32 39	10.818	10.589	+1.11

He next observed RS Crt in 2020 using a better system—though hardly state of the art! With the ST6 CCD now attached to a 130-mm f/5 reflector, photons are still under-sampled, although not as badly. Given this, and with less than perfect tracking, experience suggests that flat fielding does not noticeably improve differential photometry results (in which variable star magnitudes are obtained by subtracting instrumental variable (VAR) and comparison (COMP) magnitudes, then adding the result to an assumed catalog-based comparison star magnitude). To compensate for not taking flats, he averages many images to produce individual (normal) data points—reduced with SBIG CCDOPS software and custom spreadsheet, which computes uncertainties.

With this setup the author observed RS Crt on 13 nights between May 8 and June 15, 2020, getting 198 data points distilled from 720 V filter images, each with typical 15-second exposures. This time the comparison "star" used was an average of stars B and C in Table 2; again, see the AID for these observations. This differential (comparison star magnitude-dependent) photometry showed RS Crt to be constant at 10.582 V-magnitude with 0.042 V-mag. scatter. Note that this is somewhat brighter than the 1995 value. While averaging the 1995 and 2020 V magnitudes for RS Crt gives a value of 10.62 V magnitude, the differences between them are believed due to different comparison stars used. This is in line with the (absolute photometry) APASS DR3 listed value for RS Crt as 10.622 V magnitude with mean error 0.0482 V mag, and a Tycho Catalogue listed value of 10.625 V magnitude with mean error 0.060 V mag.

2.2. Data mining—DASCH

Software associated with the digitized Harvard Plate Collection (DASCH) project (Grindlay *et al.* 2009; Tang *et al.* 2013; Harvard Coll. Obs. 2022) was used to produce the light

Table 3. Additional times of possible minima for RS Crt from DASCH and APPLAUSE archives.

No.	*Harvard Plate No. or APPLAUSE*	*Time of min JD Heliocentric Time*	*Min. RS Crt Mag.*	*Limiting Plate Mag.*	*Status*
1	ai33793	28926.7702	11.80	12.37	Accept
2	ai38813	31200.6701	11.86	12.66	Reject
3	rh00931	25633.8588	11.49	12.82	Accept
4	ac28893	26341.9434	11.48	12.25	Accept
5	ac29159	26443.645	11.44	11.98	Accept
6	am17421	28245.4711	11.38	14.2	Accept
7	ai33850	28956.8107	11.39	13.82	Accept
8	bio1188	31170.5525	11.43	12.37	Accept
9	ai41592	32648.612	11.44	13.02	Accept
10	APPLAUSE	38500.9619	11.69	?	Accept
11	APPLAUSE	38551.0180	11.49	?	Accept
12	APPLAUSE	39210.3356	11.40	?	Accept
13	APPLAUSE	41039.3586	11.58	?	Accept

curve of RS Crt shown in Figure 2 spanning years 1900 to 1990 (with a 1955–1975 gap when no plates were taken). While the coverage seems adequate, finding real minima is a challenge for several reasons—magnitude measurement uncertainties, lengthy exposures (some exceed two hours!), occasional plate defects, weird star image shapes, etc. Some seeming minima may actually be outliers more associated with noise/statistical fluctuations (low probability coincidences expected in three sigma level statistical terms) than actual periodic eclipse variation. Shorter plate exposures have brighter limiting magnitudes and decreased signal to noise, leading to concerns about DASCH's ability to flag all the data points that it needs to.

To illustrate this, consider the two most obvious minima in Figure 2, from 1938 and 1944, #1 and #2 in Table 3. Both are consistent with Equation 1: #1 plots close to a best fit line in an O–C plot (with O–C = –0.0302 day); #2 a bit below (O–C = –0.1015 day.) Discussion with LSU professor Brad Schafer, a top expert in using Harvard plates in both glass plate and digitized (DASCH) forms, convinced the author that #2 (from plate ai38813) should be rejected. Given its bright, jagged elongated blob—not fainter, nicely circular stellar image—it's most likely due to a plate defect. But Schafer sees RS Crt on plate ai33793 as looking brighter than DASCH measured. Given his own experience with stars on CCD images occasionally looking brighter than they are measured, the author trusted the measurement and kept minimum #1 in Table 3.

2.3. Data mining—APPLAUSE

The Archives of Photographic PLates for Astronomical USE (APPLAUSE; Groote *et al.* 2014) yielded the 115 data points shown in Table 4 for the 1964–1974 era—and four minima listed in Table 3. The seemingly deepest one (#10) from 1964, considering comparison star magnitudes, may not actually be quite as deep as 1966 and 1971 minima. But since it is part of seven images spanning over three hours that show descent, faintest, slight recovery, then nearly as faint again, before ending brighter than in the first image, it is the most interesting. They suggest a four-hour or so eclipse duration—certainly more believable than six—and possibly a surrounding envelope?

3. Hypothesis testing and discussion: was RS Crt once an eclipsing binary star system?

3.1. No (skepticism), and yes (rebuttal)

The O–C diagram shown in Figure 1 hardly inspires confidence: its 0.03 Pearson R^2 correlation coefficient is just above random chance level! The point for minimum #1 in Table 1, much below the best-fit line, is supposedly for a secondary minimum (the only one plotted) observed in 1930.

More basically, is the Figure 2 light curve believable for RS Crt as an eclipsing binary as listed? To decide, we compare it with similar DASCH-derived light curves for two other nearby objects: 1) in Figure 3 for V Crt, an eclipsing binary with similar period and amplitude as RS Crt may have once had, and 2) in Figure 4 for the (supposedly) constant comparison star B (GSC5520-0628) from Table 2. While showing a bit more variation than this comparison star, the RS Crt light curve may look more like that of comparison star B than it resembles that of V Crt.

If RS Crt was once eclipsing per its catalog listing this is not what one would expect, but can it nonetheless be explained in eclipsing variable terms? Yes, for two reasons. First, V Crt, at the DASCH reported average magnitude 10.72, is brighter than RS Crt, with its similarly reported 11.18 average magnitude. Thus it's more likely that more minima of RS Crt were flagged by DASCH—something it does if the measured magnitude is not at least 0.5 magnitude brighter than the limiting plate magnitude. Second, and more importantly, one can hypothesize that RS Crt's eclipses were shallower than V Crt's. What if RS Crt eclipses were typically just 0.4 magnitude or less in amplitude, as reported for the pair observed in 1934? If that were so, in looking at its light curve, many such eclipses would be lost in "noise," whereas the deeper 0.6-magnitude eclipses of V Crt would rise up out of it.

The author did not think the above argument was strong until he started finding such shallow minima for RS Crt. Using Figure 2 and DASCH, he identified seven TOM for RS Crt between 1929 and 1948 corresponding to not so deep drops in its brightness. Whereas the minima listed in Table 1 are believed to correspond to 0.4- to 0.7-magnitude brightness drops, these seven additional DASCH/Harvard plates TOM (#3 through #9 in Table 3) correspond to magnitudes 0.20 to 0.31 fainter than the 11.18 average magnitude DASCH gives RS Crt in Figure 2.

3.2. Refining the period and eclipse predictions as in Equation 1

Returning to the problems with Figure 1, we ask whether an O–C diagram can be constructed with a better fitting regression line without assuming any of the TOM used are for secondary minima? Yes. In fact, Equation 2, with a slightly longer period, can do this:

$$\text{JD TOM} = 2428926.77 + 0.8272\ N, \qquad (2)$$

where N = number of eclipse cycle. But can all of the 20 acceptable minima from both Table 1 and Table 3 be used in doing this with a single diagram based on a single equation like Equation 2? Alas, no, as we shall see. Referring to Table 5, note that the Equation 2 period of 0.8272 day does a better job

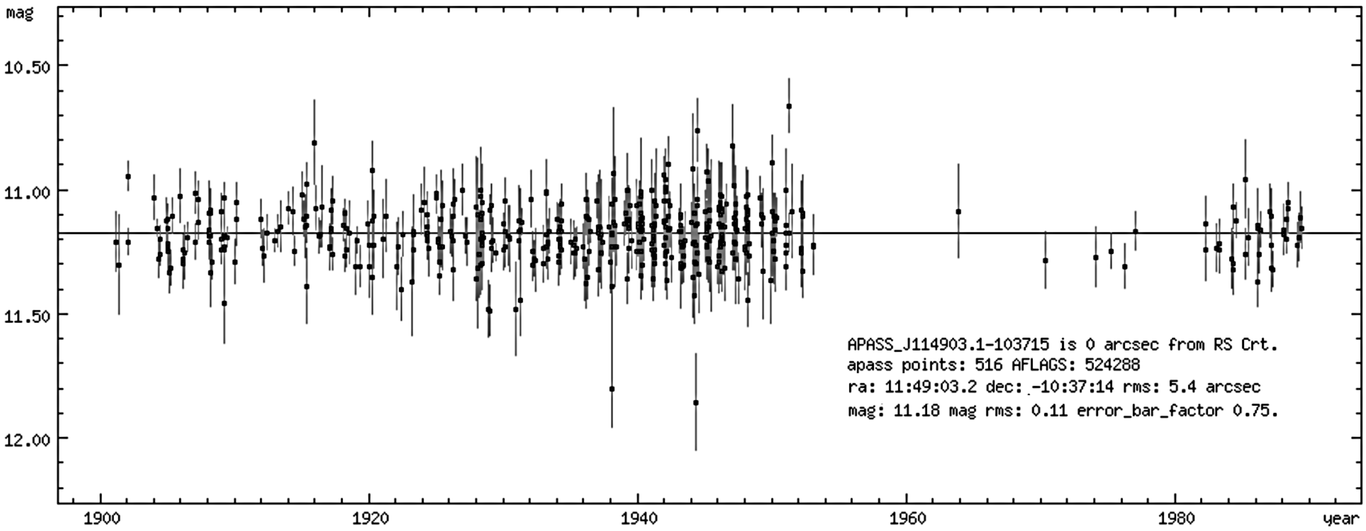

Figure 2. Light curve of RS Crt extracted from Harvard Plate Collection (DASCH project).

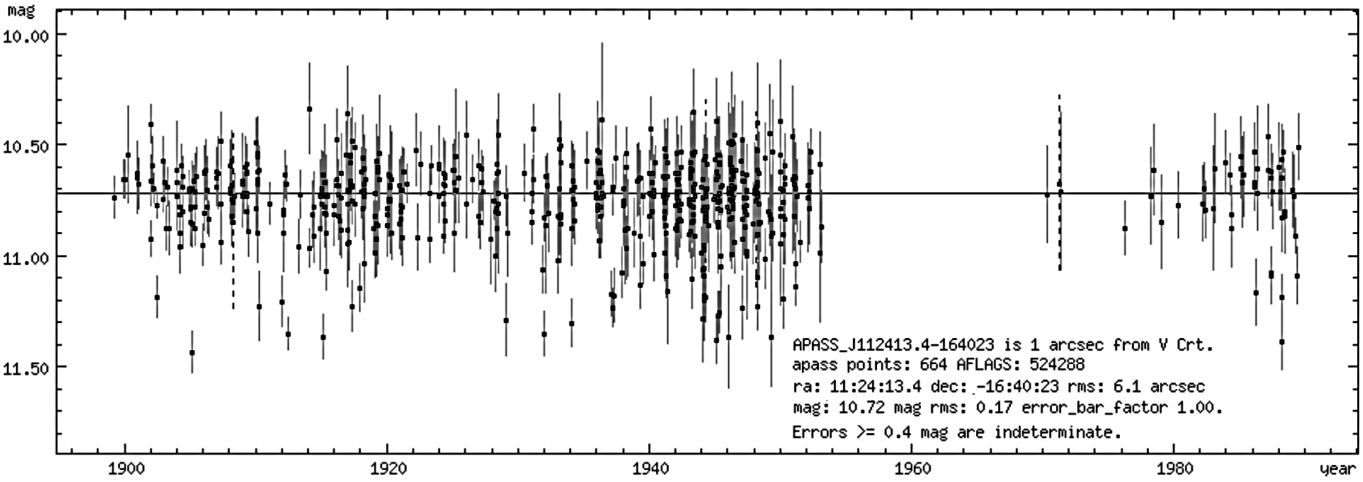

Figure 3. Light curve of V Crt extracted from Harvard Plate Collection (DASCH).

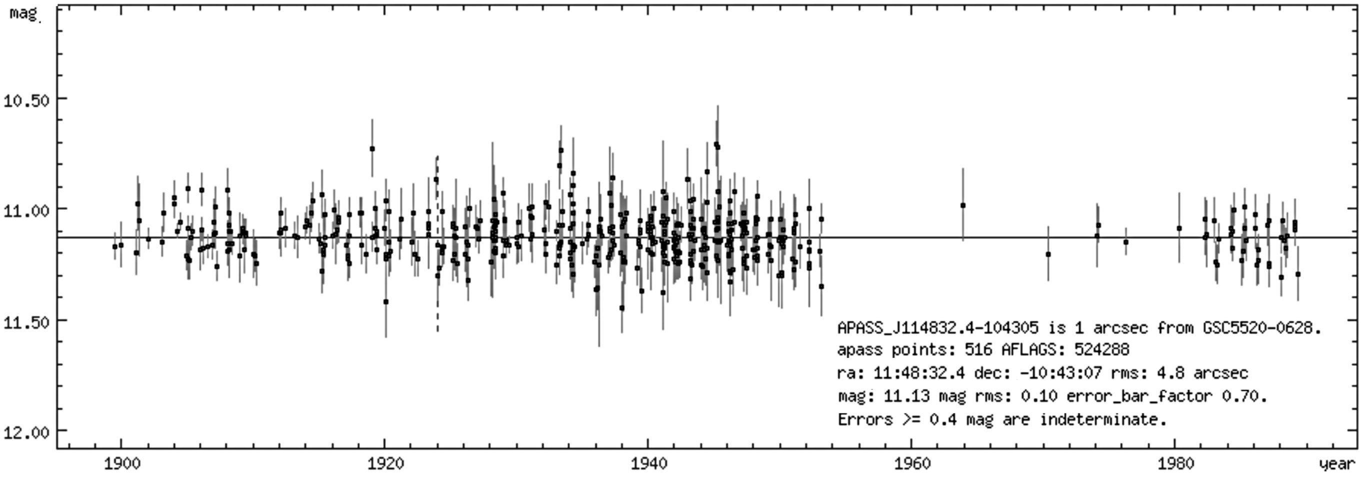

Figure 4. Light curve of GSC5520-0628 extracted from Harvard Plate Collection (DASCH).

Table 4. 1964–1974-era APPLAUSE photometry of RS Crt.

JD 2400000+	*B mag.*	*JD 2400000+*	*B mag.*
38498.0727	11.0095	38902.4118	11.2318
38499.0664	11.0100	38904.3910	11.2025
38500.0664	11.0963	38905.4132	11.1821
38500.9383	11.5103	38906.4119	11.2132
38500.9619	11.6994	38911.3557	11.0241
38500.9835	11.1769	38913.3536	11.1069
38501.0051	11.2870	38914.3536	11.0805
38501.0274	11.4316	38915.3530	11.1065
38501.0489	11.3095	38916.3523	11.2164
38501.0656	11.0591	39173.4803	10.9884
38501.0705	11.0827	39179.4672	11.2116
38502.0677	11.2121	39181.4311	11.2603
38503.0697	11.1203	39200.3890	11.1268
38504.0704	11.1952	39202.3869	11.1628
38505.0745	11.1896	39209.3696	11.1304
38517.0491	11.3021	39210.3356	11.3999
38518.0539	11.1134	39230.2928	11.3556
38519.0511	11.1066	39232.2540	11.1965
38520.0518	11.1131	39233.2505	11.1872
38521.0531	11.1626	39235.2450	11.1289
38524.0621	11.3653	39236.2484	11.1968
38525.0599	11.4508	39237.2436	11.2477
38529.0654	11.1944	39240.2443	11.0603
38530.0667	11.0855	39259.1765	11.1744
38546.0509	11.2927	39261.1828	11.2714
38547.0529	11.3517	39265.1731	11.1336
38548.0104	11.0143	39268.1620	11.0037
38549.0125	11.2051	39269.1405	11.2927
38551.0180	11.4892	41033.3516	11.1357
38553.0207	11.2989	41037.3496	11.4414
38554.0228	11.1432	41039.3586	11.5760
38555.0248	11.2041	41394.6999	11.1764
38556.0269	11.2473	41397.2996	11.2390
38557.0289	11.3925	41415.6247	11.1891
38560.0351	11.3081	41420.6607	11.2571
38561.0385	11.0855	41444.6529	11.2038
38562.0427	11.1702	41448.6368	11.2036
38796.7876	11.3160	41470.6360	11.3389
38797.7821	10.9240	41472.6311	11.3026
38816.6796	11.2036	41726.3436	11.1192
38817.7053	11.1995	41727.3464	11.0842
38818.7025	11.1715	41746.2799	11.0646
38820.7004	11.1463	41749.2675	10.9721
38822.6970	11.2075	41753.2453	11.0521
38825.6561	11.0939	41754.2335	11.0114
38855.5522	11.0418	41775.1740	11.0862
38872.4983	11.0838	41803.0709	10.9891
38877.4844	11.1928	41827.9844	11.0373
38878.4810	11.0397	41990.6256	11.2097
38879.4789	11.0644	41990.6362	11.1117
38879.4789	11.0420	42127.9588	11.1229
38880.4900	11.3171	42129.9158	11.2218
38881.4935	11.2542	42130.9435	11.1266
38883.4824	11.2001	42134.9352	11.1840
38884.4790	11.0109	42135.9165	11.0691
38885.4776	11.0261	42155.8612	11.1403
38887.4727	11.1112	42188.7401	11.2203
38901.4118	11.0134		

of representing Table 3 minima #3 through #9 (and predicting times of minima) than the 0.8168-day period of Equation 1 does.

3.3. Weighing evidence for and against RS Crt once being an eclipsing star

Without carefully studying the predictions in Table 5, one might conclude "RS Crt never was an eclipsing variable," based on comparison of its light curve with those of V Crt and the supposedly constant nearby comparison star. Also, based on spectroscopic evidence: 1) RS Crt has not been observed to have a spectrum with double lines that Doppler shift with orbital motion—either because, if double, the bright star hides the fainter star's spectral lines, or because it is not binary; and 2) Popper's three high-resolution spectra indicated a constant radial velocity, not what you'd expect for an eclipsing binary. Unfortunately, dates/times of those spectra were not reported, but unless they were taken at an unlikely sequence of orbital phases, they argue RS Crt is not part of a binary system.

Table 5 suggests a different conclusion. Its first prediction, using the 0.8272-day period, is a mere 0.0014 days = 2 minutes off predicting an event occurring two years (actually 708 days) later. Noting that other predictions based on that period (#3, #5, and #7 in Table 5) are respectably accurate to within 60 to 75 minutes, we conclude a 0.8272-day period works for 1929 to 1938 minima.

4. Data that challenge constant period models: a large period change for RS Crt?

Alas, the longer period model Equation 2 cannot adequately represent all of the acceptable minima presented in both Table 1 and Table 3. For starters those minima span 42 years or roughly 18,000 cycles of 0.8272-day eclipses. With only four significant figures, predictions made using it just 1000 cycles in the future incur a 1000 × 0.0001 = 0.1-day uncertainty, so more accurate period determinations would be nice, if possible. Limiting the time span over which the period is to be used mitigates the lacking in significant figures uncertainty. Doing this with minima from 1929 to 1938, using the 0.8272-day period creates the O–C diagram shown in Figure 5.

We attempt similarly to create another O–C diagram using just minima from 1938 to 1948, but face two challenges. First, the last five minima from Table 1 present problems—beginning with the strange 0.92-day interval between the N = 0 and N = 1 consecutive eclipses. Before attributing this to a possible light curve anomaly, the author assumed a period double that of 0.8272 day—1.6544 days—and postulated an observable secondary eclipse that was offset from the 0.5 phase. No good—one of the assumed secondary minima refused to fit. Instead, in creating Figure 6, minima #4 and #5 in Table 1 have been replaced by the Equation 1 initial epoch.

Second, trying to reconcile that 1944 initial epoch with the 1948 minimum (#9 in Table 3) presents another problem. As results presented in the last two rows in Table 5 show, using the longer 0.8272-day period requires invoking that the distant minimum observed almost four years later must be a secondary minimum, given the N = 1737.5 cycles elapsed since the initial 1944 epoch. This contradicts postulating RS Crt has

Table 5. Predicted RS Crt TOM Using 0.08272-, 0.8168-, or 0.8166-day periods.

No.	*TOM Being Predicted*	*TOM Used Initial Epoch*	*Time elapsed from Initial Epoch (d)*	*Period (d) used in Making Prediction*	*N (cycles)*	*O–C (d)*
1	#4 in Table 3	#3 in Table 3	708.0846	0.8272	856	0.0014
2	#4 in Table 3	#3 in Table 3	708.0846	0.8168	867	–0.081
3	#5 in Table 3	#3 in Table 3	809.7862	0.8272	979	–0.0426
4	#5 in Table 3	#3 in Table 3	809.7862	0.8168	991	0.3374
5	#5 in Table 3	#4 in Table 3	101.7016	0.8272	123	–0.044
6	#5 in Table 3	#4 in Table 3	101.7016	0.8168	125	–0.3984
7	#7 in Table 3	#6 in Table 3	711.3396	0.8272	860	–0.0524
8	#7 in Table 3	#6 in Table 3	711.3396	0.8168	871	–0.0932
9	Eq 1 init epoch	#8 in Table 3	40.8375	0.8168	50	–0.0025
10	#9 in Table 3	Eq 1 init epoch	1437.22	0.8272	1737.5	–0.018
11	#9 in Table 3	Eq 1 init epoch	1437.22	0.8166	1760	0.004

Note: Eq 1 Init Epoch" refers to what is used as a representative average of the last five minima in Table 1 (given their very large scatter).

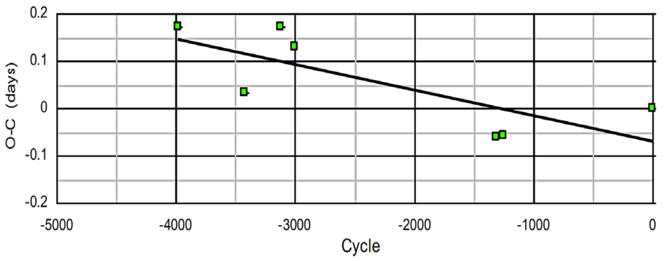

Figure 5. O–C Diagram for 1929–1938 data using period of 0.8272 day. $R^2 = 0.59$ points are for minima # 1, #2, and #3 in Table 1, and minima #1, #3, #4, and #5 in Table 3, with minimum #1 in Table 3 serving as the initial epoch.

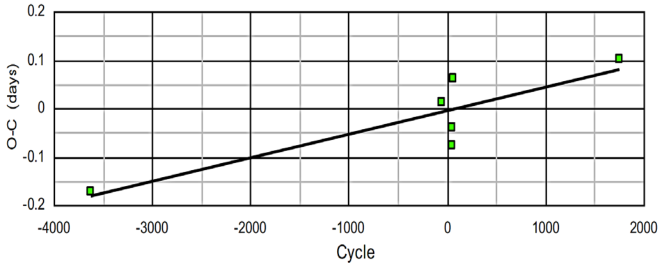

Figure 6. O–C Diagram for 1938–1948 data using period of 0.81701 day. $R^2 = 0.76$ points are for minima #6, #7, and #8 in Table 1, and minima #6, #8, and #9 in Table 3. Notes: minima #4 and #5 in Table 1 have been replaced by initial epoch from Equation 1; and minimum #7 in Table 3 would not fit—conceivably the mid-point of ai33850 was too far from minimum.

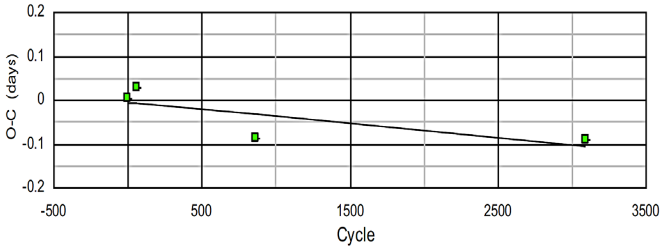

Figure 7. O–C Diagram for 1964–1971 data using period of 0.82019 day. $R^2 = 0.59$ points are for minima #10, #11, #12, and #13 in Table 3.

no observable secondary minimum. With an eclipse at N = 1737 the O–C is a big 0.3756 day; likewise with N = 1738 the O–C is –0.4516 day.

What to do—try a shorter period—is suggested by the results of prediction #9 in Table 5. There, starting with minimum #8 in Table 3, the 1944 initial epoch is nicely represented 50 cycles later (with an error of but –0.0025 day = 3.5 minutes) using the 0.8168-day period. If the period really shortens between 1929 and 1944, from 0.8272 to 0.8168 day, extrapolating a still shorter period in going forward from 1944 seems reasonable. In jumping ahead roughly four more years, that is, in predicting a minimum for 1948 (prediction #11 in Table 5), we note a shorter period of 0.8166 day works: it's accurate to 0.004 days = 5.6 minutes. Over the whole 1938–1948 time span, the best fit line in Figure 6 indicates that a period of 0.81701 works best.

What about the eclipse minima after 1948? APPLAUSE data (Table #4) seemingly capture four of them: #10, #11, #12, and #13 in Table #3, from 1964, 1964, 1966, and 1971, respectively. If the decreasing period change documented so far continues, we expect needing a still shorter period to represent 1948—1971 RS Crt TOM data. But alas, it seems the period decline has halted! That the linear fit captured in the Figure 7 O–C diagram for 1964–1971 works best for a 0.82019-day period supports that conclusion. (Note: with only four data points multiple solutions exist. One has 0.8071-day period, seemingly acceptable, but given its lower $R^2 = 0.31$—and the DFT periodicity search results of the next section—the longer 0.82019-day period is preferred.)

5. RS Crt eclipses cease around 1973?: searching for periodicity 1964–2023

A discrete Fourier transform (DFT) based-method (Belserene 1988) for searching for periodicity in time series photometric observations can be applied to the 1964–1973 APPLAUSE data for RS Crt in Table 4, parsing it in one-year (1964), two-year (1965–1966), and two-year (1972–1973) groups for three computer program runs. Table 6 provides details. Associated with the results of the second and especially the third of those three runs, where a limited number of data points are spread over two years with a big seasonal gap, is larger uncertainty than with the first run (with 1964 data). In all

Table 6. Evidence documenting large period decrease for RS Crt 1929–1973.

Time Interval	*Source of the supporting evidence leading to period*	*Period (d)*
1929–1938	O–C Diagram / Figure 5 with 7 data points	0.8272
1938–1948	O–C Diagram / Figure 6 with 7 data points	0.81701
1964–1971	O–C Diagram / Figure 7 with 4 data points	0.82019
1964	DFT period search: 37 data points, strongest signals and relative strength: 0.8204 day @ 2.50; 4.17 day @ 2.13	0.8204
1965–1966	DFT period search: 49 data points, strongest signals and relative strength: 0.8148 day @ 3.31; 7.42 day @ 2.57; 2.00 day @ 2.52	0.8148
1972–1973	DFT period search: 19 data points, strongest signals and relative strength: 0.8028 day @ 3.56 3.15 day @ 2.18	0.8028

DFT program runs signals were sought that were associated with a wide range of possible periods, from 0.4 day to 10 days.

The run using 1964 data (fourth entry in Table 6) definitely had the best coverage with 37 data points spread over just 64 days, as can be deduced from Table 4 data. It found four signals of greater than relative strength 2.0; the strongest of these was at period = 0.8204 day, a result that fits nicely with the Figure 7 O–C diagram period.

The last entry in Table 6 is the last suggestion—and a not especially strong one—that eclipses of RS Crt might have lasted as late as 1973. The 1971 minimum—#13 in Table 3—is better evidence for an eclipse. Recall (from section 1) that Locher's 1975–1976 observations reported RS Crt as constant in brightness as far as visual estimates could detect.

While Baldwin's 1987–1988 151 visual data points and the author's 198 CCD data points of spring 2020 show no sign of eclipses, do they show any signs of periodicity? If so, for what period? To facilitate DFT analysis with Baldwin's data, his step values were converted to magnitudes assuming one step = 0.03 mag. The resulting standard-deviation based scatter is large—0.154 magnitude. One explanation for it: Baldwin was seeing real changes as the common envelope of stars in contact presented itself differently. Another involves possible use of an inappropriate comparison star. RR Lyr star X Crt, 11.1 to 11.75 V magnitude range, period 0.7328 day, is in the same one-half degree square field as RS Crt. There is no evidence Baldwin used it, but it represents a possible pitfall all observers of RS Crt must avoid. DFT analysis of his data provided no evidence in support of anything close to an 0.82-day period. Its strongest signals and relative strength were: 7.395 days with 20, 3.14 days with 10.9, and 4.037 days with 6.5.

Such analysis using the author's data offered no support for that 7.395-day period, and likewise provided no evidence of an 0.82-day period. Its strongest signals and relative strength were: 3.16 days with 12.1, 1.46 days with 11.2, and 1.298 days with 10.9. Other than being a product of the cadence of the observations, the author can offer no explanations for the significance of the periods associated with the strongest signals in these last two searches for periodicity.

6. An unprecedented period decrease for an eclipsing binary star; then what?

If the period of the RS Crt binary system really shortened from 0.8272 day (Figure 5) to 0.81701 day (Figure 6) in the 1929 to 1948 interval, would this be unprecedented behavior for an eclipsing binary? The answer: an extraordinarily unusual yes, but not totally unprecedented.

Over these two decades, RS Crt, one calculates from the data presented above, had an overall 1.2% decrease in its orbital period, declining at a rate of -5.1×10^{-4} day/year. The latter is 27 times greater than the largest rate of period decrease identified in a study of 14,127 contact eclipsing binaries (CEBs) based on the OGLE-III and IV observations in the Galactic bulge (Hong *et al.* 2022). Still, this rate is much slower (roughly only one fourth of) than the catastrophic period decay rate of V1309 Sco, another star also studied using OGLE survey data, based on 2001–2007 data. This binary system, with 1.4-days period, suffered a 1% period decrease in a seven-year period at a rate of 2.0×10^{-3} day/year (Pejcha *et al.* 2017). This rapid period decay resulted in a "spiral death" and luminous red nova or luminosity optical transient outburst. It is truly a special object, thought to represent "the only confirmed non-compact stellar merger" (Mason and Shore 2022).

Finally, if its period really recovered in the 1948–1971 era from 0.81701 day to 0.82019 day (Figure 7), its rate of period increase of $+1.6 \times 10^{-4}$ day/year again exceeds by a factor of 18 the highest rate among the CEBs the Hong *et al.* group studied. If true, one wonders what stopped RS Crt's orbital period decay?; and of course, why did the eclipses stop? Consider three possibilities.

First, the eclipses stopped because the inclination of the binary star orbital plane changed, possibly due to the gravitational force of a third star, such that it was no longer enough edge-on. The expected gradual transition would have resulted in shallower and shallower eclipses, then no variation. There are three problems with this: 1) the amplitudes of the best documented later eclipses in the 1964–1971 era appear to be as great as the best documented ones from the 1930s and 1940s; 2) this changing inclination scenario does not explain the large (> 1%) period changes documented above; and 3) most recent TESS observations show no signs of what should still be preserved if just inclination changed: a roughly 0.82-day period showing (outside of any eclipses) expected very slight ellipsoidal modulation in the photometric signal.

How does RS Crt look today? Is it strictly constant in brightness today, as its VSX listing suggests? The short answer is no, as the light curve in Figure 8—from TESS, the best recent source of photometric data available—shows. Admittedly the variations shown are tiny, in the peak-to-peak range of at most 0.01 magnitude, but look to be periodic (with signs of damping and beats?). The period is around 4.05 days—not anything like the expected 0.82 day from a supposed changing-inclination, eclipses-quit past for the object.

A second possibility as to why eclipses ceased—appealing to those who like the period decay spiral death scenario—

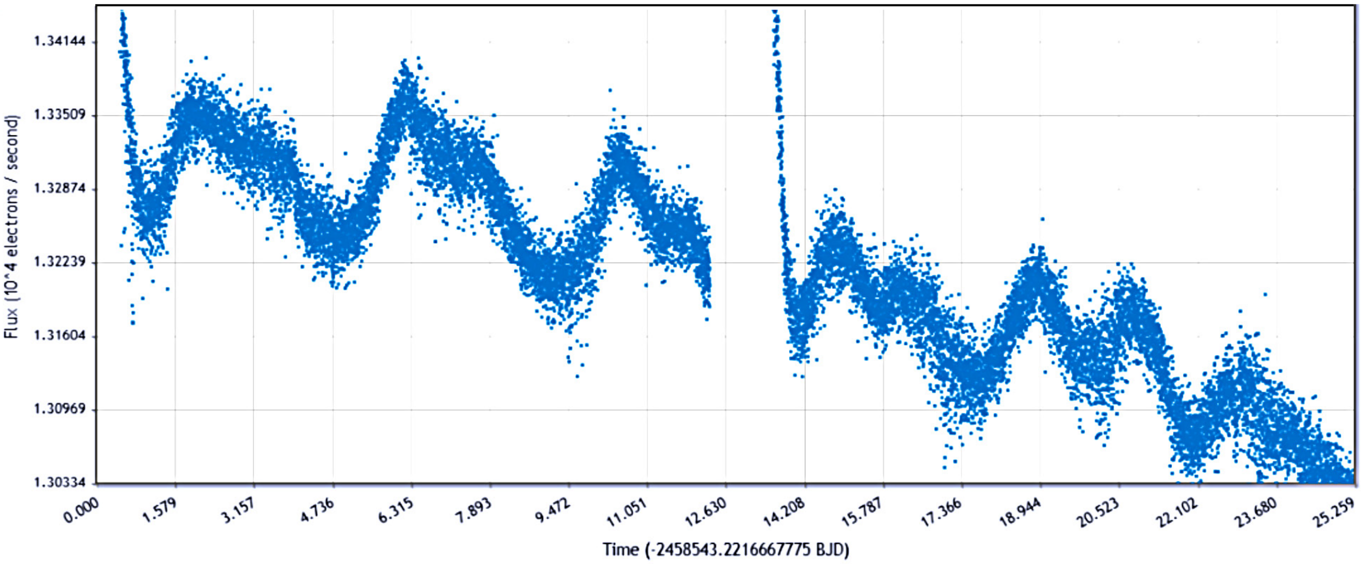

Figure 8. Recent light curve of RS Crt from TESS data.

is that the two stars in the system merged into a single object of some sort. Perhaps the observed four-day or so variation seen today is due to rotation of a common envelope that an increasingly close compact binary system evolved into after all the mass transfer/ejection and orbital angular/rotational angular momentum tradeoffs? Problems: if there was a stellar merger, why wasn't it accompanied by a dramatic, short-lived (several magnitudes) increase in luminosity as V1309 Sco exhibited? And, recall that evidence suggests the period decay stopped, suggesting no spiral death merger single object end product.

A third possibility as to why eclipses ceased: based on the previously cited astrometric discrepancy, RS Crt was jolted by a collision with some fast-moving object. The collision destroyed not only the geometric alignment producing the eclipses but also either dramatically changed (lengthened) the orbital period or destroyed the binary system altogether. Note: most likely the astrometric discrepancy is due to a long ago very poorly determined position.

7. Alternate explanation: RS Crt periodic light variation as pulsating, not eclipsing in origin

Many will find the above speculation unbelievable. Certainly, if future high-resolution spectra firmly establish RS Crt is not binary, then single star explanations including pulsating star, rotational variable, etc. may become more attractive.

7.1. A simple pulsating star model of RS Crt

Equation 1- and Equation 2-based models—instead of being associated with two periods used to predict times of eclipse minima—could be reinterpreted and used to predict a characteristic feature (minimum, maximum, inflection point, etc.) in the light curve of a pulsating star. Also, in conceiving of what was physically happening, instead of using periods, the emphasis would shift to pulsation mode frequencies. RS Crt's changing behavior and light curve might be explained in terms of the dynamic interplay of two fundamental pulsation modes.

7.2. Connecting RS Crt to real types of pulsating stars, and imagining pulsation ceases

Given its late F spectral type, one might speculate RS Crt was once a high amplitude δ Scuti (HADS) star that quit pulsating. Both its half magnitude amplitude and spectral type are at the extreme, but not implausible, edge of what is typical of HADS stars. A bigger problem is RS Crt's period of 0.82 day—it's much too long. The suggestion of a secondary minimum for it suggests the real pulsation period might have been one-half of that: around 0.4 day. This is still rather long, and more typical of RRa variables. But RS Crt's low luminosity, with its absolute visual magnitude of +4.45, disqualifies it from fitting into that category. Even if RS Crt were once pulsating, why its pulsation would so quickly—in the blink of an eye compared to typical stellar evolution time scales—diminish and cease is unknown.

8. A final mystery

DASCH-based Figure 2 suggests RS Crt wasn't doing anything unusual in 1916, just continuing to shine at around 11th (photographic) magnitude. Why then does the APPLAUSE archive contain seven data points from the early spring of that year—all from a 30 minute interval on a single night—that list it as 16th (B) magnitude? At the time in question, APPLAUSE records the magnitudes of (Table 2) nearby comparison stars as normal; and two data points from the early in 1919 again show it at 11th (B) magnitude. (These nine data points are the only ones in the APPLAUSE archive for RS Crt prior to 1948.) Was RS Crt really five magnitudes or 100 times fainter for a brief time in 1916?

9. Suggestions for future work

These are the observational priorities for RS Crt:

1) Obtaining high-resolution spectra to definitely establish whether or not RS Crt is a binary star is a top priority. If it is binary, these data could determine its orbital inclination.

2) If established to be binary, finer probing of the Harvard/DASCH, APPLAUSE, and other plate collections could help in more firmly characterizing RS Crt's eclipsing binary past and inform speculation and predictions as to the possibility of its eclipses resuming at some future date.

3) If binary, searching for a third star in the system, one responsible for changing inclination.

4) If not binary, investigating the nature of the variation suggested in Figure 8 might lead to modeling it as a pulsating star—once more active, now seeming in a quiet state. Investigation of this now barely-perceptible periodic light variation might point the way to understanding the much higher amplitude past periodic light variation this paper has documented.

10. Conclusion

As promised, the observational data have been pushed to the limit in conducting the analysis, which was in some way informed by all twenty of the acceptable minima recorded in Tables 1 and 3. Careful weighing of all data best supports the belief that RS Crt once showed a periodic light variation somewhere in the 0.3- to 0.6-magnitude range with a period around 0.82 day, and that not only can eclipses best account for that variation, but that the period of those eclipses changed, perhaps dramatically, before ceasing. This star definitely needs continuing attention—even if high-resolution time series spectroscopy establishes that it is now a single star.

11. Acknowledgements

The author wishes to thank Bradley Schafer for critically examining and commenting on what he had on RS Crt from digitized Harvard plates (DASCH); Edward Guinan for copying and sending him the card for RS Crt from The Eclipsing Binary Card Catalogue, now at Villanova University; Marvin Baldwin for answering (via email) questions regarding his 1987–1988 visual observations of RS Crt; Gary Billings for his comments; and an anonymous referee.

References

Belserene, E. P. 1988, *Sky Telesc.*, **76** (September 1988), 288.

Davenport, J. R. A., Windemuth, D., Warmbein, K., Howard, E. L., Klein, C., and Birky, J. 2021, *Astron. J.*, **162**, 189.

Dvorak, S. W. 2004, *Inf. Bull. Var. Stars*, No. 5549, 1.

Gaia Collaboration, *et al.* 2016, *Astron. Astrophys.*, **595A**, 1.

Gaia Collaboration, *et al.* 2018, *Astron. Astrophys.*, **616A**, 1.

Gaia Collaboration, *et al.* 2022, "Gaia Data Release 3: Summary of the Content and Survey Properties," arXiv e-print arXiv:2208.00211 (https://www.cosmos.esa.int/web/gaia/dr3).

Grindlay, J., Tang, S., Simcoe, R., Laycock, S., Los, E., Mink, D., Doane, A., and Champine, G. 2009, in *Preserving Astronomy's Photographic Legacy: Current State and the Future of North American Astronomical Plates*, eds. W. Osborn, L. Robbins, ASP Conf. Ser. 410, Astronomical Society of the Pacific, San Francisco, 101.

Groote, D., Tuvikene, T., Edelmann, H., Arlt, R., Heber, U., and Enke, H. 2014 in *Astroplate 2014*, eds. L. Mišková, S. Vitek, Institute of Chemical Technology, Prague, 53.

Guinan, E. F., Engle, S. G., Devinney, E. J. 2012, *J. Amer. Assoc. Var. Star Obs.*, **40**, 467.

Harvard College Observatory. 2022, "Digital Access to a Sky Century at Harvard" (http://dasch.rc.fas.harvard.edu).

Hong, K., Woo Lee, J., Park, J.-H., Kim, H.-Y., Lee, C.-U., Kim, H.-W., Kim, D.-J., and Han, C. 2022, *Astron. J.*, **163**, 157.

Kholopov, P. N. *et al.* 1985, *General Catalogue of Variable Stars*, 4th ed. Moscow.

Kloppenborg, B. 2023, Observations from the AAVSO International Database (https://www.aavso.org/data-download).

Kukarkin, B., and Parenago, P. 1968 *General Catalogue of Variable Stars*, 3rd ed. Moscow.

Lacy, C. H., Sandberg, H., Bodil, E., Vaz, L., and Paulo R. 1999, *Astron. J.*, **117**, 541.

Lange, G. 1935, *Tadjik Obs. Circ.*, No. 6, 4.

Locher, K. 1976, *BBSAG Bull.*, No. 26, 5.

Mason, E., and Shore, S. N. 2022, *Astron. Astrophys.*, **664A**, 12.

Nelson, R. 2016, AAVSO O-C database (https://www.aavso.org/bob-nelsons-o-c-files).

Pejcha, O., Metzger, B. D., Tyles, J. G., and Tomida, K. 2017, *Astrophys. J.*, **850**, 59.

Popper, D. M. 1996, *Astrophys. J., Suppl. Ser.*, **106**, 133.

Popper, D. M., and Dumont, P. J. 1977, *Astron. J.*, **82**, 216.

Samus, N. N. 2007, *Odessa Astron. Publ.*, **20**, 103.

Sandig, H.-U. 1948, *Astron. Nachr.*, **276**, 173.

Tang, S., Grindlay, J., Los, E., and Servillat, M. 2013, *Publ. Astron. Soc. Pacific*, **125**, 857.

Tsesevich, V. P. 1947, *Astron. Tsirk.*, **63**, 11.

Tsesevich, V. P. 1954, *Izv. Odessa Astron. Obs.*, **4**, 242.

Wood, F. B., Parker Oliver, J., and Koch, R. H. 1980, *A Finding List for Observers of Interacting Binary Stars*, 5th ed., Univ. Pennsylvania Press, Philadelphia.

Zasche, P., Vokrouhlický, D., Barlow, B. N., and Mašek, M. 2023, *Astron. J.*, **165**, 81.

Markov Chain Monte Carlo Optimization Applied to Dyson's Visual Double Stars

Isabella Soh Xiao Si
Department of Statistics and Data Science, National University of Singapore, Blk S16, Level 7, 6 Science Drive 2, Singapore 117546

Michael D. Rhodes
Brigham Young University, Provo, Utah 84602

Edwin Budding
Carter Observatory, 40 Salamanca Road, Kelburn, Wellington 6012, New Zealand, and
School of Chemical and Physical Sciences, Victoria University of Wellington, P.O. Box 600, Wellington 6140, New Zealand

Timothy Banks
Department of Physical Science and Engineering, Harper College, 1200 W Algonquin Road, Palatine, IL 60067, and
Data Science, Nielsen, 200 W Jackson, Chicago, IL 60606; corresponding author, tim.banks@nielsen.com

Received December 13, 2022; revised June 23, 26, 2023; accepted June 27, 2023

Abstract Estimates of orbital parameters were made using a Bayesian optimization technique on astrometric data for 25 visual binary systems catalogued a century ago by the ninth Astronomer Royal, Sir Frank Dyson. An advantage of this method is that it provides reliable, unbiased uncertainty estimates for the optimized parameters. Reasonable agreement is found for the short period (< 100 yr) systems between the current study and Dyson, with superior estimation for the longer systems through the inclusion of an additional century of data. Dynamical masses are presented for the systems through the inclusion of parallax measurements.

1. Introduction

Using the classical theory of Keplerian motion of two mass points together with reliable data on their distances and orbital periods, observations of visual binary stars reveal useful physical characteristics of stars. However, the proportion of visual binaries for which elliptic orbital motion could be clearly established using Earth-based data has been relatively small, involving periods of up to a few hundred years, while most known visual pairs have orbital periods in the thousands of years. Difficulties in finding accurate distances have also limited the extent to which double star astrometry could significantly bear on stellar astrophysics until recently. Increased precision of double star data including parallaxes, obtained from modern facilities such as the *Gaia* mission, is changing our perspective on this. It is appropriate to re-assess procedures for optimal parametrization of visual binary data. This paper describes the application of statistical optimization techniques to 25 visual binary systems, giving optimal estimates and associated uncertainties for orbital parameters.

An orbit can be described on the xy plane as (see, e.g. Ribas *et al.* 2002):

$$x = \frac{a(1-e^2)}{1+e\cos\nu}\left[\cos(\nu+\omega)\sin\Omega+\sin(\nu+\omega)\cos\Omega\cos i\right] \quad (1)$$

$$y = \frac{a(1-e^2)}{1+e\cos\nu}\left[\cos(\nu+\omega)\cos\Omega+\sin(\nu+\omega)\sin\Omega\cos i\right] \quad (2)$$

where a is the semi-major axis of the orbit, measured in arcseconds; e is the orbital eccentricity; ν is the true anomaly (or function of time) of the orbit of the stars about their barycenter; and i is the inclination, the angle between the plane of projection and the orbital plane. An inclination of 90 degrees would indicate that the orbital plane was exactly side on to our line of sight. ω is the argument of periastron, being the angle between the node and periastron (closest approach of the two stars). Ω is the position of the ascending node, which is the position angle of the intersection between the plane of projection and the actual plane the orbit lies in. These equations were used by the current study as the "model function" for an optimization algorithm. Initially we included two additional parameters, δx and δy to represent offsets in the origin of the xy coordinate system. These will be discussed later in section 4.3. A second function was used to measure how well the model, given a set of parameters, fitted the data. This is called the fitting (or optimization) function. The role of the optimization technique was to judiciously adjust estimates for the parameters until a set is reached that well fits the data set. In other words, the optimizer trialed different parameter values in the model function(s), measuring how well the model based on these functions fitted the data set. The measure of fit was based on the fitting function. Changes in the parameter estimates led to better or worse fits by the model to the data. The role of the optimizer is to adjust the parameter estimates until an optimal fit to the data is reached. In this paper we made use of optimization technique called Markov Chain Monte Carlo, fitting data of 25 double stars.

2. MCMC models

A Markov model gives the transition probabilities between one state and another. A series of such transitions or steps is called a Markov Chain. The key properties of such a process are that it is random and that each state (or step) is independent of the previous step. In other words, the future state of the process depends only on the current state of the process; it does not depend on any past states.

Markov Chain Monte Carlo models (MCMC, see Robert and Casella 2010 and Privault 2013) are a Bayesian technique which allow modelling of a distribution, and in particular statistics about that distribution such as the mean or variance. To understand a given distribution, many representative samples are taken from it. Such random samples are called Monte Carlo samples, explaining part of the process name. The actual distribution itself does not need to be known; all that is required by the technique is to be able to calculate a measure of "goodness of fit" of a model to a given data set. MCMC will vary the parameters input into the basic model, leading to model solutions with varying levels of fit to the data. A greater density of such sample points will be in regions where the parameters better fit the data. The simplest MCMC process is the Metropolis algorithm, which is a random walk. The key attribute of MCMC is that the distribution of interest is sampled again and again by taking small steps across it, building up a map of the distribution. In our case, where we fitted orbital models to observational data, MCMC allowed us to provide statistical estimates of the model parameters and how accurately we can measure those parameters.

We used the RSTAN library (Stan Dev. Team 2021) for the MCMC modelling in the R statistical programming language (R Core Team 2021). This library is an interface to the STAN programming language. STAN is a C++ library allowing Bayesian inference using the No-U-Turn (NUTS) sampler (a variant of Hamiltonian Monte Carlo (HMC), see Hoffman and Gelman 2014) or frequentist inference via optimization methods. The HMC algorithm avoids the random walk and associated sensitivity to correlated parameters experienced by earlier MCMC methods such as the Metropolis or Gibbs samplers. It does this via examination of first-order gradients to guide its steps. This improvement leads to more rapid convergence than the previously mentioned methods. HMC still suffers from high sensitivity to the step size and the number of steps required to reach convergence, which are both user-set parameters. If these are not set correctly (in particular the step size), HMC will either revert to random walk behavior (when the step size is too small) or waste computation (if the step size is too large). NUTS is a refinement to HMC which removes the need to set a number of steps through use of a recursive algorithm which scans a wide range of possible steps. The method automatically stops its steps when the chain has doubled back on itself. Hoffman and Gelman (2014) show that NUTS performs at least as efficiently as a well-tuned HMC method, with the advantage of requiring less user input. Given its advantages over earlier MCMC techniques, and the ease to implement the model inside R and STAN, we made use of this technique.

We are not the first authors to apply a MCMC method to visual double star data, although the technique is not yet widely used in the field. Mendez *et al.* (2017) modeled the orbits of 18 visual binaries using the Differential Evolution MCMC technique, which ran multiple markov chains simultaneously with sharing of information between the chains to aid convergence. Sahlman *et al.* (2013) used MCMC to estimate the orbital parameters of a low-mass companion to an ultracool dwarf star. Lucy (2014) successfully used a MCMC model to explore numerical simulations modelling total masses of visual binaries with measured parallaxes but incomplete orbits, finding that the mass estimates were unbiased when more than 40% of the orbit was covered by the data. Claveria (2019) applied MCMC to examine the impact (estimating orbital parameters) when partial measurements were included into a data set, finding that such inclusions could lead to more accurate estimation of the parameters in some circumstances.

3. Study rationale

The current paper examines the orbits of 25 visual binaries catalogued by the ninth Astronomer Royal, Sir Frank Dyson. He listed observations spanning from the early nineteenth century to his time of publication (Dyson 1921). We have supplemented the data set with further observations collected over the century since 1921, sourced from the Washington Double Star (WDS) catalog (Mason *et al.* 2022). Rhodes *et al.* (2023) applied a modified version of the Levenberg-Marquardt (see Bevington 1969) optimization technique to this data set, coupled with examination of the χ^2 Hessian matrix (for further details see Banks and Budding 1990). They provided estimates and accompanying uncertainties in the orbital parameters. Agreement between the published WDS estimates and those of Rhodes *et al.* (2023) was good. Pending issues from the paper included concerns whether the global minima have been reached by the optimization methods and that they were not local minima "trapping" the search methods. Rhodes *et al.* (2023) noted that final solutions were, for some systems, dependent on the starting estimates of the parameters—suggesting the presence of local minima. There was also interest in using an alternative technique to explore the uncertainties in the parameter estimates, perhaps allowing tuning of the step sizes applied to the curvatures from the Hessian matrix that were used to provide uncertainties for the optimized parameters. While a grid search might have given insight into the first concern, MCMC could address both and therefore led to this current study.

4. Analysis

Table 1 lists the optimal parameter values and associated standard deviations for each of the Dyson systems. The parameters δx and δy are not included in the table for reasons of space. These are zero point adjustments to the co-ordinate system, and fell within one standard deviation of zero in all cases. Position angles had been precessed to the year 2000 (see page 73 of Aitken 1964; page 121 of Cocteau 1981; and page 276 of Greaney 2004). This was important for the earlier observations which were collected nearly 175 years before the chosen epoch.

Runs continued until the $\hat{R}$ diagnostics (see Sinharay 2003) were within a thousandth of unity, which was typically achieved in 20,000 steps. Figure 1 plots data for four representative

Table 1. Parameter estimates from MCMC fitting to the Dyson systems, numbered by appearance in Dyson (e.g., 1 refers to Dyson-1 or D1).

System	*P*	*a*	*e*	*ω*	*i*	*Ω*	*Epoch*	*σ*	*BD*
1	168.28 ± 0.64	1.0118 ± 0.0057	0.319 ± 0.010	370.0 ± 1.6	44.6 ± 0.6	180.1 ± 0.1	1955.08 ± 0.72	0.1008 ± 0.0026	BD+22 146
2	144.88 ± 1.89	0.8388 ± 0.0170	0.230 ± 0.039	364.0 ± 10.3	62.2 ± 1.5	100.4 ± 1.6	1913.08 ± 3.81	0.2191 ± 0.0083	BD+46 536
3	872.48 ± 211.59	0.8439 ± 0.1208	0.825 ± 0.005	282.4 ± 46.8	157.3 ± 7.3	28.7 ± 46.0	1914.73 ± 1.41	0.1060 ± 0.0036	BD+23 473
4	187.04 ± 4.37	0.5792 ± 0.0291	0.458 ± 0.052	28.4 ± 8.5	56.9 ± 1.6	74.5 ± 2.7	1886.49 ± 3.40	0.0798 ± 0.0043	BD+31 737
5	94.12 ± 0.37	0.7487 ± 0.0170	0.597 ± 0.022	303.6 ± 2.4	53.8 ± 1.2	143.7 ± 1.5	1981.09 ± 0.46	0.0821 ± 0.0041	BD+13 728
6	57.38 ± 0.45	0.3413 ± 0.0340	0.722 ± 0.066	229.5 ± 5.4	71.4 ± 2.3	5.3 ± 2.2	1942.04 ± 0.56	0.0693 ± 0.0038	BD+1 1959
7	105.58 ± 0.55	0.3484 ± 0.0057	0.413 ± 0.024	–16.0 ± 7.1	27.4 ± 2.9	145.3 ± 5.9	1986.60 ± 0.84	0.0632 ± 0.0026	BD+54 1331
8	632.95 ± 221.39	1.4929 ± 0.4947	0.954 ± 0.024	72.4 ± 40.6	147.1 ± 19.2	150.9 ± 46.1	1894.42 ± 4.1	0.1067 ± 0.0038	BD+26 2345
9	291.69 ± 19.65	0.8702 ± 0.0616	0.604 ± 0.052	147.3 ± 11.4	134.2 ± 4.6	196.9 ± 6.5	1872.97 ± 4.4	0.1505 ± 0.0049	BD+37 2433
10	155.95 ± 0.39	2.4417 ± 0.0071	0.451 ± 0.005	199.8 ± 0.8	47.1 ± 0.3	155.7 ± 0.4	1916.72 ± 0.24	0.1307 ± 0.0030	BD+27 2296
11	273.31 ± 1.60	0.9240 ± 0.0195	0.497 ± 0.037	359.0 ± 1.0	63.8 ± 1.9	259.0 ± 1.3	1874.95 ± 2.12	0.0992 ± 0.0041	BD+10 2739
12	88.44 ± 0.45	0.3225 ± 0.0084	0.551 ± 0.029	131.5 ± 78.1	170.6 ± 5.8	37.9 ± 78.1	1883.65 ± 0.73	0.0687 ± 0.0029	BD+42 2531
13	290.86 ± 4.00	1.4049 ± 0.0090	0.599 ± 0.010	359.7 ± 0.3	138.8 ± 0.9	179.0 ± 0.8	1872.92 ± 0.39	0.1213 ± 0.0032	BD+37 2636
14	219.53 ± 0.98	2.2300 ± 0.0209	0.755 ± 0.007	107.6 ± 1.1	109.9 ± 0.9	71.8 ± 0.03	1701.34 ± 0.10	0.3547 ± 0.0109	BD+18 3182
15	129.04 ± 0.53	0.9566 ± 0.0120	0.618 ± 0.013	145.1 ± 4.6	25.9 ± 1.8	62.2 ± 4.3	1938.77 ± 0.35	0.1422 ± 0.0036	BD+2 3118
16	123.27 ± 0.89	0.9364 ± 0.0138	0.323 ± 0.025	207.7 ± 4.7	63.3 ± 0.9	59.3 ± 1.0	1893.14 ± 1.50	0.1358 ± 0.0561	BD+43 2639
17	265.57 ± 6.45	1.0063 ± 0.0141	0.552 ± 0.019	242.9 ± 4.4	30.4 ± 1.7	51.3 ± 3.3	1895.46 ± 1.04	0.1159 ± 0.0040	BD+28 2624
18	84.86 ± 0.94	0.2584 ± 0.0256	0.650 ± 0.119	12.9 ± 7.2	125.8 ± 7.1	152.7 ± 7.1	2049.18 ± 5.78	0.0545 ± 0.0045	BD+56 1959
19	299.9 ± 24.8	1.1592 ± 0.0509	0.612 ± 0.046	309.1 ± 3.8	102.0 ± 1.0	70.9 ± 1.0	1915.57 ± 1.92	0.1826 ± 0.0065	BD+03 3610
20	347.5 ± 2.4	1.0369 ± 0.0279	0.632 ± 0.004	359.3 ± 0.7	106.2 ± 2.5	103.3 ± 1.0	1882.96 ± 3.94	0.1098 ± 0.0036	BD+27 3391
21	631.5 ± 76.7	2.4856 ± 0.1480	0.468 ± 0.049	168.7 ± 97.8	170.0 ± 6.4	180.6 ± 97.5	1866.12 ± 6.60	0.2067 ± 0.0068	BD+44 3234
22	167.6 ± 2.8	0.6367 ± 0.0056	0.023 ± 0.019	92.3 ± 100.8	48.0 ± 1.2	154.0 ± 1.2	1899.67 ± 46.67	0.0725 ± 0.0029	BD+34 3727
23	200.0 ± 3.0	0.8015 ± 0.0184	0.485 ± 0.023	49.0 ± 4.1	64.7 ± 0.8	175.2 ± 1.3	1898.68 ± 1.91	0.0823 ± 0.0037	BD—6 5604
24	92.1 ± 0.4	0.7045 ± 0.0382	0.757 ± 0.027	283.0 ± 30.8	16.5 ± 8.6	180.7 ± 31.1	1905.29 ± 0.35	0.1065 ± 0.0050	BD+4 4994
25	251.3 ± 29.6	0.9086 ± 0.0571	0.594 ± 0.076	213.6± 13.9	131.1 ± 6.4	143.3 ± 7.1	1899.70 ± 4.5	0.0730 ± 0.0045	BD+38 5112

Note: Uncertainties are single σ (one standard deviation). See the text for the explanation of the symbols used as the column titles other than "Epoch," which is the time of phase zero for the orbital ephemeris, the orbital period (P) in years, and σ which is an estimate of the Gaussian noise of the data observations (the "error" in the x and y coordinates). σ is a free parameter in the MCMC fits. "BD" gives an alternative ID for each system, allowing cross referencing.

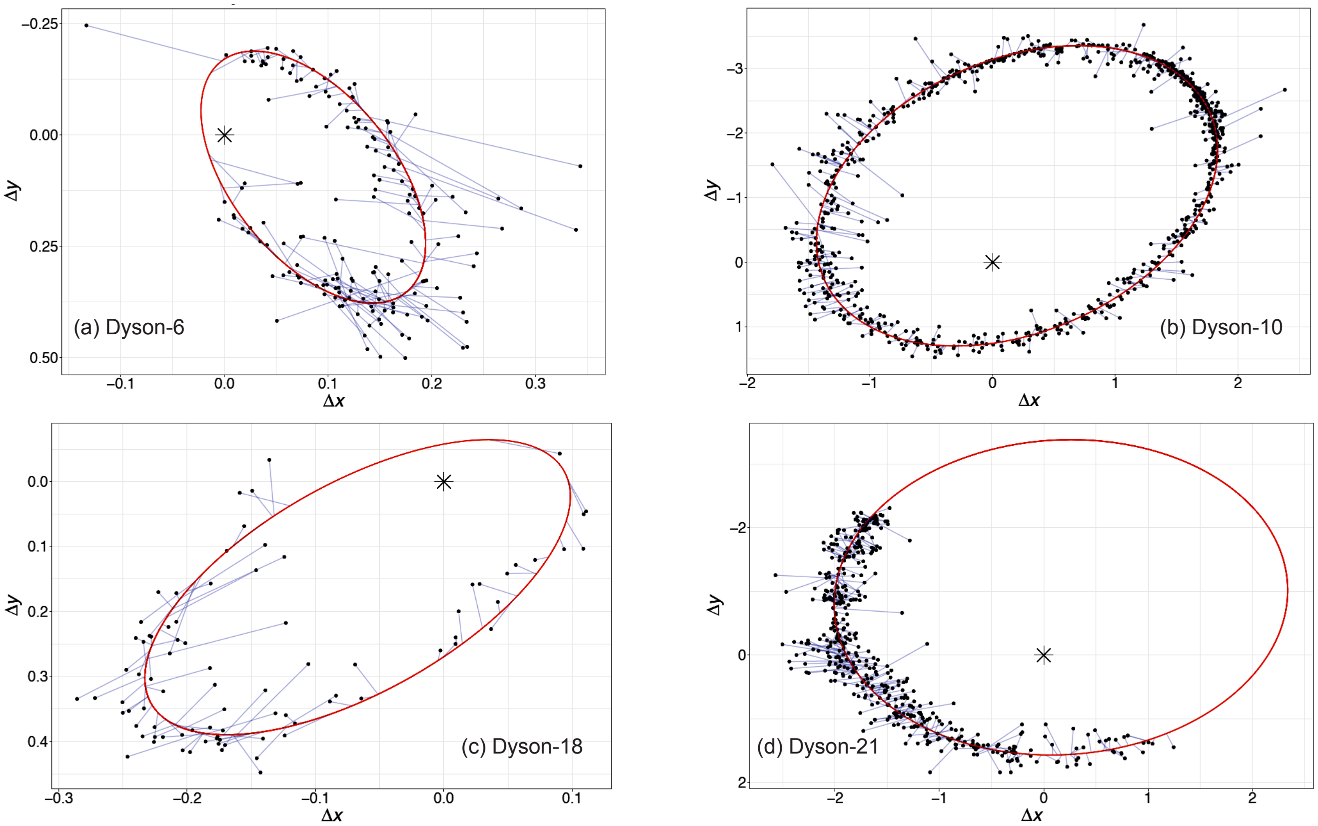

Figure 1. Observations and model orbits for representative Dyson systems selected to show a range of data sets, from complete orbits to partial and of different noise levels. East increases to the right, and down is northwards (as per convention in many visual binary papers). The model orbits are shown as the red curve, observations are plotted as black dots, and the blue lines connect the observations to their modelled positions on the model orbits. The star symbol at (Δ x, Δ y) = (0,0) is the location of the primary star in each system. These parameters should not be confused with δ x and δ y mentioned in the paper text, which are adjustments to the origin used by the optimizer to improve the fit. Orbital parameters are given in Table 1.

Dyson systems, along with the model orbit based on the optimal parameter values given in Table 1. Again, not all fits to the data are shown in this paper to conserve space.

Figure 2 is an example of a "corner plot," which were generated for all fits. This is one of the standard diagnostic tools used in MCMC analysis. This figure is representative of the corner plots for the other systems. The diagonal running from upper left to lower right plots histograms plotting parameter estimates from each of the last 10 thousand MCMC steps, for each of the parameters in turn. These are all nicely Gaussian shaped in the diagram, indicating a stable solution has been reached. Correlations between the parameters are given in the boxes to the upper right, while the charts to the lower left plot each parameter against the others. These charts clearly show the correlations between parameters, or lack thereof.

Most systems were simple convex optimizations. D8 (D for Dyson), D12, D18, D20, D21, D22, D24, and D25 were more challenging systems. Convergence was more difficult due to higher levels of noise and/or shorter orbital arcs being observed for these systems compared to the others in this set. D12, D20, and D21 exhibited double peaks in the posterior distributions, indicating problems with the symmetry of some of the angle parameters. A point optimization technique could settle in one of these two minima, depending on the starting parameter values chosen.

The dynamical (or combined stellar) mass M_d of such binary systems can be calculated if the parallax is known, via an equation (Malkov *et al.* 2012) based on Kepler's third law:

$$M_d = \frac{a^3}{\pi^3 P^2} \tag{3}$$

where both a and the parallax π are in milli-arcseconds, P is in years, and M_d is in solar masses. Estimated dynamical masses are given in Table 2, based on *Hipparcos* (Perryman *et al.* 1997a, 1997b and *Gaia* Data Release 3 (Gaia Collab. *et al.* 2022) parallaxes. Errors in a, P, and π were propagated through Equation 3 to give the single σ uncertainties presented in Table 2. Not all of the systems with parallaxes available from both catalogs have dynamical mass estimates within formal statistical agreement at 2σ.

Table 2. Dynamical masses (solar units) based on *Hipparcos* and *Gaia* DR3 parallaxes (where available). Dyson numbers are used to identify the systems. Errors are one standard deviation.

Dyson ID	*Hipparcos*	*Gaia*
1	2.00 ± 0.04	
2	1.74 ± 0.06	
3	1.83 ± 0.52	
4	5.81 ± 0.31	
5	3.20 ± 0.12	4.07 ± 0.05
6	2.87 ± 0.19	
7	14.4 ± 0.16	
8	6.11 ± 0.76	5.05 ± 0.76
9	1.75 ± 0.17	1.33 ± 0.16
10	1.44 ± 0.02	
11	0.85 ± 0.10	0.89 ± 0.04
12	2.53 ± 0.12	
13	1.37 ± 0.05	1.75 ± 0.06
14	1.75 ± 0.03	
15	7.86 ± 0.06	
16	1.07 ± 0.08	
17	2.88 ± 0.07	3.71 ± 0.04
18	1.54 ± 0.20	
19	2.85 ± 0.15	
20	2.48 ± 0.15	2.13 ± 0.05
21	4.98 ± 0.20	4.07 ± 0.20
22	2.37 ± 0.08	
23	2.88 ± 0.08	2.86 ± 0.05
24	1.36 ± 0.13	
25	1.45 ± 0.21	1.48 ± 0.20

4.1. Comparison with WinFitter results

Figure 3 plots the final parameter estimated from WinFitter (Rhodes *et al.* 2023) against this paper's MCMC results. Agreement overall is good, although we note that the longer period systems tend to have less well-constrained estimates for the parameters, as might be expected. Coefficients of Determination (R^2) between the two sets of estimates, for each parameter, are shown in the sub-figures. The regression slopes are not substantially different from unity, indicating good agreement between the two sets. Such agreement is comforting, and lends support to being able to later use the HMC-based program and technique on other systems which have not been modeled before—indeed, a key driver for this project was the need to verify that a program written to model the orbit of V410 Puppis was correct (Erdem *et al.* 2022), hence modeling the "known" systems of Dyson. The gray-shaded regions give the formal 2σ uncertainties in the regressions, showing that in general there is not a difference from a slope of perfect agreement for most of the parameters at the 95% statistical confidence level. The exception is for period, where the WinFitter solutions for the longest period systems are in general smaller than the MCMC-based estimates. It is worth noting that the uncertainties given for these systems by the HMC method are large, indicating a lack of confidence in the point estimates. Overall the estimated uncertainties from the HMC method are larger than those from WinFitter, but the value varies by parameter. Regression of the logarithm of the uncertainties gave the following relationships for the errors:

$$\log P = (0.41 \pm 0.10) + (0.94 \pm 0.12) \log P_W \text{ with } R^2 = 0.72,$$
$$\log a = (0.77 \pm 0.12) \log a_W \text{ with } R^2 = 0.97,$$
$$\log e = (0.74 \pm 0.04) \log a_W \text{ with } R^2 = 0.95,$$
$$\log i = (0.37 \pm 0.06) + (0.76 \pm 0.11) \log i_W \text{ with } R^2 = 0.69,$$
$$\log \omega = (1.09 \pm 0.0.33) \log \omega_W \text{ with } R^2 = 0.32,$$
$$\log \Omega = (0.24 \pm 0.09) + (0.66 \pm 0.14) \log \Omega_W \text{ with } R^2 = 0.52,$$

where the subscript W refers to the results from the WinFitter fits by Rhodes *et al.* (2023). In these equations, for simplicity we have used the parameter symbol as a placeholder for the error estimate of a parameter. We recommend the HMC approach as more rigorous, but given the substantially lower time required by WinFitter (seconds as opposed to MCMC runs which may take a day or more on a M1 Macbook Pro), these empirical scaling rules could be helpful for interpreting first looks using WinFitter. Rhodes *et al.* (2023) had assumed a constant 5% "mean observational error," which appears to be an underestimate of the actual scatter when compared with the σ values given in Table 1. It would be an interesting extension

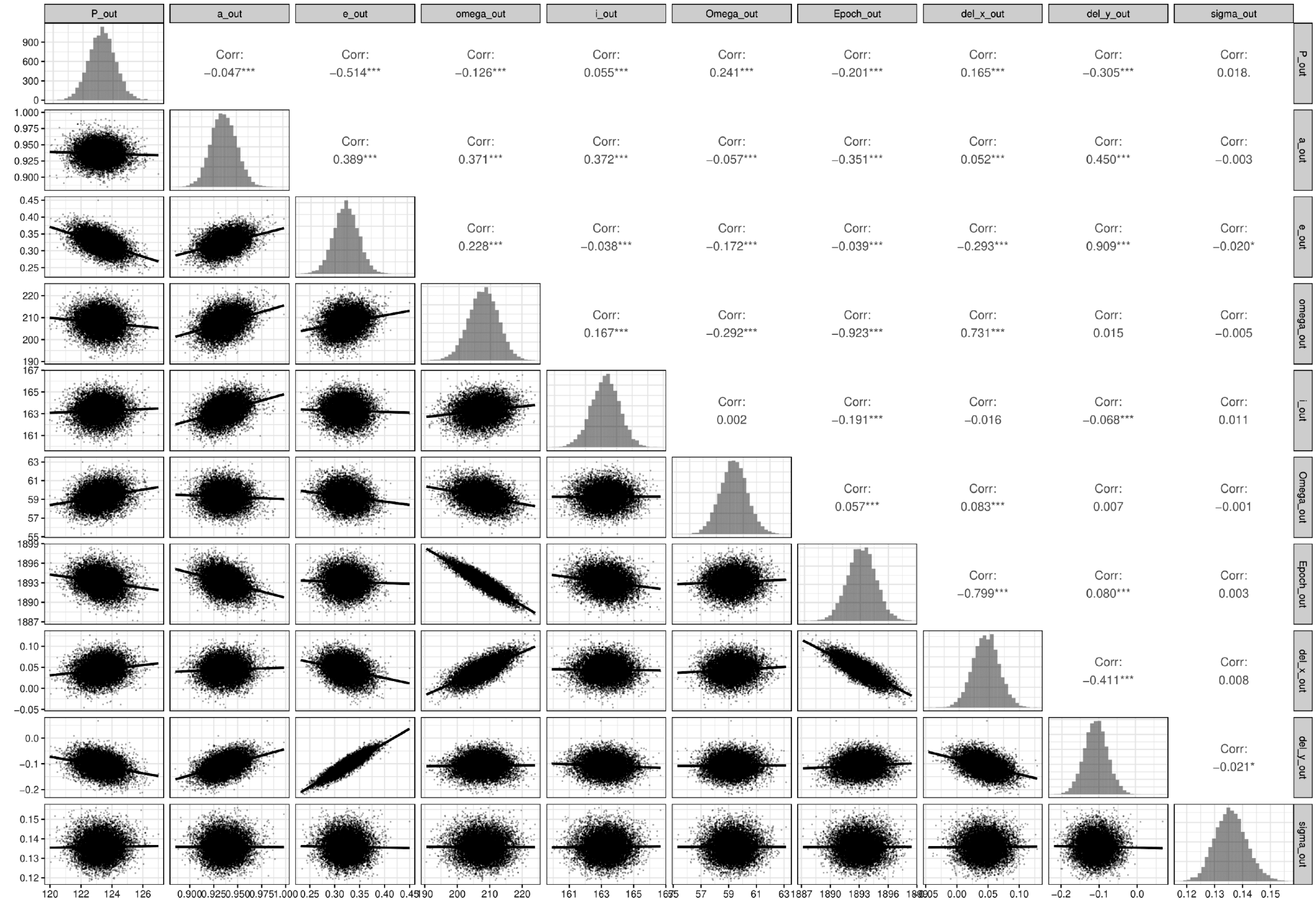

Figure 2. Example "corner plot" based on the MCMC fitting for Dyson-16, which is representative of corner plots for the other systems. This represents 10,000 steps in the Markov chain, excluding the initial 10,000 steps known as "burn-in." These steps are excluded from the final results, and are considered a result of starting the optimization in a lower probability set of parameters, leading to movement to the global minimum. The columns and rows correspond to the optimized parameters, namely P, a, e, ω, i, Ω, epoch,Δ x, Δ y, and σ, in that order. The diagonal shows histograms of the parameter estimates, the upper right of the figure gives the correlation coefficients between pairs of the parameters, and the lower left plots the parameters estimates for pairs of the parameters. See text for more information.

to this project to run the same fitting software (WINFITTER) on these systems with the noise levels set to the values of σ found by the MCMC fitting of the current paper, and see if these error estimates by WinFitter and our HMC method are in closer agreement.

4.2. Comparison with Dyson results

Figure 4 compares the optimal parameter estimates from Dyson (1921) and the HMC method of the current paper. Naturally, the HMC method had access to an extra century for further observations, which helped constrain the orbital parameter estimates further. The charts show overall good agreement between the Dyson estimates and those of this paper. The longer period systems can show weaker agreement than for the shorter period ones, such as shown in Figure 4a where systems 8, 9, and 21 have clearly different estimated periods. Removing these three systems gives a regression slope of 0.99 ± 0.08, assuming a zero intercept, and the coefficient of determination $R^2 = 0.88$, which confirm good agreement. Similarly, the agreement is good for a (slope 0.96 ± 0.04, $R^2 = 0.95$, Figure 4b and e (slope 0.93 ± 0.07, $R^2 = 0.90$, Figure 4c. It is interesting to note that in general for systems with orbits of $100 \leq P < 200$ years, Dyson's estimated ellipticities appear systematically higher than those from the HMC approach. Matters become more complicated for the remaining parameters as there are ambiguities, e.g., inclination estimates can be symmetric around 90 degrees since from astrometric measurements alone we do not know the actual orbital direction of the star. Two dotted lines are therefore shown in each of Figures 4d, 4e, and 4f to reflect this and show again good general agreement. While it is possible to "reflect" some of the results to allow calculation of linear correlations, we have chosen to leave the data unadjusted, given some uncertainty which estimates should be reflected for some systems and we do not wish to present overly optimistic correlations through biased choices.

4.3. Parameter reduction

As noted above, in results from the MCMC fits the parameters δx and δy were not statistically different from zero. This is as expected, from the fact that those variables are actually redundant in the model. We therefore reran the fittings without these parameters to see the change in the estimates of the other parameter values. Overall, agreement is good as can be seen

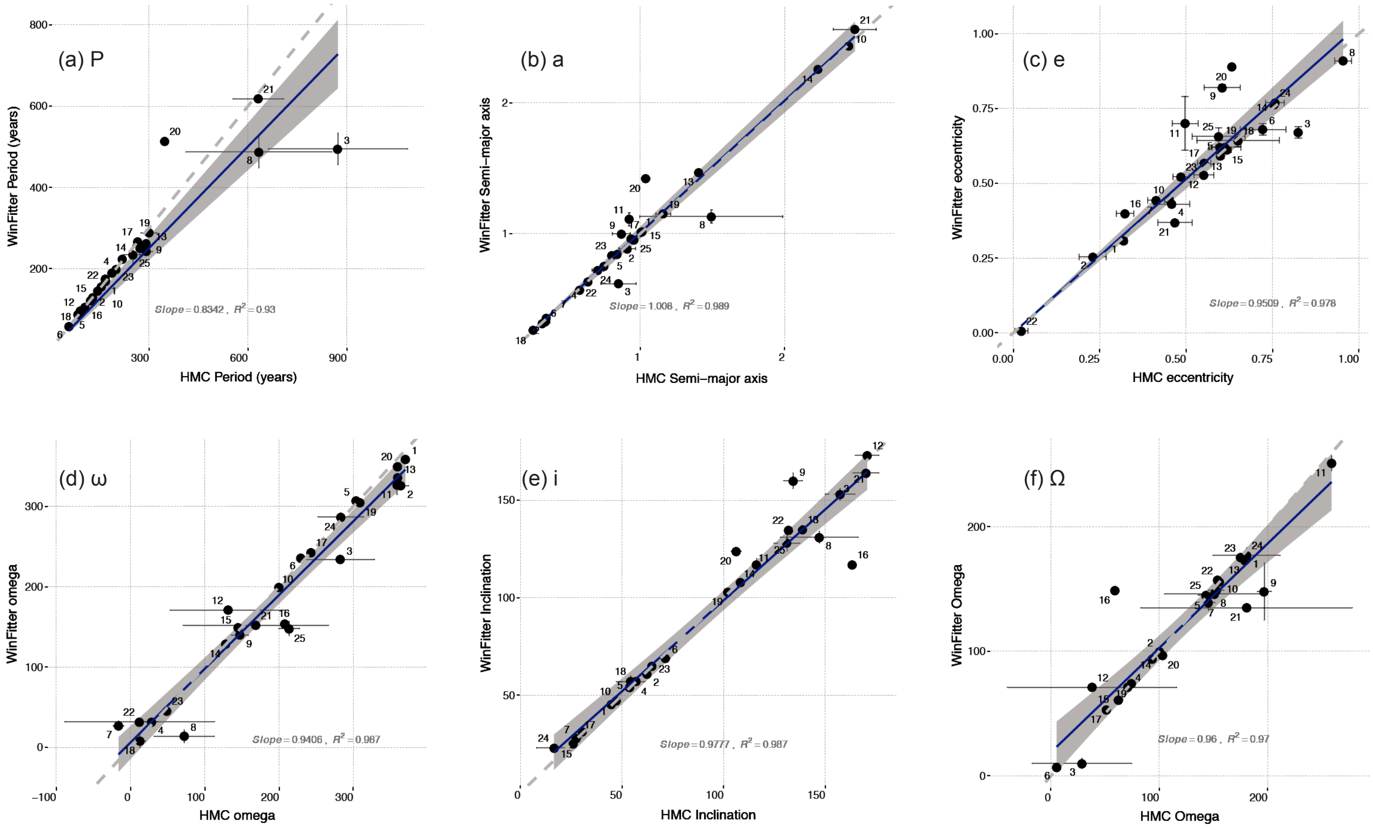

Figure 3. Comparison between HMC and WinFitter optimal parameter estimates. Systems are denoted by their Dyson number. Regressions have been fitted to the data, resulting in best-fit (blue-colored) lines in the charts. Two-sigma confidence limits are shown as the gray-shaded regions. The dotted lines are those of perfect agreement.

in Figure 5, which plots parameter estimates from both groups of MCMC fittings by system and by parameter. The dotted diagonal lines are those of perfect agreement between the two methods, with data points frequently falling within error of these lines. Longer period systems were harder to "pin down," having the larger absolute change in estimates (which was signaled by the larger estimated standard deviations). The formal errors for some systems appear to be under-estimates, such as the ellipticities for the longer period systems Dyson-3 (D3) and -20 (D20). Even if the errors are tripled to be 3σ, they will not overlap the dashed line of agreement between the two fittings. This study did not make a detailed investigation of the likely observational "errors" (i.e., there was no weighting applied to the data to reflect different observational accuracies), which likely contributes towards these underestimates. We plan to investigate improved estimation and handling of observational errors in further optimizations, extending this preliminary study.

Table 3 presents the results of these fits, where the bolded text indicates 3σ differences between the results from the original MCMC fits (Table 1) and these with a fixed origin. The significant differences are mainly in the longer period systems D3, D11, D13, and D20, with agreement being good for the other systems. The data for D3 and D20 are sparse for roughly the first half of the observation periods, while those for D11 and D13 correspond to arcs without much curvature. The parameter estimates for the other systems are overall within statistical error of those from the previous fits. Removing the four mentioned systems from regression analyses comparing the parameter estimates, we first found that intercept terms were not statistically significant. Regressions through the origin for (Ω, ω, e, i, a, P) had coefficients of determination (R^2) of (0.9979, 0.9805, 0.9940, 0.996, 0.9973, 0.9956), respectively, with slopes of (1.0004, 0.9859, 0.9844, 1.008, 0.998, 0.996) and corresponding standard errors of (0.010, 0.021, 0.017, 0.005, 0.012, 0.015). Estimates for the dynamical masses are also given in Table 3. Taking log masses (from the two sets of MCMC fits) gave regression slopes of 1.0 ± 0.1 for the systems with *Gaia* distances and 0.99 ± 0.05 for *Hipparcos* distances.

Inclusion of the parameters δx and δy is not needed for this kind of study (they act as "nuisance" parameters), and we will not include them in subsequent similar studies given this comparison. Additionally, removal of the parameters reduces by two the number of dimensions being searched in the optimization, lowering the computational load. The results given in the current section and Table 3 are this paper's final results for the analyzed systems.

5. Discussion

This paper has presented MCMC analyses of astrometric data for 25 systems, updating orbital parameters estimates given by Dyson (1921) a century ago. It has shown reasonable agreement between the two studies, and an even stronger agreement with an earlier investigation by the current team

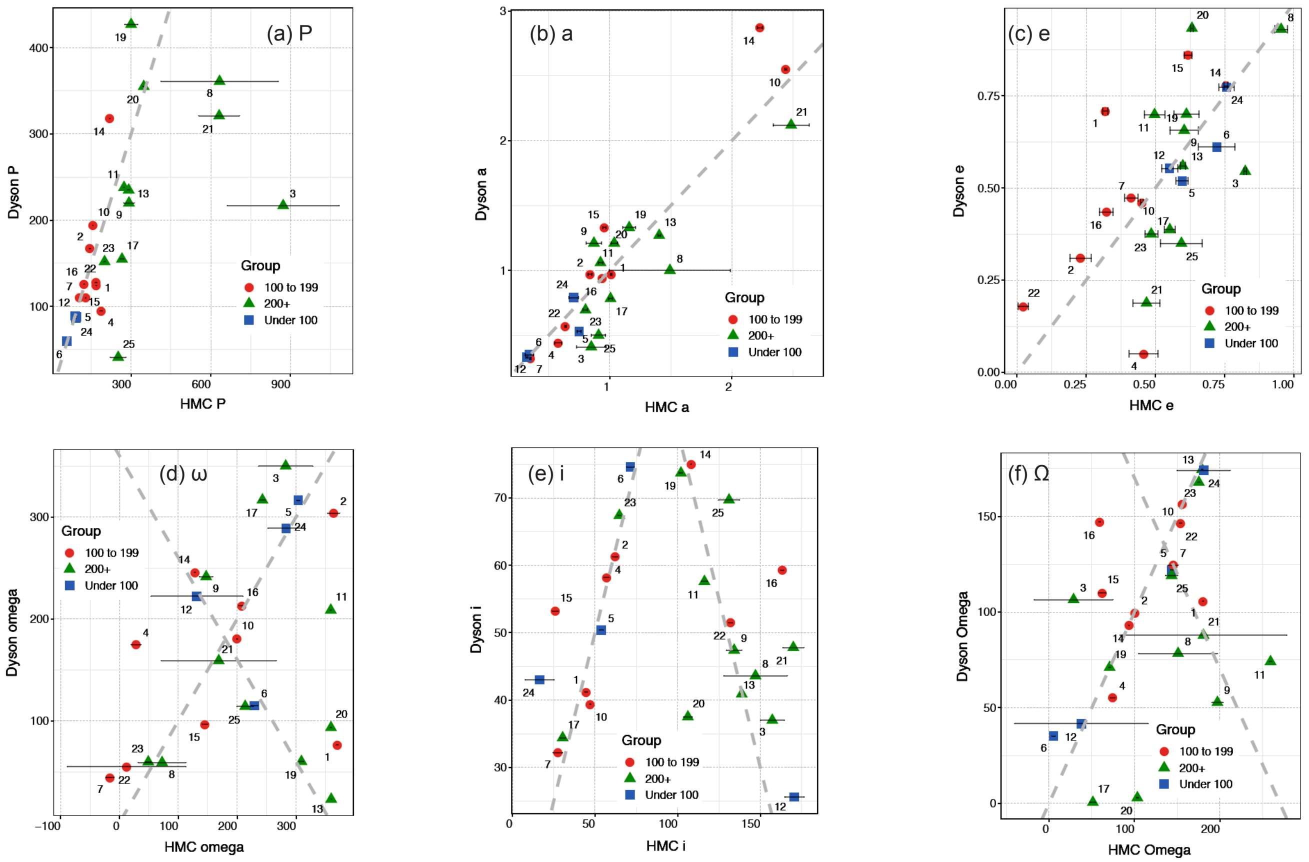

Figure 4. Comparison between HMC and Dyson optimal parameter estimates. Systems are denoted by their Dyson number. The dotted lines are those of perfect agreement between the two sets of parameter values. Observations are grouped by the HMC period estimates into less than 100 years, 100 to less than 200 years, and greater than or equal to 200 years. Dyson did not calculate uncertainties, so these are only plotted for the HMC estimates.

(Rhodes *et al.* 2023) using a tool (in WinFitter) they developed employing point estimation supplemented with examination of the Hessian matrix to estimate uncertainties in the parameters. The HMC method led to larger estimates than those calculated by WinFitter, which we believe are more robust, being based on exploration of the Bayesian posterior distribution. Finally, we include parallax estimates from the *Hipparcos* and *Gaia* missions to present estimates and associated uncertainties of the dynamical masses of the systems.

Analysis of double star orbits is a useful tool in the variable star analyst's toolkit, and can be supplemented with other techniques to better improve understanding of the system. For instance, Mendez *et al.* (2017) extend their MCMC astrometric analysis with the inclusion of radial velocities, which help to resolve issues with the direction of the orbital movement and the ambiguities noted above for some of the optimized parameters. Member stars of a double system can be variable, indeed cursory examination of the *TESS* space telescope (Ricker *et al.* 2014) photometry for the Dyson systems (see Figure 6) indicates possible variable for a number of systems (D3, D5, D9, D10, D13, D17, D18, D20, D22, and D23). Analysis of such variability, such as through asteroseismology studies (see, e.g., Aerts *et al.* 2010), could provide additional insights such as mass estimates. It is also increasingly common for systems to be recognized as multiple systems, such as with the case of V410 Puppis (Erdem *et al.* 2022), where astrometric analysis of the orbit of third system member about an inner eclipsing binary pair helped provide insights into the overall system.

Observations and analysis of visual binaries is not time-consuming (see, e.g., Cleveland and Thompson 2022) in the actual data collection, nor is the measurement of positions and angles (say from CCD images). While the "payback" of such observations may not be immediate, we end with the thoughts of Hertzsprung (as given in Mason 2006): "The debt to our ancestors for the observations they made to our benefit, we can pay only by doing the same for our descendants."

Using such astrometric data collected by previous generations of astronomers led to feelings of connection with both them and the development of astronomy with time, as well appreciation for the work by our predecessors. While missions such as *Gaia* will add data for astrometric binaries, on-going measurements (for instance in periods outside such surveys) will no doubt be appreciated by astronomers in the future.

Further details and background on this project may be found in Soh (2023).

6. Acknowledgements

This work has made use of data from the European Space Agency (ESA) mission *Gaia* (https://www.cosmos.esa.int/gaia), processed by the *Gaia* Data Processing and Analysis Consortium (DPAC (https://www.cosmos.esa.int/web/gaia/dpac/consortium). Funding for the DPAC has been provided by national institutions, in particular the institutions participating

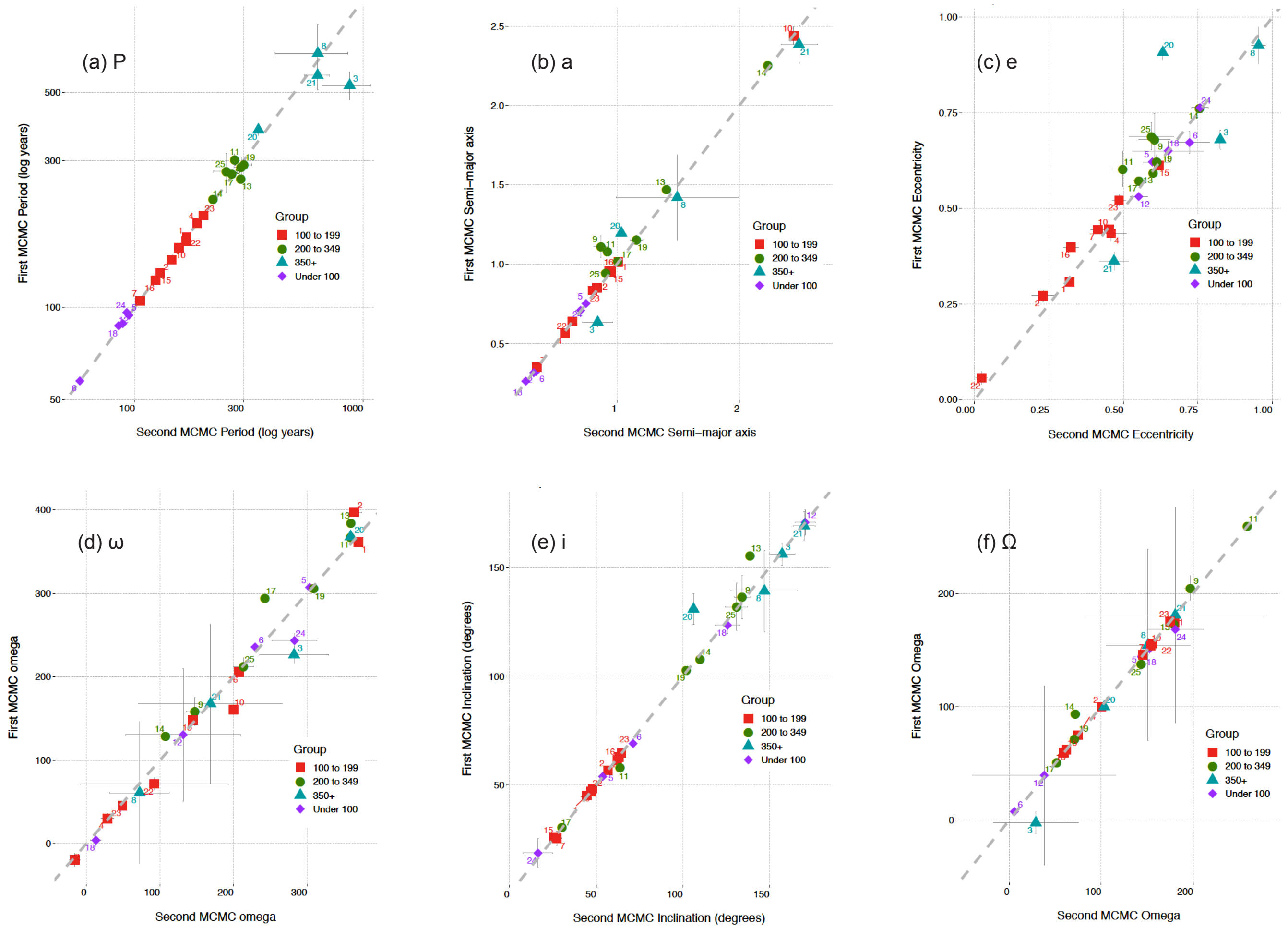

Figure 5. Comparison between the MCMC fits with δx and δy included as free variables ("First MCMC," the y axis) and those with the two parameters removed and (x,y) set to (0,0) ("Second MCMC," the x axis). Systems are denoted by their Dyson number. The dotted lines are those of perfect agreement. Points are coded by color and shape by the estimated orbital periods (under 100 years, 100 to 199 years, 200 to 349 years, and greater than 350 years). Error bars correspond to one standard deviation. Note that the orbital periods are given in log years.

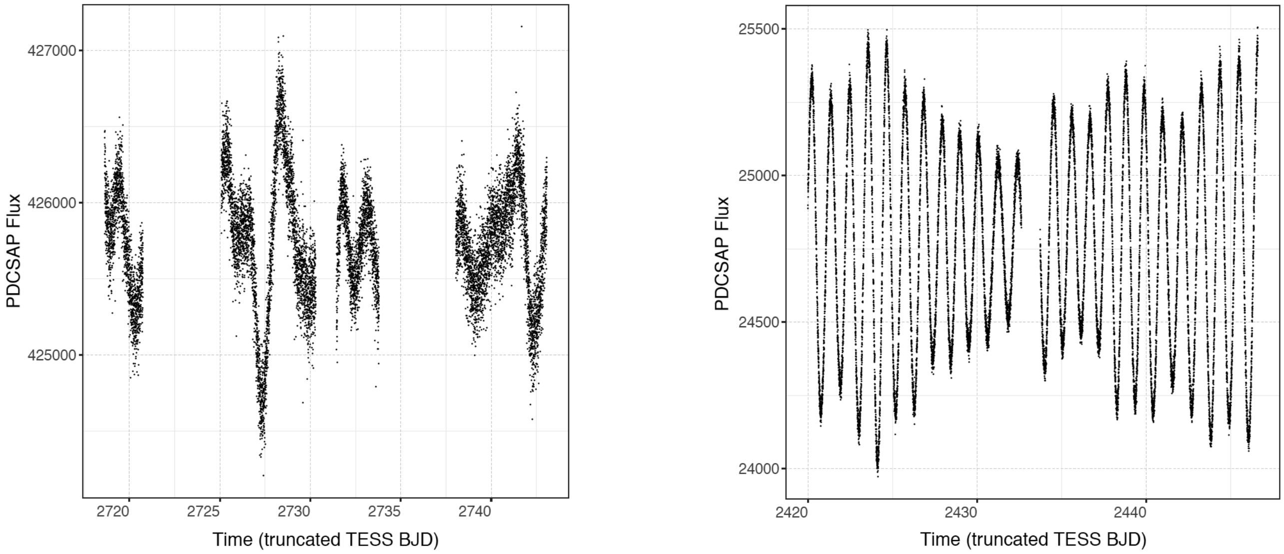

Figure 6. *TESS* photometry for two example systems (D17 and D20). The fluxes are non-normalized Pre-search Data Conditioning Simple Aperture Photometry (PDC_SAP) generated by the *TESS* team, which removed longstanding systematic trends. Time is the Barycentric Julian Date (BJD) – 2457000.

Table 3. Parameter estimates from the second MCMC fitting to the Dyson systems, numbered by appearance in Dyson (e.g., 1 refers to Dyson-1 or D1).

System	*P*	*a*	*e*	*ω*	*i*	*Ω*	*Epoch*	*σ*	Hipparcos	Gaia
1	168.56 ± 0.57	1.014 ± 0.005	0.308 ± 0.003	**1.6 ± 1.2**	45.2 ± 0.5	**173.93 ± 0.72**	1956.28 ± 0.31	0.0961 ± 0.0025	2.01 ± 0.04	
2	142.51 ± 1.63	0.852 ± 0.018	0.272 ± 0.014	37.2 ± 4.5	61.5 ± 1.5	99.72 ± 1.66	**1900.64 ± 1.42**	0.2244 ± 0.0084	1.89 ± 0.06	
3	**526.67 ± 54.22**	0.635 ± 0.029	**0.680 ± 0.024**	226.4 ± 9.8	156.2 ± 5.1	–2.56 ± 9.67	1911.40 ± 0.71	0.0867 ± 0.0035	2.10 ± 0.35	
4	187.63 ± 3.84	0.565 ± 0.011	0.435 ± 0.021	30.2 ± 6.0	56.7 ± 1.6	74.52 ± 2.50	1887.34 ± 1.87	0.0790 ± 0.0042	5.37 ± 0.30	
5	94.08 ± 0.36	0.753 ± 0.012	0.622 ± 0.010	307.2 ± 1.6	54.0 ± 1.6	143.94 ± 1.47	1887.88 ± 0.39	0.0830 ± 0.0042	3.25 ± 0.12	4.14 ± 0.05
6	57.49 ± 0.45	0.324 ± 0.014	0.672 ± 0.029	235.7 ± 3.7	69.1 ± 2.0	7.28 ± 2.17	1943.09 ± 0.42	0.0710 ± 0.0040	2.46 ± 0.11	
7	105.01 ± 0.59	0.352 ± 0.005	0.444 ± 0.009	–19.3 ± 7.6	25.6 ± 3.2	145.59 ± 6.92	1987.46 ± 0.34	0.0628 ± 0.0026	14.96 ± 0.16	
8	669.28 ± 160.97	1.420 ± 0.269	0.927 ± 0.048	61.0 ± 85.6	139.2 ± 18.7	154.31 ± 84.59	1893.64 ± 3.12	0.1064 ± 0.0037	4.70 ± 0.48	3.89 ± 0.69
9	285.07 ± 23.37	1.113 ± 0.068	0.680 ± 0.068	158.4 ± 16.5	136.4 ± 10.0	204.51 ± 10.88	1857.78 ± 4.03	0.1517 ± 0.0050	3.83 ± 0.17	2.92 ± 0.15
10	155.79 ± 0.35	2.438 ± 0.057	0.446 ± 0.002	**160.6 ± 0.6**	47.2 ± 0.3	155.73 ± 0.36	1916.62 ± 0.11	0.1307 ± 0.0031	1.44 ± 0.04	
11	**302.08 ± 12.96**	**1.079 ± 0.023**	0.603 ± 0.046	367.4 ± 6.2	58.1 ± 2.9	259.04 ± 2.68	1864.90 ± 3.79	0.0960 ± 0.0040	1.11 ± 0.12	1.16 ± 0.07
12	88.43 ± 0.45	0.318 ± 0.005	0.531 ± 0.010	130.5 ± 79.1	170.7 ± 5.7	129.30 ± 79.13	1883.56 ± 0.47	0.0684 ± 0.0029	2.41 ± 0.12	
13	**261.54 ± 2.65**	**1.470 ± 0.008**	0.592 ± 0.004	**384.7 ± 1.1**	**155.3 ± 1.1**	**172.70 ± 0.96**	**1864.31 ± 0.32**	0.1150 ± 0.0030	1.94 ± 0.05	2.47 ± 0.05
14	224.05 ± 2.64	2.254 ± 0.019	0.762 ± 0.004	**128.9 ± 0.5**	108.1 ± 0.2	**93.35 ± 0.34**	**1921.08 ± 0.16**	0.1198 ± 0.0037	1.73 ± 0.03	
15	128.91 ± 0.53	0.952 ± 0.007	0.612 ± 0.005	148.0 ± 4.4	25.9 ± 1.8	61.93 ± 4.19	1939.50 ± 0.20	0.1426 ± 0.0036	7.75 ± 0.05	
16	122.36 ± 0.83	0.956 ± 0.012	0.398 ± 0.010	205.9 ± 2.5	63.0 ± 1.0	59.20 ± 1.03	1894.24 ± 0.72	0.1379 ± 0.0057	1.15 ± 0.08	
17	270.66 ± 5.12	1.017 ± 0.011	0.572 ± 0.008	**294.6 ± 3.4**	30.7 ± 1.7	50.57 ± 3.17	1896.33 ± 0.34	0.1158 ± 0.0039	2.86 ± 0.06	3.69 ± 0.04
18	86.97 ± 1.19	0.264 ± 0.008	0.651 ± 0.025	4.1 ± 8.2	123.5 ± 3.7	151.10 ± 4.24	2054.76 ± 1.63	0.1768 ± 0.0146	1.57 ± 0.12	
19	290.23 ± 13.31	1.154 ± 0.029	0.622 ± 0.018	305.9 ± 2.0	102.9 ± 0.6	71.02 ± 1.00	1914.13 ± 0.81	0.1832 ± 0.0065	3.00 ± 0.10	
20	**377.31 ± 15.01**	**1.197 ± 0.003**	**0.908 ± 0.019**	368.1 ± 3.8	**130.9 ± 7.0**	99.75 ± 2.70	1886.48 ± 1.66	0.1101 ± 0.0037	3.23 ± 0.15	2.77 ± 0.07
21	567.53 ± 42.83	2.384 ± 0.119	0.362 ± 0.024	167.8 ± 95.4	169.1 ± 6.5	180.74 ± 94.94	1866.16 ± 3.82	0.2103 ± 0.0068	5.44 ± 0.14	4.45 ± 0.16
22	164.14 ± 2.58	0.641 ± 0.06	0.057 ± 0.016	71.7 ± 7.1	48.3 ± 1.3	153.62 ± 1.19	1873.57 ± 3.17	0.0725 ± 0.0028	2.52 ± 0.08	
23	198.56 ± 2.54	0.824 ± 0.011	0.521 ± 0.015	45.7 ± 2.5	64.8 ± 0.8	175.19 ± 1.15	1896.37 ± 0.82	0.0830 ± 0.0038	3.29 ± 0.07	3.27 ± 0.04
24	96.09 ± 0.40	0.710 ± 0.018	0.764 ± 0.008	243.4 ± 8.3	18.8 ± 6.6	168.00 ± 8.29	1905.42 ± 0.24	0.1063 ± 0.0050	1.28 ± 0.10	
25	276.56 ± 39.81	0.946 ± 0.041	0.688 ± 0.35	212.4 ± 10.9	131.9 ± 10.9	137.61 ± 5.33	1904.85 ± 1.14	0.0734 ± 0.0045	1.35 ± 0.23	1.38 ± 0.23

*Note: Parameter columns are the same as in Table 1. Text in **bold** indicates 3-σ differences with the results of the initial MCMC modeling given in Table 1. A high σ was chosen to reduce the number of false positives that will occur in repeated statistical testing like this, to clearly show the systems with differences. System masses (in solar units) are calculated using the Hipparcos and Gaia parallaxes (given in the columns labelled “*Hipparcos*” *and* “*Gaia*”).*

in the *Gaia* Multilateral Agreement. We thank the University of Queensland for collaboration software. This paper includes data collected with the *TESS* mission, obtained from the MAST data archive at the Space Telescope Science Institute (STScI). Funding for the *TESS* mission is provided by the NASA Explorer Program. STScI is operated by the Association of Universities for Research in Astronomy, Inc., under NASA contract NAS 5–26555. This research has made use of the Washington Double Star Catalog maintained at the U.S. Naval Observatory (USNO). We thank the USNO and Dr. Rachel Matson for access to the WDS data. We thank the anonymous referee for their comments and guidance which improved the paper.

References

Aerts, C., Christensen-Dalsgaard, J., and Kurtz, D. W. 2010, *Asteroseismology*, Springer, Dordrecht.

Aitken, R. G. 1964, *The Binary Stars*, Dover, New York.

Banks, T., and Budding, E. 1990, *Astrophys. Space Sci.*, **167**, 221.

Bevington, P. R. 1969, *Data Reduction and Analysis for the Physical Sciences*, McGraw-Hill, New York.

Claveria, R. M., Mendez, R. A., Silva, J. F., and Orchard, M. E. 2019, *Publ. Astron. Soc. Pacific*, **131**, 084502.

Cleveland, J., and Thompson, K. 2022, *J. Double Star Obs.*, **18**, 384.

Cocteau, P. 1981, *Observing Visual Double Stars*, trans, Alan Batten, MIT Press, Cambridge, MA.

Dyson, F. W. 1921, *Catalogue of Double Stars from Observations Made at the Royal Observatory, Greenwich*, H. M. Stationery Office, London.

Erdem, A., *et al.* 2022, *Mon. Not. Roy. Astron. Soc.*, **515**, 6151.

Gaia Collaboration, *et al.* 2022, “Gaia Data Release 3: Summary of the Content and Survey Properties,” arXiv:2208.00211.

Greaney, M. 2004, in *Observing and Measuring Visual Double Stars*, ed. B. Argyle, Springer, London, 273.

Hoffman, M. D., and Gelman, A. 2014, *J. Machine Learning Res.*, **15**, 1593.

Lucy, L. B. 2014, *Astron. Astrophys.*, **563A**, 126.

Malkov, O. Yu., Tamaziani, V. S., Docobol, J. A., and Chulkov, D. A. 2012, *Astron. Astrophys.*, **546A**, 69.

Mason, B. D. 2006, in *Resolving the Rise and Fall of Star Formation in Galaxies*, Proc. IAU 2(S240), doi:10.1017/S1743921307003857, Cambridge Univ. Press, Cambridge, 88.

Mason, B. D., Wycoff, G. L., Hartkopf, W. I., Douglass, G. G., and Worley, C. E. 2022, VizieR Online Data Catalog: The Washington Visual Double Star Catalog (Mason+ 2001–2020), originally published in 2001, *Astron. J.*, **122**, 3466.

Mendez, R. A., Claveria, R. M., Orchard, M. E., and Silva, J. F. 2017, *Astron. J.*, **154**, 187.

Perryman, M. A. C., European Space Agency Space Science Department, and the Hipparcos Science Team. 1997a, The Hipparcos and Tycho Catalogues, ESA SP-1200 (VizieR On-line Data Catalog: I/239), ESA Publications Division, Noordwijk, The Netherlands.

Perryman, M.A.C., *et al.* 1997b, *Astron. Astrophys.*, **323**, L49.

Privault, N. 2013, *Understanding Markov Chains*, Springer Undergraduate Mathematics Series, Springer, Singapore.

R Core Team. 2021, R: A Language and Environment for Statistical Computing, R Foundation for Statistical Computing, Vienna, Austria (https://www.R-project.org).

Rhodes, M. D., Banks, T. S., Budding, E., and Love, T. 2023, *Observatory*. submitted.

Ribas, I., Arenou, F., and Guinan, E. F. 2002, *Astron. J.*, **123**, 2033.

Ricker, G. R., *et al.* 2014, *Proc. Space Telesc. Instrum.*, **9143**, 914320, doi: 10.1117/12.2063489.

Robert, C. P., and Casella, G. 2010, *Introducing Monte Carlo Methods with R*, “Use R!” series, Springer-Verlag, New York.

Sahlmann, J., Lazorenko, P. F., Ségransan, D., Martín, E. L., Queloz, D., Mayor, M., and Udry, S. 2013, *Astron. Astrophys.*, **556A**, 133.

Sinharay, S., 2003, “Assessing Convergence of the Markov Chain Monte Carlo Algorithms: A Review,” ETS Res. Rep. Ser. 2003, No. 1, Educational Testing Service, Princeton, NJ.

Soh, I. X. S. 2023, unpublished honours thesis, Department of Statistics and Data Science, National University of Singapore, Singapore.

Stan Development Team. 2021, RStan: the R interface to Stan, http://mc-stan.org/.

Ninety-Seven New Variable Stars in ω Centauri

Douglas Walker
Department of Mathematics, Embry-Riddle University Worldwide; walked35@erau.edu

Michael Albrow
Department of Physics and Astronomy, Private Bag 4800, University of Canterbury, Christchurch, New Zealand; michael.albrow@canterbury.ac.nz

Received February 19, 2023; revised June 19, 2023; accepted June 29, 2023

Abstract High-cadence photometry of the globular cluster NGC 5139 (ω Centauri) was conducted using the ULTRACAM high-speed frame transfer CCD camera at the 8.2-m Very Large Telescope (VLT) at La Silla, Chile. This research employs difference imaging algorithms to produce time-series photometry data to search for new variable stars within the ω Centauri cluster. The search produced the detection of 117 variable type stars, 19 which were identified and recovered from earlier surveys. An additional set of checks against the Strasbourg astronomical Data Center (CDS) and *General Catalogue of Variable Stars* (GCVS database, Version 2022 June) listed 20 entries, 10 of which were listed as either Horizonal Branch (HB) or Red Giant Branch Stars but not as variables. A single star identified in the CDS is listed as a new RR Lyrae variable. Removing these counts from the 117 identified variables leaves 97 previously unidentified variable stars in ω Centauri. This new variable list includes 5 possible new RR Lyrae types, 13 eclipsing binary type systems, 11 BY Draconis, 3 SX Phoenicis, and 65 variables which have been identified as unknown general Irregular/Semiregular type variables.

1. Introduction

NGC 5139, also known as omega Centauri (ω Cen), is a globular cluster (GC) in the constellation of Centaurus visible from the southern hemisphere. ω Centauri had been listed in Ptolemy's catalog as a star and it was Edmond Halley who was the first to document its nonstellar nature in 1677 by listing it as a "luminous spot or patch in Centaurus" in his historical list of six such objects. Lacaille included it in his catalog as number I.5.

NGC 5139 is located at R.A. $13^h 26^m 47.28^s$, Dec. –47° 28' 46.1", has a heliocentric radial velocity of 231.1 km/s, distance modulus of 13.94, and a [Fe/H] value of –1.53 (Harris 1996). It is the biggest of all globular clusters in the Milky Way galaxy, being about 10 times as massive as other globular clusters and containing about the same mass as the smallest whole galaxies. It is also the most luminous Milky Way globular, and the brightest globular cluster in the sky. In the Local Group, it is outshone only by the brightest globular cluster G1 in the Andromeda Galaxy M31. NGC 5139 may not actually be a classical globular cluster but instead a remnant of a dwarf galaxy that has merged with the Milky Way (Bekki and Freeman 2003).

NGC 5139 contains a dense concentration of variable stars with only the cluster M3 surpassing it in total number of variables. Bailey (1902) identified 128 variables in the cluster and by 1938, 161 variables had been identified by Martin (1938). The catalog of Sawyer Hogg (1973) provided data for variables V1-V183, where four stars were deemed to be non-variable and therefore excluded from the data set. The number was increased by 83 variables as a result of the study of Niss *et al.* (1978). Additional new and suspected variables have been reported by Dickens *et al.* (1972), Fourcade *et al.* (1978), Jorgensen and Hansen (1984), and Mukherjee *et al.* (1992). Currently, the identified number of variables in the cluster is 460 (Clement 2017). Recent publications have focused on the populations of RR Lyraes (e.g. Magurno *et al.* (2018), Braga *et al.* (2018), Braga *et al.* (2016), Navarrete *et al.* (2015)) and near-IR period-luminosities (e.g. Navarrete *et al.* (2017)).

2. Observations

Observational time series data for this project were collected over six observing nights from 22 to 27 April 2011 at the European Southern Observatory's 8.2-m Very Large Telescope on Cerro Paranal in the Atacama Desert of northern Chile. A total of eight observation runs over the six nights with a frame-rate of 6 Hz were obtained. Each observation run contains between 90 and 320 exposures. Image data were acquired using ULTRACAM, an ultra-fast, triple-beam CCD camera designed to provide imaging photometry at high temporal resolutions. The CCDs in ULTRACAM are E2V 47-20 frame-transfer devices of cosmetic quality (grade 0) and quantum efficiency. The chips are Peltier and water-cooled to 233 K, giving approximately 0.05 electron/pixel/second dark current. The readout noise of the chips is low at just over 3 electrons when reading out at 10 microseconds/pixel and just under 6 electrons when reading out at 2 microseconds/pixel (Dhillon *et al.* 2007). The SDSS photometric system (Fukugita *et al.* 1996) was adopted as the primary filter set for ULTRACAM. This system consists of five color filter bands (u', g', r', i', and z').

ULTRACAM contains two CCD chips. The CCD chip FOV coverage for NGC 5139 is a region from the outer edge to the inner part of the cluster as shown in Figure 1.

Area coverage for detectors 1 and 2 is shown along with a scale marker, orientation, and half-light radius in Figure 1. The FOV covers a sky patch approximately 5 × 5 arcmin^2 at a scale of 0.3 arcsec pixel^{-1}, comprising the two CCD chips where each chip contains 1024 pixels on a side. Telescope pointing was located off the center of the cluster at R.A. $13^h 27.0^m 07.46^s$ and Dec. –47° 032.0' 46.110". The FOV

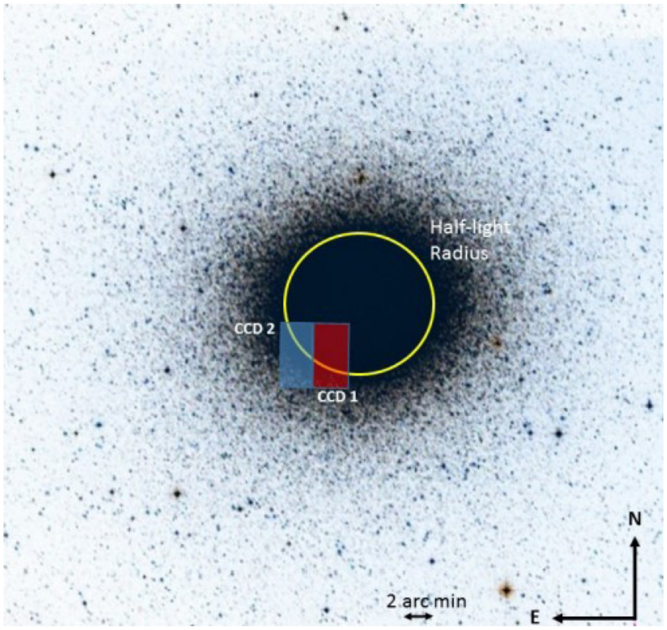

Figure 1. ULTRACAM science camera FOV for NGC 5139.

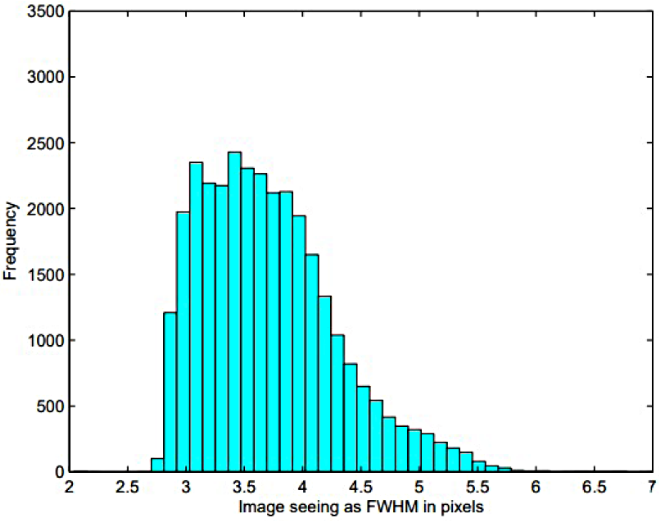

Figure 2. Image seeing as FWHM in pixels for u' filter band.

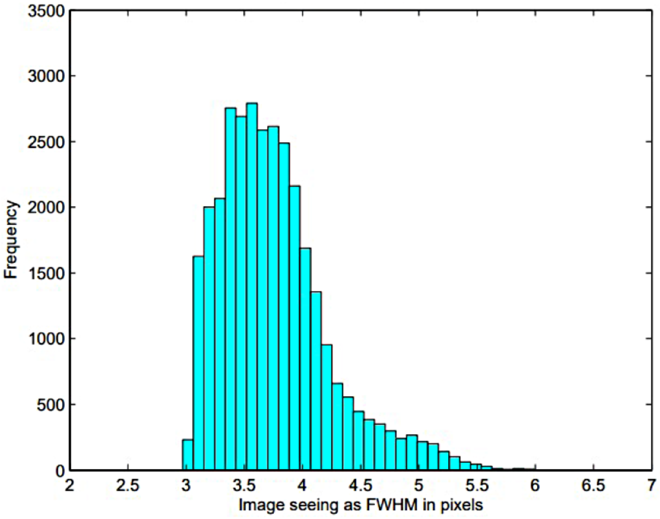

Figure 3. Image seeing as FWHM in pixels for g' filter band.

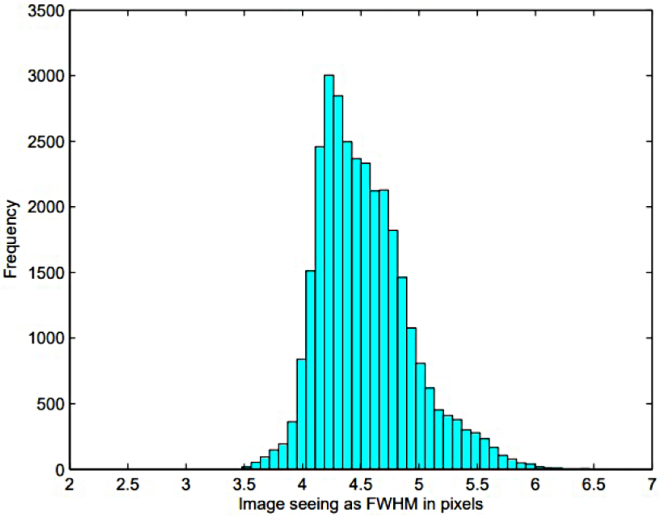

Figure 4. Image seeing as FWHM in pixels for r' filter band.

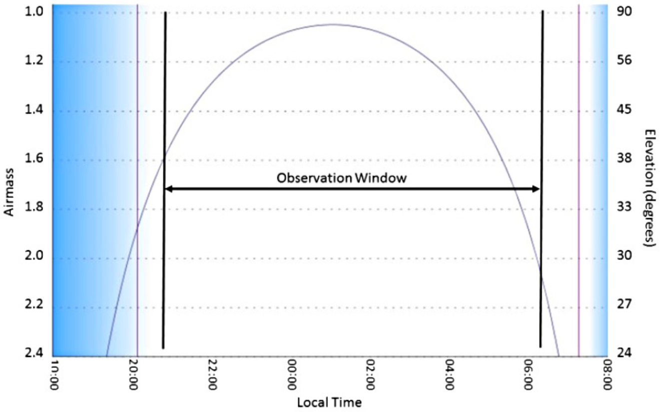

Figure 5. Air mass and observation window for NGC 5139 ULTRACAM.

covered by VLT is from R.A. 13^h 26^m 49.70^s to 13^h 27^m 07.50^s and Dec. –47° 029.00' 45.300" to –47° 035.00' 46.500" for the detector CCD1. Likewise for detector CCD2, the coverage area is R.A. 13^h 27.0^m 07.50^s to 13^h 27.0^m 25.30^s with the same coverage for Dec.

Images were collected over the three filter bands of SDSS u' filter (300–400 nm), SDSS g' filter (400–540 nm), and SDSS r' filters (540-700 nm).

Photometric conditions for images given in Full Width Half Maximum (FWHM) pixels are given in Figures 2 through 4 for filters u', g', and r', respectively. As period searching and analysis was conducted over a combined set of data and not on single observation days, histograms of seeing conditions are given over the complete data set.

The median FWHM for the u' and g' filters is approximately 3.5 pixels. The r' filter conditions were somewhat worse at 4.5 pixels. Combined airmass reading covering the observation cycle was calculated using the on-line tool TAPIR as shown in Figure 5. Optimum observation times were between 22:00 and 04:00 hours local time, which is at minimum airmass. As shown in Figure 5, the observations covered approximately the complete observing cycle.

3. Data reduction and light curve generation

In order to prepare the collected image frames for the discovery steps of new variable star detection and corresponding verification, a series of processing steps was executed. These steps include image preprocessing, image registration, reference image generation, image subtraction, and finally light curve generation, which includes detrending and positional correlation.

To extract photometry from the time-series images, the data frames were initially put through a standard calibration pipeline which involved bias and dark subtraction and flat-field correction. Initial data reduction consisted of splitting the FITS images into separate CCD1/2 detector images and performing cosmic ray removal using the Laplacian edge detection cosmic removal algorithm (van Dokkum 2001).

A detailed sequence flow to carry out the difference image and light curve generation for the GCs was created which included the input/output conditions between discrete steps. Initial inputs into the processing flow consisted of the VLT image data, and outputs were corrected light curves ready for applications of variable star search techniques. Major processing steps are indicated by the gray boxes shown in Figure 8. The process flow was generic and accommodated both the Bramich (2008) and (2013) algorithm implementations.

3.1. Difference image analysis

The Difference Image Analysis (DIA) method attempts to match one image to another by deriving a convolution kernel describing the changes in the Point Spread Function (PSF) between images. When applied to time-series data with a high signal-to-noise reference image, the differential photometry approach regularly provides superior precision to more traditional profile-fitting photometry methods. Achieving errors close to the theoretical Poisson limit is possible. Moreover, DIA is the only reliable way to analyze the most crowded stellar fields (Bramich 2008). The potential of DIA as a powerful tool for unveiling short period variable stars or small amplitude variations in Blazhko RR Lyrs in the densely populated central regions of GCs has been demonstrated in Kains *et al.* (2012), Arellano Ferro *et al.* (2012), Bramich *et al.* (2011), Corwin *et al.* (2006), and Strader *et al.* (2002).

DIA using the PySIS3 code (Albrow 2017) was used to obtain high-precision photometry of the point sources. A stacked reference image was produced in each band by selecting the best-seeing images (500 images for u' band, 500–1000 images for g' and r' bands), taking care to minimize the number of saturated stars. The resulting reference image in the u' filter consists of a single image with an exposure time of 3000s, and FWHM of the point spread function (PSF) of 4.0–4.2 pixels. In the g' band, the reference image is made from stacked images with a total exposure time of 6000s and a PSF FWHM of 3.9–4.0 pixels. In the r' band, the reference image is again made from stacked images with a total exposure time of 6000s and a PSF FWHM of 1.7–4.0 pixels. The reference image, convolved with the kernel solution, is subtracted from each of the time-binned images to create difference images, and, in each difference image, the differential flux for each star is measured by scaling the PSF at the position of the star.

Because of the way difference imaging works, measured reference fluxes of a star on the reference image might be systematically too large due to contamination from other nearby point objects. Non-variable sources are fully subtracted on the difference images and as such, this problem does not occur for detection of variable stars. Variable sources with overestimated reference fluxes will have an underestimated variation amplitude. Once DIA was completed, DAOphot was used to detect and measure the magnitude of the stars in the reference images (Stetson 2015). The star positions, magnitudes, and associated statistics were used as inputs into the light curve generation process.

3.2. Light curve generation

Light curves for all identified stars were achieved by transforming the reference star list to image coordinates and performing PSF photometry on the residual image at the location of the transformed stars. Differential light curves were generated in all three bands for a total of 1451 curves in the u' band, 5267 in the g' band, and 5727 in the r' band.

For the VLT time series data, differential light curves were generated in the u', g', and r' filter bands using the modified PySIS3 code. Independent reference images were created for each band utilizing different combinations of images which are co-aligned. Stars were detected independently on each of the three reference images such that each filter has its own list of stars. Light curves were generated for all stars that were identified in each filter band.

Table 1 lists the light curves for the three filters for a total of 15,629 light curves in the u' band, 14,950 light curves in the g' band, and 9,156 light curves in the r' band. Cross-referencing stars across filter bands, light curves in one or more filters were generated for 24,106 individual stars.

Table 1. Generated light curves for NGC 5139.

Filter	*CCD Detector*	*No. Light Curves*
u'	1	8,917
	2	6,712
g'	1	10,120
	2	4,830
r'	1	3,532
	2	5,624
Total		24,106

3.3. Detrending of data

Noise in signals is the result of effects such as 1) instrumentation: focus, drift, electronic noise, pointing tweaks, and even thermal effects; 2) atmospheric: extinction and turbulence; and 3) astronomic: cosmic rays. The image subtraction process removes some of the noise components but others remain. Additional correlated trends in the light curve data can be removed by detrending techniques. Multiple methods are available for detrending. These include the boxcar moving average smoothing algorithm where a sliding moving average is used to smooth the data which is subtracted from the original curve. This takes out the low-frequency trends but leaves the higher-frequency changes in the flux in place. Other techniques include the Savitzky and Golay (1964) (S-G) smoothing algorithm. The idea behind S-G is that it also uses a sliding window along the light curve, but instead of computing a moving average, it performs a polynomial regression fit. Other techniques include RC circuit (high and low pass filter) and Fast Fourier Transforms (FFTs). The technique utilized in this research is the Trend Filtering Algorithm (TFA) (Kovács *et al.* 2005). TFA assumes that a substantial portion of the large number of stars in the target space are non-varying. See Walker (2016) for a detailed mathematical derivation.

The number of template stars used was dependent on the individual case. The total number of template stars used for the light curves being corrected typically ranged from 50 to 100 stars. Plots of star magnitudes vs. the RMS of the light curves were generated to determine the range of correction. An example of detrended data set for the g' band is shown in Figure 6.

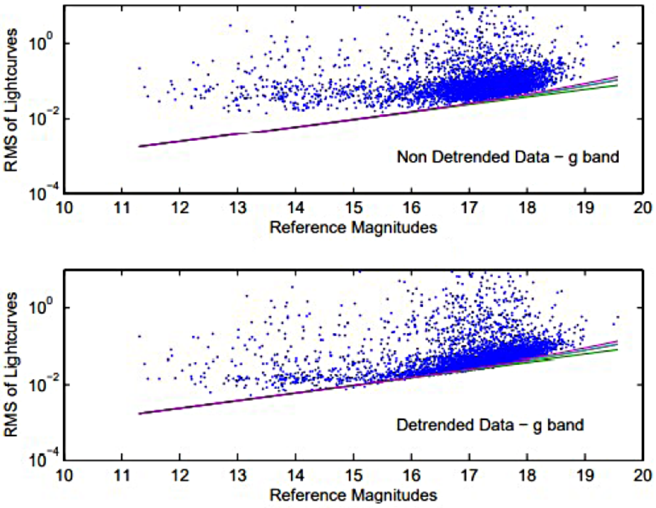

Figure 6. Example of detrended data set for g'. Top panel: RMS of light curves which have not been detrended. Bottom panel: RMS of light curves after detrending. Plotted in the figure are the readout noise (lower green line) and the Poisson noise (red and blue lines) with and without the mean sky background added, respectively.

3.4. Color magnitude diagrams

The Hertzsprung-Russell (HR) diagram plots log luminosity vs. log temperature (or absolute magnitudes vs. spectral types). Color Magnitude Diagrams (CMDs) are a variant of the HR diagram dedicated to the study of star clusters. A CMD is a scatter graph showing the relationship between each object's absolute magnitude and its estimated surface temperature or between optical or perceptual proxies for these quantities. Plots of CMDs are particularly useful in the study of GCs.

Before utilizing the CMDs in analysis, it is important that the generated CMDs are calibrated with a standard photometry catalog. For each GC data set, a calibrated catalog of stars for that GC in the UBVR$_c$I$_c$ system was acquired from the Photometric Standard Fields in the Canadian Astronomy Data Centre (CADC) (Stetson 2015).

CMDs for the fields under analysis were generated as follows. A calibrated catalog of over 140,000 stars in the UBVR$_c$I$_c$ system was provided by Bono (2015). The transformation provided by Chonis and Gaskell (2008) was used to transform values from the Johnson/Cousins to the SDSS system in order to match the generated color differences to those provided in the catalog data set.

A calibration to the catalog system was performed by first selecting a subset of stars with comparable magnitudes from both sets. Using World Coordinate System (WCS) reference coordinates, matching stars were found in both data sets. A statistical average of the color magnitude difference was calculated for the selected stars in all three color bands. This average was applied to all stars and differences used to generate corresponding CMDs. CMD plots for the data sets plotted on top of the catalog data are shown in Figure 7. Green color points represent the calibration data set, while the cyan color data points are the generated band differences. A greater number of overlap of stars identified in the g' and r' bands results in a larger number of stars plotted on the g'–r' vs g' plot compared to the u'–g' vs u' plot. The g'–r' vs g' shows a few stars in the split sequence which is clearly visible in the catalog data set.

The black lines in Figure 7 represent the theoretical stellar isochrone for this cluster. The Dartmouth Stellar Evolution

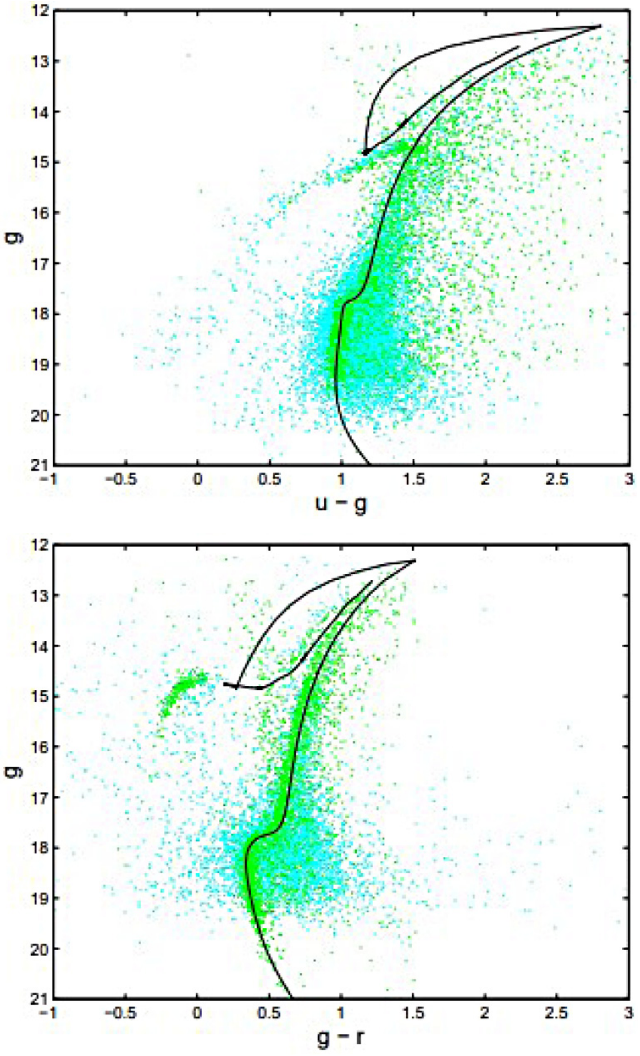

Figure 7. Calibrated Color Magnitude Diagrams. top-panel: u' vs u'–g': bottom-panel: g' vs g'–r'. Green color points represent the calibration data set while the cyan color data points are the statistical average for the generated band differences as described. The black lines is the stellar isochrone.

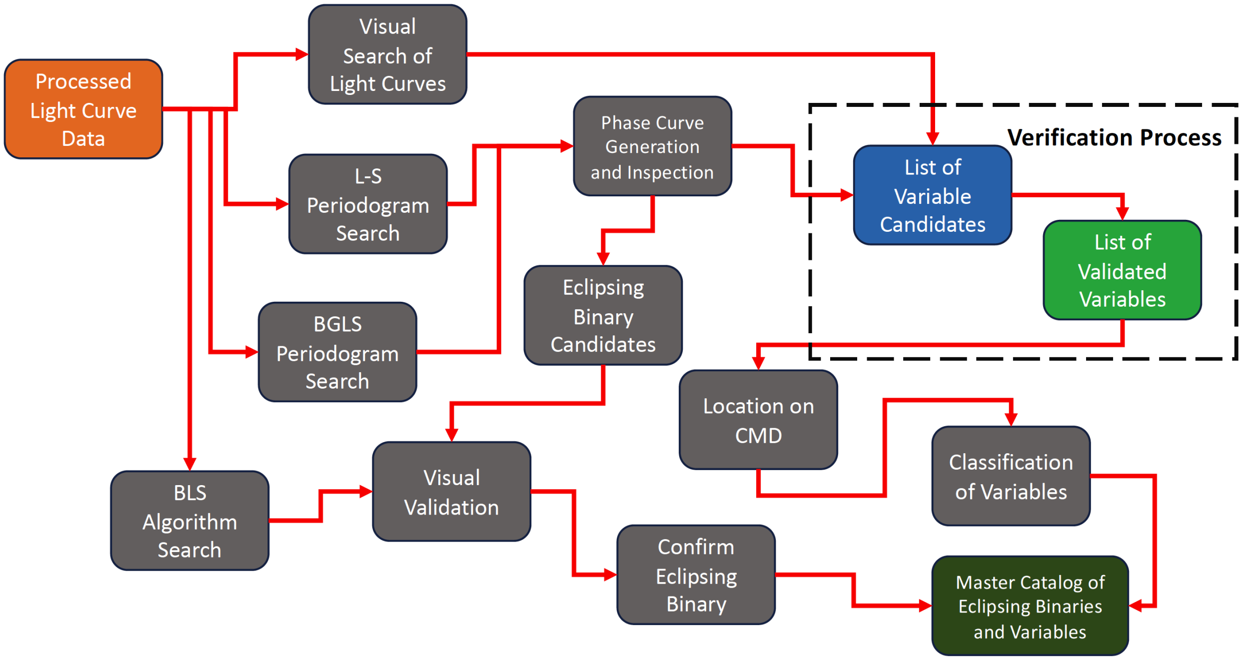

Figure 8. Variable star and eclipsing binary search processing flow.

Database 2 was used to generate the isochrones for this study. The fit of the isochrone to the photometry is to a first approximation only and is used for general location of variables. The fit was achieved in a two-step process. A pixel shift was first used to closely align the isochrone to the main sequence in the photometry. Once an alignment was completed, a least-squares fit was used to minimize the isochrone line to the mean of the photometry data. The isochrones generated used an alpha-enhanced chemical mixture.

The isochrone from the base of the main sequence through to the tip of the giant branch is designated as the Main Sequence Giant Branch Ridge Line (MSGBRL).

4. Variable star search algorithms

A set of variable star search algorithms was utilized in the search methodology. For searches for variable star demonstrating periodicity these included the Lomb-Scargle (L-S) periodogram (Scargle 1982), Bayesian Generalized Lomb-Scargle (BGLS) Periodogram (Mortier *et al.* 2015), and the Phase Dispersion Minimization (PDM) method (Stellingwerf 1978). For eclipsing type systems, algorithms included Box Least Squares (BLS) (Kovács *et al.* 2002) and the Plavchan periodogram (Plavchan *et al.* 2008).

Using these periodic search algorithms and complementing with visual search techniques, a series of steps are executed taking the light curve data and producing a candidate list of variables. All major process steps are detailed below and illustrated in the process flow shown in Figure 8.

All light curve time series data are first processed through the L-S and BGLS search algorithms, producing a list of potential variable star candidates. A cursory inspection is performed on the corresponding set of phased light curves produced with the periods found in the search algorithms. If an eclipsing binary is suspected, the candidate is separated for additional analysis. The original light curves are also passed through the BLS search algorithm for possible Detached Eclipsing Binaries (DEBs). In addition, a rapid visual examination of the raw light curves is conducted looking for candidate variable stars which may not be periodic in nature. If candidates are found, they are sent to the verification process, as shown in Figure 8. Once a list of variable star candidates is generated, it is submitted to a series of verification steps that are contained in the dotted box in Figure 8. By processing the candidate list through these verification steps (multiple iterations are required), a strict quality control approach for inclusion of variables and DEBs into the final GC variable candidate list is followed, ensuring a high level of confidence that identified variable stars are actually varying.

4.1. Analysis for validation of variability

A confidence validation step was performed to show that the detection of stellar variability was above certain threshold levels, providing a high confidence level that actual stellar variability is occurring. A decision analysis approach was utilized using a Simple Additive Weighting (SAW) method. The outcome from the SAW process resulted in a confidence rating of variables based on where the variable resides in a specific confidence level which is generated on the weighted inputs from the process steps.

Inputs to the SAW algorithm were based on measures from the following:

- Signal-to-Noise Ratio (SNR)
- RMS values of all stars across all filter bands
- Cross-correlations between filter bands
- Cross-correlation to nearby stars
- Stetson Variability Index
- Period comparison to window aliasing

The Signal-to-Noise Ratio is classically defined as the ratio of the power of a signal (meaningful information) to the power of background noise (unwanted signal). The simplest form is:

$$\mathrm{SNR} = P_{\mathrm{signal}} / P_{\mathrm{noise}} \qquad (1)$$

where P is average power. Both signal and noise power must be measured at the same or equivalent points in a system, and within the same system bandwidth. A ratio higher than 1:1 indicates more signal than noise. As described above, the SNR as used in all analysis and recorded on all plots is defined as:

$$\mathrm{SNR} = \mathrm{signalampltitude} / X_{\mathrm{RMS}} . \qquad (2)$$

The Root Mean Square, also known as the quadratic mean in statistics, is a statistical measure defined as the square root of the mean of the squares of a sample (Bird 2007).

For the SNR of the 117 variables, the numbers ranged from a value of 0.234 to 4.401. Measuring the amplitude in magnitudes of the fitted sinusoidal phases, the SNR of the phased light curves were generated and plotted. The RMS values of all stars across all filters as a function of magnitude were generated. Examining these results shows that the majority of variables with magnitudes brighter than 17 have a RMS value greater than the 1σ value of the set of stars that are found within 0.1 magnitude of the target star. Variables which have strong variability compared to other stars within a magnitude band should have values above the one sigma range. Conversely, stars that do not show variability to other stars within that 0.1-magnitude band will fall close to the mean of the set and within the 1σ bounds.

Cross-correlations between filter bands were calculated at zero-lag due to phase differences being generally restricted to ±10% between filters. These cross-correlations between filter bands ranged from very weak to strong. Examination of the cross-correlation results indicates that while many variables have zero lag values greater than the 1σ range of the companion magnitude stars, many have values below the mean and some even below the lower end of the 1σ range.

To validate that the variability in the primary filter band is not an artifact of the image detector or the difference image processing, the cross-correlation of the variable star and a set of nearby stars in that filter band within a defined pixel radius was performed. The autocorrelation values for all the variables at zero lag is 1. All variables in the g' filter, all except one have mean cross-correlation values of nearby stars less than 0.6. The values for the variables in the r' have a wider sigma range, with the highest value being 0.8 and the mean value of the nearby stars approximately 0.55. For the u' filter, values are 0.4 or below.

The Stetson Variability Index (SVI) statistic has been widely used to characterize variability in multiwavelength observations (Carpenter *et al.* 2001; Rice *et al.* 2012). Since it accounts for the correlated changes in multiband magnitudes, the Stetson index can be used to identify variables with relatively low variability compared with photometric errors.

The basic idea behind the SVI is that if a star is truly variable, independent time series observations taken closely in time should consistently agree more closely, on average, than observations taken further apart. This distinguishes variability from noise and image defects, such as cosmic rays.

Numeric inputs to SAW are the values generated from the SNR, RMS, cross-correlation, and SVI analysis processes. These numeric inputs were generated directly from the analytical MATLAB programs. The inputs for the visual analysis are subjective and as such, are inherently uncertain, as they depend on interpretation and knowledge. After investigations for the optimum set of weights, the values assigned to the associated inputs for the VLT data are shown in Figure 9. The visual, SNR, and cross-correlation between filter bands were considered the most important parameters. The RMS and SVI are closely associated with the SNR and cross-correlation respectively, thus they are assigned smaller weight values.

Applying this approach to all 117 detected variables results in the confidence rating bands as shown in Figure 10. The tabular listing for each variable and its confidence rating is in Table 2.

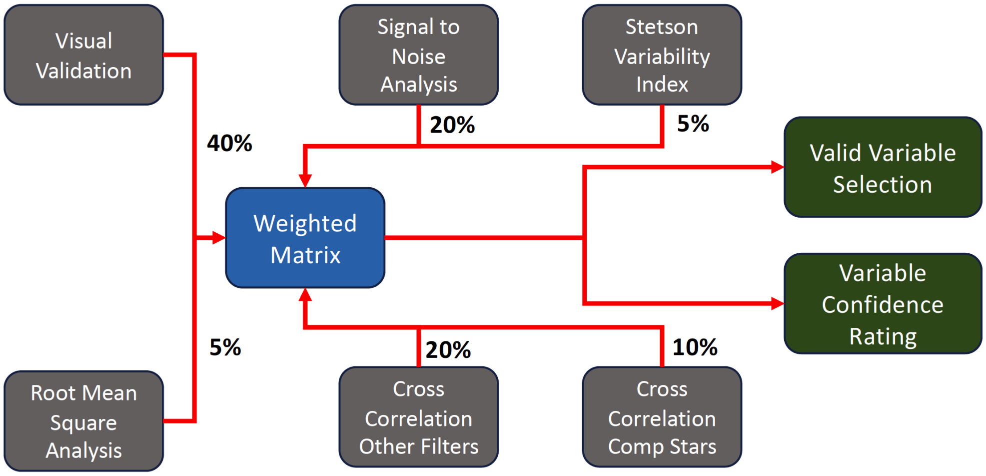

Figure 9. Variable star selection and verification processing flow. Percentages represent the weighted values of the inputs into the matrix.

4.2. Recovery of known variables

In order to determine the efficiency of the detection algorithms and approaches, a concentrated effort was made to recover the known variables in the ULTRACAM CCD detector FOVs which have been published in the literature and listed on astronomical databases.

Once the GC variables were identified, the x,y pixel positions from the reference image were mapped to J2000 R.A. and Dec. coordinates. After these coordinates were obtained, they were checked against the *Catalogue of Variable Stars* (Clement 2017). In addition, the list of coordinates was checked utilizing both the SIMBAD Astronomical Database and the AAVSO International Variable Star Index (VSX) coordinate query with a search radius of 1.5 arc sec around the targets. Cross-referencing these lists, the variables displayed in Table 3 have been recovered from earlier surveys.

Table 3 lists the variables survey ID from this survey, the corresponding ID obtained from the SIMBAD Astronomical Database, the identified variable type, ICRS coordinates, identified period from the search algorithm, and magnitudes in the SDSS u', g', r' filters as well as the B and V filters from the SIMBAD website.

4.2.1. Search detection efficiency

The list in Table 3 was generated by comparing the FOV with earlier surveys which generated a total of 32 variables which had been identified in the VLT FOV. The search space was targeted at variables with periods less than one day, which eliminates five variables from the tables that have longer periods. One of the pulsating subdwarf O star (sdOV) variables was not identified in the photometry process so no star was available for light curve analysis. Three of the variables were stars which happen to be chosen as part of the set utilized for detrending of the light curves. These were removed from the detrending process, which leaves 23 variables which could have been recovered. The list in Table 3 shows 20 variables were recovered, producing an overall detection efficiency of 87%. Breaking down specifics: 13 of 13 RR Lyr variables were found for a detection efficiency of 100%, 3 of 4 SX Phe variables were found for a detection efficiency of 75%, and 4 of 4 EA/EB/EW eclipsing systems were found for 100% efficiency. Other variables that were not recovered were the Semiregular (SR) and the sdOV variables.

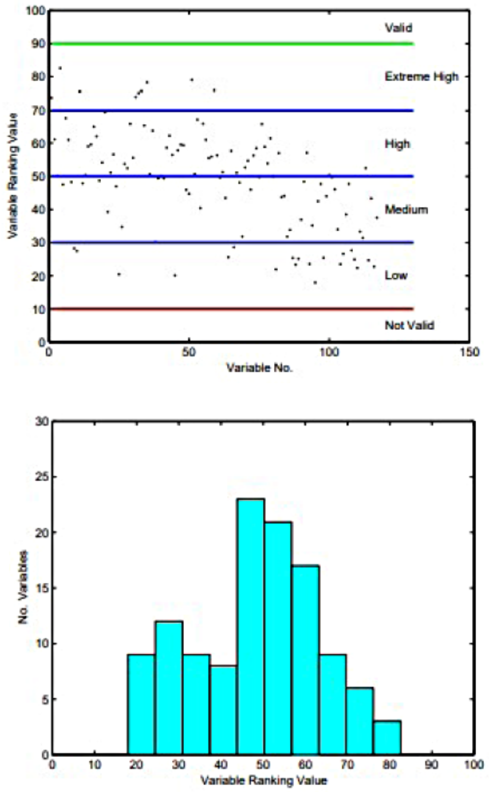

Figure 10. Variable confidence rating. Upper panel: Confidence rating of variables. Lower panel: Histogram of rating values.

Table 2. Confidence level of variables.

ID 5139 No.	Confidence Level	ID 5139 No.	Confidence Level	ID 5139 No.	Confidence Level
5139v-1	EH	5139v-40	H	5139v-79	H
5139v-2	H	5139v-41	M	5139v-80	H
5139v-3	H	5139v-42	H	5139v-81	L
5139v-4	EH	5139v-43	H	5139v-82	H
5139v-5	M	5139v-44	H	5139v-83	M
5139v-6	H	5139v-45	L	5139v-84	M
5139v-7	H	5139v-46	H	5139v-85	M
5139v-8	M	5139v-47	H	5139v-86	M
5139v-9	L	5139v-48	H	5139v-87	L
5139v-10	L	5139v-49	M	5139v-88	L
5139v-11	EH	5139v-50	M	5139v-89	L
5139v-12	M	5139v-51	EH	5139v-90	M
5139v-13	H	5139v-52	H	5139v-91	M
5139v-14	H	5139v-53	H	5139v-92	H
5139v-15	H	5139v-54	M	5139v-93	L
5139v-16	H	5139v-55	H	5139v-94	M
5139v-17	H	5139v-56	H	5139v-95	L
5139v-18	M	5139v-57	H	5139v-96	M
5139v-19	H	5139v-58	H	5139v-97	M
5139v-20	H	5139v-59	EH	5139v-98	L
5139v-21	M	5139v-60	H	5139v-99	M
5139v-22	H	5139v-61	M	5139v-100	H
5139v-23	H	5139v-62	H	5139v-101	M
5139v-24	M	5139v-63	M	5139v-102	M
5139v-25	L	5139v-64	L	5139v-103	M
5139v-26	M	5139v-65	H	5139v-104	L
5139v-27	H	5139v-66	L	5139v-105	L
5139v-28	H	5139v-67	H	5139v-106	M
5139v-29	H	5139v-68	M	5139v-107	M
5139v-30	H	5139v-69	L	5139v-108	L
5139v-31	EH	5139v-70	H	5139v-109	L
5139v-32	EH	5139v-71	H	5139v-110	L
5139v-33	EH	5139v-72	M	5139v-111	M
5139v-34	H	5139v-73	H	5139v-112	M
5139v-35	EH	5139v-74	H	5139v-113	H
5139v-36	H	5139v-75	M	5139v-114	L
5139v-37	H	5139v-76	H	5139v-115	M
5139v-38	M	5139v-77	H	5139v-116	L
5139v-39	M	5139v-78	M	5139v-117	M

Confidence levels: EH, Extremely High; H, High; M. Medium; L, Low

4.2.2. Analysis of recovered variables

An analysis of a subset of the recovered variables was undertaken to determine the efficiency of the signal processing

Table 3. Recovered variables.

Survey ID	*SIMBAD ID - NGC*	*Type*	*ICRS Coordinates R.A.*		*Period Days*	*U'*	*G'*	*R'*	*B*	*V*
			R.A. *h m s*	*Dec.* *° ' "*						
5139v-1	5139 B V120	RR Lyrae	13 26 25.512	–47 32 49.059	0.36574	15.51	14.62	14.54	15.47	15.03
5139v-2	5139 BPB 164847	RR Lyrae	13 26 56.529	–47 30 06.196	0.31250	15.07	14.51	14.51	14.88	14.64
5139v-3	5139 B V41	RR Lyrae	13 27 01.381	–47 31 02.053	0.65741	15.05	14.48	—	14.76	14.63
5139v-4	5139 B V110	RR Lyrae	13 27 02.050	–47 30 07.052	0.33102	15.17	14.46	14.59	15.26	14.58
5139v-5	5139 SAW V154	RR Lyrae	13 27 03.119	–47 30 33.085	0.32176	15.04	14.49	14.40	14.88	14.58
5139v-6	5139 SAW V145	RR Lyrae	13 26 51.213	–47 31 08.850	0.37384	15.26	14.48	—	15.11	14.67
5139v-7	5139 B V112	RR Lyrae	13 26 54.242	–47 30 23.655	0.47222	15.44	14.69	14.27	15.00	15.03
5139v-11	5139 BPB 149574	RR Lyrae	13 26 56.177	–47 30 50.578	0.38079	15.17	14.42	14.44	15.02	14.62
5139v-13	5139 SAW V311	SX Phe	13 26 58.713	–47 29 50.980	0.04149	17.39	—	16.62	17.12	16.79
5139v-14	5139 SAW V328	SX Phe	13 27 01.259	–47 31 49.940	0.09896	17.69	—	17.17	18.20	17.68
5139v-16	5139 SAW V298	SX Phe	13 26 50.235	–47 34 03.490	0.03304	17.74	—	17.18	17.73	17.36
5139v-29	5139 BPB 143269	RR Lyrae	13 27 15.891	–47 31 10.242	0.42245	15.09	14.33	—	14.96	14.43
5139v-30	5139 SAW V276	RR Lyrae	13 27 16.487	–47 33 18.096	0.30903	15.04	14.47	14.33	14.86	14.59
5139v-31	5139 NJL 8	RR Lyra	13 27 22.094	–47 30 12.855	0.69213	15.06	14.46	14.15	14.73	14.64
5139v-32	5139 SAW V365	Variable Star	13 27 11.591	–47 35 02.552	0.47338	15.67	15.19	15.07	15.53	15.29
5139v-33	5139 B V107	RR Lyrae	13 27 14.027	–47 30 58.388	0.34028	14.93	14.64	14.89	15.92	14.91
5139v-35	5139 SAW V358	Variable Star	13 27 20.203	–47 31 49.854	0.30002	17.26	16.90	16.82	17.30	17.03
5139v-37	5139 SAW V337	Eclipsing	13 27 13.776	–47 32 25.030	0.13466	17.53	—	16.87	17.88	17.42
5139v–38	5139 WSB V68	Eclipsing	13 27 22.950	–47 32 19.100	0.12032	—	—	—	—	17.28
5139v-60	N[ALJ2017] 255	Red Giant	13 27 14.281	–47 30 59.882	0.33824	—	14.33	—	15.55	14.61

algorithms and if the variable determination process matched what is recognized in the open literature.

Figure 11 shows the RR Lyr variable identified as 5139 B V120 and has an estimated period of 0.36574 day in the g' band only. Its distinctive shape for a RR Lyr is clearly shown and it has been verified in followup observations taken with a private 1-meter telescope. The magnitude is slightly dimmer in the B and V filters.

Figures 12 and 13 show the phase and light curves for variables identified as eclipsing binary systems according to the SIMBAD Astronomical Database. The estimated periods are 0.13466 and 0.13480 day, respectively. The individual light curves show the frequency of the eclipsing systems better than the phase curves.

Figure 14 shows the distinctive shape of an eclipsing system in which the light curves show both the primary and secondary eclipses and the phase curves shows the secondary eclipse as a shallower eclipse than the primary. The SIMBAD Astronomical Database identifies this eclipsing system as a variable star with no additional references identified. This is clearly an eclipsing system and needs further observation and analysis. At magnitude 16.6 in the g' filter, larger telescope systems will be required to completely resolve the details of the eclipse.

5. Newly discovered variables

Utilizing the search techniques as identified above, 97 new variables in addition to those recovered above were detected across both CCD detectors of the image field. Reviewing the phase and light curves, a variety of variable star classes has been discovered. If we exclude the stars which have been identified as either Red Giant Branch stars or Horizontal Branch stars, we get 78 new detections whose classifications include 14 eclipsing type systems, 8 potential new RR Lyr, 3 SX Phe, 13 BY Dra, and 40 stars which we identify as general pulsating types. If we include the SIMBAD-designated stars as general pulsating type variables, our detection count increases to 97.

5.1. Validation of variables being newly discovered

In addition to the literature search as described in the introduction, in order to validate that the newly detected variables have not been previously reported in the open literature, a search using the variable coordinates was conducted against both the SIMBAD Astronomical Database and the AAVSO's International Variable Star Index (VSX). The accuracy of stellar positions generated in this study for the recovered variables was collected, resulting in an average of 0.486-arcsecond difference. Based on this, a two-second arcsecond search radius was utilized for checking the list of newly detected variables, which validates the list in Appendix A: Master catalog of detected variable stars. Appendix B contains the master catalog of light curves of all the variable stars.

5.2. Location of discovered variables on CMD

Figures 15 and 16 show the location of a subset of the variables on the CMD. 72 of the 78 variables are analyzed and are located on the CMD. The cyan color data points are the statistical average for the generated band differences as described in section 3.4. A majority of the variables are concentrated along the MSGBRL, as well as many located in the HB, as demonstrated in the u'–g' plot in Figure 15. Figure 16 shows the variables largely scattered across the g'–r' CMD. Variables which lie along the MSGBRL are considered part of the GC while those farther out on the redder and blue regions could possibly be field stars.

Note: Due to the wide scatter of the variables on the g' vs. g' – r' CMD, only the g' vs. u' – g' plot is used forvariable location.

5.3. Classification of variables on CMD

Figure 17 shows the location of groups of specific variables

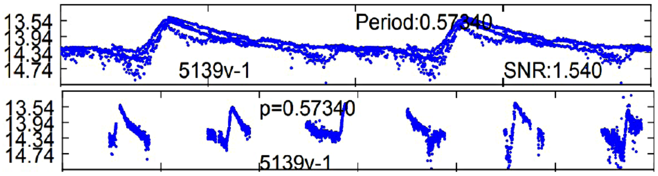

Figure 11. Light curve of RR Lyr SIMBAD 5139 B V120. Top panel: Phase light curve. Bottom panel: Individual light curves over observation periods.

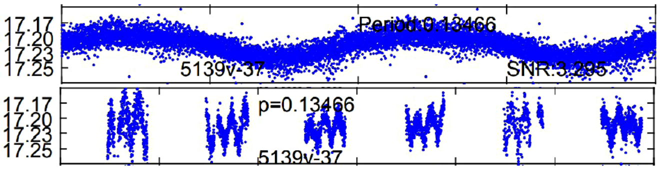

Figure 12. Light curve of Eclipsing system SIMBAD 5139 SAW V337. Top panel: Phase light curve. Bottom panel: Individual light curves over observation periods.

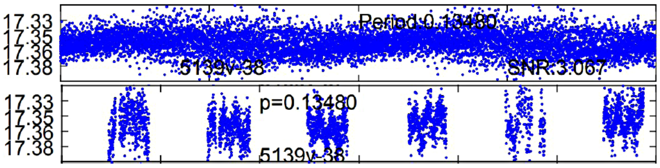

Figure 13. Light curve of Eclipsing system SIMBAD 5139 WSB V68. Top panel: Phase light curve. Bottom panel: Individual light curves over observation periods.

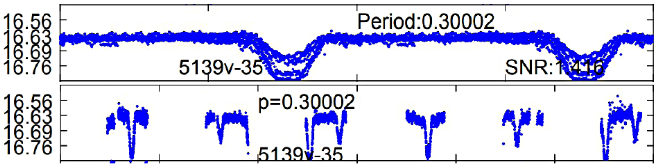

Figure 14. Light curve of variable star SIMBAD 5139 SAW V358. Top panel: Phase light curve. Bottom panel: Individual light curves over observation periods.

on the CMD. As expected, the RR Lyr lie along the HB as indicated by the yellow line. Eclipsing systems (EAs and EBs) are distributed along the MSGBRL with a couple scattered on the HB. BY Dra variables are concentrated in the red box of Figure 17 with the lone exception of variable 5139v-71, which resides in the small red box. The observed g' magnitudes of the BY Dra are consistent for K- or M-type dwarfs. The variable 5139v-71 is possibly a foreground star as it is located too far off the main sequence. It has been given the BY Dra classification based on the light curve characteristic only.

6. Classification of variable stars

This section describes the new variables that have been discovered. For purposes of variable classification, the CMD is divided into four main regions centered on the MSGBRL. A general example is shown in Figure 18.

A corridor region containing the majority of stars concentrated along the MSGBRL was developed in order to separate these stars from the ones in the other defined regions. To develop the corridor boundaries, stars were binned at the one-half magnitude scale. For each bin, the mean and sigma values

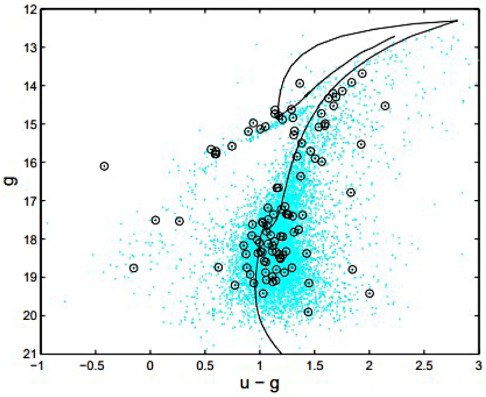

Figure 15. Location of variables on CMD. u'–g'. The cyan color data points are the statistical average for the generated band differences as described in section 3.5.

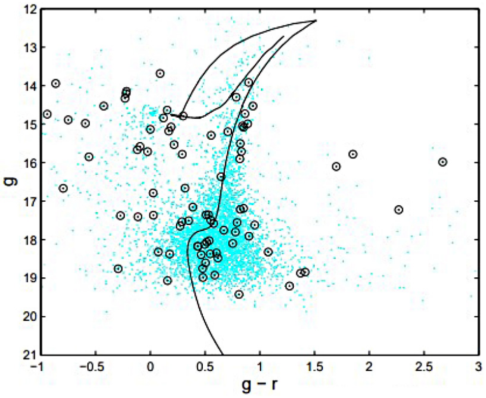

Figure 16. Location of variables on CMD. g'–r'.

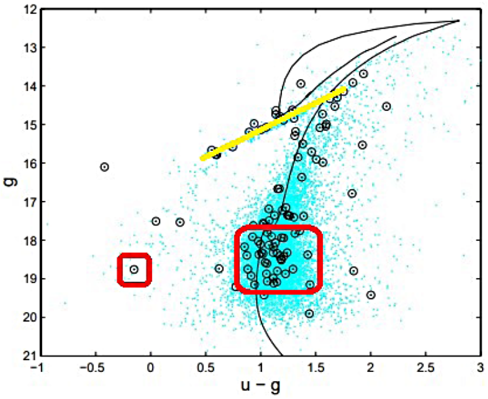

Figure 17. Groupings of variables on CMD. u'–g'. The yellow line represents RR Lyr variables while the red box contains BY Dra variables.

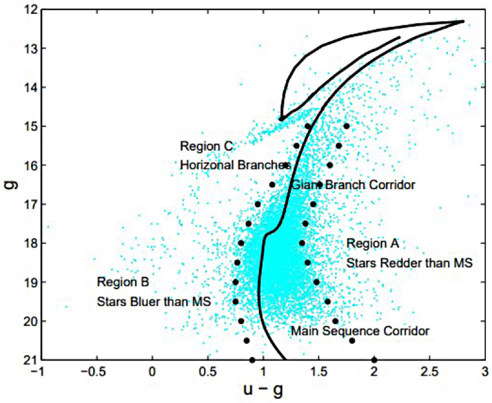

Figure 18. Example of MSGBRL and associated corridor, redder, bluer, and horizontal branch regions.

Table 4. Variables on Main Branch.

ID *5139 No.*	*R.A. (J2000)* *h m s*	*Dec. (J2000)* *° ′ ″*	*Period* *(days)*	*Type*
5139v-14	13 27 01.231	–47 31 49.58	0.09896	SX Phe
5139v-15	13 26 55.151	–47 31 09.49	0.04052	SX Phe
5139v-16	13 26 50.191	–47 34 03.44	0.03304	SX Phe
5139v-17	13 26 58.219	–47 34 29.86	0.03764	SX Phe
5139v-18	13 27 00.810	–47 32 41.36	0.43750	Irr/Semi
5139v-19	13 26 59.249	–47 31 38.20	0.50463	BY Dra
5139v-20	13 26 56.361	–47 31 45.61	0.36458	Irr/Semi
5139v-21	13 27 16.465	–47 33 18.10	0.30903	EA
5139v-36	13 27 12.740	–47 33 23.63	0.36921	EA
5139v-41	13 27 19.858	–47 32 17.87	0.33102	EA
5139v-42	13 27 19.999	–47 33 08.13	0.51389	Irr/Semi
5139v-45	13 27 19.732	–47 31 32.39	0.52083	Irr/Semi
5139v-47	13 27 20.947	–47 34 46.36	0.48727	RR1
5139v-48	13 27 17.820	–47 34 37.42	0.48611	Irr/Semi
5139v-49	13 27 14.128	–47 30 33.10	0.20000	BY Dra
5139v-51	13 27 13.908	–47 31 00.87	0.34060	RR0
5139v-52	13 27 16.648	–47 31 09.64	0.16703	BY Dra
5139v-53	13 27 17.108	–47 35 14.55	0.33303	Irr/Semi
5139v-55	13 27 07.985	–47 31 51.79	0.33058	Irr/Semi
5139v-56	13 27 11.793	–47 35 10.82	0.31866	BY Dra
5139v-57	13 27 19.809	–47 31 11.87	0.27778	BY Dra
5139v-58	13 27 08.163	–47 31 45.07	0.16819	Irr/Sem
5139v-59	13 27 13.788	–47 30 56.09	0.33860	RR0
5139v-62	13 27 20.284	–47 31 55.77	0.11023	BY Dra
5139v-64	13 27 16.423	–47 34 30.64	0.33064	Irr/Sem
5139v-65	13 27 15.688	–47 31 06.78	0.12426	Irr/Sem
5139v-67	13 27 21.239	–47 35 03.71	0.48958	EB
5139v-68	13 27 16.421	–47 31 07.16	0.14247	Irr/Semi
5139v-69	13 27 08.964	–47 30 18.05	0.46991	Irr/Sem
5139v-70	13 27 23.290	–47 32 51.07	0.46181	Irr/Semi
5139v-71	13 27 19.581	–47 32 07.78	0.16830	BY Dra
5139v-72	13 27 19.954	–47 30 52.41	0.56829	Irr/Sem
5139v-73	13 27 22.110	–47 31 26.10	0.14284	BY Dra
5139v-74	13 27 10.078	–47 32 02.49	0.16694	Irr/Sem
5139v-81	13 27 04.900	–47 32 27.85	0.14513	Irr/Sem
5139v-82	13 27 01.617	–47 31 00.75	0.18461	Irr/Semi
5139v-83	13 27 16.465	–47 33 18.10	0.30903	EA
5139v-84	13 26 56.922	–47 31 03.00	0.15952	Irr/Sem
5139v-101	13 27 00.303	–47 30 22.29	0.13356	Irr/Sem
5139v-104	13 26 56.589	–47 30 48.88	0.35648	Irr/Sem
5139v-106	13 26 56.430	–47 31 07.30	0.31945	EA?
5139v-108	13 26 56.537	–47 33 19.04	0.11690	Irr/Sem
5139v-110	13 26 56.741	–47 32 45.29	0.05787	Irr/Sem
5139v-112	13 27 16.465	–47 33 18.10	0.30903	Irr/Sem
5139v-116	13 27 10.511	–47 33 49.03	0.19121	Irr/Sem

were calculated and plotted. Based on preliminary results, it was determined that corridor boundaries containing approximately a 2-σ range of stars provided the best separation. The boundaries on the plots are at the ± 2-σ level.

Note: This is a very rough guide for initial classification purposes only. A variable residing outside but close to the MSGBRL corridor could very well belong to this GC MS. Differences in stellar color can cause a star to move position from the u'–g' to g'–r' diagrams. To avoid confusion, only the g' vs. u'–g' CMD diagrams are shown in this section.

6.1. Variable stars in the main sequence and giant branch corridor

Table 4 lists the variables that are located within the defined MS portion of the corridor for the g' vs. u'-g' CMD. Forty-five variables are located within this boundary just below the MS turn-off point.

Table 5. Variables redder than Main Sequence.

ID *5139 No.*	*R.A. (J2000)* *h m s*	*Dec. (J2000)* *° ′ ″*	*Period* *(days)*	*Type*
5139v-26	13 26 52.150	–47 31 20.52	0.46991	Irr/Sem
5139v-76	13 27 02.103	–47 35 13.15	0.15108	Irr/Sem
5139v-83	13 27 00.337	–47 31 40.88	0.14792	EA
5139v-99	13 26 56.669	–47 30 11.60	0.06223	Irr/Sem
5139v-102	13 27 00.053	–47 29 55.05	0.11868	Irr/Sem
5139v-114	13 26 57.283	–47 34 34.90	0.13371	Irr/Sem

Table 6. Stars bluer than Main Sequence.

ID *5139 No.*	*R.A. (J2000)* *h m s*	*Dec. (J2000)* *° ′ ″*	*Period* *(J2000)*	*Type* *(days)*
5139v-39	13 27 13.812	–47 30 36.45	0.24794	Irr/Sem
5139v-40	13 27 19.637	–47 31 55.75	0.33333	EW
5139v-63	13 27 18.287	–47 30 22.63	0.49769	Irr/Sem
5139v-66	13 27 17.048	–47 34 46.41	0.47222	BY Dra

Table 7. Stars on Horzional Branch.

ID *5139 No.*	*R.A. (J2000)* *h m s*	*Dec. (J2000)* *° ′ ″*	*Period* *(days)*	*Type*
5139v-2	13 26 56.505	–47 30 05.77	0.3125	RR1
5139v-3	13 27 01.357	–47 31 01.96	0.65741	RR0
5139v-4	13 27 02.031	–47 30 06.80	0.33102	RR1
5139v-5	13 27 03.098	–47 30 32.83	0.32176	RR1
5139v-6	13 26 51.186	–47 31 08.57	0.37384	RR1
5139v-7	13 26 54.216	–47 30 23.15	0.47222	RR0
5139v-9	13 27 00.751	–47 34 28.71	0.58449	Irr/Semi
5139v-33	13 27 14.014	–47 30 58.22	0.34028	RR0
5139v-34	13 27 20.823	–47 33 56.82	0.48727	RR1
5139v-87	13 26 56.278	–47 30 23.24	0.1178	Irr/Sem
5139v-88	13 26 56.864	–47 32 08.87	0.06187	Irr/Sem
5139v-89	13 26 58.662	–47 32 34.72	0.11863	Irr/Sem
5139v-90	13 26 56.460	–47 34 12.50	0.09365	Irr/Sem

6.2. Stars redder than the main sequence

Variables located to the right of the MSGBRL corridor are designated as belonging to Region A, variables that are redder in color than the MS. Since the MSGBRL corridor is a rough guide to stars residing on the MS, variables that are located just outside the boundary areas could possibly belong to the MS and as such, these stars are not included in either this set or Region B.

By definition, all variables in Region A are in the extreme redder star region to the right of the MSGBRL corridor. Reviewing the phased light curves, v-26 has the characteristic shape of a BY Dra variable but it is not located on the MS and is classified as an unknown or Irr/Semiregular.

Variables v-76 and v-114 have the shape of RR Lyr but are located in the wrong region and are classified as unknown types. Variable v-99 has the general shape and period of a SX Phe. These variables are frequently referred to as pulsating blue stragglers, appearing more blue from having a higher temperature. These are located in the redder region and so cannot be classified as SX Phe and are left as unknowns. Variable v-102 seems to show some type of possible outburst activity after a short period of quiet activity and so is classified as an unknown in the list shown in Table 5.

6.3. Stars bluer than the main sequence

Variables located to the left of the MSGBRL corridor are designated as belonging to Region B, variables that are bluer than those on the MS. Following the same procedure as for Region A above, Table 6 list the variables that appear in this designated region.

This region contains EWs, CVs, white dwarfs and blue stragglers to the left of the MS turn-off point. Reviewing the phased light curves, variable v-40 has a shape that could resemble a low-mass contact eclipse and has the right period and is classified as an EW. Variables v-39 and v-63 phased light curves do not match well with any of the established templates and are classified as unknowns or Irr/Semi. Variable v-66 has a characteristic lightcurve of a BY Dra variable.

6.4. Variable stars on the horizontal branch

Thirteen variables are identified as belonging to the horizontal branch of the cluster.

This region of the cluster typically harbors RR Lyr variables. Reviewing these phased light curves, variables v-2, v-3, v-4, v-5, v-6, v-7, and v-33 have shapes matching the template of a RR Lyr. All have the correct periods and these variables have been recovered and are classified as RR Lyr. Variable v-9 looks like an EB type system, and v-34 has the phased light curve characteristic of an EW type system but its period is too long and so is likely a RR Lyr. Variables v-87, v-88, and v-90 have indications of sinusoidal activity but are classified as unknowns. Variable v-89 also has an Irr type phased light curve. The summary is shown in Table 7.

Note: For RR Lyr variables that have been designated in previous surveys, the designation is carried into the table, i.e., RR0 or RR1. For variables that have RR Lyr type light curves but have not been classified before, the table designation is RR Type.

7. Conclusions

The dataset for NGC 5139 comprises 32,072 ULTRACAM images taken over a six-day observation run in April 2011. The FOV covers a sky patch approximately 5×5 arc min^2, comprising two CCD chips. Using the PySIS3 software and associated processing steps resulted in 15,629, 14,950, and 9,156 light curves in the u', g', and r' SDSS filter bands, respectively. Analysis of these light curves for variable stars has produced 117 variables for the ULTRACAM data. Twenty of these were recovered from earlier surveys, leaving 97 variables that are new discoveries. A subset of the variables from ULTRACAM has been classified as belonging to classes EA, EB, EW, BY Dra, SX Phe, CV, and RR Lyr. The rest are reclassified from unknowns to general pulsating types.

Additional work would consist of follow-up observations on selected variables, especially the eclipsing binary candidates.

8. Acknowledgements

Funding for this work was provided by the University of Canterbury scholarship program. The observational data set for globular cluster NGC 5139 was provided by Associate Professor Giuseppe Bono from the University of Rome.

Many thanks to Joyce Guzik with the Los Alamos National Laboratory, Los Alamos, New Mexico, United States for reviewing the draft and especially encouraging me to publish these results.

Variable star references are contributed by Samus *et al.* (2017).

This research has made use of the SIMBAD database, operated at CDS, Strasbourg, France, 2000 (Wenger *et al.* 2000).

References

Albrow, M. 2017, “MichaelDAlbrow/pyDIA: Initial release on github” (doi:10.5281/zenodo.268049).

Arellano Ferro, A., Bramich, D. M., Figuera Jaimes, R., Giridhar, S., and Kuppuswamy, K. 2012, *Mon. Not. Roy. Astron. Soc.*, **420**, 1333.

Bailey S. I. 1902, *Ann. Astron. Obs. Harvard Coll.*, **38**, 1.

Bekki, K. and Freeman, K. C. 2003, *Mon. Not. Roy. Astron. Soc.*, **346**, L11.

Bird, J. 2007, *Basic Engineering Mathematics*, 5th ed., Elsevier Ltd., Kidlington, Oxford, UK.

Bono, G. 2015, private email correspondence (25 October).

Braga V. F., *et al.* 2016, VizieR Online Data Catalog: RRLs in globulars. IV. UBVRI photometry in Omega Cen (Braga+, 2016 *Astron. J.*, **152**, 170).

Braga V. F, *et al.* 2018, VizieR Online Data Catalog: RRLs in globulars. V. ω Centauri NIR photometry (Braga+, 2018 *Astron. J.*, **155**, 137).

Bramich D. M. 2008, *Mon. Not. Roy. Astron. Soc.*, **386**, L77.

Bramich, D. M., Figuera J. R., Giridhar, S., Arellano Ferro, A. 2011, *Mon. Not. Roy. Astron. Soc.*, **413**, 1275.

Carpenter, J. M., Hillenbrand, L. A., Skrutskie, M. F., and Meyer, M. R. 2002, *Astron. J.*, **124**, 1001.

Chonis, T. S., and Gaskell, C. M. 2008, *Astron. J.*, **135**, 264.

Clement, C., 2017, in Wide-Field Variability Surveys: A 21st Century Perspective, eds. M. Catelan, W. Gieren, EPJ Web Conf., 152, 01021 (http://www.astro.utoronto.ca/~cclement/cat/listngc.html).

Corwin, T. M., Sumerel, A. N., Pritzl, B. J., Smith, H. A., Catelan, M., Sweigart, A. V., and Stetson, P. B. 2006, *Astron. J.*, **132**, 1014.

Covey, K. R., *et al.* 2007, *Astron. J.*, **134**, 2398.

Dhillon, V. S., *et al.* 2007, *Mon. Not. Roy. Astron. Soc.*, **378**, 825.

Dickens, R. J., Feast, M. W., and Lloyd Evans, T. 1972, *Mon. Not. Roy. Astron. Soc.*, **159**, 337.

Fourcade, C. R., Laborde, J. R. and Yurquina, E. 1978, *Inf. Bull. Var. Stars*, No. 1380, 1.

Fukugita, M., Ichikawa, T., Gunn, J. E., Doi, M., Shimasaku, K., and Schneider, D. P. 1996, *Astron. J.*, **111**, 1748.

Harris, W. E. 1996, *Astron. J.*, **112**, 1487.

Jorgensen, H. E., and Hansen, L. 1984, *Astron. Astrophys.*, **133**, 165.

Kains, N., Bramich, D. M., Figuera Jaimes, R., Arellano Ferro, A., Giridhar, S., and Kuppuswamy, K. 2012, *Astron. Astrophys.*, **548A**, 92.

Kovács, G., Bakos, G., and Noyes, R. W. 2005, *Mon. Not. Roy. Astron. Soc.*, **356**, 557.

Kovács, G., Zucker, S., and Mazeh, T. 2002, *Astron. Astrophys.*, **391**, 369.

Magurno, D., *et al.* 2018, *Astrophys. J.*, **864**, 57.

Martin, W. C. 1938, *Ann. Sterrewacht Leiden*, **17**, B1.

Mortier, A., Faria, J. P., Correia, C. M., Santerne, A., and Santos, N. C. 2015, *Astron. Astrophys.*, **573A**, 101.

Mukherjee, K., Anthony-Twarog, B. J., and Twarog, B. A. 1992, *Publ. Astron. Soc. Pacific*, **104**, 561.

Navarrete, C., Catelan, M., Contreras Ramos, R., Alonso-García, J., Gran, F., Dékány, I., and Minniti, D. 2017, *Astron. Astrophys.*, **604A**, 120.

Navarrete, C., *et al.* 2015, *Astron. Astrophys.*, **577A**, 99.

Niss, B., Jorgensen, H. E., and Laustsen, S. 1978, *Astron. Astrophys., Suppl. Ser.*, **32**, 387.

Plavchan, P., Jura, M., Kirkpatrick, J. D., Cutri, R. M., and Gallagher, S. C. 2008, *Astrophys. J., Suppl. Ser.*, **175**, 191.

Rice, T. S., Wolk, S. J., and Aspin, C. 2012, *Astrophys. J.*, **755**, 65.

Samus, N. N., Kazarovets, E. V., Durlevich, O. V., Kireeva, N. N., and Pastukhova, E. N. 2017, *Astron. Rep.*, **61**, 80 (*General Catalogue of Variable Stars*: version GCVS 5.1, http://www.sai.msu.su/groups/cluster/gcvs/gcvs).

Savitzky, A., and Golay, M. J. E. 1964, *Anal. Chem.*, **36**, 1627.

Sawyer Hogg, H. 1973, *Publ. David Dunlap Obs.*, **3**, 6.

Scargle, J. D. 1982, *Astrophys. J.*, **263**, 835.

Stellingwerf, R. F. 1978, *Astrophys. J.*, **224**, 953.

Stetson, P. B. 2015, Photometric standard fields, Canadian Astronomy Data Centre. Canadian Astronomy Data Centre.[1]

Strader, J., Everitt, H. O., and Danford, S. 2002, *Mon. Not. Roy. Astron. Soc.*, **335**, 621.

van Dokkum, P. 2001, *Publ. Astron. Soc. Pacific*, **113**, 1420.

Walker, D. 2016, *A High Cadence Photometric Survey of Five Southern Hemisphere Milky Way Globular Clusters*, doctoral dissertation, University of Canterbury, Christchurch, New Zealand.

Wenger, M., *et al.* 2000, *Astron. Astrophys., Suppl. Ser.*, **143**, 9.

---

[1] Stetson (2015), (http://www4.cadc-ccda.hia-iha.nrc-cnrc. gc.ca/en/community/STETSON/standards/)

Appendix A: Master catalog of detected variable stars.

Table A1. Master catalog.

Variable	*R.A. (J2000)*			*Dec. (J2000)*			*Period*			*Mag*	*Confidence*	*Variable*	*Recovered*	*Recovered*
ID	*h*	*m*	*s*	*°*	*′*	*″*	*(days)*	*u′*	*g′*	*r′*	*Level*	*Class*	*Survey*	*Class*
5139v-1	13	26	56.269	–47	31	47.67	0.36574	15.90	14.15	14.36	EH	RR0	Yes	RR0
5139v-2	13	26	56.505	–47	30	05.77	0.31250	15.91	14.62	15.81	H	RR0	Yes	RR1
5139v-3	13	27	01.357	–47	31	01.96	0.65741	15.77	14.63	—	H	RR0	Yes	RR0
5139v-4	13	27	02.031	–47	30	06.80	0.33102	15.88	14.74	15.68	EH	RR0	Yes	RR1
5139v-5	13	27	03.098	–47	30	32.83	0.32176	15.96	14.79	—	M	RR1	Yes	RR1
5139v-6	13	26	51.186	–47	31	08.57	0.37384	16.09	14.89	15.64	H	RR0	Yes	RR1
5139v-7	13	26	54.216	–47	30	23.15	0.47222	15.92	14.98	—	H	RR0	Yes	RR0
5139v-8	13	27	00.962	–47	31	24.56	0.18539	16.88	15.50	—	M	Irr/Semi	No	NA
5139v-9	13	27	00.751	–47	34	28.71	0.58449	16.31	15.71	15.74	L	Irr/Semi	No	NA
5139v-10	13	27	00.788	–47	31	57.91	0.56250	16.38	15.78	—	L	EA	No	NA
5139v-11	13	26	56.273	–47	30	50.05	0.38079	—	16.10	—	EH	RR1	Yes	RR1
5139v-12	13	27	00.886	–47	32	48.18	0.65857	17.74	16.36	15.72	M	EA	No	NA
5139v-13	13	26	58.684	–47	29	50.82	0.04140	17.82	16.67	—	H	SX Phe	Yes	SX Phe
5139v-14	13	27	01.231	–47	31	49.58	0.09896	18.38	17.15	16.77	H	SX Phe	Yes	SX Phe
5139v-15	13	26	55.151	–47	31	09.49	0.04052	18.63	17.37	—	H	SX Phe	No	NA
5139v-16	13	26	50.191	–47	34	03.44	0.03304	18.71	17.41	—	H	SX Phe	Yes	SX Phe
5139v-17	13	26	58.219	–47	34	29.86	0.03764	18.57	17.49	16.94	H	SX Phe	No	NA
5139v-18	13	27	00.810	–47	32	41.36	0.43750	18.61	17.58	17	M	Irr/Semi	No	NA
5139v-19	13	26	59.249	–47	31	38.20	0.50463	19.14	17.82	—	H	BY Dra	No	NA
5139v-20	13	26	56.361	–47	31	45.61	0.36458	19.12	17.93	—	H	Irr/Semi	No	NA
5139v-21	13	27	00.636	–47	33	13.04	0.39120	19.20	18.13	17.63	M	EA	No	NA
5139v-22	13	26	53.172	–47	34	22.95	0.11088	19.56	18.32	—	H	BY Dra	No	NA
5139v-23	13	26	57.278	–47	32	34.48	0.33333	19.49	18.34	—	H	EA	No	NA
5139v-24	13	26	58.270	–47	34	52.76	0.66088	19.62	18.41	—	M	EA	No	NA
5139v-25	13	26	57.819	–47	35	33.01	0.57755	19.70	18.51	—	L	EA	No	NA
5139v-26	13	26	52.150	–47	31	20.52	0.46991	20.64	18.79	—	M	Irr/Semi	No	NA
5139v-27	13	27	06.428	–47	30	03.29	0.18615	—	18.84	—	H	Irr/Semi	No	NA
5139v-28	13	26	53.910	–47	34	17.99	0.09954	—	19.66	—	H	SX Phe	No	NA
5139v-29	13	27	15.879	–47	31	10.14	0.42245	15.87	14.20	14.42	H	RR1	Yes	NA
5139v-30	13	27	16.465	–47	33	18.10	0.30903	15.96	14.33	14.56	H	RR1	Yes	NA
5139v-31	13	27	22.097	–47	30	12.66	0.69213	16.20	14.53	14.95	EH	RR0	Yes	RR0
5139v-32	13	27	11.551	–47	35	02.68	0.47338	16.50	15.18	15.01	EH	EA	Yes	EA
5139v-33	13	27	14.014	–47	30	58.22	0.34028	16.09	15.19	14.49	EH	RR0	No	NA
5139v-34	13	27	20.823	–47	33	56.82	0.48727	16.33	15.58	15.67	H	RR1	No	NA
5139v-35	13	27	20.198	–47	31	49.75	0.30002	17.83	16.66	16.35	EH	EA	Yes	EA
5139v-36	13	27	12.740	–47	33	23.63	0.36921	18.26	17.19	16.34	H	EA	No	NA
5139v-37	13	27	13.757	–47	32	24.92	0.13466	—	17.21	16.39	H	EW	Yes	EW
5139v-38	13	27	22.950	–47	32	18.85	0.12032	18.61	17.36	16.85	M	EW	Yes	EW
5139v-39	13	27	13.812	–47	30	36.45	0.24794	17.56	17.51	17.16	M	Irr/Semi	No	NA
5139v-40	13	27	19.637	–47	31	55.75	0.33333	17.80	17.54	17.25	H	EW	No	NA
5139v-41	13	27	19.858	–47	32	17.87	0.33102	18.58	17.56	16.76	M	EA	No	NA
5139v-42	13	27	19.999	–47	33	08.13	0.51389	18.55	17.62	16.67	H	Irr/Semi	No	NA
5139v-43	—	—	—	—	—	—	0.12000	17.74	17.08	19.10	H	Irr/Semi	No	NA
5139v-44	13	27	15.141	–47	31	21.80	0.16464	18.86	17.80	17.02	H	EW	No	NA
5139v-45	13	27	19.732	–47	31	32.39	0.52083	19.00	17.90	—	L	Irr/Semi	No	NA
5139v-46	13	27	12.715	–47	32	55.32	0.32870	18.84	17.91	17.01	H	Irr/Semi	No	NA
5139v-47	13	27	20.947	–47	34	46.36	0.48727	19.15	17.94	—	H	RR1	No	NA
5139v-48	13	27	17.820	–47	34	37.42	0.48611	19.00	18.03	17.49	H	Irr/Semi	No	NA
5139v-49	13	27	14.128	–47	30	33.10	0.20000	19.20	18.07	17.55	M	BY Dra	No	NA
5139v-50	13	27	17.786	–47	30	59.77	0.14167	—	18.09	—	M	BY Dra	No	NA
5139v-51	13	27	13.908	–47	31	00.87	0.34060	19.10	18.10	17.35	EH	RR0	No	NA
5139v-52	13	27	16.648	–47	31	09.64	0.16703	19.02	18.17	17.74	H	BY Dra	No	NA
5139v-53	13	27	17.108	–47	35	14.55	0.33303	19.29	18.18	17.74	H	Irr/Semi	No	NA
5139v-54	13	27	12.941	–47	30	31.47	0.16826	—	18.28	—	M	Irr/Semi	No	NA
5139v-55	13	27	07.985	–47	31	51.79	0.33058	19.33	18.32	17.24	H	Irr/Semi	No	NA
5139v-56	13	27	11.793	–47	35	10.82	0.31866	19.37	18.35	17.74	H	BY Dra	No	NA
5139v-57	13	27	19.809	–47	31	11.87	0.27778	19.35	18.37	17.83	H	BY Dra	No	NA
5139v-58	13	27	08.163	–47	31	45.07	0.16819	19.27	18.39	17.93	H	Irr/Semi	No	NA
5139v-59	13	27	13.788	–47	30	56.09	0.33860	19.66	18.48	17.86	EH	RR0	No	NA
5139v-60	13	27	14.521	–47	30	57.36	0.33824	19.62	18.58	—	H	RR0	Yes	RR0
5139v-61	—	—	—	—	—	—	0.33824	19.62	18.58	—	H	Irr/Semi	No	NA
5139v-62	13	27	20.284	–47	31	55.77	0.11023	19.66	18.60	18.1	H	BY Dra	No	NA
5139v-63	13	27	18.287	–47	30	22.63	0.49769	19.36	18.74	—	M	Irr/Semi	No	NA

Table continued on next page

Table A1. Master catalogue, cont.

Variable ID	*R.A. (J2000)*			*Dec. (J2000)*			*Period (days)*			*Mag*	*Confidence Level*	*Variable Class*	*Recovered Survey*	*Recovered Class*
	h	*m*	*s*	*°*	*′*	*″*		*u′*	*g′*	*r′*				
5139v-64	13	27	16.423	–47	34	30.64	0.33064	19.63	18.75	18.27	L	Irr/Semi	No	NA
5139v-65	13	27	15.688	–47	31	06.78	0.12426	20.04	18.75	—	H	Irr/Semi	No	NA
5139v-66	13	27	17.048	–47	34	46.41	0.47222	18.60	18.76	19.05	L	BY Dra	No	NA
5139v-67	13	27	21.239	–47	35	03.71	0.48958	19.95	18.80	—	H	EB	No	NA
5139v-68	13	27	16.421	–47	31	07.16	0.14247	20.10	18.87	—	M	Irr/Semi	No	NA
5139v-69	13	27	08.964	–47	30	18.05	0.46991	19.92	18.87	17.5	L	Irr/Semi	No	NA
5139v-70	13	27	23.290	–47	32	51.07	0.46181	19.83	18.92	18.33	H	Irr/Semi	No	NA
5139v-71	13	27	19.581	–47	32	07.78	0.16830	20.10	18.98	18.5	H	BY Dra	No	NA
5139v-72	13	27	19.954	–47	30	52.41	0.56829	20.13	19.07	18.91	M	Irr/Semi	No	NA
5139v-73	13	27	22.110	–47	31	26.10	0.14284	20.24	19.12	—	H	BY Dra	No	NA
5139v-74	13	27	10.078	–47	32	02.49	0.16694	20.45	19.42	18.61	H	Irr/Semi	No	NA
5139v-75	13	27	01.120	–47	31	05.83	0.16212	—	—	13.51	M	Irr/Semi	No	NA
5139v-76	13	27	02.103	–47	35	13.15	0.15108	16.67	14.53	13.59	H	Irr/Semi	No	NA
5139v-77	13	27	01.571	–47	31	07.12	0.21840	16.37	15.78	13.93	H	RR0	No	NA
5139v-78	—	—	—	—	—	—	0.16308	14.61	15.49	16.76	H	Irr/Semi	No	NA
5139v-79	13	26	59.358	–47	35	26.63	0.28026	16.60	15.29	14.73	H	Irr/Semi	No	NA
5139v-80	13	26	50.531	–47	35	19.36	0.21150	—	—	16.41	H	Irr/Semi	No	NA
5139v-81	13	27	04.900	–47	32	27.85	0.14513	18.48	17.35	16.82	L	Irr/Semi	No	NA
5139v-82	13	27	01.617	–47	31	00.75	0.18461	—	—	17.38	H	Irr/Semi	No	NA
5139v-83	13	27	00.337	–47	31	40.88	0.14792	—	—	18.2	M	EA	No	NA
5139v-84	13	26	56.922	–47	31	03.00	0.15952	19.43	18.32	18.25	M	Irr/Semi	No	NA
5139v-85	13	26	56.656	–47	29	51.98	0.05888	15.62	13.68	—	M	Irr/Semi	No	NA
5139v-86	13	26	56.551	–47	30	54.78	0.09482	15.75	13.92	—	M	Irr/Semi	No	NA
5139v-87	13	26	56.278	–47	30	23.24	0.11780	16.12	15.07	—	L	Irr/Semi	No	NA
5139v-88	13	26	56.864	–47	32	08.87	0.06187	16.14	15.13	15.13	L	Irr/Semi	No	NA
5139v-89	13	26	58.662	–47	32	34.72	0.11863	16.14	14.84	14.72	L	Irr/Semi	No	NA
5139v-90	13	26	56.460	–47	34	12.50	0.09365	16.22	15.66	15.78	M	Irr/Semi	No	NA
5139v-91	13	26	58.212	–47	31	22.12	0.13339	16.29	14.73	—	M	Irr/Semi	No	NA
5139v-92	13	27	04.258	–47	30	28.90	0.13393	16.36	—	16.37	H	Irr/Semi	No	NA
5139v-93	13	26	56.756	–47	32	35.74	0.54977	16.59	14.99	14.1	L	Irr/Semi	No	NA
5139v-94	13	26	56.473	–47	33	21.68	0.09410	16.62	15.08	14.23	M	Irr/Semi	No	NA
5139v-95	13	26	56.799	–47	31	40.88	0.04438	16.64	15.04	—	L	Irr/Semi	No	NA
5139v-96	13	27	00.845	–47	30	14.24	0.09660	17.09	—	15.13	M	Irr/Semi	No	NA
5139v-97	13	26	56.418	–47	33	41.34	0.26620	17.17	15.71	14.88	M	Irr/Semi	No	NA
5139v-98	13	26	56.458	–47	34	05.44	0.09375	17.41	15.90	15.08	L	Irr/Semi	No	NA
5139v-99	13	26	56.669	–47	30	11.60	0.06223	17.46	15.53	—	M	Irr/Semi	No	NA
5139v-100	13	27	02.386	–47	31	26.65	0.13283	17.55	15.98	13.31	H	Irr/Semi	No	NA
5139v-101	13	27	00.303	–47	30	22.29	0.13356	18.60	17.36	—	M	Irr/Semi	No	NA
5139v-102	13	27	00.053	–47	29	55.05	0.11868	18.62	16.79	—	M	Irr/Semi	No	NA
5139v-103	13	26	55.615	–47	30	06.55	0.10621	18.73	—	16.88	M	Irr/Semi	No	NA
5139v-104	13	26	56.589	–47	30	48.88	0.35648	18.77	17.38	—	L	Irr/Semi	No	NA
5139v-105	13	27	00.636	–47	33	58.03	0.06008	19.50	—	—	L	Irr/Semi	No	NA
5139v-106	13	26	56.430	–47	31	07.30	0.31945	19.58	18.40	—	M	EA?	No	NA
5139v-107	13	27	00.608	–47	31	13.27	0.10728	20.03	—	—	M	Irr/Semi	No	NA
5139v-108	13	26	56.537	–47	33	19.04	0.11690	20.10	19.15	—	L	Irr/Semi	No	NA
5139v-109	13	26	55.795	–47	29	56.66	0.13407	20.12	—	—	L	Irr/Semi	No	NA
5139v-110	13	26	56.741	–47	32	45.29	0.05787	20.23	19.08	—	L	Irr/Semi	No	NA
5139v-111	13	26	56.514	–47	32	42.52	0.13277	20.38	—	—	M	Irr/Semi	No	NA
5139v-112	13	26	58.523	–47	32	37.24	0.13354	20.60	19.15	—	M	Irr/Semi	No	NA
5139v-113	13	26	53.782	–47	35	28.42	0.13320	21.34	19.90	—	H	Irr/Semi	No	NA
5139v-114	13	26	57.283	–47	34	34.90	0.13371	21.42	19.42	—	L	Irr/Semi	No	NA
5139v-115	13	27	21.678	–47	32	08.55	0.17780	15.31	13.94	14.81	M	Irr/Semi	No	NA
5139v-116	13	27	10.511	–47	33	49.03	0.19121	18.42	17.22	14.95	L	Irr/Semi	No	NA
5139v-117	13	27	09.921	–47	32	48.49	0.18986	19.98	19.21	17.93	M	Irr/Semi	No	NA

Appendix B: Master catalog of light curves of variable stars.

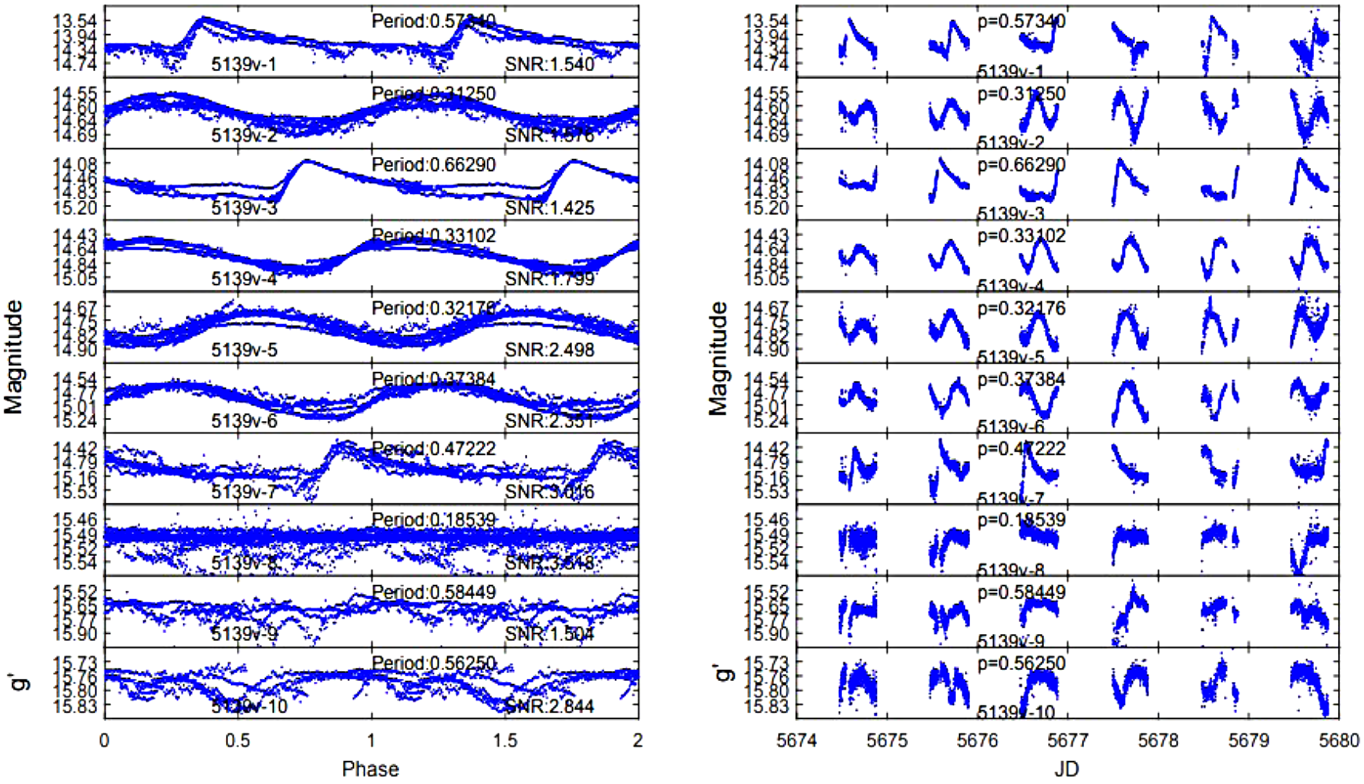

Figure B1. Phase and light curves for g' primary band for variables 5139v- 1–10. Left panel: phased light curves. Right panel: time series light curves.

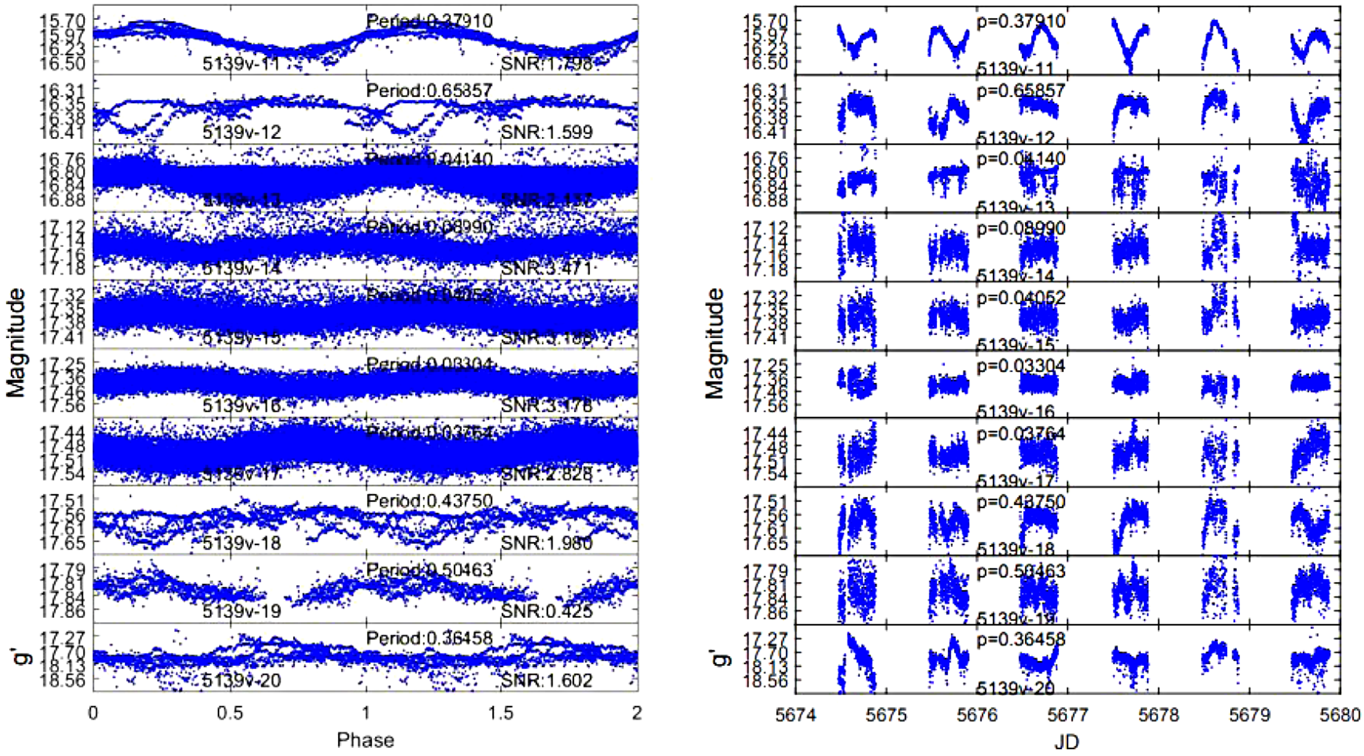

Figure B2. Phase and light curves for g' primary band for variables 5139v- 11–20. Left panel: phased light curves. Right panel: time series light curves.

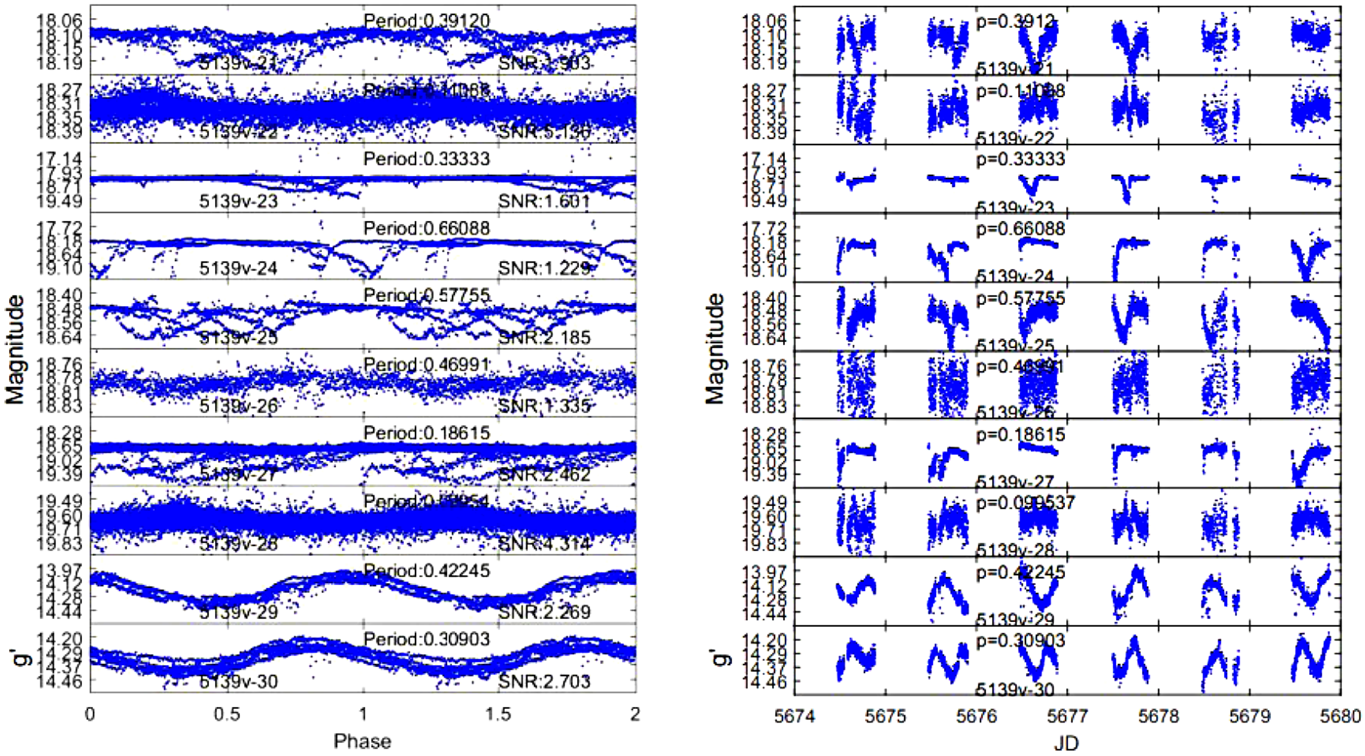

Figure B3. Phase and light curves for g' primary band for variables 5139v- 21–30. Left panel: phased light curves. Right panel: time series light curves.

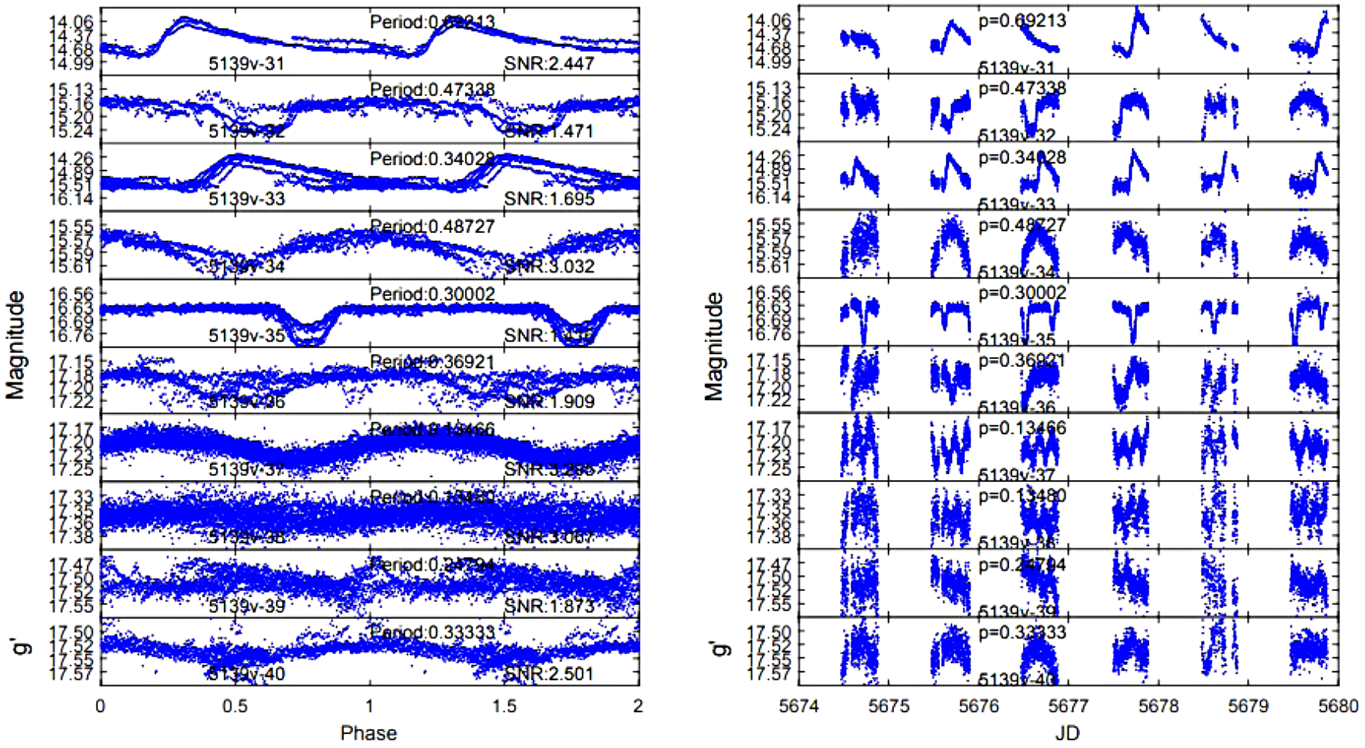

Figure B4. Phase and light curves for g' primary band for variables 5139v- 31–40. Left panel: phased light curves. Right panel: time series light curves.

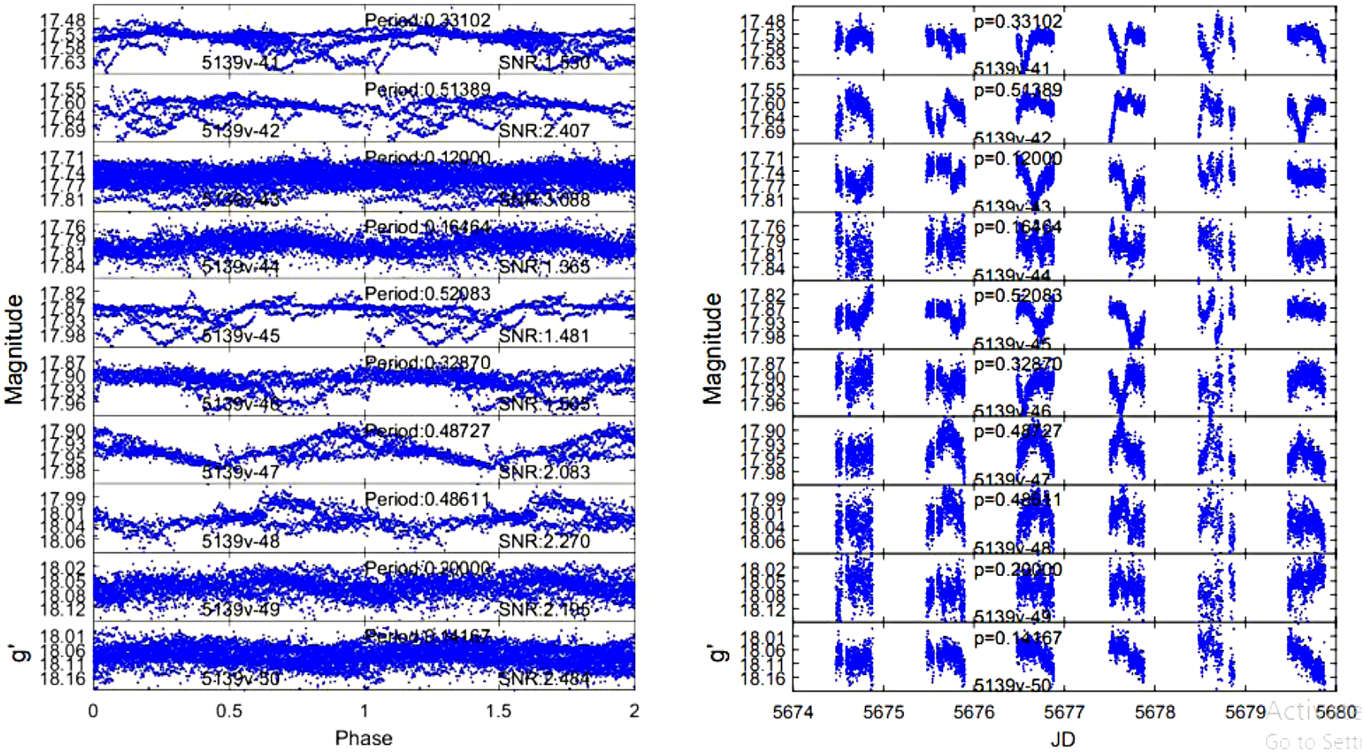

Figure B5. Phase and light curves for g' primary band for variables 5139v- 41–50. Left panel: phased light curves. Right panel: time series light curves.

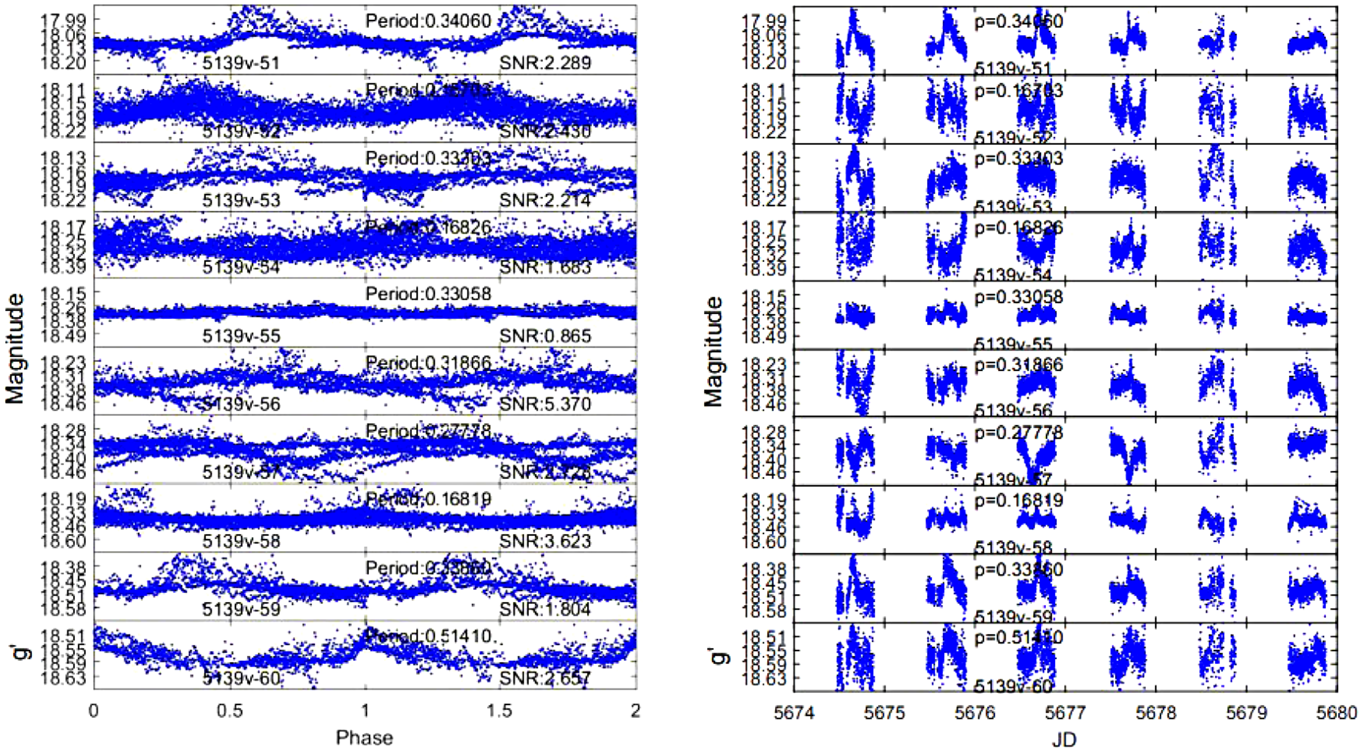

Figure B6. Phase and light curves for g' primary band for variables 5139v- 51–60. Left panel: phased light curves. Right panel: time series light curves.

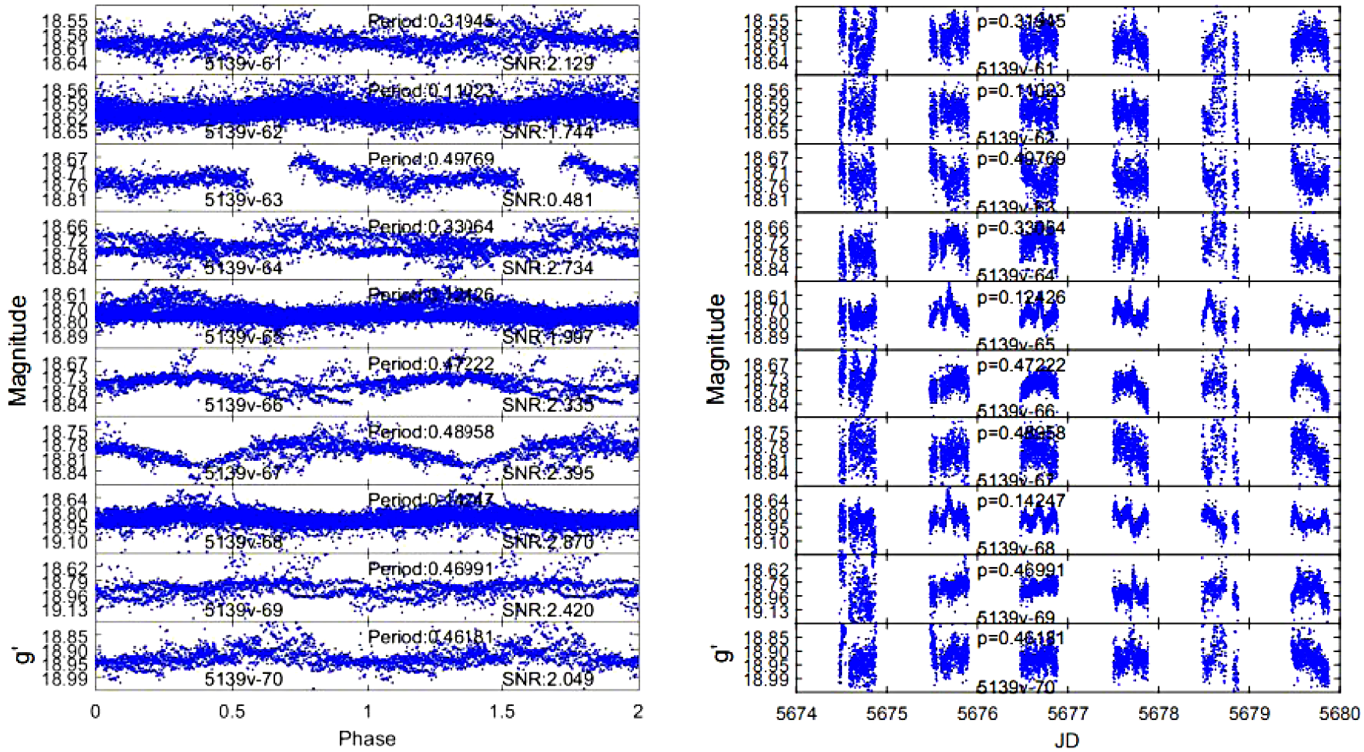

Figure B7. Phase and light curves for g' primary band for variables 5139v- 61–70. Left panel: phased light curves. Right panel: time series light curves.

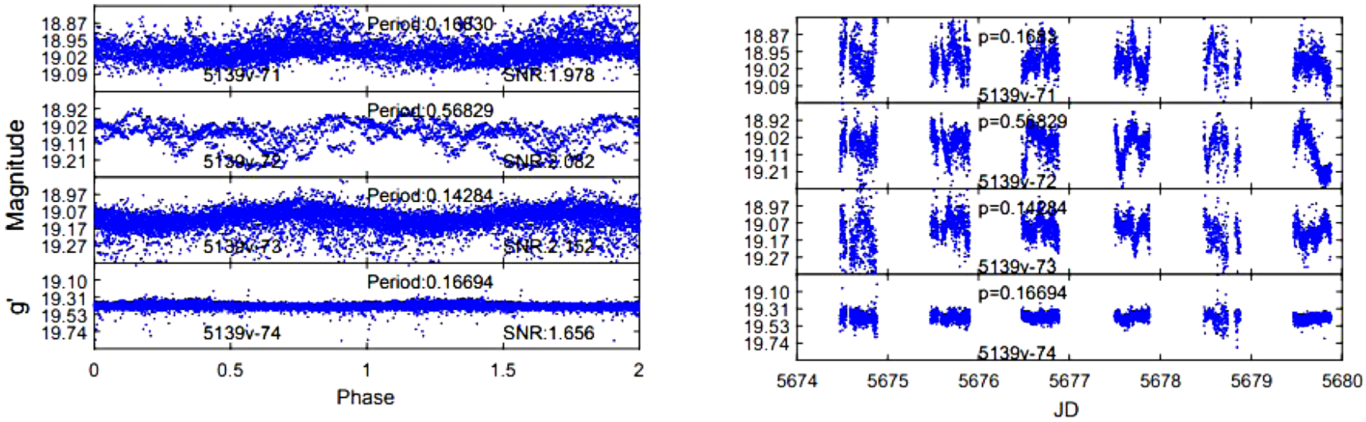

Figure B8. Phase and light curves for g' primary band for variables 5139v- 71–74. Left panel: phased light curves. Right panel: time series light curves.

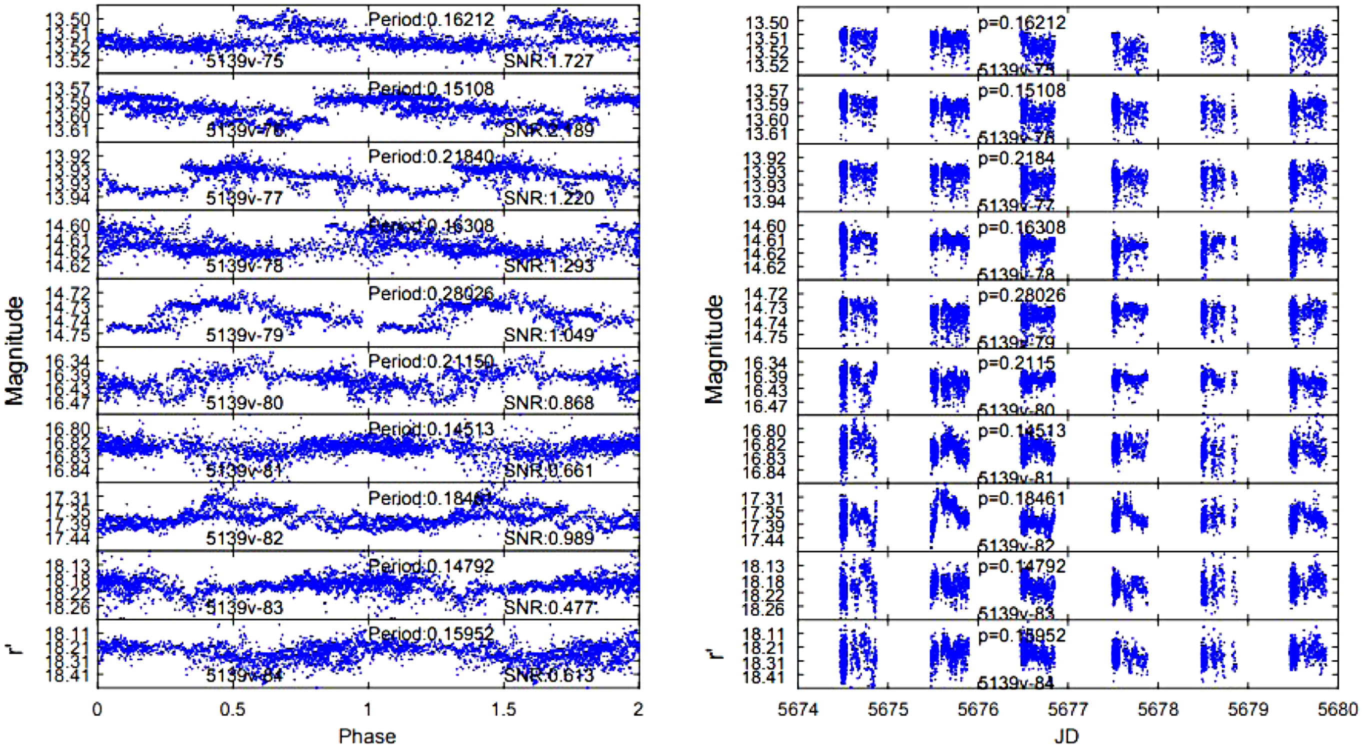

Figure B9. Phase and light curves for r' primary band for variables 5139v- 75–84. Left panel: phased light curves. Right panel: time series light curves.

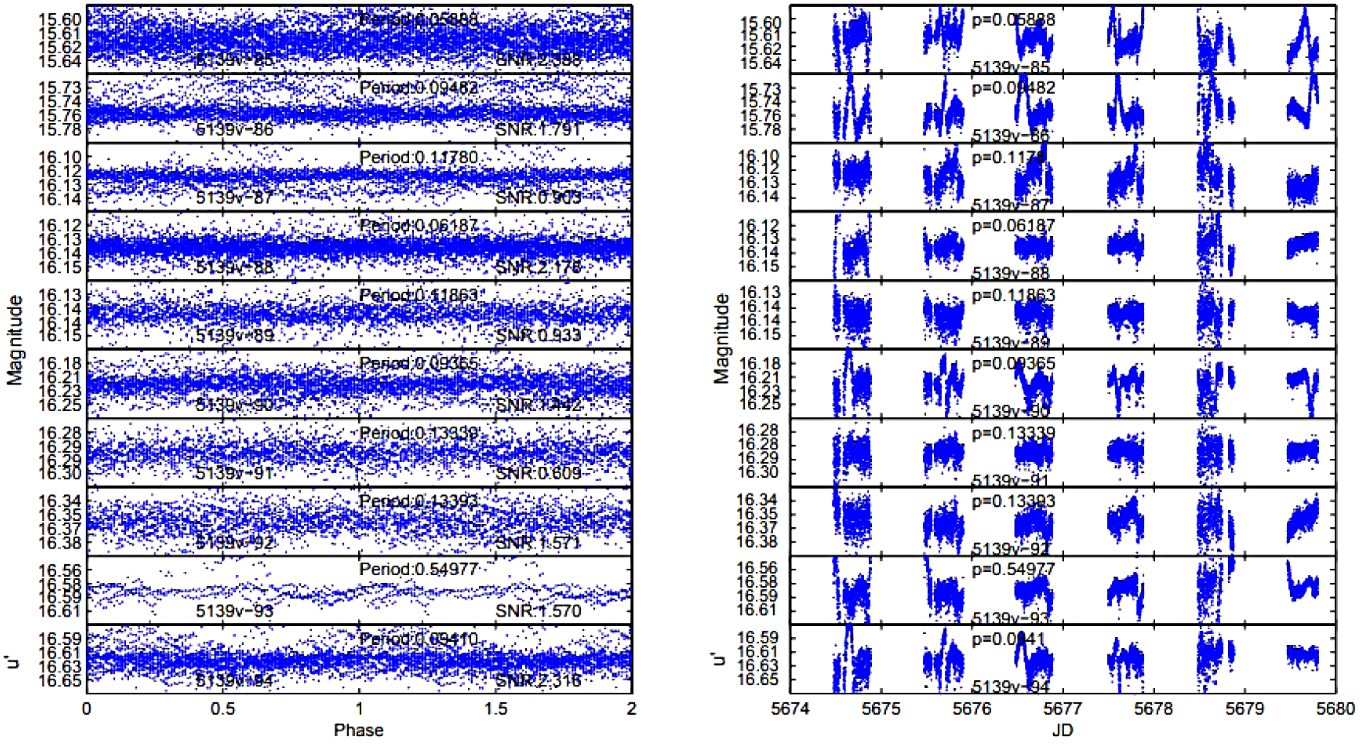

Figure B10. Phase and light curves for u' primary band for variables 5139v- 85–94. Left panel: phased light curves. Right panel: time series light curves.

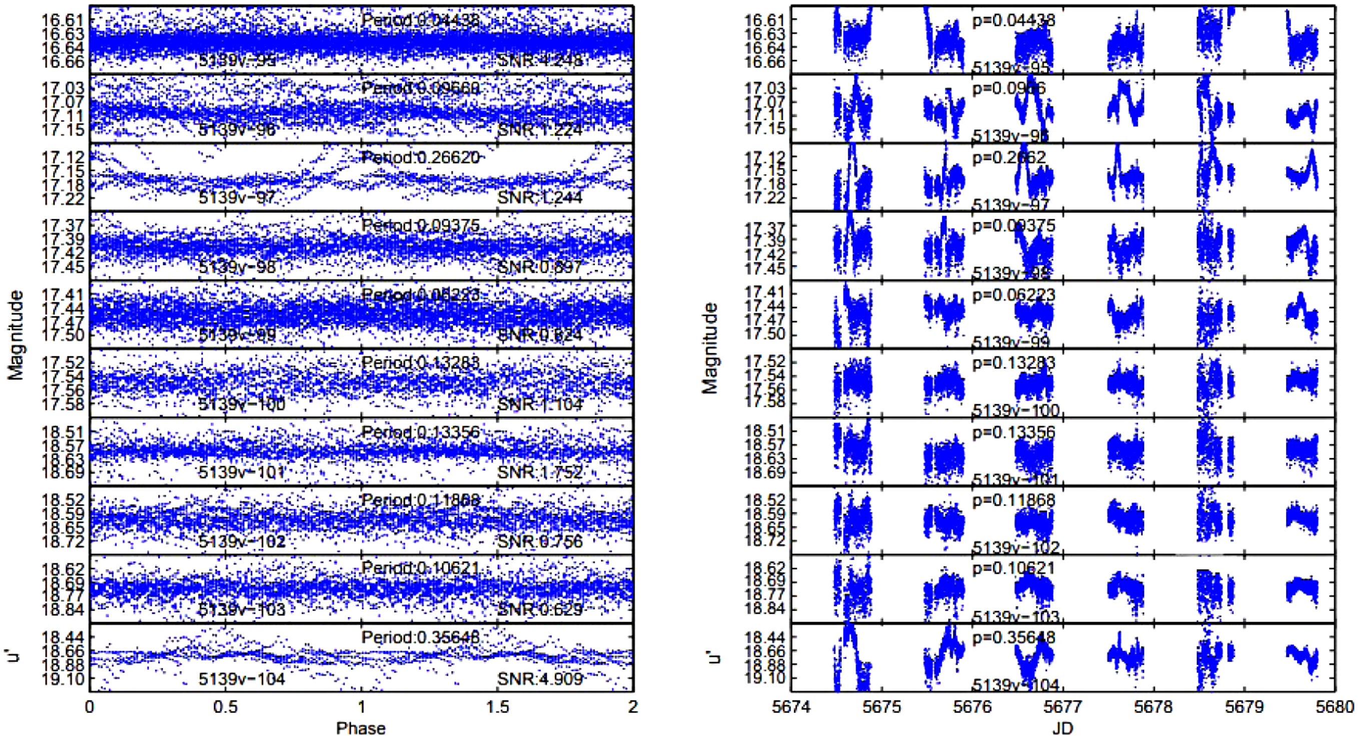

Figure B11. Phase and light curves for u' primary band for variables 5139v- 95–104. Left panel: phased light curves. Right panel: time series light curves.

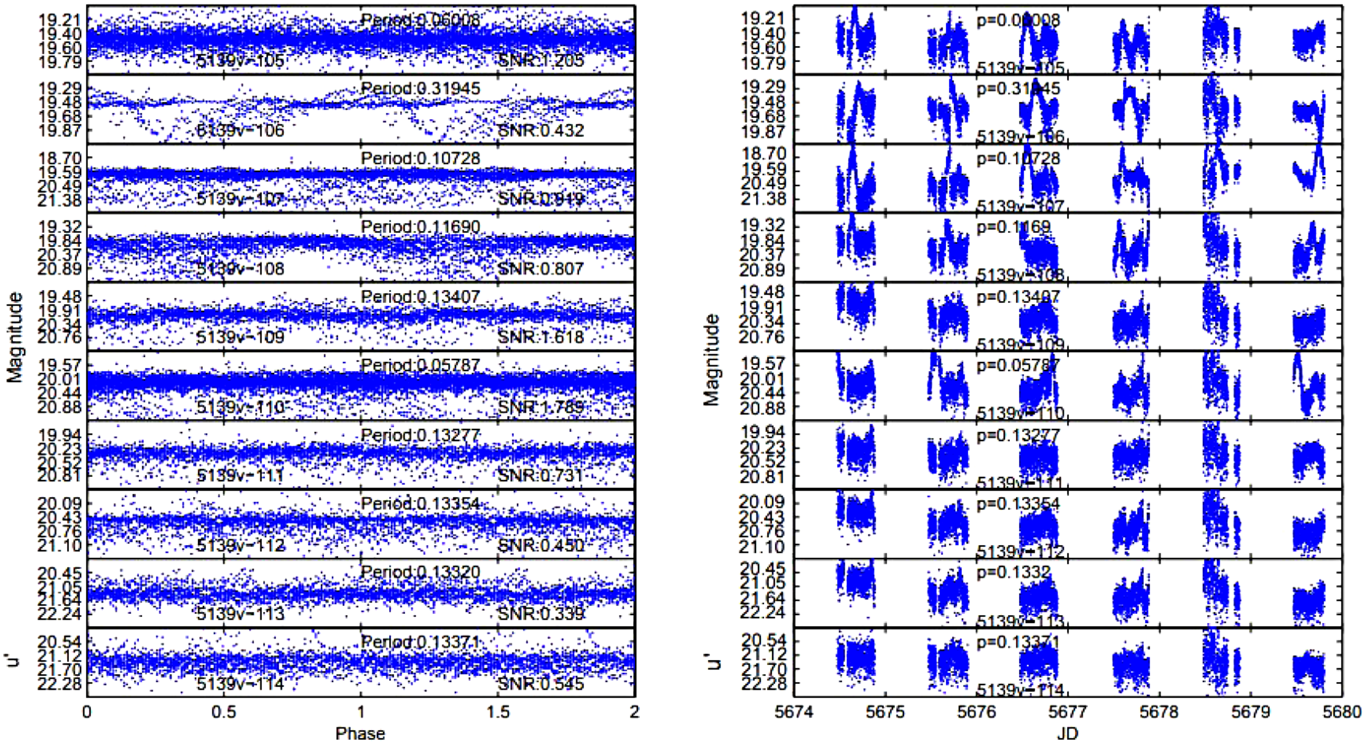

Figure B12. Phase and light curves for u' primary band for variables 5139v- 105–114. Left panel: phased light curves. Right panel: time series light curves.

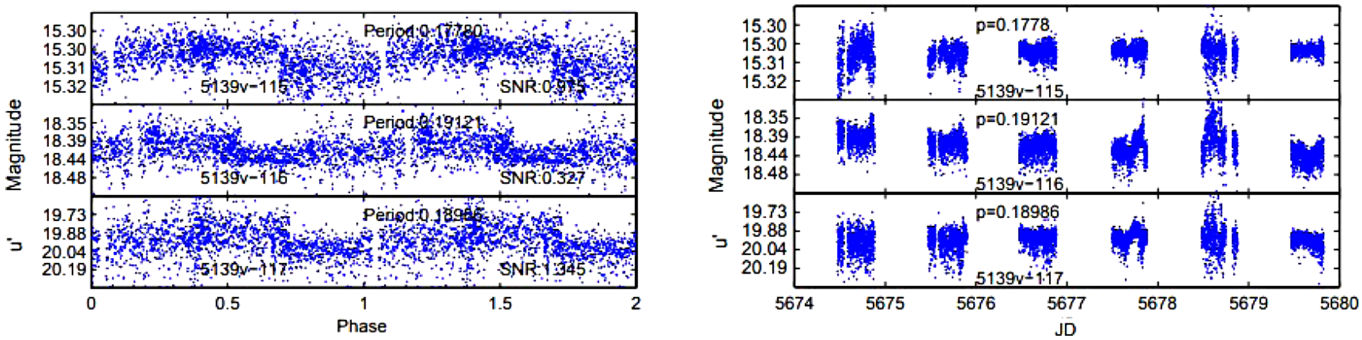

Figure B13. Phase and light curves for u' primary band for variables 5139v- 115–117. Left panel: phased light curves. Right panel: time series light curves.

CCD Photometry, Light Curve Deconvolution, Period Analysis, and Evolutionary Status of the HADS Variable V1116 Herculis

W. Allen Gilchrist, Jr.
Stonecrest Observatory, 104 Deer Ridge Drive, Fort Davis, TX 79734; gilchrist.allen@ymail.com

Kevin B. Alton
UnderOak and Desert Blooms Observatories, 70 Summit Avenue, Cedar Knolls, NJ; kbalton@optonline.net

Received June 9, 2023; revised September 15, 2023; accepted September 16, 2023

Abstract CCD-derived photometric B-, V-, R_c-, and I_c-magnitude data were acquired for V1116 Her, an intrinsic pulsating variable classified as a High Amplitude δ Scuti (HADS) star. Precise time-series light curve data were deconvolved using discrete Fourier transformation, revealing a fundamental mode (f_0) of oscillation at 10.5610 d^{-1} along with at least three other partial harmonics ($2f_0$—$4f_0$). At least nine other statistically significant frequencies were resolved following successive pre-whitening of each residual signal. An assessment of potential period changes over time was performed using 46 new times of maximum (ToMx) light produced from the present study (2022) along with 160 other ToMx values extracted from the TESS survey earlier in 2022. These results indicate that no substantive change in the fundamental period of oscillation or amplitude (nominally I_c-mag) has likely occurred over the past two years. Finally, an investigation with PARSEC models for generating stellar tracks and isochrones provided a better understanding about the evolutionary status of this star.

1. Introduction

V1116 Herculis (GSC 1510-1091) is a pulsating variable classified as a High Amplitude δ Scuti (HADS) star. The star was listed as a short period variable designated as 61.1935 Her in the article 162 Neue Veränderliche (Hoffmeister 1935). This variable was included in "The All Sky Automated Survey. Catalog of Variable Stars. I. 0 h–6 h Quarter of the Southern Hemisphere" (Pojmaņski 2002), and was classified as either a δ Sct or β Cep star. V1116 Her was also imaged during the Robotic Optical Transient Search Experiment (ROTSE-I) survey (Woźniak, *et al.* 2004). Khruslov (2006) identified the star as a δ Sct pulsating variable. The "79th Name-List of Variable Stars" (Kazarovets *et al.* 2008) also lists the object as a δ Sct (DSCT) star with the name V1116 Her. Mining "The All-Sky Automated Survey for Supernovae (ASAS-SN) Light Curve Server v1.0" also uncovered a light curve for this intrinsic variable (Kochanek *et al.* 2017).

Less than 1% of δ Sct variables are HADS stars (Lee *et al.* 2008), but they are interesting targets for amateur photometrists with CCD or CMOS cameras installed on modestly-sized telescopes. With their relatively short pulsation periods (< 0.2 d), high variation amplitude (> 0.2 mag), and luminosity ($> 10\,L_\odot$), it is possible to acquire a complete light curve (LC) in just a few observing sessions. Common among A- through F-type variable stars are the periodic or multi-periodic δ Scuti-type (hereafter δ Sct) pulsating stars. Such stars occupy a small space at the intersection of the classical instability strip, the pre-main sequence, and the main sequence (MS) on the Hertzsprung-Russell diagram. Observationally as a group, they represent the middle ground between high-amplitude radial pulsators, like Cepheid variables, and non-radial multi-periodic pulsators (Breger 2000). Main sequence δ Sct stars typically have spectral types between F2 and A2 (Rodríguez and Breger 2001) with temperatures ranging from 6300 to 8600 K (Uytterhoeven *et al.* 2011). Generally, hotter δ Sct stars have shorter pulsation periods (i.e. higher pulsation mode frequencies) than cooler ones.

Pulsations in δ Sct stars are generated by the kappa-mechanism operating in a He II partial ionization zone (T ~ 50000 K). Variations in levels of ionization and transparency in these zones cause low-order pressure (p) modes similar to acoustic waves (Cox 1963; Chevalier 1971). These can produce either radial pulsations evoking symmetrical changes in stellar size or non-radial pulsations giving rise to asymmetric changes in shape but not volume, or a combination of both radial and non-radial components. Although shorter periods (< 30 min) have been observed (Holdsworth *et al.* 2014) in some A-type stars, the fundamental mode radial pulsations of Galactic δ Sct variables with near solar metallicity are generally between 0.05 and 0.25 d. Masses range from ~ 1.2 $M_\odot$ to 2.5 $M_\odot$, so they are more luminous and larger than our Sun.

Stars with slower rotational velocities ($< 30\,\mathrm{Km \cdot s^{-1}}$) tend to be radial pulsators with light curve amplitudes (V-mag) in excess of 0.20–0.30 mag. These stars belong to a δ Sct subgroup called HADS variables.

HADS variables usually oscillate with low-order single or double radial pulsation modes (Poretti 2003a, 2003b; Niu *et al.* 2013, 2017). About 40% of HADS variables are double pulsators with simultaneous pulsations in the fundamental mode and the first overtone mode with amplitudes generally higher in the fundamental mode (McNamara 2000). HADS stars have historically been divided corresponding to their metallicity relative to our Sun ([Fe/H] = 0 dex). Stars in the metal-poor ([Fe/H] << 0) group are called SX Phe stars, based on the prototype SX Phoenicis.

A large number of HADS stars have been detected with precise photometry using much more sensitive space telescopes like the European Space Agency's CoRoT (Baglin 2003), the Canadian Microvariability and Oscillations of STars (MOST)

(Walker *et al.* 2003), NASA's Kepler (Gilliland *et al.* 2010; Guzik 2021; Yang *et al.* 2021), and the Transiting Exoplanet Survey Satellite (TESS) (Ricker *et al.* 2015; Bedding *et al.* 2020).

Pulsating stars have served as standard candles for determining celestial distances ever since Henrietta Leavitt discovered a period-luminosity (P-L) relationship of 25 Cepheid variables in the Small Magellanic Cloud (Leavitt and Pickering 1912). This P-L relationship has been improved over time based on differences between metal-rich (Population I) and metal-poor (Population II) Cepheids (Baade 1956). Ziaali *et al.* (2019) reported a refinement of the P-L relationship for δ Sct variables based on the more accurate values from the Gaia Mission (Lindegren *et al.* 2016; Gaia Collab. *et al.* 2018). A more recent investigation by Poro *et al.* (2021) resulted in another derivation of P-L relationships for δ Sct stars oscillating in the fundamental mode (adopted herein) as well as first through third overtones.

2. Observations, data reduction, and photometric processing

2.1. Photometry

Precisely timed photometric observations were made from the Stonecrest Observatory (SO) near Fort Davis, Texas (103.9767 W, 30.6167 N), with an SBIG ST10-XME CCD camera at the secondary focus of a 0.3-m f/8 Ritchey-Chretien telescope. This instrument produces a field of view (FOV) of 21' × 14' with an image scale of 1.73 arcsec/pixel (bin = 3 × 3). This binning produces images with adequate resolution compared to the typical seeing during summer in the mountains of west Texas. SO data used in this study were taken between July 12 and September 5, 2022. Images were acquired using TheSkyX Pro Version 10.5.0 (Software Bisque 2019) which controlled an Astro-Physics AP-1200 GTO German equatorial mount. The CCD-camera was equipped with B, V, R_c, and I_c filters manufactured to match the Johnson-Cousins Bessell specification. Dark subtraction, flat correction, and registration of all images collected at SO were performed with ImagesPlus Ver. 6.5 (ImagesPlus 2020). A few images were registered using AIP4Win V. 2.4.0 (Berry and Burnell 2005). These programs were also used to determine FWHM or HFD values to aid in aperture selection for photometric analysis. Exposures varied somewhat during the observations depending on sky conditions. Instrumental readings were reduced to catalog-based magnitudes using the APASS star fields (Henden *et al.* 2009, 2010, 2011; Smith *et al.* 2011) built into MPO Canopus v10.8.5.0 (Minor Planet Observer 2010). LCs were generated using ensembles of five non-varying comparison stars. The identities, J2000 coordinates, APASS V-magnitudes, and color indices (B–V) for V1116 Her and the comparison stars are provided in Table 1; a corresponding image showing the target and comparison stars is presented in Figure 1. Only data from images taken above 30° altitude (airmass < 2) were included; considering the proximity of all program stars, differential atmospheric extinction was ignored. The average uncertainty in the target star magnitudes for all four filters was less than 0.007, and in no case was the uncertainty greater than 0.014 mag. All photometric data acquired and used in this study can be retrieved from the AAVSO International Database (Kafka 2021; observer code GWAA).

Table 1. Astrometric coordinates (J2000), V-mag and color indices (B–V) for V1116 Her and five comparison stars (1–5) used during this photometric study.

FOV ID		*R.A. (J2000) h m s*	*Dec. (J2000) ° ' "*	*APASS^a V mag*	*APASS^a (B–V)*
T	V1116 Her	16 30 16.40	+16 55 06.0	11.284	0.291
1	GSC 1510-1179	16 30 39.02	+16 59 24.1	12.477	0.751
2	GSC 1510-1221	16 30 33.78	+17 02 40.7	12.417	0.673
3	GSC 1510-1191	16 30 27.43	+17 00 30.8	12.757	0.543
4	GSC 1510-1134	16 29 52.73	+16 57 42.0	12.556	0.542
5	GSC 1510-1104	16 30 56.29	+16 54 48.9	12.743	1.18

[a] *V-mag and (B–V) for comparison stars derived from APASS database described by Henden* et al. *(2009, 2010, 2011) and Smith* et al. *(2011), as well as on the AAVSO web site (http://www.aavso.org/apass).*

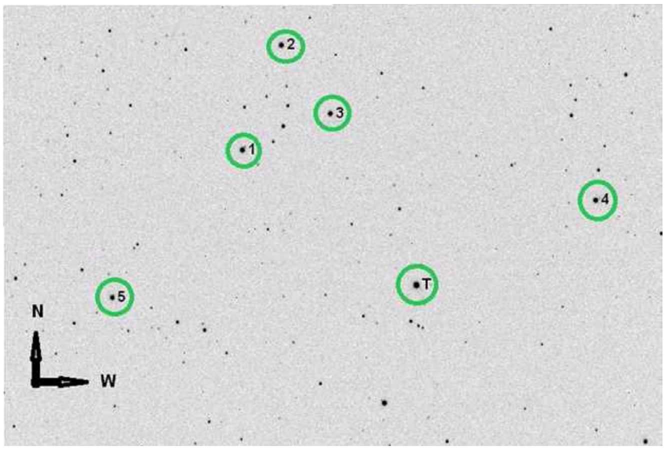

Figure 1. V1116 Her (T) along with the five comparison stars (1–5) used to reduce time-series images to APASS-catalog based magnitudes.

3. Results and discussion

3.1. Photometry and ephemerides

A total of 1247 measurements (316 B, 314 V, 309 R_c, and 308 I_c) were acquired between July 15 and September 5, 2022 (JD2459775.42014–2459827.48472). Figure 2 shows folded LCs for each filter produced with MPO Canopus. Period determinations were initially performed using Peranso v2.5 (Paunzen and Vanmunster 2016) by applying periodic orthogonals (Schwarzenberg-Czerny 1996) to fit observations and analysis of variance (ANOVA) to assess fit quality. Period solutions for different passbands can be slightly different. In this case, values of 0.094697 ± 0.00006 d were found for the B filter, with 0.094667 ± 0.00003 d for the V, R_c, and I_c filters. We also found 10,876 time-series values taken (cadence = 120 s) by the Transiting Exoplanet Survey Satellite (TESS) (Ricker *et al.* 2015; Bedding *et al.* 2020). These data (18 May 2022–13 June 2022) are available through the Mikulski Archive for Space Telescopes (mast.stsci.edu). Processing (ANOVA) these values (BJD_TDB vs. PDCSAP_FLUX) through Peranso 3 produced a folded light curve (Figure 3) with a period of 0.0946783 ± 0.0000093 d.

Another way to historically evaluate the period of oscillation is to compare the measured times of maximum light (ToMx) with those predicted by a reference ephemeris. An updated ephemeris can be determined by adjusting the parameters to achieve the best fit to a plot of predicted time differences (PTD) versus cycle number. One advantage of this type of analysis is that data from different sources can be easily combined. In this case, for example, the star brightness in the TESS data is presented as normalized flux while the SO values are magnitudes estimated from APASS standards. The TESS data yielded 160 ToMx results, while a total of 46 new ToMx values were estimated from the SO data. The polynomial extremum fit utility in Peranso 2.5 (Paunzen and Vanmunster 2016) was used for all ToMx determinations. No obvious color dependencies were seen in the SO timings. Table 2 contains a representative sampling of data acquired from TESS and SO. A complete set of 206 ToMx values from TESS and SO are available in a table found at:

ftp://ftp.aavso.org/public/datasets/3893-Gilchrist-V1116 Her.xlsx

and

ftp://ftp.aavso.org/public/datasets/3893-Gilchrist-V1116 Her..csv.

While determining ToMx times from the TESS data, it was clear that the amplitude of the variation and the mean brightness for V1116 Her are not constant. This will be discussed more fully in the section on Fourier analysis. The AAVSO International Variable Star Index (VSX; Kafka 2021) reference epoch (August 08, 2020) was initially defined by the following linear ephemeris (Equation 1):

$$\text{Max (HJD)} = 2459070.222 + 0.09468113\ E. \qquad (1)$$

Table 2. Differences between the times-of-maximum light (HJD) predicted from the updated linear ephemeris (Equation 2) and those observed for V1116 Her by the TESS satellite (18 May 2022–13 June 2022) and at Stonecrest Observatory (12 July 2022 and 05 Sept 2022). Sample table (see note).

Source	*Bandpass*	*ToMx HJD = 2400000+*	*ToMx Uncertainty*	*Cycle No.*	*PTD*[a]
TESS	I_c[b]	59718.70104	0.00115	–1151	0.00161
TESS	I_c	59718.79370	0.00128	–1150	–0.00041
TESS	I_c	59718.88866	0.00131	–1149	–0.00012
TESS	I_c	59718.98245	0.00120	–1148	–0.00101
TESS	I_c	59719.07954	0.00107	–1147	0.00139
TESS	I_c	59719.17131	0.00130	–1146	–0.00151
TESS	I_c	59719.26726	0.00118	–1145	–0.00023
TESS	I_c	59719.36418	0.00117	–1144	0.00200
SO	V	59772.66405	0.00130	–581	–0.00189
SO	R_c	59772.66462	0.00104	–581	–0.00132
SO	I_c	59772.66575	0.00155	–581	–0.00018
SO	B	59772.66620	0.00212	–581	0.00026
SO	I_c	59804.66630	0.00172	–243	–0.00083
SO	R_c	59827.67087	0.00118	0	–0.00303
SO	B	59827.67655	0.00184	0	0.00265
SO	V	59827.67760	0.00002	0	0.00370

[a] *(PTD) = Time difference between observed fundamental mode pulsation time-of-maximum and that calculated using the reference ephemeris (Equation 2).* [b] *(I_c) = Bandpass for TESS satellite detector is between 600 and 1000 nm, centered near Cousins I. Note: Only the first eight values from TESS and the last eight from SO are shown in this sample table. Full table available at: ftp://ftp.aavso.org/public/datasets/3893-Gilchrist-V1116 Her.xlsx and .csv.*

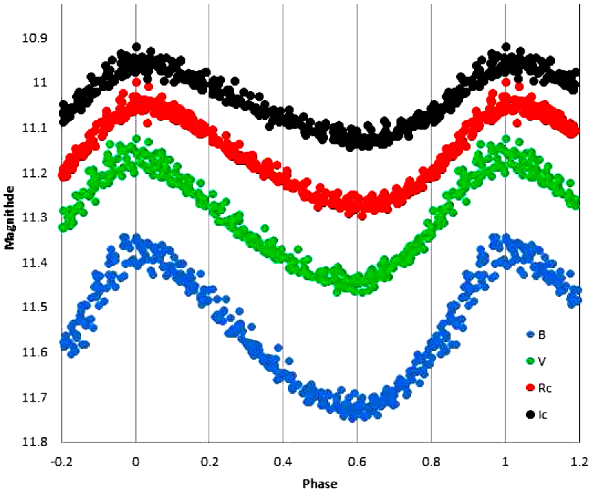

Figure 2. Period-folded (0.0946781 d) LCs for V1116 Her produced from photometric data obtained between July 15 and September 5, 2022, at SO. LCs shown top to the bottom are I_c, R_c, V, and B passbands and represent catalog-based (APASS) magnitudes determined using MPO Canopus.

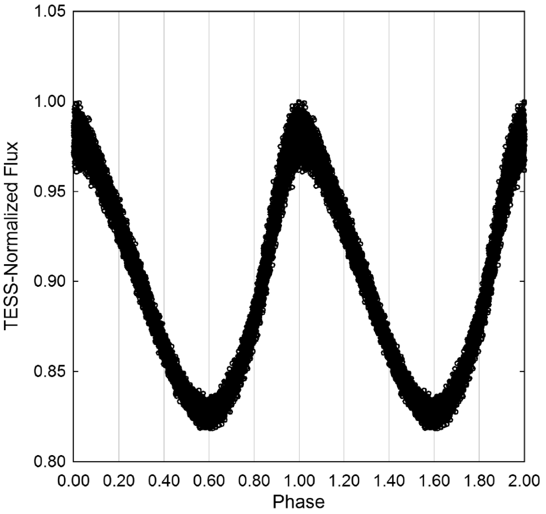

Figure 3. Period-folded (0.0946783 ± 0.0000093 d) LC for V1116 Her produced from peak height normalized photometric data obtained from the TESS satellite between 18 May 2022 and 13 Jun 2022.

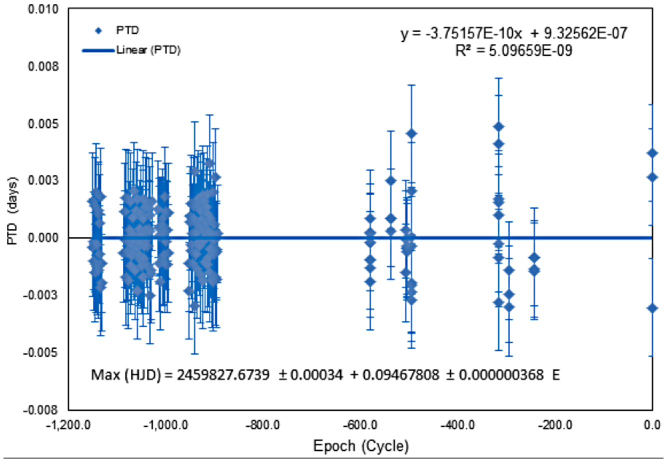

Figure 4. Straight line fit (PTD vs. cycle number) suggesting that little or no change to the fundamental mode pulsation period of V1116 Her had occurred between 1999 and 2018.

Table 3. V1116 Her color indices (B–V) with uncertainty determined at SO along with survey values reported from other sources which were used to estimate $(B–V)_0{}^a$ and $T_{eff}{}^b$.

Source	*(B–V)*	*(B–V) Error*	$(B–V)_0{}^a$	$(B–V)_0$ *Error*	log T_{eff}	log T_{eff} *Error*	$T_{eff}{}^a$	T_{eff} *Error*
SO nr max	0.206	0.007	0.159	0.007	3.908	0.003	8093	48
SO nr min	0.277	0.010	0.231	0.010	3.882	0.004	7613	67
SO average	0.242	0.012	0.195	0.012	3.895	0.005	7849	83
APASS[c]	0.291	0.150	0.240	0.150	3.879	0.052	7575	918
2MASS[c]	0.280	0.046	0.234	0.046	3.865	0.014	7320	243
UCAC4[c]	0.362	N/A	0.316	N/A	3.850	N/A	7084	N/A

[a] *$(B–V)_0 = (B–V) – E(B–V)$ where $E(B–V) = 0.0462 \pm 0.0008$ ((Amôres and Lépine 2005).* [b] *T_{eff} = effective temperature (K) from Pecaut and Mamajek (2013).* [c] *Unknown when data acquired during pulsation cycle.*

An updated linear ephemeris complete with uncertainties was produced by plotting (Figure 4) the PTD residuals vs. epoch (or cycle number) as follows:

$$\text{Max (HJD)} = 2459827.6739\ (3) + 0.0946781\ (4)\ E. \qquad (2)$$

where the times of maxima are in Heliocentric Julian Dates (HJD), and E is an integral cycle number chosen so that E = 0 represents the most recent maximum measurement. A comparison of equations 1 and 2 shows that our data yield a period slightly shorter that the VSX value from August 2020.

B- and V-magnitudes can be combined to produce a (B–V) or color index LC (Figure 5). Care was taken in making this plot to insure that the phase values were the same as those in Figure 2. There is a slight phase shift (~0.05 or about 7 min) between the single-color LCs and the B–V LC. The blue points in Figure 5 were averaged to determine a B–V value near maximum brightness, and the red points were used to find a near-minimum brightness value.

3.2. Light curve behavior

Light curves from HADS variables are usually asymmetrical with a faster rise from minimum to maximum light and a slower decline back to minimum brightness. V1116 Her appears to be a good example in this regard (Figure 2). The zero phase point in this plot was arbitrarily chosen at maximum brightness. The largest difference between maximum and minimum light is in the B passband (ΔB mag = 0.3443 ± 0.0271), followed by V (ΔV mag = 0.2751 ± 0.0254), R_c (ΔR_c mag = 0.2260 ± 0.0237), and finally I_c (ΔI_c mag = 0.1737 ± 0.0194). This is typical for pulsating F- to A-type stars.

The B–V LC from the SO data shows noticeable reddening (higher B–V value) near minimum light. Averaging a few points near the maximum and minimum of the B–V plot (the blue and red points in Figure 5) yields a quantitative estimate. In this case color excess (B–V) ranges between 0.206 ± 0.007 and 0.277 ± 0.010 mag. Additional color information was found in the APASS, 2MASS, and UCAC4 databases. Both the APASS and UCAC4 listings included B- and V-magnitudes, although no uncertainty was given in the UCAC4 database. The 2MASS information includes only J and K magnitudes with the associated uncertainties so it was necessary to convert these to B and V for comparison. A web site at http://brucegary.net/dummies/method0.html provides equations to convert from J and K to B and V magnitudes. Table 3 lists B–V values from several sources with propagated errors along with $(B–V)_0$ values corrected for interstellar extinction (Amôres and Lépine 2005) and corresponding temperatures, T_{eff} (Pecaut and Mamajek 2013).

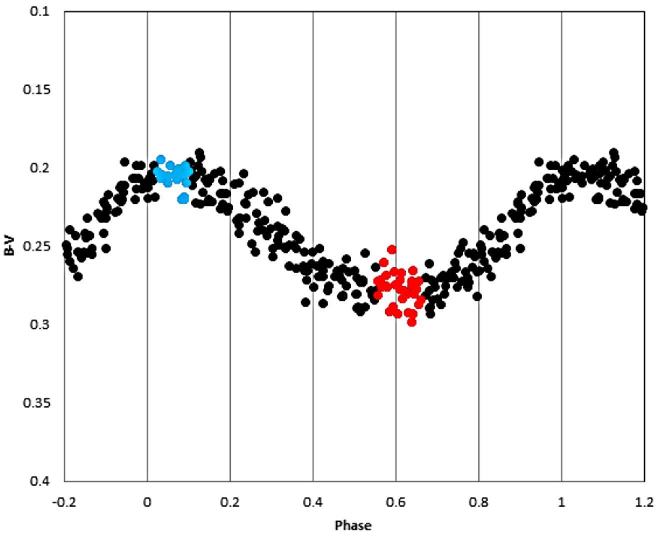

Figure 5. A color excess (B–V) LC for V1116 Her shows significant changes ($0.20 < (B–V) < 0.28$) as maximum light slowly descends to minimum light. This effect is most closely associated with a decrease in the effective surface temperature during minimum light. Note also the small phase shift (~0.05 or about 7 min) compared to the LCs in Figure 2. The blue points were averaged to determine a B–V value near maximum brightness, and the red points were used to find a near-minimum brightness value.

The color indices from the surveys are all larger than the average value from the SO data, and either present no uncertainty or have uncertainties that are much larger than the value from the SO data. It is unknown when light curve data from APASS, 2MASS, or UCAC4 were acquired during a pulsation cycle. Before attempting to determine T_{eff} from B–V, it is necessary to consider interstellar extinction, A_V. A value for Galactic (Milky Way) dust reddening or color excess, E(B–V), can be determined from A_V as below:

$$E(B–V) = A_V / 3.1. \qquad (3)$$

E(B–V) is commonly used to correct B–V according to:

$$(B–V)_0 = (B–V) – E(B–V). \qquad (4)$$

where $(B–V)_0$ is also known as intrinsic color.

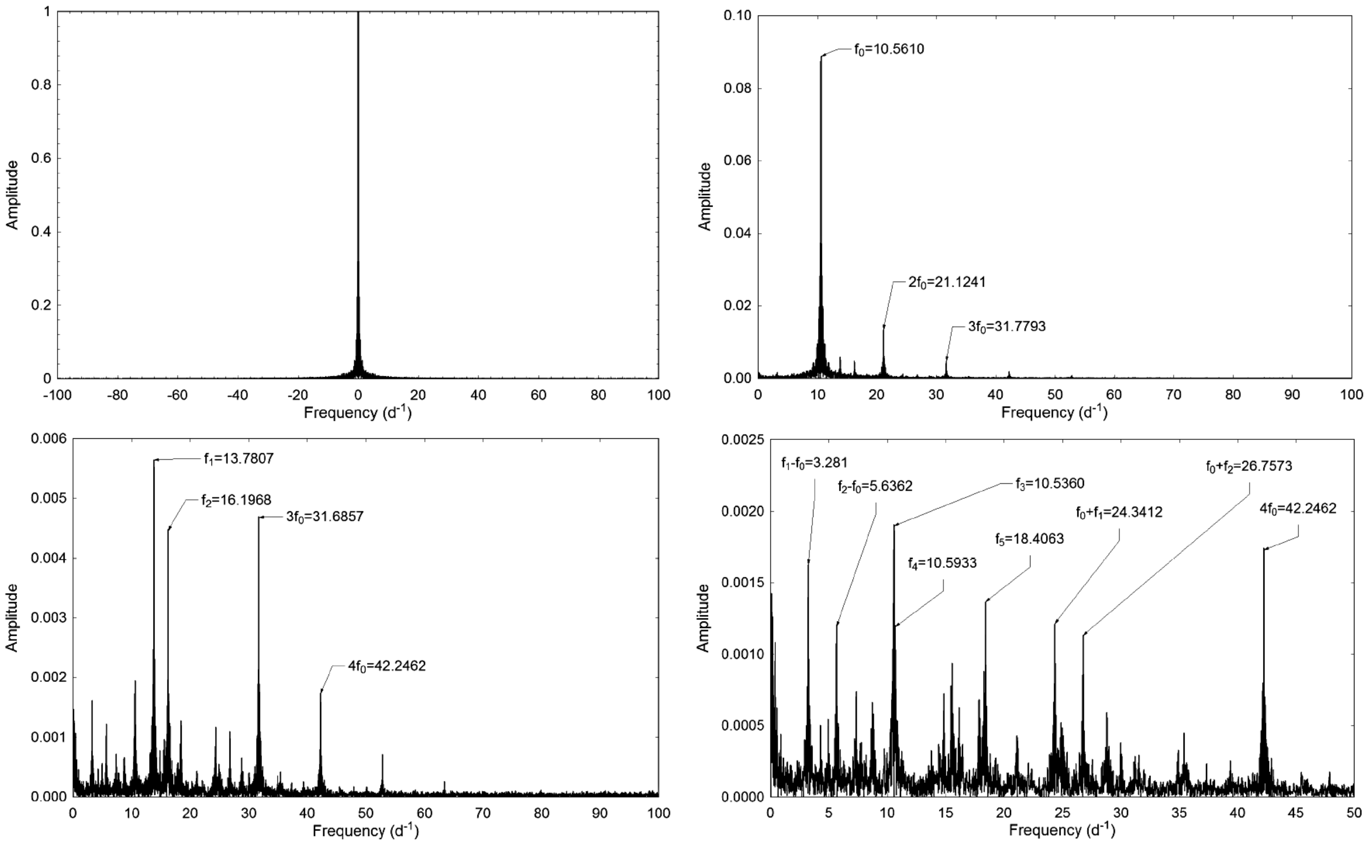

Figure 6. V1116 Her spectrum window and power spectrum plots for all significant frequencies detected (n = 13) from TESS photometry using Discrete Fourier Transformation (Period04).

Estimates for values for E(B–V) can vary depending on the model selected (Amôres and Lépine 2005, 2007; Schlegel *et al.* 1998; Schlafly and Finkbeiner 2011; Schlafly *et al.* 2014). These models can be conveniently accessed via the GALextin website at http://www.galextin.org/ (Amôres *et al.* 2021). For this study, we use the reddening value based on Amôres and Lépine (2005) yielding $A_V = 0.143 \pm 0.003$. From equation 3, E(B–V) = 0.0462 ± 0.0008 mag. From Equation 4, this results in an intrinsic color index $(B–V)_0$ for V1116 Her that varies between 0.159 ± 0.007 at maximum light and 0.231 ± 0.010 mag at minimum brightness, with a mean value of 0.195 ± 0.012. Interpolating these numbers between values from Table 5 in Pecaut and Mamajek (2013) yields a mean effective temperature (T_{eff}) of 7849 ± 83 K, with a minimum T_{eff} of 7613 ± 48 K and a maximum T_{eff} of 8093 ± 48 K. Based solely on B–V photometry at SO, these results compare with the $T_{eff} = 7978^{+373}_{-228}$ K listed in the Gaia DR2. Interestingly, the average B–V from the APASS and 2MASS data yields a value of $T_{eff} = 7450 \pm 470$ K. The SO result corresponds to a spectral class of A7V, while the Gaia DR2 value represents an A6V and the APASS and 2MASS average suggests an A9V. Qian *et al.* (2018) proposed a classification scheme based on a star's T_{eff}. Stars with T_{eff} between 6700 and 8500 K, like V1116 Her, are considered normal δ Scuti (NDST) stars, while cooler ones are classified as unusual and cool variable (UCV) stars.

Table 4. Fundamental frequency (f_0 = d^{-1}), corresponding harmonics and combinations detected following DFT analysis of time-series photometric data (TESS) from V1116 Her.

	Freq. (d^{-1})	*Freq. Error**	*Amp. (mag.)*	*Amp. Error**	*Phase*	*Phase Error**	*SNR*
f_0	10.5610	0.0001	0.0728	0.0003	0.8603	0.0007	573.4
$2f_0$	21.1232	0.0001	0.0120	0.0001	0.0120	0.0004	171.8
f_1	13.7807	0.0002	0.0047	0.0001	0.8935	0.0011	49.2
$3f_0$	31.6857	0.0002	0.0043	0.0001	0.5055	0.0012	58.7
f_2	16.1968	0.0002	0.0037	0.0001	0.4487	0.0018	24.7
f_3	10.5360	0.7676	0.0022	0.0001	0.0857	0.2598	17.3
$4f_0$	42.2462	0.0005	0.0016	0.0001	0.4255	0.0041	33.1
$f_1 - f_0$	3.2181	0.0005	0.0015	0.0001	0.2359	0.0033	26.4
$f_0 + f_1$	24.3412	0.0007	0.0012	0.0001	0.7667	0.0049	10.3
f_4	10.5933	0.9934	0.0011	0.0004	0.8033	0.2662	11.4
f_5	18.4063	0.0009	0.0011	0.0001	0.6250	0.0052	11
$f_0 + f_2$	26.7573	0.0512	0.0011	0.0002	0.2684	0.0421	10.7
$f_2 - f_0$	5.6362	0.0007	0.0011	0.0001	0.4879	0.0048	15.6

3.3. Light curve analysis by Discrete Fourier Transformation

Discrete Fourier transformation (DFT) was performed using Period04 (Lenz and Breger 2005). This provided the fundamental mode pulsating frequency (spectral window = 100 d^{-1}).

Successive steps employed pre-whitening to remove the previous most significant signals to look for oscillations within the residuals. This analysis was performed on the BVR_cI_c data from the SO measurements. However, the TESS data are so precise that they produced the most detailed Fourier analysis. According to Baran *et al.* (2015) and Baran and Koen (2021), the detection threshold for frequencies derived from space-based photometry is significantly higher (S/N ≥ 5.4) than that

Table 5. Global stellar parameters for V1116 Her using values reported from observations at SO and those predicted from evolutionary modelling (PARSEC).

Parameter	*PARSEC*[a]	*PARSEC*[b]	*SO*
Mean T_{eff} [K]	7722 ± 278	7722 ± 278	7722 ± 278
Mass [$M_{\odot}$]	1.97 ± 0.03	1.55 ± 0.04	2.02 ± 0.04
Radius [$R_{\odot}$]	2.55 ± 0.09	2.61 ± 0.06	2.60 ± 0.21
Luminosity [$L_{\odot}$]	21.65 ± 1.74	21.65 ± 1.74	21.65 ± 1.74
rho [g/cm^3]	0.168 ± 0.018	0.123 ± 0.008	0.164 ± 0.041
log g [cgs]	3.92 ± 0.07	3.80 ± 0.02	3.92 ± 0.07
Q [d]	0.032 ± 0.002	0.028 ± 0.001	0.032 ± 0.003
Age [Gyr]	0.934 ± 0.040	1.76 ± 0.01	—

[a] *Bressan* et al. *(2012), Z = 0.020.* [b] *Bressan* et al. *(2012), Z = 0.004.*

typically used for ground-based measurements (S/N ≥ 4). Analysis of the TESS data yielded the 13 frequency components listed in Table 4. Uncertainties in frequency, amplitude, and phase were all estimated using the Monte Carlo simulation (n = 400) routine built into Period04. The column at the left is the authors' assignment of each component as a fundamental mode, f_0, harmonic, nf_0 (n = 1–4), or combination frequency.

The pre-whitening process uncovered two additional oscillation modes, f_3 and f_4, very close to the fundamental mode frequency but with comparatively low amplitudes. Figure 6 includes a spectral window and power spectrum plots for all statistically signficant (n = 13) frequency components revealed by Period04.

Collectively, the results strongly indicate that V1116 Her is not a simple monoperiodic radial pulsator. The presence of at least two other independent oscillations at 13.7807^{-1} (f_1) and 16.1968 d^{-1} (f_2) are diagnostic (Stellingwerf 1979) for radial modes at the first ($P_1/P_0 = 0.766$) and second overtones ($P_2/P_0 = 0.652$), where P_0, P_1, and P_2 are the fundamental mode, first overtone, and second overtone periods (d). The spectral window and amplitude spectra derived from the B-, V-, R_c-, and I_c-passbands are not included since they are essentially redundant with respect to the fundamental mode frequency (10.5610 d^{-1}) out to the third harmonic. These ground-based observations did not consistently reveal the first overtone (f_1), and failed to show f_3, f_4, or any of the other independent oscillations beyond $3f_0$. It is unlikely that f_3 and f_4 are rotationally split components of the fundamental mode (f_0), which has been shown to be radial according to the diagnostic calculation ($P_1/P_0 = 0.77$) attributed to Stellingwerf (1979). A more likely explanation is that f_3 and f_4 are low amplitude non-radial modes which are close in frequency to the fundamental radial mode. Additional high resolution spectroscopy designed to establish the rotational velocity of V1116 Her along with high cadence multi-bandpass photometry would prove useful in this regard.

3.4. Global Parameters

Absolute V_{mag} (M_V) was calculated (1.374 ± 0.087) after substituting the Gaia EDR3 distance (907.2 ± 19.1 pc), the observed value for m ($V_{avg} = 11.306 \pm 0.026$), and interstellar reddening ($A_V = 0.143 \pm 0.003$) into the reddening corrected distance modulus:

$$d(pc) = 10^{(m - M_V - A_V + 5)/5}. \qquad (5)$$

The luminosity of V1116 Her in solar units ($L_* = 21.65 \pm 1.74\ L_{\odot}$) was calculated according to:

$$L_*/L_{\odot} = 10^{((M_{bol\odot} - M_{bol*})/2.5)}, \qquad (6)$$

where $M_{bol\odot} = 4.74$ and $M_{bol*} = 1.401 \pm 0.087$. Finally, the radius of V1116 Her in solar units ($R_* = 2.60 \pm 0.21$) was estimated using the well-known relationship where:

$$L_* / L_{\odot} = (R_* / R_{\odot})^2\ (T_* / T_{\odot})^4. \qquad (7)$$

The mass of a single isolated field star is very challenging to determine directly. Nonetheless, according to a model using MS stars in detached binary systems, Eker *et al.* (2018) developed a mass-luminosity relationship ($1.05 < M/M_{\odot} \leq 2.40$) according to the following equation:

$$\log(L) = 4.329\ (\pm 0.087) \cdot \log(M) + 0.010\ (\pm 0.019). \qquad (8)$$

This expression leads to a mass ($M_* = 2.046 \pm 0.041$) in solar units as derived from Equation 7 where $L_* = 21.65 \pm 1.74\ L_{\odot}$. All of these values ($M_*$, R_*, L_*, and T_{eff}) summarized in Table 5 fall well within expectations for a HADS variable. Furthermore, stellar radius was independently estimated from an empirically derived period-radius (P-R) relationship reported by Laney *et al.* (2003) for HADS and classical Cepheids:

$$\log(R_*) = a + b \cdot \log(P) + c, \qquad (9)$$

where a = 1.106 ± 0.012, b = 0.725 ± 0.010, and c = 0.029 ± 0.024. In this case the value for R_* ($2.47 \pm 0.38\ R_{\odot}$) was somewhat smaller than the value derived from observations at SO ($2.60 \pm 0.21\ R_{\odot}$).

Results obtained for density ($\rho_{\odot}$), surface gravity (log g), and pulsation constant (Q) are also included in Table 5. Stellar density (ρ_*) in solar units (g/cm^3) was calculated according to:

$$\rho_* = 3 \cdot M_* \cdot m_{\odot} / (4\pi\ (R_* \cdot r_{\odot})^3), \qquad (10)$$

where $m_{\odot}$ = solar mass (g), $r_{\odot}$ = solar radius (cm), M_* is the mass, and R_* the radius of V1116 Her in solar units. Using the same algebraic assignments, surface gravity (log g) was determined by the following expression:

$$\log g = \log\ (M_* \cdot m_{\odot} \cdot G) / (R_* \cdot r_{\odot})^2). \qquad (11)$$

In Equation 11, the gravitational constant G = 6.67408×10^8 cm^3 g^{-1} sec^{-2}.

When attempting to characterize p-mode pulsations (radial) it is helpful to introduce the concept of a pulsation constant (Q). The dynamical time that it takes a p-mode acoustic wave to internally traverse a star is related to its size but more accurately the mean density. The mean density of an isolated field star like V1116 Her can not be determined without great difficulty. However, it can be expressed in terms of other measurable stellar parameters where:

$$\log(Q) = -6.545 + \log(P) + 0.5 \log(g) + 0.1 M_{bol} + \log(T_{eff}). \qquad (12)$$

The full derivation of this expression is provided in Breger (1990). The resulting Q values (Table 5) derived from observations at SO are consistent with theory (Q = 0.032 d) and the distribution of Q-values (0.03–0.04 d) from fundamental mode radial pulsations observed with other δ Sct variables (Breger 1979; Joshi and Joshi 2015; Antonello and Pastori 1981).

Finally, we attempted to get a relative sense of how the physical size, temperature, and brightness of V1116 Her change over the course of a single 2.27-hour pulsation. As shown in Figure 5 there is a significant increase in reddening (B–V) as maximum light descends to minimum light. Intrinsic color reveals that at maximum light, where $(B–V)_0 = 0.163 \pm 0.035$, the corresponding effective temperature is 7997 ± 79 K, whereas at minimum light ($(B–V)_0 = 0.235 \pm 0.021$) the estimated effective temperature is 7565 ± 76 K. Between these two extremes the putative rise in temperature (+433 K) would correspond to a 1.3-fold increase in luminosity but only a relatively small increase ($+0.05\,R_\odot$) in radius. Should radial velocity data become available for this system over an entire oscillation cycle, this rather crude estimate for changes in stellar radius would be best performed using the Baade-Wesselink method developed by Wesselink (1946).

3.5. Evolutionary status of V1116 Her

Now armed with reasonable estimates for luminosity and the effective temperature of V1116 Her, we can attempt to describe the evolutionary status of this variable. These values are plotted in the theoretical Hertzsprung-Russell diagram (HRD) shown in Figure 7. Here, the thick solid line gives the ZAMS position for stars with solar metallicity while two broken lines nearly perpendicular to the ZAMS delimit the blue and red edges of the theoretical instability strip for radial low-p modes (Xiong *et al.* 2016). Asterisks mark the positions of several known HADS, ostensibly both δ Sct and SX Phe types (Balona 2018). The filled circle indicates the position of V1116 Her using the SO derived parameters and corresponding error estimates provided in Table 4. To determine the mass and age of V1116 Her from theoretical evolutionary tracks its metallicity, Z, needs to be known. Unfortunately, this star has not been observed with a high resolution spectrograph so no direct measurement of Z exists, however, we can at least try to estimate its value indirectly. Its distance from the galactic plane (~567 pc) favors a thick disc membership rather than halo. It can therefore be assumed that V1116 Her approaches solar metallicity, or at most a few times lower, which also corresponds to the metallicity of metal-rich globular clusters classified as Oosterhoff type I.

Ironically, a true value for the metallicity of our closest star remains a point of contention. The numbers obtained in the last few decades range between 0.012 and 0.020. Asplund *et al.* (2009) proposed a value where $Z_\odot = 0.0142$. However, von Steiger and Zurbuchen (2016) questioned this result and obtained the value of Z_sun = 0.0196 ± 0.0014 based on the analysis of the chemical composition of the solar wind. Soon thereafter, Serenelli *et al.* (2016) showed that the derived composition is in serious disagreement with observables from the basic solar model so it cannot be representative of the solar interior. Obviously, the problem of a definitive value for $Z_\odot$ still remains an open question. Two different PARSEC evolutionary models (Bressan *et al.* 2012) are plotted in Figure 7: the red solid lines show the models when Z = 0.020 and blue solid lines define the models with Z = 0.004. The latter models would correspond to a decrease in metallicity by a factor of 3 to 5 depending on the reference solar metallicity. Opacity (absorption properties in the gas phase) was estimated according to the solar distribution of heavy metals adopted from Caffau and Ludwig (2007) and Caffau *et al.* (2007, 2008a, 2008b, 2009, 2010, 2011) where Z≃0.0152. Assuming Z = 0.020, it can be seen (Figure 7) that V1116 Her has a solar mass of 1.97 ± 0.03, solar radius of 2.55 ± 0.09, and an average age of 0.932 ± 0.040 Gyr. Alternatively, a metal-poor (Z = 0.004) star would likely be slightly larger ($R_\odot = 2.61 \pm 0.06$), less massive ($M_\odot = 1.55 \pm 0.04$), and older (1.76 ± 0.01 Gyr). Under these conditions V1116 Her would fall in the HR diagram region where evolutionary tracks of low metallicity stars zigzag due to a stellar contraction near the end of hydrogen burning in the core. Uncertainty in the determination of mass will hopefully improve in the future should high resolution spectroscopic data become available for the V1116 Her.

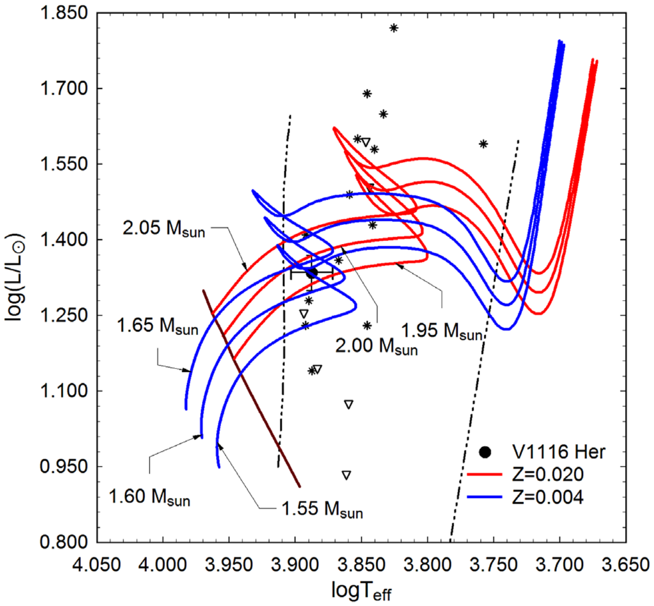

Figure 7. Evolutionary tracks (red solid line: Z = 0.020 and blue solid line: Z = 0.004) derived from PARSEC models (Bressan *et al.* 2012) showing position of V1116 Her (black filled circle) relative to ZAMS (thick maroon line) within the theoretical instability strip (dashed lines) for radial low degree p-mode pulsators. Asterisks denote the positions of known HADS, while open triangles indicate the position of SX Phe pulsators (Balona 2018).

4. Conclusions

This first multi-color (BVR_cI_c) CCD study of V1116 Her has produced 206 new times of maximum which lead to an updated linear ephemeris. Potential changes in the pulsation period assessed using the observed and predicted times of maximum suggest that since 1999 no significant change has occurred. Deconvolution of time-series photometric data by discrete Fourier transformation indicates that V1116 Her is a multi-mode radial pulsator dominated by a fundamental mode oscillation ($f_0 \simeq 10.5610\,d^{-1}$) with three other harmonics ($2f_0$–$4f_0$). The existence of two other independent oscillations at 13.7807 d^{-1}

(f_1) and 16.1968 d^{-1} (f_2) are diagnostic (Stellingwerf 1979) for radial modes at the first ($P_1/P_0 = 0.766$) and second overtones ($P_2/P_0 = 0.652$), where P_0, P_1, and P_2 are the fundamental mode, first overtone, and second overtone periods (d). Our adopted T_{eff} (7792 ± 278 K) was consistent with spectral results from the Large Sky Area Multi-Object Fiber Spectroscopic Telescope (LAMOST) survey (Zhao *et al.* 2012) which classified this intrinsic variable as A7V. The fundamental mode pulsation period (0.094682 d), oscillation mode (radial), V_{mag} amplitude (0.275 mag), and LC morphology are all consistent with the defining characteristics of a HADS variable. These criteria alone do not necessarily exclude the possibility that V1116 Her is an example of a field SX Phe-type pulsator. In this case, the estimated mass of V1116 Her (2.01–2.09 $M_\odot$) according to Eker *et al.* (2018) exceeds the generally accepted threshold ($M < 1.3\,M_\odot$) for SX Phe stars (McNamara 2011). Furthermore, evolutionary tracks from the PARSEC model which assume near-solar abundance ($Z = 0.020$) for V1116 Her are best matched by a MS star with a mass of $1.97 \pm 0.03\,M_\odot$ and radius of $2.55 \pm 0.09\,R_\odot$. Given these results, the sum total of evidence points to a HADS rather than an SX Phe variable. Not unexpectedly, Fourier analysis of highly precise light curve data acquired during the TESS satellite mission uncovered pulsation modes not detected from our ground-based observatory.

5. Acknowledgements

Critical data and references related to V1116 Her were identified in the International Variable Star Index (VSX) maintained by the AAVSO. The CDS/VizieR web site (https://vizier.cds.unistra.fr/viz-bin/VizieR) operated at Centre de Données astronomiques de Strasbourg, France proved to be a valuable portal for access to such databases as Gaia DR2, Gaia EDR3, TESS, and other sources. The Gaia DR2 data can be found at http://vizier.cds.unistra.fr/viz-bin/VizieR?-source=I/345/gaia2, and the Gaia EDR3 at http://vizier.cds.unistra.fr/viz-bin/VizieR-2?-source=I%2F350%2Fgaiaedr3&. Publicly-accessible data from LAMOST were also used. The Guoshoujing Telescope (the Large Sky Area Multi-Object Fiber Spectroscopic Telescope LAMOST) is a National Major Scientific Project built by the Chinese Academy of Sciences with funding for the project from the National Development and Reform Commission. LAMOST is operated and managed by the National Astronomical Observatories, Chinese Academy of Sciences. The diligence and dedication shown by all associated with these organizations is very much appreciated.

This work has made use of data from the European Space Agency (ESA) mission Gaia (https://www.cosmos.esa.int/gaia), processed by the Gaia Data Processing and Analysis Consortium (DPAC, https://www.cosmos.esa.int/web/gaia/dpac/consortium). Funding for the DPAC has been provided by national institutions, in particular the institutions participating in the Gaia Multilateral Agreement.

This paper includes data collected by the TESS mission and obtained from the MAST data archive at the Space Telescope Science Institute (STScI). STScI is operated by the Association of Universities for Research in Astronomy, Inc., under NASA contract NAS 5-26555.

We gratefully acknowledge the careful review and helpful commentary provided by the *JAAVSO* referees and editors.

References

Amôres, E. B., and Lépine, J. R. D. 2005, *Astron. J.*, **130**, 659.

Amôres, E. B., and Lépine, J. R. D. 2007, *Astron. J.*, **133**, 1519.

Amôres, E. B., *et al.* 2021, *Mon. Not. Roy. Astron. Soc.*, **508**, 1788.

Antonello, E., and Pastori, L. 1981, *Publ. Astron. Soc. Pacific*, **93**, 237.

Asplund, M., Grevesse, N., Sauval, A. J., and Scott, P. 2009, *Ann. Rev. Astron. Astrophys.*, **47**, 481.

Baade, W. 1956, *Publ. Astron. Soc. Pacific*, **68**, 5.

Baglin, A. 2003, *Adv. Space Res.*, **31**, 345.

Balona, L. A. 2018, *Mon. Not. Roy. Astron. Soc.*, **479**, 183.

Baran, A. S., and Koen, C. 2021, *Acta Astron.*, **71**, 113.

Baran, A. S., Koen, C., and Porkrzywka, B. 2015, *Mon. Not. Roy. Astron. Soc.*, **448**, L16.

Bedding, T. R., *et al.* 2020, *Nature*, **581**, 147.

Berry, R., and Burnell, J. 2005,*The Handbook of Astronomical Image Processing*, 2nd ed., Willmann-Bell, Richmond, VA.

Breger, M. 1979, *Publ. Astron. Soc. Pacific*, **91**, 5.

Breger, M. 1990, *Delta Scuti Newsl.*, **2**, 13.

Breger, M. 2000, *Baltic Astron.*, **9**, 149.

Bressan, A., Marigo, P., Girardi, L., Salasnich, B., Dal Cero, C., Rubele, S., and Nanni, A. 2012, *Mon. Not. Roy. Astron. Soc.*, **427**, 127.

Caffau, E., and Ludwig, H. -G. 2007, *Astron. Astrophys.*, **467**, L11.

Caffau, E., Ludwig, H. -G., Bonifacio, P., Faraggiana, R., Steffen, M., Freytag, B., Kamp, I., and Ayres, T. R. 2010, *Astron. Astrophys.*, **514A**, 92.

Caffau, E., Ludwig, H. -G., Steffen, M., Ayres, T. R., Bonifacio, P., Cayrel, R., Freytag, B., and Plez, B. 2008b, *Astron. Astrophys.*, **488**, 1031.

Caffau, E., Ludwig, H. -G., Steffen, M., Freytag, B., and Bonifacio, P. 2011, *Sol. Phys.*, **268**, 255.

Caffau, E., Maiorca, E., Bonifacio, P., Faraggiana, R., Steffen, M., Ludwig, H. -G., Kamp, I., and Busso, M. 2009, *Astron. Astrophys.*, **498**, 877.

Caffau, E., Sbordone, L., Ludwig, H. -G., Bonifacio, P., Steffen, M., and Behara, N. T. 2008a, *Astron. Astrophys.*, **483**, 591.

Caffau, E., Steffen, M., Sbordone, L., Ludwig, H. -G., and Bonifacio, P. 2007, *Astron. Astrophys.*, **473**, L9.

Chevalier, C. 1971, *Astron. Astrophys.*, **14**, 24.

Cox, J. P. 1963, *Astrophys. J.*, **138**, 487.

Eker, Z., *et al.* 2018, *Mon. Not. Roy. Astron. Soc.*, **479**, 5491.

Gaia Collaboration, *et al.* 2018, *Astron. Astrophys.*, **649A**, 1.

Gilliland, R. L., *et al.* 2010, *Publ. Astron. Soc. Pacific*, **122**, 131.

Guzik, J. A. 2021, *Frontiers Astron. Space Sci.*, **8**, 1.

Henden, A. A., Levine, S. E., Terrell, D., Smith, T. C., and Welch, D. L. 2011, *Bull. Amer. Astron. Soc.*, **43**.

Henden, A. A., Terrell, D., Welch, D., and Smith, T. C. 2010, *Bull. Amer. Astron. Soc.*, **42**, 515.

Henden, A. A., Welch, D. L., Terrell, D., and Levine, S. E. 2009, *Bull. Amer. Astron. Soc.*, **41**, 669.

Hoffmeister, C. 1935, *Astron. Nachr.*, **255**, 401.

Holdsworth, D. L., *et al.* 2014, *Mon. Not. Roy. Astron. Soc.*, **439**, 2078.

ImagesPlus. 2020, ImagesPlus Ver. 6.5 (http://www.mlunsold.com).

Joshi, S., and Joshi, Y. C 2015, *J. Astrophys. Astron.*, **36**, 33.

Kafka, S. 2021, Observations from the AAVSO International Database (https://www.aavso.org/data-download).

Kazarovets, E.V., Samus, N. N., Durlevich, O. V., Kireeva, N. N., and Pastukhova, E. N. 2008, *Inf. Bull. Var. Stars*, No. 5863, 1.

Khruslov, A. V. 2006, *Inf. Bull, Var. Stars*, No. 5699, 1.

Kochanek, C. S., *et al.* 2017, *Publ. Astron. Soc. Pacific*, **129**, 104502.

Laney, C. D., Joner, M., and Rodriguez, E. 2003, in *Interplay of Periodic, Cyclic and Stochastic Variability in Selected Areas of the H-R Diagram*, ed. C. Sterken. Astron. Soc. Pacific Conf. Ser. 292, Astronomical Society of the Pacific, San Francisco, 203.

Leavitt, H. S., and Pickering, E. C. 1912, *Harvard Coll. Obs. Circ.*, **173**, 1.

Lee, Y.-H., Kim, S. S., Shin, J., Lee, J., and Jin, H. 2008, *Publ. Astron. Soc. Japan*, **60**, 551.

Lenz, P., and Breger, M. 2005, *Commun. Asteroseismology*, **146**, 53.

Lindegren, L., *et al.* 2016, *Astron. Astrophys.*, **595A**, 4.

McNamara, D. H. 2000, in *Delta Scuti and Related Stars, Reference Handbook and Proceedings of the 6th Vienna Workshop in Astrophysics*, eds. M. Breger, M. Montgomery, Astron. Soc. Pacific Conf. Ser., 210, Astronomical Society of the Pacific, San Francisco, 373.

McNamara, D. H. 2011, *Astron. J.*, **142**, 110.

Minor Planet Observer. 2010, MPO Software Suite (http://www.minorplanetobserver.com), BDW Publishing, Colorado Springs.

Niu, J.-S., Fu, J.-N., and Zong, W.-K. 2013, *Res. Astron. Astrophys.*, **13**, 1181.

Niu, J.-S., *et al.* 2017, *Mon. Not. Roy. Astron. Soc.*, **467**, 3122.

Paunzen, E., and Vanmunster, T. 2016, *Astron. Nachr.*, **337**, 239.

Pecaut, M. J., and Mamajek, E. E. 2013, *Astrophys. J., Suppl. Ser.*, **208**, 9.

Pojmanski, G. 2002, *Acta Astron.*, **52**, 397.

Poretti, E. 2003a, *Astron. Astrophys.*, **409**, 1031.

Poretti, E. 2003b, in *Interplay of Periodic, Cyclic and Stochastic Variability in Selected Areas of the H-R Diagram*, ed. C. Sterken, ASP Conf. Ser. 292, Astronomical Society of the Pacific, San Francisco, 145.

Poro, A., *et al.* 2021, *Publ. Astron. Soc. Pacific*, **133**, 084201.

Qian, S.-B., Li, L.-J., He, J.-J., Zhang, J., Zhu, L.-Y., and Han, Z.-T. 2018, *Mon. Not. Roy. Astron. Soc.*, **475**, 478.

Ricker, G. R., *et al.* 2015, *J. Astron. Telesc. Instrum. Syst.*, **1**, 014003.

Rodríguez, E., and Breger, M. 2001, *Astron. Astrophys.*, **366**, 178.

Schlafly, E. F., and Finkbeiner, D. P. 2011, *Astrophys. J.*, **737**, 103.

Schlafly, E. F., *et al.* 2014, *Astrophys. J.*, **789**, 15.

Schlegel, D. J., Finkbeiner, D. P., and Davis, M. 1998, *Astrophys. J.*, **500**, 525.

Schwarzenberg-Czerny, A. 1996, *Astrophys. J., Lett.*, **460**, L107.

Serenelli, A., Scott, P., Villante, F. L., Vincent, A. C., Asplund, M., Basu, S., Grevesse, N., and Peña-Garay, C. 2016, *Mon. Not. Roy. Astron. Soc.*, **463**, 2.

Smith, T. C., Henden, A. A., and Starkey, D. R. 2011, in *The Society for Astronomical Sciences 30th Annual Symposium on Telescope Science*, Society for Astronomical Sciences, Rancho Cucamonga, CA, 121.

Software Bisque 2019, TheSky professional edition (https://www.bisque.com).

Stellingwerf, R. F. 1979, *Astrophys. J.*, **227**, 935.

Uytterhoeven K., *et al.* 2011, *Astron. Astrophys.*, **534A**, 125.

von Steiger, R., and Zurbuchen, T. H. 2016, *Astrophys. J.*, **816**, 13.

Walker, G., *et al.* 2003, *Publ. Astron. Soc. Pacific*, **115**, 1023.

Wesselink, W. J. 1946, *Bull. Astron. Inst. Netherlands*, **10**, 91.

Woźniak, P. R., *et al.* 2004, *Astron. J.*, **127**, 2436.

Xiong, D. R., Deng, L., Zhang, C., and Wang, K. 2016, *Mon. Not. Roy. Astron. Soc.*, **457**, 3163.

Yang, T.-Z, Sun, X.-Y., Zuo, Z.-Y., and Liu, H.-W. 2021, *Astron. J.*, **161** 27.

Zhao, G., Zhao, Y.-H., Chu, Y.-Q., Jing, Y.-P., and Deng, L.-C. 2012, *Res. Astron. Astrophys.*, **12**, 723.

Ziaali, E., *et al.* 2019, *Physics of Oscillating Stars*, Banyuls-sur-mer, France (DOI 10.5281/zenodo.1494351).

Spectroscopic and Photometric Study of the Asymptotic Giant Branch Star T Cephei

David Boyd
West Challow Observatory, OX12 9TX, UK; davidboyd@orion.me.uk

Received August 2, 2023; revised October 12, 2023; accepted November 1, 2023

Abstract Spectroscopy and photometry of the Asymptotic Giant Branch star T Cephei were recorded concurrently on 36 nights during its 387-day pulsation cycle in 2022. Photometry was used to calibrate all spectra in absolute flux. We report on the variation of B and V magnitudes, B–V color index, spectral type, effective temperature, and Balmer emission line flux during one complete pulsation cycle.

1. Introduction

T Cep is an oxygen-rich Mira star discovered by Ceraski in 1880 (Schmidt 1881). Miras are red giant stars with spectral type M on the Asymptotic Giant Branch (AGB) of the Hertzsprung-Russell diagram (Percy 2007). They are in the final stages of their lives prior to becoming planetary nebulae and eventually white dwarfs. Pulsation in their atmospheres with a typical period of around a year drives mass loss through a slow wind and forms a tenuous outer atmosphere. The temperature in the atmosphere is low enough for molecules such as TiO to form. These molecules absorb light from the stellar continuum in the visual part of the spectrum, causing TiO molecular absorption bands which are a prominent feature in the spectrum of oxygen-rich Miras. During each pulsation cycle the star brightens as more light is emitted in the visual part of the spectrum and its effective temperature rises. This causes some of the TiO molecules to dissociate, reducing the strength of the molecular absorption bands and making its apparent spectral type earlier. As the star fades, it becomes cooler, redder, molecules reform, and its spectral type becomes later. Phase zero of the pulsation cycle in Miras is normally taken as the time of maximum brightness. In some oxygen-rich Miras, emission lines of the hydrogen Balmer series appear around this time then gradually disappear. A comprehensive review of our knowledge about Mira stars is given in Willson and Marengo (2012).

A short introduction to T Cep is given in the "Star of the Year" article in the 2023 *BAA Handbook* (BAA 2023c). An article about T Cep in the December 2021 issue of the BAA Variable Star Circular (Heywood 2021) highlighted its complex behavior during the rise to maximum in recent pulsation cycles (see Figure 1) and invited spectroscopic observations of T Cep as there appeared to be relatively little spectroscopic data available on the star. In response to this invitation, spectra of T Cep were recorded on 36 nights between December 2021 and January 2023, covering the complete 2022 pulsation cycle. B and V magnitudes were measured concurrently with the spectra.

2. Determining the current pulsation cycle epoch and phase

The pulsation cycle of T Cep has been shown to vary in period and amplitude by Isles and Saw (1989). In order to find the current pulsation period, we downloaded V-band magnitude data for the 2019 to 2022 pulsation cycles from the AAVSO International Database (AID; Kloppenborg 2022) as shown in Figure 1. These include data reported by the author for the 2022 cycle and analyzed here. To establish parameters of the current pulsation cycle, we carried out period analyses of these data in groups of cycles using the ANOVA method in Peranso (Paunzen and Vanmunster 2016). Table 1 shows how the mean pulsation period varies depending on how many cycles are included in the analysis. The most recent period of 387 days has been adopted as the current pulsation period for the purpose of calculating the pulsation phase of our 2022 observations. Given the irregular profile of the peak in recent cycles, we used the more clearly defined minima as the basis for defining the epoch and phase of the 2022 cycle. A quadratic polynomial fitted to the lower part of the minimum at the start of this cycle gave the epoch of phase –0.5 as JD = 2459553.2(3).

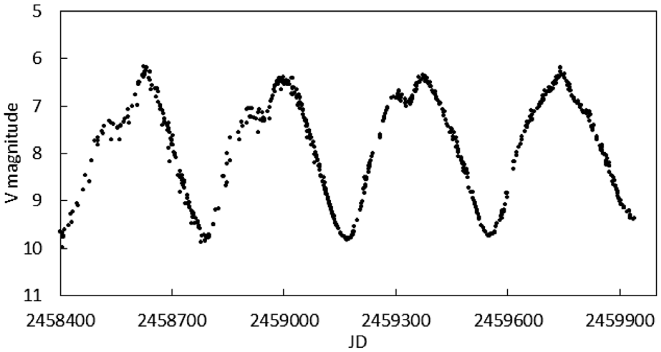

Figure 1. V-magnitude light curve for the 2019 to 2022 pulsation cycles from the AAVSO International Database (cleaned to remove obvious outliers).

Table 1. Fitted pulsation periods for recent pulsation cycles.

Cycles included in analysis	*Fitted pulsation period (d)*
2019–2022	382 ± 2
2020–2022	385 ± 3
2021–2022	387 ± 4

3. Equipment and data reduction

Spectra of T Cep were obtained with a 0.28-m Schmidt-Cassegrain Telescope (SCT) operating at f/5 equipped with an auto-guided Shelyak LISA slit spectrograph and a SXVR-H694

CCD camera. The slit width was 23μ, giving a mean spectral resolving power of ~1000. Spectra were processed with the ISIS spectral analysis software (Buil 2021). Spectroscopic images were bias, dark, and flat corrected, geometrically corrected, sky background subtracted, spectrum extracted, and finally wavelength calibrated using the integrated ArNe calibration source. Each T Cep spectrum was then corrected for instrumental and atmospheric losses by recording the spectrum of a nearby reference star with a known spectral profile from the MILES library of stellar spectra (Falcón-Barroso *et al.* 2011). Each reference star was chosen as close as possible in airmass to T Cep and its spectrum obtained immediately prior to the T Cep spectrum. Typically, ten five-minute guided integrations were recorded for each spectrum of T Cep, giving signal-to-noise ratios ranging from 110 at maximum brightness to 70 at minimum. Spectra were calibrated in absolute flux in FLAM units as erg/cm^2/s/Å using the V magnitudes measured concurrently with the spectra as described in Boyd (2020). All spectra were submitted to, and are available from, the BAA Spectroscopy Database (BAA 2023b).

The distance to T Cep according to Gaia DR2 is 176 –12 +14 parsecs (Gaia Collaboration *et al.* 2018). According to Schlafly and Finkbeiner (2011), the total galactic extinction in the direction towards T Cep is E(B–V) = 0.057. As T Cep lies relatively nearby at galactic latitude +13°, the interstellar extinction it experiences is likely to be considerably smaller than this. Therefore no correction for interstellar reddening is applied to spectra of T Cep.

Each night, while spectra were being recorded, photometry of T Cep was obtained with a 0.35-m SCT operating at f/5 equipped with Astrodon Johnson-Cousins photometric filters and a Starlight Xpress SXVR-H9 CCD camera. All photometric observations were made through alternating B and V filters with typically 10 to 15 images recorded in each filter. Photometric images were bias, dark, and flat corrected and instrumental magnitudes obtained by aperture photometry using the software AIP4WIN (Berry and Burnell 2005). An ensemble of five nearby comparison stars was used whose B and V magnitudes were obtained from the AAVSO Photometric All-Sky Survey (APASS; Henden *et al.* 2021). Instrumental B and V magnitudes were transformed to the Johnson UBV photometric standard using the measured B–V color index and atmospheric airmass with the algorithm published in Boyd (2011). As the star approached peak brightness, exposures had to be shortened to ensure the CCD camera continued to operate in the linear region. These shorter exposures resulted in larger uncertainties on the individual measurements because of scintillation. Magnitude measurements for each night were averaged and nightly mean B and V magnitudes were converted to absolute B- and V-band flux using photometric zero points derived from CALSPEC spectrophotometric standard stars (Bohlin *et al.* 2014; STScI 2021). Times are recorded as Julian Date (JD). All measured magnitudes were submitted to, and are available from, the BAA Photometry Database (BAA 2023a) and nightly means are available in the AAVSO International Database.

4. Photometric observations

Julian Date, pulsation phase, nightly mean B and V magnitudes, and B–V color index for T Cep during the 2022 pulsation cycle are listed in Table 2. Uncertainties in nightly means in B and V range from 0.013 around minimum to 0.043 around maximum. These uncertainties are propagated into the uncertainties in the B–V color index and absolute flux. Nightly mean B and V magnitudes, B–V color indices, and B- and V-band absolute fluxes are plotted vs phase in Figure 2. Uncertainties in B and V magnitudes in Figure 2 are within the plotted symbols.

The pronounced dip in the light curve as the star approaches maximum seen in the previous three years is absent in 2022 and replaced by a flattening of the slope in magnitude and steepening of the slope in flux. While the B and V magnitudes have a broad peak at phase zero, flux peaks more sharply. Figure 3 shows the correlation between B–V color index and V magnitude through the pulsation cycle. The B–V color index reaches its bluest before the magnitude peaks, approximately at the phase where the magnitude dipped in previous years, then reddens as

Table 2. Julian Date, pulsation phase, nightly mean B and V magnitude and B–V color index for T Cep during the 2022 pulsation cycle.

Julian Date	*Phase*	*B (mag)*	*V (mag)*	*B–V (mag)*
2459570	–0.46	11.49	9.49	2.00
2459584	–0.42	11.19	9.22	1.96
2459597	–0.39	10.77	8.85	1.92
2459617	–0.33	9.95	8.17	1.78
2459637	–0.28	9.35	7.66	1.69
2459653	–0.24	8.98	7.33	1.64
2459661	–0.22	8.84	7.23	1.61
2459665	–0.21	8.80	7.19	1.61
2459672	–0.19	8.71	7.12	1.59
2459685	–0.16	8.48	6.96	1.51
2459694	–0.14	8.34	6.80	1.54
2459704	–0.11	8.22	6.70	1.52
2459711	–0.09	8.17	6.61	1.56
2459721	–0.07	8.12	6.52	1.60
2459742	–0.01	7.92	6.27	1.65
2459753	0.02	8.08	6.33	1.75
2459762	0.04	8.20	6.50	1.70
2459770	0.06	8.37	6.68	1.70
2459779	0.08	8.61	6.85	1.76
2459797	0.13	8.64	6.99	1.65
2459804	0.15	8.84	7.14	1.70
2459811	0.17	8.85	7.17	1.68
2459821	0.19	8.97	7.31	1.66
2459840	0.24	9.31	7.64	1.67
2459852	0.27	9.60	7.88	1.72
2459859	0.29	9.74	8.02	1.72
2459870	0.32	10.00	8.23	1.77
2459881	0.35	10.28	8.48	1.80
2459896	0.38	10.68	8.81	1.87
2459904	0.40	10.83	8.99	1.84
2459912	0.43	11.00	9.12	1.88
2459921	0.45	11.14	9.24	1.90
2459928	0.47	11.25	9.30	1.95
2459940	0.50	11.31	9.33	1.98
2459954	–0.47	11.17	9.19	1.98
2459961	–0.45	10.98	9.03	1.95
2459962	–0.45	10.95	9.00	1.96

Note: Uncertainties in nightly means in B and V range from 0.013 around minimum to 0.043 around maximum.

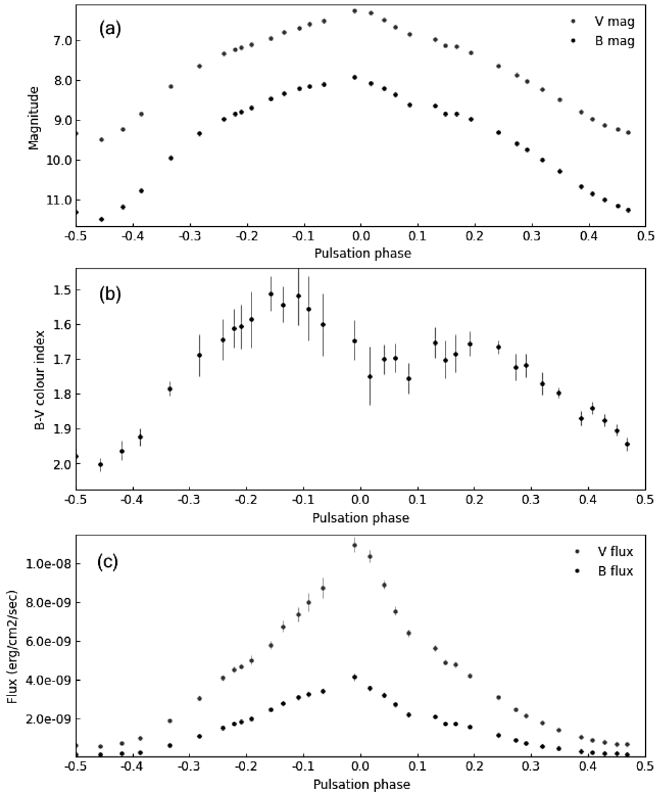

Figure 2. Variation of nightly means of (a) B and V magnitude, (b) B–V color index, and (c) V and B absolute flux with phase during the 2022 pulsation cycle of T Cep. Uncertainties in B and V magnitude are within the plotted symbols.

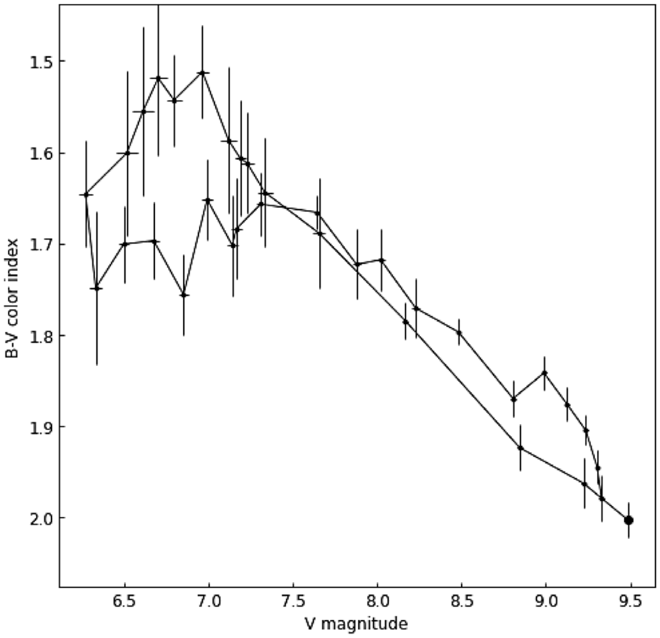

Figure 3. Correlation between B–V color index and V magnitude through the 2022 pulsation cycle of T Cep. The dot marks the beginning of the cycle.

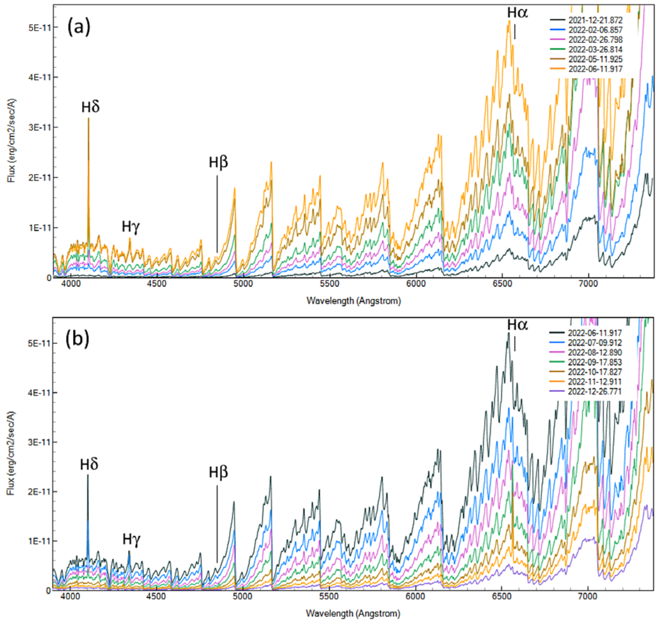

Figure 4. Selected absolute flux calibrated spectra of T Cep (a) on the rise to maximum and (b) on the decline during the 2022 pulsation cycle. The locations of hydrogen Balmer emission lines are marked. The Hδ line is most prominent followed by Hγ, while Hβ and Hα are indistinguishable on this scale.

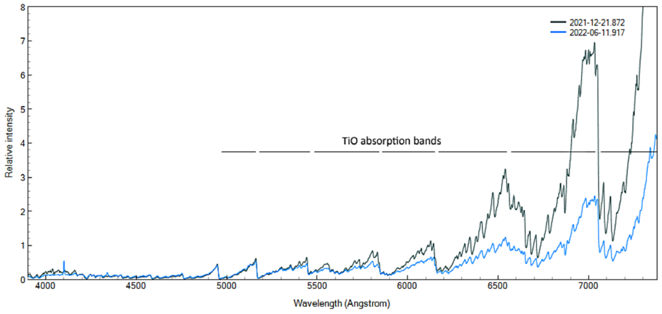

Figure 5. Relative flux spectra of T Cep close to minimum brightness at phase 0.54 (black) and maximum brightness at phase –0.01 (blue), with fluxes mutually normalized in the range 4500 to 5500 Å. The TiO absorption bands indicated are proportionally shallower with increasing wavelength at maximum brightness.

the magnitude peaks before becoming slightly bluer again and finally reddening as the star fades and the cycle ends.

5. Spectroscopic observations

Figure 4 shows two composite plots of selected spectra of T Cep calibrated in absolute flux during the rise and the fall of the 2022 pulsation cycle. The location of hydrogen Balmer emission lines are marked. The M giant spectra are punctuated by TiO absorption bands where molecules in the star's atmosphere absorb some of the light emitted from deeper in the star. These plots are deceptive as they appear to show the TiO bands becoming deeper as the star brightens. To get a truer picture of the relative depth of the bands, Figure 5 shows relative flux spectra close to minimum brightness at phase 0.54 (black) and maximum brightness at phase –0.01 (blue) with fluxes mutually normalized in the range 4500 to 5500 Å. This shows that the TiO absorption bands indicated are proportionally shallower with increasing wavelength at maximum brightness.

Table 3. Julian Date, spectral sub-type, effective temperature (T_{eff}) and Balmer line absolute flux for T Cep spectra recorded during the 2022 pulsation cycle.

Julian Date	*Spectral Sub-Type*	*T_{eff} (K)*	*Hα Line Flux (ergs/cm$_2$/sec)*	*Hβ Line Flux (ergs/cm$_2$/sec)*	*Hγ Line Flux (ergs/cm$_2$/sec)*	*Hδ Line Flux (ergs/cm$_2$/sec)*
2459570	M9.4	2630	0.00E+00	0.00E+00	0.00E+00	1.67E–13
2459584	M9.0	2718	6.41E–14	0.00E+00	0.00E+00	2.86E–13
2459597	M8.4	2845	0.00E+00	0.00E+00	0.00E+00	9.72E–13
2459617	M8.1	2906	0.00E+00	0.00E+00	0.00E+00	4.23E–12
2459637	M8.0	2926	5.59E–13	0.00E+00	3.44E–14	1.39E–11
2459653	M8.0	2926	2.50E–12	0.00E+00	6.98E–13	2.56E–11
2459661	M8.0	2926	0.00E+00	0.00E+00	1.76E–12	5.11E–11
2459665	M8.0	2926	0.00E+00	0.00E+00	2.40E–12	5.52E–11
2459672	M7.9	2946	0.00E+00	0.00E+00	3.28E–12	6.24E–11
2459685	M7.8	2965	0.00E+00	6.86E–14	5.39E–12	7.15E–11
2459694	M7.8	2965	0.00E+00	1.65E–13	7.77E–12	7.03E–11
2459704	M7.5	3022	0.00E+00	6.58E–15	1.39E–11	1.05E–10
2459711	M7.5	3022	8.49E–13	2.40E–13	1.68E–11	1.23E–10
2459721	M7.6	3003	1.56E–12	5.53E–13	1.66E–11	1.07E–10
2459742	M7.5	3022	9.90E–12	1.69E–12	2.50E–11	8.12E–11
2459753	M7.5	3022	1.85E–11	2.97E–12	2.82E–11	7.46E–11
2459762	M7.5	3022	2.31E–11	3.40E–12	2.78E–11	6.24E–11
2459770	M7.5	3022	2.49E–11	2.86E–12	2.36E–11	4.43E–11
2459779	M7.6	3003	2.22E–11	2.49E–12	1.52E–11	2.31E–11
2459797	M7.7	2984	1.80E–11	1.77E–12	6.81E–12	5.37E–12
2459804	M7.7	2984	1.56E–11	1.43E–12	4.92E–12	2.42E–12
2459811	M7.9	2946	2.16E–11	1.11E–12	4.64E–12	2.44E–12
2459821	M7.8	2965	2.16E–11	1.56E–12	6.52E–12	4.91E–12
2459840	M7.9	2946	4.70E–11	3.53E–12	8.84E–12	5.93E–12
2459852	M7.9	2946	5.30E–11	3.83E–12	6.45E–12	2.41E–12
2459859	M8.0	2926	5.13E–11	3.36E–12	4.42E–12	1.06E–12
2459870	M8.0	2926	4.81E–11	3.15E–12	2.67E–12	5.38E–13
2459881	M8.2	2886	4.41E–11	2.85E–12	1.61E–12	7.85E–14
2459896	M8.3	2866	2.93E–11	1.99E–12	6.55E–13	0.00E+00
2459904	M8.7	2782	2.22E–11	1.48E–12	4.73E–13	1.24E–13
2459912	M8.6	2804	1.58E–11	1.08E–12	3.17E–13	0.00E+00
2459921	M8.2	2886	9.53E–12	7.58E–13	8.37E–14	0.00E+00
2459928	M8.4	2845	7.16E–12	4.73E–13	2.61E–14	0.00E+00
2459940	M9.0	2718	3.79E–12	2.19E–13	6.25E–15	0.00E+00
2459954	M8.9	2740	1.72E–12	1.01E–13	0.00E+00	0.00E+00
2459962	M9.0	2718	1.51E–12	6.87E–14	0.00E+00	8.72E–14

Note: Line flux too small to measure is shown as zero. Estimated uncertainty in spectral sub-type is ± 0.2, in T_{eff} is ± 40 K and in line flux is ± 15%.

6. Measuring absolute flux in the Balmer emission lines

The presence of hydrogen emission lines in the spectrum of o Ceti was first mentioned in 1887 by Pickering at Harvard College Observatory (Pickering 1887). Observation of Hδ and Hγ emission in the spectra of Mira stars around maximum brightness was subsequently reported by, among others, Merrill (1921), Frost and Lowater (1923), and Joy (1926), although their cause was not understood. At that time observation of the longer wavelength Balmer lines was hampered by the low red sensitivity of photographic plates. Observation of Hα emission lines using small telescopes with objective prisms and photographic plates chemically sensitized to red light was encouraged by Merrill (1920).

Current understanding is that the hydrogen Balmer emission lines in oxygen-rich Mira stars are caused by shock waves generated deep in the star's atmosphere below the level of molecular absorption as the outward pressure of radiation is countered by the inward pressure of gravity. These shock waves propagate radially outwards, ionizing hydrogen in the atmosphere and driving mass loss. Recombination then generates emission lines that rise above the M-giant continuum as the star passes through its pulsation cycle (Willson 1976; Gillet *et al.* 1983).

To measure the absolute flux in an emission line, we have to subtract the contribution to the flux at that wavelength from the M-giant continuum. Here we describe the process adopted for the Hα line. To establish the M-giant continuum under the Hα Balmer line, we selected those absolute flux spectra which clearly showed no additional emission at that wavelength. We then averaged these spectra to construct a reference continuum spectrum under the Hα line. For each absolute flux spectrum with visible Hα emission, we scaled this Hα reference spectrum so it aligned in flux with the profile of that absolute flux spectrum in regions on either side of the Hα line. The scaled Hα reference spectrum was then subtracted from the absolute flux spectrum to give the absolute flux profile of only the Hα emission line in that spectrum. This was integrated over the wavelengths of the line to give the absolute flux emitted in the Hα line in that spectrum. This process was repeated for the other Balmer lines and for each spectrum. We checked that this procedure was robust against any small changes in the M-giant continuum during the pulsation cycle. The absolute fluxes found for each Balmer line in each of our spectra are listed in Table 3

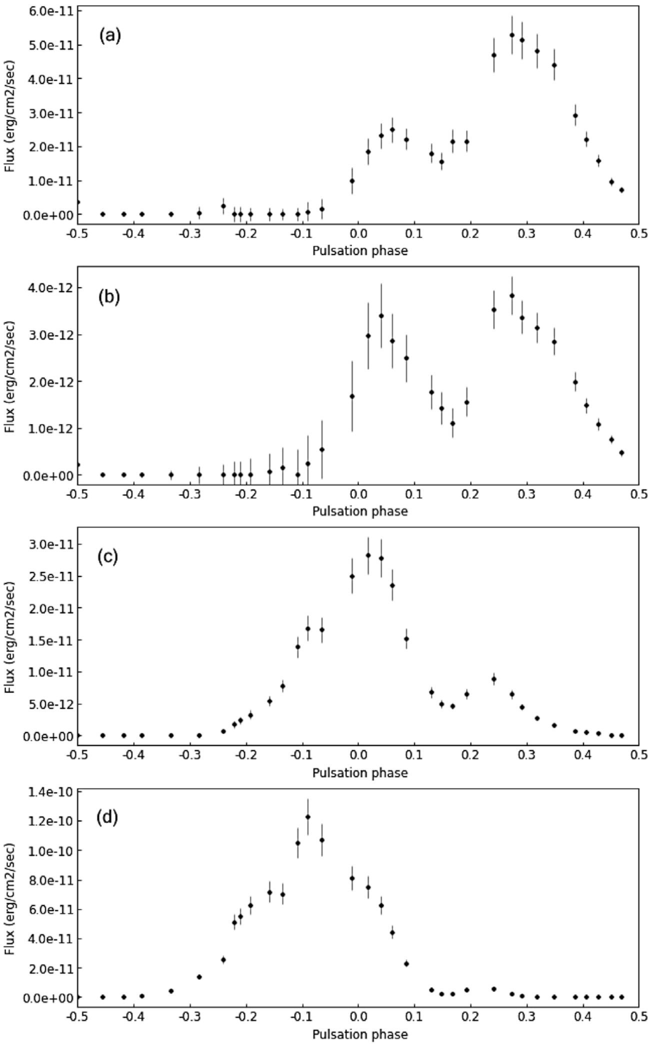

Figure 6. Absolute flux of the (a) Hα, (b) Hβ, (c) Hγ, and (d) Hδ Balmer lines vs pulsation phase. The uncertainties are calculated as described in the text and the average uncertainty for each Balmer line is between 13% and 17%.

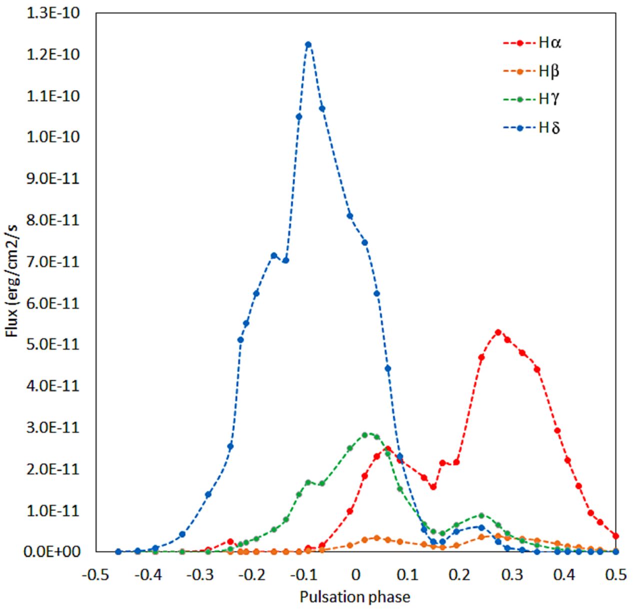

Figure 7. Composite plot showing the variation of absolute flux of the Balmer lines with pulsation phase using a consistent flux scale.

and plotted vs pulsation phase in Figure 6. The uncertainties in each line flux measurement in Figure 6 are a combination of uncertainties in determining the absolute flux level of the continuum in the region of the line and in integrating the line profile over the interpolated continuum level. This uncertainty is calculated for each measurement and the average for each Balmer line is between 13% and 17%.

Figure 7 is a composite plot showing the variation of absolute flux of the Balmer lines with pulsation phase using a consistent flux scale. It is noteworthy that the behavior of these lines in T Cep during its 2022 pulsation cycle is very different from that observed in the oxygen-rich Miras RY Cep and SU Cam (Boyd 2021). Whereas in those stars the behavior of all four Balmer lines was broadly similar with a maximum around the phase of maximum V flux, in T Cep flux in Hδ peaks before the maximum of the cycle while Hα peaks much later, and all lines have double peaks. This points to a more complex phase relationship in the atmosphere of T Cep between propagation of the shock wave and generation of each Balmer line.

7. Assigning a spectral type and effective temperature to each spectrum

The strength of TiO molecular absorption bands in the spectra of oxygen-rich M-giant stars has been used to estimate spectral type (Wing 1992). Because the strength of the molecular bands changes over the pulsation cycle in Mira stars, the spectral type of the star determined in this way will also change. Assigning a spectral type to an individual spectrum is commonly achieved by comparing it morphologically to a range of standard star spectra in the MK spectral classification system and identifying the closest match (Gray and Corbally 2009). MK standard stars available with the MKCLASS stellar spectral classification system (Gray and Corbally 2014) cover the wavelength range 3800–5600 Å, where atomic absorption lines are concentrated, a legacy of the use of blue-sensitive photographic plates in the early days of the MK standard. In our spectra the flux in this region is relatively low, whereas it is considerably stronger towards the red end of the visual range where the molecular bands are prominent. Given our limited spectral resolution and therefore inability to clearly resolve some of the lines in the blue part of the spectrum used for classification, using the full visual range to classify our spectra offers a more practical and robust way of assigning a spectral type.

As all our T Cep spectra fell within range of the M spectral type, we decided to use the M-giant spectra published in Fluks *et al.* (1994), which are classified on the MK system, to assign an apparent spectral type to each spectrum. The Fluks spectra for spectral types M0 to M10 are defined on the wavelength range 3500–10000 Å at an interval of 1 Å. We normalized the flux of each standard spectrum to a mean flux value of unity in the wavelength interval 5610 Å to 5630 Å, which contains no strong spectral features.

To estimate a spectral type for each of our measured spectra, we obtained the closest match between each of our spectra and M-giant standard spectra in the Fluks Spectral Flux Library. To do this we quadratically interpolated all our spectra onto a 1 Å grid, normalized the flux of each spectrum to a mean flux

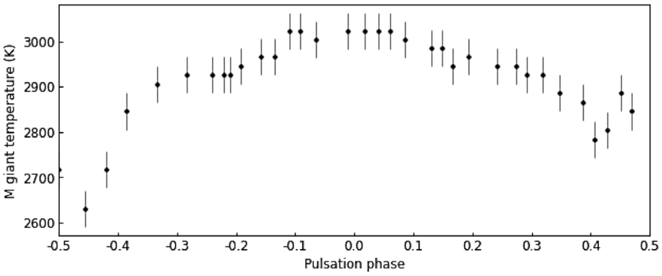

Figure 8. M-giant assigned effective temperatures of T Cep spectra vs pulsation phase.

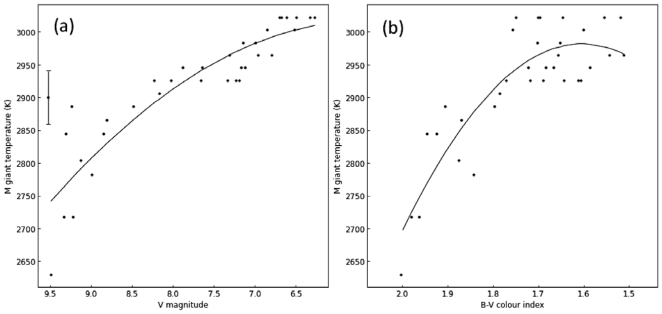

Figure 9. Relationships between M-giant effective temperature of T Cep and (a) V magnitude and (b) B–V color index in the 2022 pulsation cycle. The error bar shows the estimated uncertainty in effective temperature. The lines are quadratic fits to the data but have no physical significance.

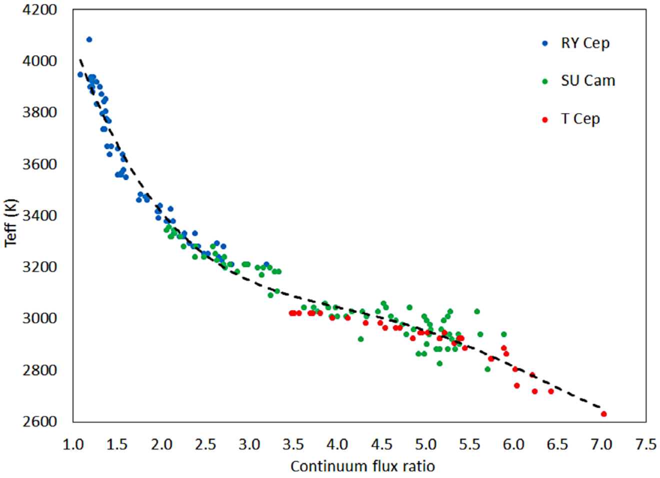

Figure 10. Effective temperature (T_{eff}) vs continuum flux ratio for RY Cep (blue), SU Cam (green), and T Cep (red) spectra plus a fitted fourth-order polynomial.

value of unity in the 5610 Å to 5630 Å wavelength interval, and removed the region of each spectrum around the four Balmer lines. We then computed the total squared flux difference between each of our spectra and each of the standard spectra over the wavelength range 4000 Å to 6600 Å. We identified the spectral type of the standard spectrum which gave the minimum squared flux difference for each of our spectra. We consider this to be the best match integral spectral type. We then fitted a quadratic polynomial to the residuals between the best match integral spectral type and the two adjacent spectral types and used the minimum of this to assign a spectral sub-type to the nearest tenth which best matched each of our spectra. We found the spectral type of T Cep to be M7.5 at phase 0 and M9.4 at phase 0.5. These results are consistent with Keenan *et al.* (1974), who gave the spectral type of T Cep as M6e to M9e.

We calculated mean values of effective temperature for M giant spectral types between M6 and M10 from data given in Fluks *et al.* (1994), van Belle *et al.* (1999), and Gray and Corbally (2009). We then fitted a fourth-order polynomial to these mean effective temperatures as a function of spectral type and used this to assign an effective temperature for each of our spectra based on their assigned spectral sub-type. These assigned spectral sub-types and effective temperatures for our T Cep spectra are listed in Table 3 and the effective temperatures plotted vs pulsation phase in Figure 8. We estimate the uncertainty in assigning a spectral sub-type is ± 0.2 and in assigning an effective temperature is ± 40 K.

The relationships between effective temperature of T Cep and (a) V magnitude and (b) B–V color index are shown in Figure 9. This confirms that B–V color index is a relatively poor indicator of effective temperature in Mira stars. This may be partly due to a relatively weak correlation between the B-band region of the spectrum and the longer wavelength region, which has a strong influence on the calculation of effective temperature.

8. Estimating effective temperature from continuum flux ratios

Wing (1992) introduced the concept of measuring spectral flux of red variables using three narrow-band interference filters with defined passbands to derive an index of TiO band strength which enabled a spectral type to be assigned. A practical difficulty in using this technique for many amateurs, besides the need to purchase these filters, is that the wavelength regions used in this system extend beyond the range of most spectrographs in use by amateurs.

Inspired by the work of Wing, in Boyd (2021) we devised a simpler approach to estimating spectral type which does not require the use of Wing filters. This involves measuring the mean flux in two narrow wavelength regions, 6130–6140 Å and 6970–6980 Å, and calculating their flux ratio. These regions are included in many amateur spectra and are adjacent to TiO molecular band heads so are likely to be as close as possible to the original unabsorbed photospheric continuum. This flux ratio is in effect measuring a color index based on magnitudes corresponding to mean fluxes in these two spectral regions. Because this involves calculating a flux ratio, it does require the spectrum to be calibrated in relative flux across this spectral range but not necessarily in absolute flux. It also requires any interstellar extinction which would affect the continuum slope to have been corrected. We first applied this approach to the Mira stars RY Cep and SU Cam as reported in Boyd (2021), where we found this calculated continuum flux ratio to be strongly correlated to assigned effective temperature and therefore could be used to estimate effective temperature.

To investigate whether this relationship would also hold for T Cep, where our assigned effective temperatures were generally cooler than those of RY Cep and SU Cam, we computed continuum flux ratios as described above for our T Cep spectra. In Figure 10 we combine those new data with our published data for RY Cep and SU Cam and show that a fourth-order polynomial gives a reasonable fit to the data for all three stars. The mean spread in effective temperatures with respect to this polynomial fit is ±38 K, consistent with our estimated uncertainty in effective temperature. It therefore appears that there is a consistent relationship between effective temperature and this continuum flux ratio for three oxygen-rich Miras spanning a temperature range from 2600 K to 4000 K. Whether this relationship holds more widely remains to be seen.

9. Summary

We observed one complete pulsation cycle of the oxygen-rich Mira star T Cep using concurrent spectroscopy and photometry. We used our photometry to calibrate spectra in absolute flux and measured how flux in four Balmer emission lines varied during the cycle. Rather than peaking once around the phase of maximum flux in the pulsation cycle, as we saw in other Mira stars, the Balmer emission lines in T Cep peak twice during each cycle and the phase at which these peaks occur is different for each emission line. We established the likely spectral sub-type of each spectrum by comparison with M-giant spectra on the MK system and used published data to estimate its corresponding effective temperature. We found a consistent relationship for three oxygen-rich Miras between assigned effective temperature and a ratio of fluxes measured at two high points on the spectral continuum.

10. Acknowledgements

The author thanks the anonymous referee for a helpful report which has improved the paper. He is also grateful to Lee Anne Willson for her valuable comments and advice. This research made use of the AAVSO Photometric All-Sky Survey (APASS) and the AAVSO Variable Star Index (VSX). The software developed for this project made extensive use of the Astropy package and the efforts of many contributors to this valuable community resource are gratefully acknowledged. We are also grateful to Tim Lester for his PlotSpectra software which saw everyday use in this project.

This research was made possible through the use of the AAVSO Photometric All-Sky Survey (APASS), funded by the Robert Martin Ayers Sciences Fund and NSF AST-1412587.

References

Berry, R., and Burnell, J. 2005, *The Handbook of Astronomical Image Processing*, Willmann-Bell, Richmond, VA.

Bohlin, Ralph C., Gordon, Karl D., and Tremblay, P.-E. 2014, *Proc. Astron. Soc. Pacific*, **126**, 711.

Boyd, D. 2011, *The Society for Astronomical Sciences 30th Annual Symposium on Telescope Science*, Society for Astronomical Sciences, Rancho Cucamonga, CA, 127 (http://www.socastrosci.org/Publications.html).

Boyd, D. 2020, "A method of calibrating spectra in absolute flux using V magnitudes" (https://britastro.org/sites/default/files/absfluxcalibration.pdf).

Boyd, D. 2021, *J. Amer. Assoc. Var. Star Obs.*, **49**, 157.

British Astronomical Association. 2023a, BAA Photometry Database (https://britastro.org/photdb).

British Astronomical Association. 2023b, BAA Spectroscopy Database (https://britastro.org/specdb).

British Astronomical Association. 2023c, *The Handbook of the British Astronomical Association* (ISSN 0068-130-X).

Buil, C. 2021, ISIS Integrated Spectrographic Innovative Software (http://www.astrosurf.com/buil/isis-software.html).

Falcón-Barroso, J., Sánchez-Blázquez, P., Vazdekis, A., Ricciardelli, E., Cardiel, N., Cenarro, A. J., Gorgas, J., and Peletier, R. F. 2011, *Astron. Astrophys.*, **532A**, 95.

Fluks, M. A., Plez, B., The, P. S., de Winter, D., Westerlund, B. E., and Steenman, H. C. 1994, *Astron. Astrophys, Suppl. Ser.*, **105**, 311 (http://cdsarc.u-strasbg.fr/cgi-bin/Cat?J/A+AS/105/311).

Frost, E. B., and Lowater, F. 1923, *Astrophys. J.*, **58**, 265.

Gaia Collaboration, Brown, A. G. A., *et al.* 2018, *Astron. Astrophys.*, **616A**, 1.

Gillet, D., Maurice, E., and Baade, D. 1983, *Astron. Astrophys.*, **128**, 384.

Gray, R. O., and Corbally, C. J. 2009, *Stellar Spectral Classification*, Princeton Univ. Press, Princeton, NJ.

Gray, R. O., and Corbally, C. J. 2014, *Astron. J.*, **147**, 80 (http://www.appstate.edu/~grayro/mkclass/mkclassdoc.pdf).

Henden, A. A., Templeton, M., Terrell, D., Smith, T. C., Levine, S., and Welch, D. 2021, AAVSO Photometric All-Sky Survey (APASS), data release 10 (https://www.aavso.org/apass).

Heywood, T. L. 2021, *Br. Astron. Assoc. Circ.*, **190**, 8 (https://britastro.org/vss/VSSC190.pdf).

Isles, J. E., and Saw, D. R. B. 1989, *J. Br. Astron. Assoc.*, **99**, 121.

Joy, A. H. 1926, *Astrophys. J.*, **63**, 281.

Keenan, P. C., Garrison, R. F., and Deutsch, A. J. 1974, *Astrophys. J., Suppl. Ser.*, **28**, 271.

Kloppenborg, B. 2022, variable star observations from the AAVSO International Database (https://www.aavso.org/databases).

Merrill, P. W. 1920, *Publ. Astron. Soc. Pacific*, **32**, 318.

Merrill, P. W. 1921, *Astrophys. J.*, **53**, 185.

Paunzen, E., and Vanmunster, T. 2016, *Astron. Nachr.*, **337**, 239.

Percy, J. R. 2007, *Understanding Variable Stars*, Cambridge Univ. Press, Cambridge, UK.

Pickering, E. C. 1887, *Nature*, **36**, 31 (DOI: 10.1038/036031b0).

Schlafly, E. F., and Finkbeiner, D. P. 2011, *Astrophys. J.*, **737**, 103.

Schmidt, J. F. J. 1881, *Astron. Nachr.*, **99**, 87

Space Telescope Science Institute. 2021, CALSPEC.[1]

van Belle, G. T., *et al.* 1999, Astron. J., 117, 521.

Willson, L. A. 1976, *Astrophys. J.*, **205**, 172.

Willson, L. A., and Marengo, M. 2012, *J. Amer. Assoc. Var. Star Obs.*, **40**, 516.

Wing, R. F. 1992, *J. Amer. Assoc. Var. Star Obs.*, **21**, 42.

---

[1] Space Telescope Science Institute. 2021, CALSPEC (https://www.stsci.edu/hst/instrumentation/reference-data-for-calibration-and-tools/astronomical-catalogs/calspec).

X-ray Luminosity Versus Orbital Period of AM CVn Systems

Teja Begari
Hyderabad, India; begariteja@gmail.com

Thomas J. Maccarone
Department of Physics and Astronomy, Texas Tech University, Lubbock, TX 79410-1051; thomas.maccarone@ttu.edu

Received August 3, 2023; revised November 16, 27, 2023; accepted November 29, 2023

Abstract AM CVn systems are a rare type of cataclysmic variable star consisting of a white dwarf accreting material from a low-mass, hydrogen-poor donor star. These helium-rich systems usually have orbital periods that are less than 65 minutes and are predicted to be sources of gravitational waves. We have analyzed the catalogued x-ray data from the Chandra, XMM-Newton, and The Neil Gehrels Swift Observatory (hereafter referred to as "Swift") to investigate the relationship between x-ray luminosity and the orbital period of AM CVn systems. We find that the high accretion-rate systems which are likely to have optically thick boundary layers are sub-luminous in x-rays relative to theoretical model predictions for the boundary layer luminosity, while the longer orbital period, lower bolometric luminosity systems match fairly well to the model predictions, with the exception of an overluminous system which has already been suggested to show magnetic accretion.

1. Introduction

AM CVn stars are binary systems that have very short orbital periods that range from 5 to 65 minutes. These systems consist of white dwarfs accreting material from a Roche lobe-filling companion star that usually is a lower-mass white dwarf star, but occasionally is a helium star. These systems are expected to be strong sources of gravitational waves (Nelemans *et al.* 2004). In this paper, we discuss the relationship between x-ray luminosity and orbital period for a sample of 28 AM CVn systems. We use the data from XMM, Chandra, and Swift observatories for collecting the x-ray flux and obtaining orbital period values from the literature. Studying the relationship between x-ray luminosity and orbital period can provide insights into the accretion process in AM CVn systems and techniques for searching for more of them.

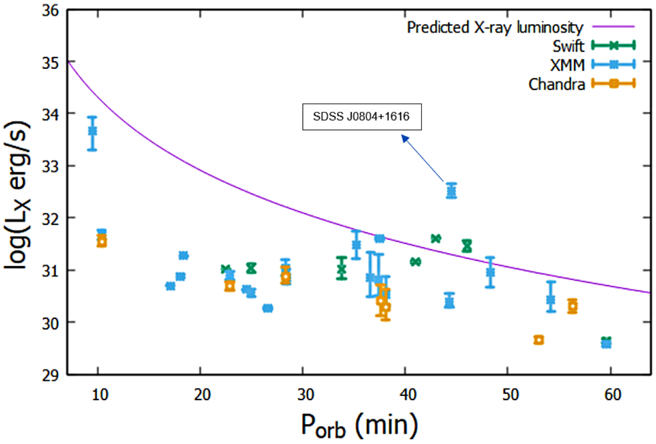

Figure 1. X-ray luminosity versus orbital period of selected AM CVn systems from Table 1.

2. Data and analysis

We collected the x-ray flux from Chandra, XMM-Newton, and Swift for all AM CVn systems listed in Table 1. Using the Chandra Source Catalog (CSC), we collected the flux from 0.5 to 7.0 keV from Release 2.0 (Evans *et al.* 2010). For XMM-Newton, using 4XMM-DR11, we collected the flux from 0.2 to 12.0 keV from Webb *et al.* (2020). For Swift, using the 2SXPS Swift x-ray telescope point source catalogue, we collected the flux from 0.3 to 10.0 keV from Tranin *et al.* (2022). We collected the distances from Gaia parallax measurements corrected for the Gaia zero-point offset, and which used Bayseian analysis to convert the measured parallaxes into inferred distances (Bailer-Jones *et al.* 2021). Using the flux we calculated the x-ray luminosity for each system. We also obtained the orbital periods of these systems from Ramsay *et al.* (2018). For the newly discovered AM CVn system, TIC 378898110, we collected the orbital period, x-ray flux, and the distance from Green *et al.* (2023). In Table 1, we see that a few systems have periods estimated using superhumps. Superhump periods are typically within a few percent of the real periods, which is acceptable for the purposes of comparing luminosities with orbital periods. Using the uncertainty in the distances, we calculated 16% and 84% values for the luminosity. Using these values we made the error bars.

Our primary analysis involved plotting the x-ray luminosity versus the orbital period for the sample of AM CVn systems. Figure 1 shows a comparison between the observational data and a model prediction for x-ray luminosity from van Haaften *et al.* (2012),

$$L = \frac{GM_a}{2R_a} \cdot \frac{48}{5} \cdot \frac{G^{2/3}}{2c^5} \cdot \frac{M_a (9\pi)^2 \cdot 10^{-6} M_\odot R_\odot^3}{\left(M_a + \frac{9\pi \cdot 10^{-3} \sqrt{\frac{M_\odot R_\odot^3}{2G}}}{P_{orb}} \right)^{1/3}} \cdot \frac{(2\pi)^{8/3}}{P_{orb}^{14/3}} \qquad (1)$$

where M_a is the mass of the accretor, P_{orb} is the orbital period, and R_a is the radius of the accretor over the observed data. For plotting the predicted x-ray luminosity, we substituted the value of M_a as 0.8 $M_\odot$ from the work by Wong and Bildsten (2021)and

Table 1. AM CVn systems in this study.

		Log (x-ray luminosity) (erg/sec)			*Distance (parsec)*		
Star System	*P_{orb} (min)*	*XMM*	*Chandra*	*Swift*	*Best Estimate*	*b_{pc} (16%)*	*B_{pc} (84%)*
V407 Vul	9.5	33.66	—	—	4813.76	3214.56	6584.68
ES Cet	10.4	31.67	31.55	—	1786.57	1612.83	2013.34
AM Cvn	17.1	30.7	—	—	300.02	297.24	303.06
SDSS J190817.07+394036.4	18.1	30.88	—	—	968.33	935.96	1004.87
HP Lib	18.4	31.28	—	—	277.91	275.38	280.4
TIC 378898110	20.5	—	—	31.02	309.3	307.5	311.1
CX361	22.9	30.9	30.69	—	963.45	878.92	1058.7
CR Boo	24.5	30.63	—	—	349.55	344.79	353.67
KL Dra	25	30.56	—	31.04	907.92	829.11	985.06
V803 Cen	26.6	30.27	—	—	284.08	279.26	290.12
YZ LMi	28.3	31.04	30.89	—	815.72	694.03	994.31
CP Eri	28.4	30.86	—	—	725.62	623.87	874.06
V406 Hya	33.8	—	—	31.02	753.68	616.76	966.01
SDSS J173047.59+554518.5	35.2	31.49	—	—	1317.93	977.98	1771.03
V558 Vir	36.6 (sh)	30.86	—	—	1548.05	1015.78	2692.72
SDSS J124058.03-015919.2	37.4	30.81	—	—	764.3	544.51	1358.88
NSV1440	37.5 (sh)	31.6	—	—	1861.73	1814.65	1917.21
SDSS J172102.48+273301.2	38.1	30.54	30.29	—	674.02	510.86	997.94
V493 Gem = ASASSN-14mv	41 (sh)	—	—	31.15	247.06	240.59	253.23
QX Eri = ASASSN-14ei	43 (sh)	—	—	31.61	256.89	253.71	259.87
SDSS J152509.57+360054.5	44.3	30.4	—	—	538.6	469.63	639.85
SDSS J080449.49+161624.8	44.5	32.51	—	—	998.97	865.22	1184.42
SDSS J141118.31+481257.6	46	—	—	31.46	452.01	397.95	502.2
SDSS J090221.35+381941.9	48.3	30.96	—	—	709	512.44	976.22
SDSS J120841.96+355025.2	53	—	29.66		210.7	198.89	223.64
SDSS J164228.06+193410.0	54.2	30.42	—	—	554.84	432.7	824.24
SDSS J155252.48+320150.9	56.3	—	30.31	—	422.52	369.72	481.38
SDSS J113732.32+405458.3	59.6	29.58	—	29.64	209.06	199.36	218.5

Notes: b_{pc} and B_{pc} refer to the lower and upper limit in the uncertainty in the the distances, respectively; (sh) indicates that the orbital period was derived from superhumps.

that the luminosity generated in the boundary layer is one-half of the total accretion power, and that all of the boundary layer luminosity goes into x-rays and the evolution of ultra-compact binaries by Nelemans *et al.* (2004); van Haaften *et al.* (2012).

We conduct a Spearman's rank correlation test for the sources that have the orbital period greater than 30 minutes, yielding a correlation coefficient of –0.48235 with a two-tailed p-value of 0.05846. This suggests a marginally significant association between the two variables. If we exclude the system SDSSJ0804+1616 and re-run the test, we obtained rs = –0.575, with a two-tailed p-value of 0.02494, again marginally significant.

Our findings also indicate that, at short orbital periods, the accretion rates are high enough to keep the system in a state at which the system is constantly accreting material from its companion star at a very high rate, where the boundary layer is optically thick. In this regime, the x-rays produced at the white dwarf surface are thermalized into UV photons, leading to suppression of the x-ray emission, as seen in transient outbursts in dwarf novae (Wheatley *et al.* 2003).

Two systems stand out as overluminous relative to the trend of sources at similar orbital periods. One is V407 Vul, the shortest period object, which is a direct impact accretor (Marsh and Steeghs 2002), which may lead to a higher fraction of its accretion power coming out in x-rays. The other is SDSS J0804+1616, which shows a strong magnetic field for the accretor, which may drive its orbital evolution to be faster than that due to gravitational radiation (Maccarone *et al.* 2023).

3. Conclusion

In conclusion, we observe that AM CVn systems with short orbital periods have x-ray luminosities below those from literature model predictions, but which, in hindsight, should have been anticipated given the expectation that bright systems will have optically thick boundary layers. We find a clear anti-correlation between x-ray luminosity and orbital period for the longer orbital period systems, in agreement with the theoretical expectations for the accretion process in these systems.

References

Bailer-Jones, C. A. L., Rybizki, J., Fouesneau, M., Demleitner, M., and Andrae, R. 2021, *Astron. J.*, **161**, 147 (DOI: 10.3847/1538-3881/abd806).

Evans, I. N., *et al.* 2010, *Astrophys. J., Suppl. Ser.*, **189**, 37 (DOI: 10.1088/0067-0049/189/1/37).

Green, M. J., Hermes, J. J., Barlow, B. N., *et al.* 2023, arXiv:2311.01255.

Maccarone, T. J., Kupfer, T., Najera Casarrubias, E., Rivera Sandoval, L., Shaw, A., Britt, C., van Roestel, J., and Zurek, D. 2023, arXiv:2302.12318 (DOI: 10.48550/arXiv.2302.12318).

Marsh, T. R., and Steeghs, D. 2002, *Mon. Not. Roy. Astron. Soc.*, **331**, L7 (DOI: 10.1046/j.1365-8711.2002.05346.x).

Nelemans, G., Yungelson, L. R., and Portegies Zwart, S. F. 2004, *Mon. Not. Roy. Astron. Soc.*, **349**, 181 (DOI: 10.1111/j.1365-2966.2004.07479.x).

Ramsay, G., *et al.* 2018, *Astron. Astrophys.*, **620A**, 141 (DOI: 10.1051/0004-6361/201834261).

Tranin, H., Godet, O., Webb, N., and Primorac, D. 2022, *Astron. Astrophys.*, **657A**, 138 (DOI: 10.1051/0004-6361/202141259).

van Haaften, L. M., Nelemans, G., Voss, R., Wood, M. A., and Kuijpers, J. 2012, *Astron. Astrophys.*, **537A**, 104 (DOI: 10.1051/0004-6361/201117880).

Webb, N. A., *et al.* 2020, *Astron. Astrophys.*, **641A**, 136 (DOI: 10.1051/0004-6361/201937353).

Wheatley, P. J., Mauche, C. W., and Mattei, J. A. 2003, *Mon. Not. Roy. Astron. Soc.*, **345**, 49 (DOI: 10.1046/j.1365-8711.2003.06936.x).

Wong, T. L. S., and Bildsten, L. 2021, *Astrophys. J.*, **923**, 125 (DOI: 10.3847/1538-4357/ac2b2a).

Variability Properties of Red Giants and Supergiants in the AAVSO Binocular Observing Program

John R. Percy
Sandra Zhitkova
Department of Astronomy and Astrophysics, and Dunlap Institute for Astronomy and Astrophysics, University of Toronto, 50 St. George Street, Toronto, ON M5S 3H4, Canada; john.percy@utoronto.ca

Received September 7, 2023; revised October 28, 2023; accepted October 29, 2023

Abstract The AAVSO Binocular Observing Program contains 153 stars, almost all of them red giants (127) or red supergiants (10). In this paper, we use Fourier and light curve analysis of visual and photoelectric observations in the AAVSO International Database to determine periods and amplitudes of these stars. Of the stars analyzed, 110 stars had sufficient data and periodicity to yield results. The stars pulsate in the fundamental and/or first overtone (at least 24 are bimodal); more luminous stars tend to pulsate in the fundamental. In addition, at least 61 of the stars had a "long secondary period" (LSP) 5 to 10 times the pulsation period. We determine and discuss the pulsation and LSP amplitudes. These are known to be variable with time. The variability properties of our stars are determined, to some extent, by the way in which the program stars were originally selected. The results are also affected by the limitations of the data, including limited accuracy of the visual data, seasonal and other gaps in the data, and the complexity of the stars' variability, including time-variable periods and amplitudes.

1. Introduction

There are 153 stars in the AAVSO Binocular Observing Program, for visual and other observers. The majority of them are red giant or supergiant stars. These stars are unstable to radial pulsation, in one or more modes, usually the fundamental and/or first overtone mode.

About a third of such stars also have a "long secondary period" (LSP), 5 to 10 times the pulsation period. The cause of these LSPs was unknown for almost a century. Recently, Soszyński *et al.* (2021) have ascribed them to eclipses by dust-enshrouded companions which were originally planets, but which have subsequently accreted gas and dust from the star, and become brown dwarfs or low-mass stars.

The variability of these stars is complicated in other ways. The periods "wander" by a percent or two, on long time scales. The pulsation amplitudes vary significantly, on time scales of 20 to 30 pulsation periods (Percy and Abachi 2013). The maximum and minimum brightnesses of the large-amplitude Mira stars also vary randomly. Some of these complications may be due to the fact that the outer layers of these stars are dominated by large convection cells.

Despite the success of the Soszyński *et al.* mechanism for explaining the LSP phenomenon, there are still some puzzling aspects. One is the existence of so-called "LSP stars" in the All-Sky Automated Search for Supernovae (ASAS-SN) variable star catalog (https://asas-sn.osu.edu/variables): there are 185 red giants in which the LSP amplitude was much larger than that corresponding to the pulsation period, so the period given in the catalog is the LSP, not the pulsation period, and the star is classified as an LSP star. (The ASAS-SN catalog contains only the dominant period, not multiple periods.) We began a study of some of these LSP stars (Percy and Shenoy 2023). But we realized that there were much more extensive data on red giants in the AAVSO International Database (AID), which would help to put the LSP stars in context. We had previously used some of these data in several studies of LSPs in red giants (e.g. Percy and Diebert 2016; Percy and Leung 2017), but we realized that there was even more information which could be derived.

Most of the stars in the AAVSO Binocular Observing Program have periods given in the program star list, which we refer to as "catalog periods." We decided to use our analyses to re-examine the periods, because some are missing or incorrect. Many stars have LSPs or multiple pulsation modes, so they cannot be described by a single period.

Another important motivation was to provide feedback to the hundreds of AAVSO observers who have contributed the tens of thousands of observations of these stars. What science can be derived from their data? This project also provided an important research experience for co-author Zhitkova, an undergraduate astronomy major.

2. Data and analysis

Visual and photoelectric Johnson V observations were downloaded from the AAVSO website (Kloppenborg 2023) and analyzed carefully using light-curve and time-series routines in the AAVSO VStar software package (Benn 2013). All data were used; the visual and V data were analyzed separately. The V data tend to be recent—from the last decade or two—whereas the visual data may stretch back for many decades. Because of the wandering of the periods, and the different densities of the two datasets, the derived periods from the visual and V data could be slightly different. We generally adopted a weighted mean of the two. The visual and V amplitudes often differed significantly, for various reasons; we have listed both of them separately in Tables 1–3. Note that they are semi-amplitudes, not full amplitudes or max-to-min ranges. Because the pulsation periods "wander" in time, we generally rounded off the pulsation periods to the nearest day.

We occasionally consulted the light curves and other data in the variable star catalog of the ASAS-SN survey (Jayasinghe *et al.* 2018; Jayasinghe *et al.* 2019; Shappee *et al.* 2014).

Absolute K magnitudes, MK, were determined from the GAIA parallaxes and K magnitudes, and corrected for interstellar absorption by converting E(B–V) reddening to K absorption. These data were generally taken from the ASAS-SN variable star catalog. A few stars had highly anomalous E(B–V); MKs are not listed for these stars.

We recognize that our results are affected by the sparseness of the data for some stars, the limited accuracy of the visual observations, especially for red variables (Cadmus 2020), the seasonal and other gaps in the data, and whatever selection effects are present in choosing the stars for the Binocular Observing Program, as well as by the complexity of the stars' variability.

We also suspect that some of the low-amplitude "periods" near one year may be due to the Ceraski effect (Percy 2015), which is a physiological phenomenon which affects visual observations.

3. Results

The results of the analyses are given in Tables 1–3, which list: the star name, the variable star type, the absolute K-magnitude MK, the adopted dominant pulsation period PP, its amplitude in visual and Johnson V, the adopted LSP, and its amplitude in visual and Johnson V. As mentioned, the amplitudes are actually semi-amplitudes, as determined by Fourier analysis, not full max-to-min ranges. There are a total of 110 stars in Tables 1–3.

Some stars showed evidence of bimodal pulsation, generally in the fundamental and first overtone modes. These stars are listed in Table 4, which gives: the star name, the longer pulsation period Pa, the shorter pulsation period Pb, and the ratio Pb/Pa. There are 24 stars in this table.

Figure 1 shows the period-luminosity diagram (MK vs. log P(d)) for the stars in Tables 1–3. Three sequences are seen; from the left, they are: first overtone pulsation period, fundamental pulsation period, and LSP. The sequences are approximately parallel, but the results in Figure 2 indicate that the two pulsation sequences are not exactly parallel. Note that the lower-luminosity stars are more likely to pulsate in the first overtone, whereas higher-luminosity stars are more likely to pulsate in the fundamental.

Figure 2 shows the so-called Petersen diagram for the stars in Table 4: Pb/Pa vs. log Pa. There is some scatter, but the figure is very similar, in placement and slope, to that for a different sample of red giants (Percy and Huang 2015). Note that the analysis of bimodal pulsators has to be done with great care. The Fourier spectra contain alias periods, separated from the true period by multiples of 0.00274 cycle/day, and caused by the seasonal gaps in the data. They may also contain harmonics, with periods of 1/2 or sometimes 1/3 of the true period, and caused by a non-sinusoidal phase curve. For red giants, the first-overtone period is close to 1/2 the fundamental period, so period ratios of 0.50 must be treated with some suspicion. But Figure 2 slopes; it is not horizontal. And, as mentioned, it is consistent with other studies, and with theoretical pulsation models.

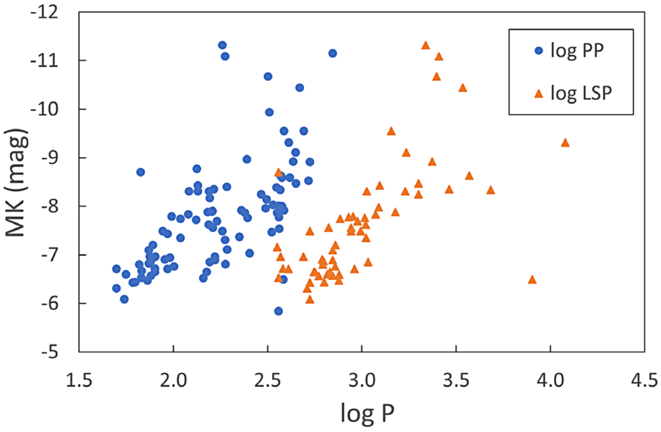

Figure 1: The relationship between the absolute K-magnitude MK and log period. Blue circles correspond to pulsation periods, orange triangles to LSPs. The outliers in the right side are BM Sco and Y Pav.

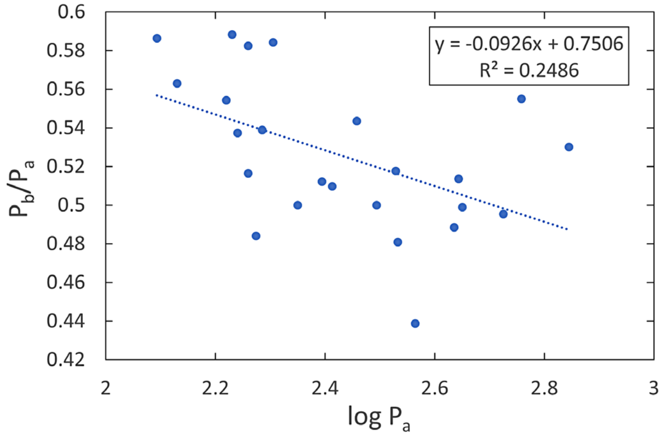

Figure 2: For bimodal pulsators, the relationship between the ratio of the shorter (first overtone) period to the longer (fundamental) period and the logarithm of the latter. The star with the smallest ratio is T Ind.

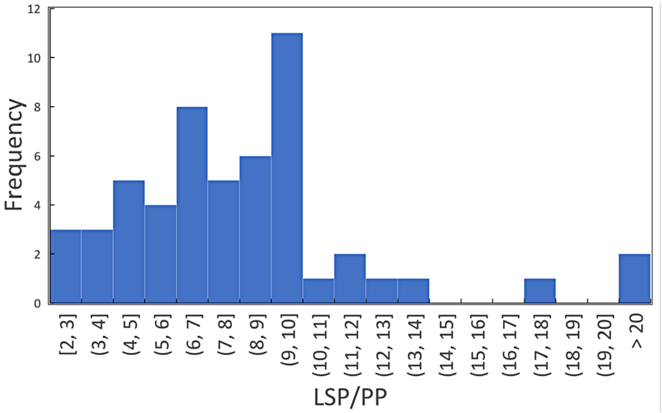

Figure 3: Histogram showing the distribution of the ratios of the LSP to the dominant pulsation period (LSP/PP).

Figure 3 shows a histogram of LSP/PP values. They peak at about 6 and 9, as previous studies have shown, presumably depending on whether the PP is the fundamental or the first overtone. The peak at LSP/PP = 6 is rather flat.

We were curious as to whether these ratios were constant, or a function of the size and luminosity of the star, but we found no such clear trend.

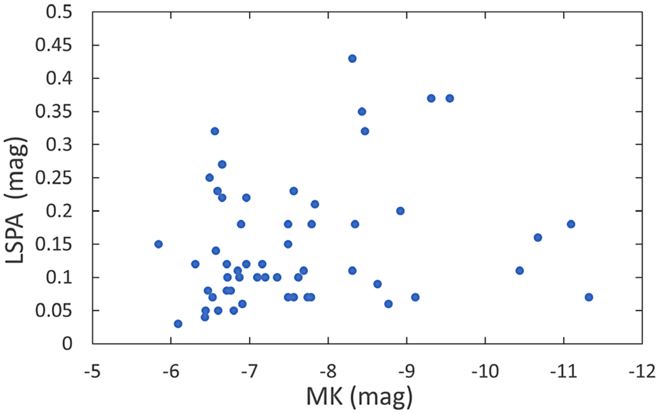

Figure 4: The relationship between the visual LSP semi-amplitude LSPA and the absolute K-magnitude MK.

Figure 4 shows the relation between the LSP semi-amplitude and MK. The data are sparse, but it appears that, on average, amplitudes are smaller in low and high-luminosity stars, and larger for moderate-luminosity ones. This is consistent with results from our parallel study of "LSP stars" in the ASAS-SN database (Percy and Shenoy 2023).

It is generally true that red giant pulsation amplitudes are greater in higher-luminosity stars. In our case, that relation is not clear, but is at least partly a result of the selection of stars in the Binocular Observer Program, which is a mixture of SR, M, and supergiant stars.

The following program stars had insufficient data, or had no obvious periods in the Fourier spectrum or light curves: X Cnc, TU CVn, AG Car, BZ Car, CK Car, EV Car, IX Car, ASAS J110135-6102.9, T Cen, V766 Cen, AR Cep, μ Cap, RR CrB, SV Crv, CH Cyg, AY Dor, CL Hyi, R Lep, CF Mic, SX Mon, X Oph, V407 Pup, WX Ret, UX Sgr, V905 Sco, τ^4 Ser, RX Tel, RW Vir, BK Vir.

3.1 Notes on individual stars

RW Boo There is an ~50-day period in the light curve, so the 407-day period is an LSP.

R Dor This star is possibly bimodal, with periods of 172 and 323 days.

UX Dra This star was initially considered "unsolved." There were three comparable peaks in the Fourier spectrum, separated by approximately 0.00274 cycle/day, suggesting that one or two peaks might be aliases. But the light curve shows evidence of the periods given in Table 1, so those periods may be correct.

U Hya The catalog period is 183 days. The 360-day period that we have derived is also present in the AAVSO light curve. This star may possibly be bimodal.

CE Lyn There appears to be an 50-day period in the ASAS-SN light curve, so the 512-day period that we have derived may be an LSP.

HK Lyr This star may possibly be bimodal, but the evidence is weak.

RV Mon There is some evidence in the Fourier spectrum for an 80-day period, and the catalog period is 121.3 days, so the 355-day period that we have derived may be an LSP. There is also some evidence for this period in the ASAS-SN light curve.

BO Mus The catalog period is 132.4 days, and there is a 134-day period in the light curve. There may be an LSP in the range 1800–2500 days.

GO Peg The catalog period is 79.3 days, and there is a period of this order in the ASAS-SN light curve, so the 382-day period that we have derived may be an LSP.

PV Peg The ASAS-SN light curve shows a time scale of 50–70 days, so the 700-day period that we have derived may be an LSP. The catalog period is 520: days.

BM Sco It is not clear whether the derived period is a pulsation period or an LSP; we think it is the former.

RY UMa There is a 30-day period in the ASAS-SN light curve, so the 284-day period that we have derived may be an LSP. The catalog period is 310 days.

FP Vir There is a 70- to 80-day period in the light curve, so the 373-day period that we have derived may be an LSP.

4. Discussion

Figure 1 can be compared with the P–L relations given by Wood (2000) and Soszyński *et al.* (2021) for stars in the Magellanic Clouds. There are sequences for first overtone (1O) and fundamental (F) mode pulsators, and for LSPs. The 1O and F sequences may appear to be parallel, indicating a constant period ratio, but Figure 2 shows that the period ratio varies slightly. Figure 2 is consistent with period ratios from a different sample of red giants (Percy and Huang 2015) and with theoretical pulsation models (Xiong and Deng 2007).

In Figure 3, the lack of LSP/PP values greater than about 12 is presumably because red giants pulsate primarily in the fundamental and first overtone, with very few in the second overtone, and hardly any in higher overtones. This is consistent with the period-luminosity diagrams given by Wood (2000) and Soszyński *et al.* (2021).

The correlation between the pulsation period and the luminosity in Figure 1 is easy to understand; both depend primarily on the radius of the star. The correlation between the LSP and the luminosity is less easy to understand. The luminosity depends on the radius of the star; the LSP depends on the radius of the dusty companion's orbit. Specifically, the actual relation implies that the latter radius is about two stellar radii, on average (Kim and Percy 2022).

There are stars in Tables 1–3 in which the LSP amplitude is significantly larger than the pulsation amplitudes. The ASAS-SN variable star catalog would have probably determined the dominant period to be the LSP, and classified these as "LSP stars." There are also stars in Tables 1–3 for which the period and the MK suggest that the catalog period is actually the LSP, not a pulsation period. These include the following stars: RW Boo, BM Eri, PV Peg, CI Phe, RY UMa, VW UMa, and GO Vel. There are also stars for which the catalog period differs from ours by a factor of approximately two. In these cases, our analyses and previous ones may have picked up different pulsation modes, the amplitudes of which vary with time.

Tables 1–3 include a few variables which are classified as supergiant (SRc, Lc) variables. In most cases, the MK and

Table 1. Variability properties of red giants and supergiants in the AAVSO Binocular Observing Program.

Star Name	*Type*	*MK*	*PP(d)*	*SA(PP)v*	*SA(PP)V*	*LSP(d)*	*SA(LSP)v*	*LSP(SA)V*
V373 And	SRB	—	202	0.11	—	1067	—	0.12
θ Aps	SRB	–7.35	109	0.14	0.26	1054	0.10	0.15
R Aqr	M + Z And	–9.55	387	1.72	1.36	—	—	—
R Aql	M	—	276	0.79	1.54	—	—	—
UU Aur	SRB	–9.11	445	0.13	—	1721	0.07	—
ψ^1 Aur	Lc	–11.32	182	0.07	—	2176	0.07	—
R Boo	M	–7.37	224	2.43	2.25	—	—	—
RV Boo	SRB	–7.92	230	0.06	—	—	—	
RW Boo	SRB	–6.71	407	0.12	—	—	—	
RX Boo	SRB	–7.89	160	0.07	—	—	—	
FG Boo	SRB	–6.65	—	—	—	556	0.22	0.20
RS Cnc	SRB	–7.87	239	0.13	0.24	—	—	—
RT Cnc	SRB	–6.94	96	0.06	—	—	—	—
V CVn	SRA	–7.31	188	0.25	0.37 —	—	—	
Y CVn	SRB	–8.25	292	—	—	2000	—	—
W CMa	SR	–8.63	370	0.09	—	3717	0.09	—
VY CMa	Lc	–9.55	492	0.18	—	1433	0.37	—
RT Cap	SRB	–8.40	192	0.11	—	—	—	—
R Car	M	–7.96	308	2.30	2.22	—	—	—
S Car	M	–6.65	150	1.20	1.27	—	—	—
BO Car	SRc	—	367	0.09	0.13	—	—	—
R Cen	M	—	546	0.80	—	—	—	—
RV Cen	M	–8.47	447	0.91	—	1996	0.32	—
V744 Cen	SRB	–6.96	166	0.10	—	—	—	—
W Cep	SRc	—	408	0.07	—	—	—	—
SS Cep	SRB	–7.69	170	0.02	0.17	947	0.11	0.28
T Cet	SRB	–7.90	161	0.16	0.25	—	—	—
o Cet	M	—	333	2.38	2.34	—	—	—
RU Crt	SRB	–6.56	—	—	—	590	0.32	0.28
BH Cru	M	–8.53	522	1.10	—	—	—	—
W Cyg	SRB	–7.72	132	0.14	0.19	—	—	—
RS Cyg	SRA	–8.59	414	0.48	0.58	—	—	—
AF Cyg	SRB	–6.71	93	0.11	0.18	913	0.08	—
V460 Cyg	SRB	–8.35	164	0.05	0.13	2906	—	0.14
V1070 Cyg	SRB	–6.43	61	0.03	0.07	529	0.04	0.12
U Del	SRB	–7.83	120	0.05	0.08	1180	0.21	0.29
CT Del	SRB	–6.96	80	0.06	0.11	370	0.22	0.16
EU Del	SRB	–6.44	63	0.05	0.10	630	0.05	0.08
R Dor	SRB	–9.94	323	0.14	0.31	—	—	—
RY Dra	SRB	–7.62	154	0.04	0.09	1050	0.10	0.10

Note: The columns are: star name, variability type, absolute K magnitude, pulsation period (PP), PP semi-amplitude in v, PP semi-amplitude in V, long secondary period (LSP), LSP semi-amplitude in v, and LSP semi-amplitude in V.

Table 2. Variability properties of red giants and supergiants in the AAVSO Binocular Observing Program.

Star Name	*Type*	*MK*	*PP(d)*	*SA(PP)v*	*SA(PP)V*	*LSP(d)*	*SA(LSP)v*	*LSP(SA)V*
TX Dra	SRB	–6.57	76	0.08	0.12	700	0.14	0.16
UX Dra	SRB	–8.02	177	0.06	0.13	720	—	0.07
AH Dra	SRB	–7.11	193	0.23	0.20	—	—	—
Z Eri	SRB	–7.20	78	0.05	0.10	725	0.10	0.12
RR Eri	SRB	–7.43	93	0.06	0.11	—	—	—
BM Eri	SR	–6.65	—	—	—	565	0.27	—
BR Eri	SRB	–6.65	80	—	0.17	677	—	0.12
TV Gem	Lc	–11.09	188	0.04	0.22	2564	0.18	—
BU Gem	SRc	–10.67	318	0.09	—	2493	0.16	0.24
π^1 Gru	SRB	—	195	0.10	0.40	—	—	—
X Her	SRB	–6.76	101	0.06	0.18	722	0.08	0.22
ST Her	SRB	–7.88	152	0.08	0.20	1504	—	0.11
UW Her	SRB	–7.49	182	—	0.17	986	0.07	—
IQ Her	SRB	–6.87	76	0.05	—	625	0.10	—
OP Her	SRB	–7.10	74	0.05	0.06	699	0.10	0.10
V939 Her	LB	–6.67	68	0.06	—	—	—	—
g Her	SRB	–7.49	88	0.03	0.07	877	0.15	0.15
R Hya	M	–8.59	377	1.06	1.18	—	—	—
U Hya	SRB	–6.93	360	0.08	0.50	—	—	—
V Hya	SRA	–8.91	530	0.53	—	—	—	—
Y Hya	SRB	–7.78	363	0.13	0.23	852	0.07	—
RT Hya	SRB	–7.03	254	0.09	0.25	—	—	—
RV Hya	SRB	–7.54	365	0.15	—	—	—	—
T Ind	SRB	–8.34	369	0.14	0.17	4830	0.18	—
R Leo	M	–8.14	312	1.72	0.18	—	—	—
S Lep	SRB	–7.56	—	—	—	878	0.23	0.38
RX Lep	SRB	–7.56	162	0.05	—	667	0.07	0.22
Y Lyn	SRc	–8.43	135	0.08	—	1245	0.35	0.52
SV Lyn	SRB	–6.53	68	0.06	—	361	0.07	—
CE Lyn	SRB	–6.31	50	—	—	512	0.12	—
XY Lyr	SRC	–8.31	121	0.03	0.10	—	—	—
HK Lyr	SR	–8.00	376	0.09	0.13	—	—	—
T Mic	SRB	–8.01	363	0.34	—	—	—	—
X Mon	SRB	–6.85	156	0.50	0.55	1080	0.11	0.30
RV Mon	SRB	–7.16	—	—	—	355	0.12	0.31
BO Mus	SRB	–8.77	133	0.06	—	1700	0.06	—
X Oph	M	–7.47	333	0.51	0.83	—	—	—
W Ori	SRB	–8.92	432	0.13	—	2358	0.20	—
BL Ori	SRB	—	156	0.05	0.10	1290	0.05	—
BQ Ori	SRB	–7.76	248	0.18	0.50	1035	—	0.28

Note: Columns as in Table 1.

Table 3. Variability properties of red giants and supergiants in the AAVSO Binocular Observing Program.

Star Name	*Type*	*MK*	*PP(d)*	*SA(PP)v*	*SA(PP)V*	*LSP(d)*	*SA(LSP)v*	*LSP(SA)V*
S Pav	SRA	–7.92	387	0.57	—	—	—	—
Y Pav	SRB	–9.31	410	0.14	0.22	12000	0.37	—
GO Peg	SRB	–6.72	80	—	—	382	0.10	0.15
PV Peg	SRB	–6.89	—	—	—	700	0.18	0.25
SU Per	SRc	–10.44	467	0.07	—	3424	0.11	—
CI Phe	SRB	–6.59	—	—	—	758	0.23	—
R Pic	SR	–6.89	166	0.48	—	—	—	—
Z Psc	SRB	–8.17	156	0.13	0.19	—	—	—
TV Psc	SR	–6.09	55	0.02	0.05	530	0.03	0.06
L^2 Pup	SRB	–5.84	361	0.30	1.09	—	—	—
V1943 Sgr	SRB	–8.03	338	0.41	—	—	—	—
AH Sco	SRc	–11.15	700	0.31	—	—	—	—
BM Sco	L	—	383	0.19	0.23	8000	0.25	—
SW Scl	SRc	–6.52	144	0.30	—	—	—	—
Y Tau	SRB	–8.97	245	0.10	0.18	—	—	—
W Tri	SR	–7.74	109	0.04	—	768	0.07	—
X TrA	SR	–8.39	353	0.12	0.19	—	—	—
DM Tuc	SRB	–6.82	74	0.20	—	—	—	—
Z UMa	SRB	–6.81	189	0.40	0.90	—	—	—
RY UMa	SRA	–5.84	30	—	—	284	0.15	0.38
ST UMa	SRB	–6.91	90	0.04	0.13	615	0.06	0.16
TV UMa	SRB	–6.60	56	0.02	0.08	654	0.05	0.07
VW UMa	SRB	–6.80	66	—	—	620	0.05	0.07
V UMi	SRB	–6.47	73	0.10	0.19	755	0.08	0.20
GO Vel	SRB	–7.49	—	—	—	530	0.18	—
MN Vel	SRA	–8.31	135	0.16	—	1060	0.43	0.60
RT Vir	SRB	–7.98	371	0.17	—	1227	—	0.26
SS Vir	SRA	–7.87	355	0.70	1.10	—	—	—
SW Vir	SRB	–8.31	155	0.18	0.41	1700	0.11	0.20
FP Vir	SRB	–8.70	67	0.05	0.09	362	—	0.19
FI Vir	SR	-6.96	75	0.11	0.20	490	0.12	0.13

Note: Columns as in Table 1.

Table 4. For bimodal pulsators, the star name, the longer (fundamental) period Pa, the shorter (first overtone) period, and the ratio Pb/Pa.

Star Name	*Pa(d)*	*Pb(d)*	*Pb/Pa*
V373 And	202	118	0.584
ψ^1 Aur	182	94	0.516
R Boo	224	112	0.500
V CVn	188	91	0.484
R Cen	531	263	0.495
RV Cen	447	223	0.499
V744 Cen	166	92	0.554
SS Cep	170	100	0.588
W Cyg	259	132	0.510
AF Cyg	174	94	0.537
V460 Cyg	341	164	0.481
TX Dra	135	76	0.563
AH Dra	193	104	0.539
BU Gem	573	318	0.555
UW Her	182	106	0.582
T Ind	367	161	0.439
R Leo	312	156	0.555
W Ori	432	211	0.488
BL Ori	287	156	0.544
BQ Ori	248	127	0.512
Y Pav	440	226	0.514
V1943 Sgr	338	175	0.518
AH Sco	700	371	0.530
V UMi	124	73	0.586

pulsation period are consistent with this class but, for V939 Her, the MK (–6.67) and the pulsation period (68 days) are more consistent with an SR classification.

Figure 4 relates to the amplitude of the LSP. This amplitude would be expected to depend on the ratio of the effective area of the dust-enshrouded companion to the area of the red giant, and also on the angle of the companion's orbit place to the line of sight. It is not surprising, then, that the amplitude decreases for larger, more luminous stars, assuming that the size of the companion is not larger in more luminous stars. It is less clear why it also decreases for smaller, less luminous stars. Perhaps, since these have weaker winds, the companion has not accreted much matter, and is therefore smaller. Also, at each value of MK, there is a range of amplitudes, depending on the inclination of the companion's orbit.

5. Conclusions

This analysis of the variability properties of the red giant and supergiant stars in the AAVSO Binocular Observing Program has displayed the full gamut of phenomena which are expected to occur in these stars. They pulsate in the fundamental (F) and/or first overtone (1O) mode; 24 are bimodal pulsators. 58 show long secondary periods which are about five times the fundamental pulsation period, or about ten times the first overtone period. For the bimodal pulsators, the period ratio varies slowly with the luminosity of the star. The period-luminosity graph shows approximately parallel sequences for the 1O or F pulsation and for the LSPs. The pulsation amplitude increases with increasing pulsation period in a complex way, which may be partly due to the way in which the program stars were selected. The LSP amplitude seems to be greatest for moderate-luminosity stars.

We hope that the observers in the AAVSO Binocular Program will read this paper, and derive some satisfaction from knowing that they are contributing to our understanding of these very complex stars.

6. Acknowledgements

We thank the AAVSO observers and headquarters staff for their work in making and compiling the data, and making them publicly and easily available; this was essential to our project. We also thank the creators and maintainers of the AAVSO VStar package for making it user-friendly and publicly available. And we thank the referee and the editor for helpful suggestions to improve this manuscript. We thank the University of Toronto Work-Study Program for financial support. The Dunlap Institute is funded through an endowment created by the David Dunlap Family and the University of Toronto.

References

Benn, D. 2013, VStar data analysis software (https://www.aavso.org/vstar-overview).

Cadmus, R. R., Jr. (2020), *J. Amer. Assoc. Var. Star Obs.*, **48**, 140.

Jayasinghe, T., *et al.* 2018, *Mon. Not. Roy. Astron. Soc.*, **477**, 3145.

Jayasinghe, T., *et al.* 2019, *Mon. Not. Roy. Astron. Soc.*, **486**, 1907.

Kim, J. V. E., and Percy, J. R. 2022, *J. Amer. Assoc. Var. Star Obs.*, **50**, 178.

Kloppenborg, B. 2023, Observations from the AAVSO International Database (https://www.aavso.org/data-download).

Percy, J. R. 2015, *J. Amer. Assoc. Var. Star Obs.*, **43**, 223.

Percy, J. R., and Abachi, R. 2013, *J. Amer. Assoc. Var. Star Obs.*, **41**, 193.

Percy, J. R., and Deibert, E. 2016, *J. Amer. Assoc. Var. Star Obs.*, **44**, 94.

Percy, J. R., and Huang, D. J. 2015, *J. Amer. Assoc. Var. Star Obs.*, **43**, 118.

Percy, J. R., and Leung, H. W. 2017, *J. Amer. Assoc. Var. Star Obs.*, **45**, 30.

Percy, J. R., and Shenoy, M. H. 2023, *J. Amer. Assoc. Var. Star Obs.*, submitted.

Shappee, B. J., *et al.* 2014, *Astrophys. J.*, **788**, 48.

Soszyński, I., *et al.* 2021, *Astrophys. J., Lett.*, **911**, L22.

Wood, P. R. 2000, *Publ. Astron. Soc. Australia*, **17**, 18.

Xiong, D. R., and Deng, L. 2007, *Mon. Not. Roy. Astron. Soc.*, **378**, 1270.

The "Long Secondary Period (LSP) Variables": Overview and Some Analysis

John R. Percy
Mayank H. Shenoy
Department of Astronomy and Astrophysics, and Dunlap Institute for Astronomy and Astrophysics, University of Toronto, 50 St. George Street, Toronto ON M5S 3H4, Canada; john.percy@utoronto.ca

Received October 26, 2023; revised November 29, 2023; accepted December 1, 2023

Abstract We briefly review the phenomenon of "long secondary periods" (LSPs) in red giants, and the "LSP variable stars" classification introduced in the All-Sky Automated Survey for Supernovae (ASAS-SN) variable star catalog; they are red giant Long Period Variables (LPVs) in which their LSP variability is significantly greater than their pulsational variability. We then describe and discuss the results of a period and amplitude analysis of a random sample of 35 LSP variables in the ASAS-SN catalog, using ASAS-SN data and the AAVSO VStar time-series analysis software. The pulsation period and amplitude, and LSP, all increase with increasing luminosity or size of the star, as expected. The behavior of the LSP amplitude is more complicated; it appears to be larger in moderate-luminosity stars, and smaller in low- and high-luminosity stars. In particular, it is relatively small in a sample of 27 Mira stars, analyzed separately using AAVSO visual data. These results are discussed in the context of the current model for the LSP phenomenon, namely that it is caused by eclipses of the red giant star by a dust-enshrouded companion.

1. Introduction

Red giant stars vary in brightness in complex ways, and for a multitude of reasons. The All-Sky Automated Survey for Supernovae variable star catalog (ASAS-SN; Shappee *et al.* 2014; Kochanek *et al.* 2017) has recently introduced a new subclass of red giant variables—ones whose variability is dominated by a "long secondary period" (LSP) which is very common in red giants but, until recently, poorly understood. The purpose of the present paper is to introduce these variables and the LSP phenomenon, to present an analysis of a sample of 35 LSP variables from the ASAS-SN catalog, and to discuss why they continue to be rather enigmatic.

Red giants are unstable to low-order radial pulsation. The periods and amplitudes are greater for larger, more luminous stars, ranging from a few days and a few thousandths of a magnitude in the least luminous stars, to hundreds of days and several magnitudes in the most luminous stars. The smaller-amplitude variables are classified as semiregular (SR) or irregular (L) and sometimes OGLE small amplitude red giants (OSARG); the variables with pulsation amplitudes of 2.5 or greater are classified as Mira (M) stars. Collectively, these stars are often referred to as Long Period Variables (LPVs), but the terminology is complicated; the LPV Observing Section of the American Association of Variable Star Observers (AAVSO) includes yellow supergiant variables such as RV Tauri stars. In the Hertzsprung-Russell Diagram of luminosity vs. surface temperature, these stars are on or approaching the upper end of the hydrogen-burning Red Giant Branch, or the subsequent helium-burning Asymptotic Giant Branch. As the star becomes more luminous, mass loss increases, and eventually becomes so great that the star loses the outer half of its mass, which forms a slowly-expanding planetary nebula around the star. The core of the star becomes a white dwarf.

One-third to one-half of red giants display another form of variability—long secondary periods, 5 to 10 times the radial pulsation period. These LSPs were identified in large numbers by photographic photometry, especially at the Harvard College Observatory (O'Connell 1933; Payne-Gaposchkin 1954; Houk 1963). Houk (1963) listed over a hundred LPVs with LSPs. Subsequent visual observations of Houk's stars confirmed that the vast majority of these LSPs were correct (Percy 2022).

The Harvard photographic program was gradually phased out, but the study of LSPs continued, thanks in part to visual observations by skilled amateur astronomers, working through organizations such as the AAVSO; see Percy and Deibert (2016), for instance, for an example of the analysis of these observations.

By 1980, there were two more important contributors to the study of LSPs: remote robotic observatories (e.g. a survey of two dozen red giants by Percy *et al.* 2001), and long-term photoelectric photometry by skilled amateur astronomers (e.g. through the photoelectric photometry program of the AAVSO: Percy *et al.* 1989), made possible by the availability of reasonably-priced, off-the-shelf photometers.

The 1990s brought a wave of massive automated long-term photometric surveys of large numbers of stars by the professional astronomical community (ASAS: All-Sky Automated Survey, MACHO: MAssive Compact Halo Objects, and OGLE: Optical Gravitational Lensing Experiment). LSPs were so prevalent that they were quickly discovered in red giants in large numbers. Wood (2000), in particular, called attention to the period-luminosity sequences for red giants in the Large Magellanic Cloud. There were sequences for low-order modes of pulsation, and also a well-defined sequence for LSPs.

But what was the cause of the LSPs? Wood *et al.* (2004) referred to LSPs as "the only unexplained type of large-amplitude stellar variability known at this time." Was it due to non-radial pulsation, some form of eclipse, rotation, convection cells, magnetic phenomena, or something else? For two decades, the problem of LSPs was a vigorous area of study.

A proposal by Soszyński *et al.* (2021) seemed to provide an answer: "The LSP light changes are due to the presence of a dusty cloud orbiting the red giant, together with a companion, and obscuring the star once per orbit.... In this scenario, the low-mass companion is a former planet that has accreted a significant amount of mass from the envelope of its host star and grown into a brown dwarf."

This proposal was based on a study of about 700 LPVs in the OGLE survey (Udalski *et al.* 2015) of the Magellanic Clouds and Galactic bulge, using both visual and infrared photometry. The strongest new evidence for this proposal was the observation that, in the infra-red, there is a secondary eclipse which occurs when the very cool companion and its cloud—which are infra-red sources but not optical sources—are eclipsed by the red giant star.

There are, nevertheless, some mysteries arising from this proposal. Surveys show that about one-third of red giants show LSPs. But the Soszyński *et al.* (2021) mechanism implies that there would also be systems in which the companion's orbit was seen face-on, in which case there would be no eclipse, and no LSP, so the actual fraction of systems having dusty companions would be even greater than the fraction showing LSPs. It is surprising that such systems had not been discovered much earlier, among the brighter, nearby, well-studied red giants.

LSPs appear to be common in globular clusters (Lebzelter and Wood 2005; Percy and Gupta 2021; Kim and Percy 2022), as well as in the Magellanic Clouds. That would imply that, in order to provide the mechanism for LSPs, both planet formation and dust formation were common enough in these ancient star systems with low abundances of elements heavier than helium to provide the ingredients for the LSP process.

Another mystery is the relatively tight LSP-luminosity relation found by Wood (2000). Soszyński *et al.* (2021) deliberately selected stars for their study which lay in the center of the LSP-luminosity relation to ensure that they were truly stars with LSPs so in their study there is a bias or selection effect in producing a tight period-luminosity relation. This bias is not present in Wood's (2000) study.

However, the luminosity of the red giant depends on its radius. The LSP depends on the radius of the companion's orbit. Why should these be closely related? Kim and Percy (2022) discussed this, and estimated that, for the stars in their sample, the latter should be about twice the former. This seems reasonable: the orbit of the companion cannot be too close to the star, and if it is too far from the star, the accretion process may be inefficient, and/or the probability of eclipses may also be smaller, since the orbit needs to be seen edge-on in order to produce LSP variations.

The present paper deals with another mystery: there are red giant stars in which the pulsation period and amplitude are small, suggesting that the luminosity of the red giant is low, yet an LSP is present with an amplitude larger than that of the pulsation. If the luminosity of the red giant is low, its mass-loss rate will presumably be low. In that case, how did the companion accrete enough material to become massive and dusty enough to cause the LSP phenomenon? In the ASAS-SN variable star catalog, there are 185 such stars in which the LSP variation dominates the pulsation variation. The catalog classifies these stars as "LSP variables," though that classification is not (yet) found in the *General Catalogue of Variable Stars* (Samus *et al.* 2017). In the present paper, we analyze a sample of 35 such stars, and study the periods and amplitudes of the LSP and the pulsation in order to study the systematics of this new "class" of stars.

Because the results of this first project suggested that more luminous LPVs had smaller LSP amplitudes, we also analyzed visual measurements of a sample of 27 Mira stars—larger, more luminous variables with periods of hundreds of days, and ranges of 2.5 magnitudes or more.

Pawlak (2023), using a different approach, analyzed OGLE observations of 1663 Mira stars in the LMC, and concluded that seven percent of the Mira stars in the sample might have LSPs. This is a much smaller percentage than found among SR variables in similar surveys.

2. Data and analysis

From the ASAS-SN variable star website and catalog (Shappee *et al.* 2014; Jayasinghe *et al.* 2018, 2019), data on a random sample of 35 stars classified as LSP variables were downloaded and analyzed with careful light-curve analysis and time-series analysis using the AAVSO VSTAR software package (Benn 2013). The sample size was determined by the fact that detailed star-by-star analysis could be accomplished within the time available for this student project. It was large enough to point to any interesting and/or unusual results, which could be followed up, such as in our parallel study (Percy and Zhitkova 2023).

The stars and results are listed in Table 1, which gives the ASAS-SN star name, the apparent V magnitude and absolute K magnitude, and the period and (semi) amplitude of the LSP (LSP, LSP-A) and of the dominant pulsation period (PP, PP-A). The absolute K magnitude M_K, which is more representative of the luminosity of red variables than the absolute V magnitude, was determined from the K magnitude, Gaia distance, and interstellar reddening, as given in the ASAS-SN variable star catalog. Figures 1 and 2 show ASAS-SN light curves of two representative LSP variables.

Note that the ASAS-SN datasets are only about 1500 days long. This limits the precision of the periods determined from them, especially the LSP, which is typically hundreds of days. The ASAS-SN data also have the usual seasonal gaps in the data (see Figures 1 and 2) which introduce the possibility of spurious "alias" periods in the Fourier spectra.

3. Results

The PP increases with increasing luminosity MK, as expected (Figure 3). Much of the scatter is probably due to the fact that the stars may be pulsating in different low-order modes, or possibly a mixture of modes. The pulsation of LPVs is semi-regular at best, in part because they vary significantly in amplitude.

The LSP also increases with increasing luminosity or size of the star (Figure 4), as expected from the Soszyński *et al.* (2021) mechanism. Much of the scatter is due to the difficulty in determining the LSP accurately from the short ASAS-SN datasets. The shortness of the datasets also produces a slight bias in favor of shorter LSPs.

The ratio LSP/PP averages about 9 for all $_{MK}$, but with considerable scatter, which is not surprising, given the difficulty in measuring the LSP accurately from short datasets. This ratio

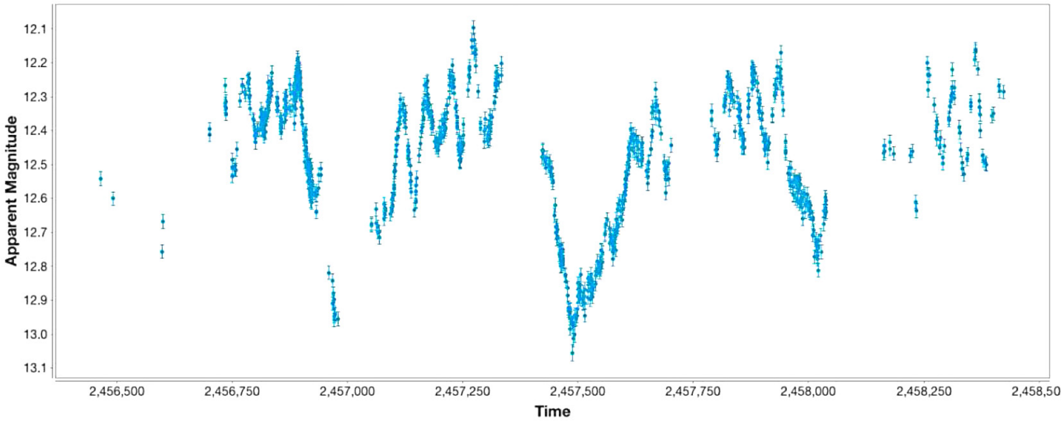

Figure 1. ASAS-SN V light curve of the LSP star ASAS-SN-V J191616.35+475823.7, showing both the LSP variation and the smaller pulsational variation.

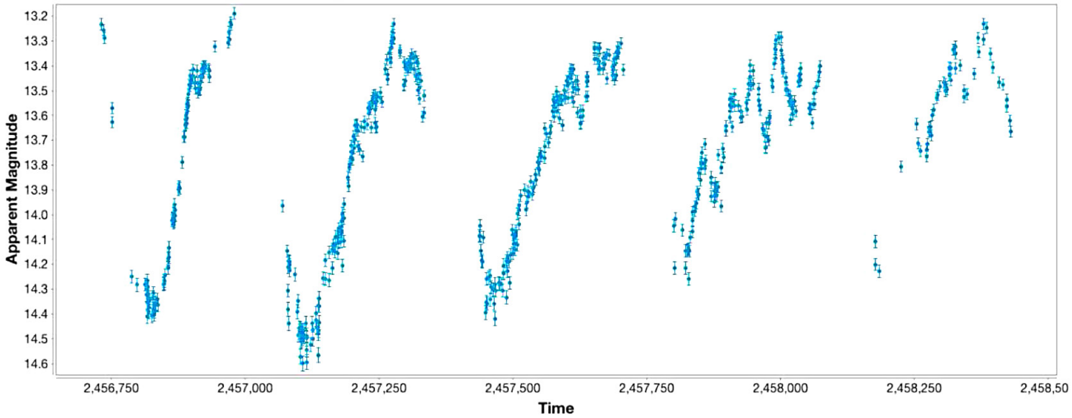

Figure 2. ASAS-SN V light curve of the LSP star ASAS-SN-V J195427.42+474921.2, showing both the LSP variation and the smaller pulsational variation.

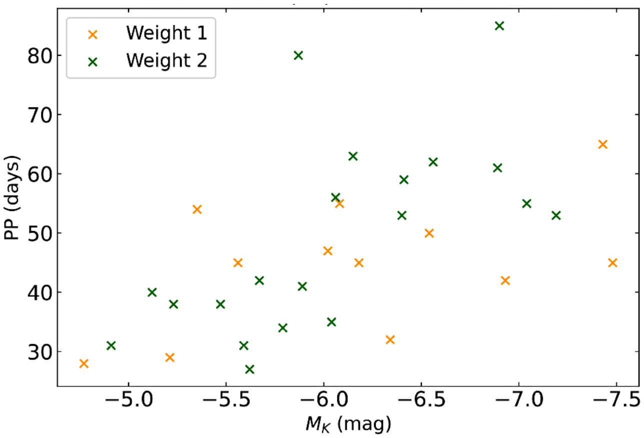

Figure 3. The period-luminosity (M_K) relation for the stars in Table 1. The scatter suggests that the stars are not all pulsating in the same mode and/or that the choice of “LSP stars” from the ASAS-SN catalog introduces a selection effect in the sample.

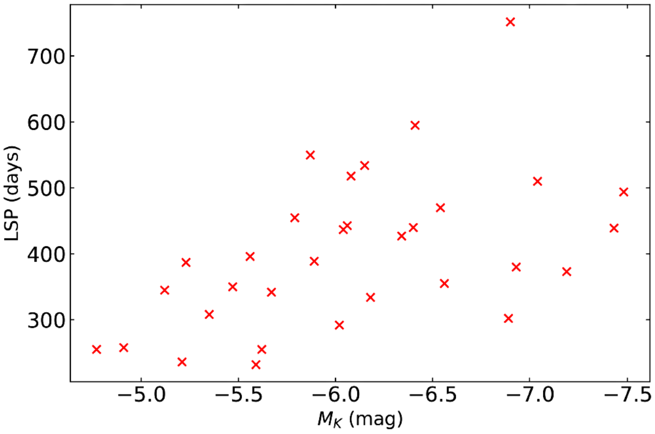

Figure 4. The relation between the LSP and the luminosity M_K. There is a general trend, as we would expect from the Soszyński *et al.* mechanism. See text for discussion.

Table 1. Period and amplitude analysis of ASAS-SN observations of LSP stars.

ASAS-SN-V Name	*V*	*MK*	*LSP (d)*	*SA (LSP)*	*PP (d)*	*SA (P)*
J003836.62+510342.1	13.70	–6.41	595	0.19	59	0.120
J020359.53+141132.4	12.00	–5.56	396	0.39	45	0.087
J031644.30+790013.7	12.49	–6.06	443	0.28	56	0.084
J051411.00+475413.4	13.57	–7.37	599	0.31	30	0.110
J100459.29+470246.9	12.70	–5.23	387	0.08	38	0.027
J122246.23+152052.5	12.01	–5.12	345	0.04	40	0.022
J134521.91+010137.6	13.66	–4.74	327	0.22	14	0.055
J134533.58+010408.8	12.27	–5.35	308	0.10	54	0.045
J142127.71+463131.7	13.20	–5.47	350	0.07	38	0.026
J154021.56+290510.8	13.53	–6.93	380	0.08	42	0.027
J162106.89+304132.5	13.78	–4.91	258	0.07	31	0.030
J162708.92+261624.2	12.61	–4.77	255	0.07	28	0.019
J164815.57–195122.3	13.11	–5.79	455	0.14	34	0.041
J173239.14–171835.7	12.96	–6.40	440	0.25	53	0.100
J185255.04+290949.6	13.90	–6.35	811	0.08	48	0.042
J185735.62–282447.4	12.76	–6.04	437	0.12	35	0.048
J185802.67+421553.1	13.21	–6.54	470	0.08	50	0.063
J185957.97+404745.5	13.48	–7.19	373	0.23	53	0.064
J190119.21+460405.7	12.90	–5.59	232	0.10	31	0.035
J190424.97+382941.9	13.89	–6.34	427	0.30	32	0.087
J190445.35+320054.7	13.02	–6.15	534	0.23	63	0.160
J191456.72+421950.0	13.90	–6.90	752	0.16	85	0.110
J191516.97+475851.2	12.91	–7.43	439	0.11	65	0.081
J191616.35+475823.7	12.47	–7.04	510	0.21	55	0.079
J192201.47+442631.0	12.59	–5.21	236	0.08	29	0.024
J192439.93+453046.1	13.78	–7.48	494	0.12	45	0.060
J193000.06+413632.3	12.57	–6.02	292	0.19	47	0.074
J193220.91+490643.2	12.26	–6.18	334	0.16	45	0.023
J193701.71+444317.8	12.99	–6.56	355	0.08	62	0.072
J195427.42+474921.2	13.76	–5.67	342	0.44	42	0.074
J204505.70+002505.6	11.80	–5.89	389	0.09	41	0.041
J212114.88+455019.1	13.30	–6.89	302	0.08	61	0.065
J213355.20–001944.3	11.50	–5.62	255	0.09	27	0.031
J213751.82+423137.1	13.03	–6.08	518	0.16	55	0.050
J233235.02+480155.4	13.70	–5.87	550	0.15	80	0.055

suggests that most of these lower-luminosity red giants are pulsating in the first overtone, as previous results have suggested (e.g. Wood 2000). There are some short-period stars with LSP/PP ratios of 13, which may be second-overtone pulsators, and a few longer-period stars with ratios less than 7, which may be fundamental-mode pulsators.

The PP amplitude increases with luminosity (Figure 5), as would be expected from previous results. Almost all the stars have PP amplitudes less than 0.1, and about half have PP amplitudes less than 0.05. This is in part due to the selection effect in choosing "LSP variables," in which, by definition, the LSP amplitude is significantly larger than the PP amplitude.

There is a clear correlation between LSP amplitude and PP amplitude, with the former increasing from 0.05 to about 0.25 when the latter increases from 0.02 to 0.10 (Figure 6). This is to be expected, since both are correlated with luminosity. This reminds us, however, that we are dealing with small and variable amplitudes, so both periods and amplitudes are challenging to determine.

Figure 7 is probably the most interesting in this study, since there have been few, if any, studies of the amplitudes and phase curves of the LSP phenomenon, which is an eclipse phenomenon; Derekas *et al.* (2006) is an exception. The figure suggests that the LSP amplitude is smaller for lower- and higher-luminosity stars, and larger for moderate-luminosity ones.

Table 2. Amplitudes of the LSP variability in some Mira stars.

Star	*PP (days)*	*LSP-A*
R And	409	≤ 0.25
W And	396	≤ 0.20
R Aur	458	≤ 0.20:
T Cam	373	≤ 0.10
T Cas	445	≤ 0.10
o Cet	332	0.53
U Cet	235	≤ 0.20
R CMi	338	≤ 0.10
S CMi	333	0.21
R Cnc	362	≤ 0.12
V Cnc	272	≤ 0.15
S CrB	361	0.23
R Gem	370	≤ 0.20
S Hya	257	≤ 0.15
T Hya	289	≤ 0.15
R Leo	310	≤ 0.15
R Lep	427	≤ 0.10:
R LMi	372	≤ 0.20
R Lyn	365	≤ 0.10
V Mon	340	≤ 0.20
U Ori	369	0.20:
RZ Per	369	≤ 0.10
Z Sco	363	≤ 0.10
R Tri	267	≤ 0.15
R UMa	302	≤ 0.15
S Vir	367	≤ 0.15
SS Vir	364	≤ 0.10

In part to test this result, we studied a small sample of 27 Mira stars—the largest, highest-luminosity red giants—for LSPs and LSP amplitudes, using visual data from the AAVSO International Database, and VStar. In almost every case, there was no obvious LSP which rose above the noise level, so the best we could do was to give an upper limit to the LSP amplitude, namely, the noise level. The results are given in Table 2 which, in most cases, gives these upper limits. Almost all of these upper limits are in the range 0.10 to 0.20, consistent with the results in Figure 7.

4. Discussion

In the course of a parallel study—inspired by this one—of the variability properties of LPVs in the AAVSO Binocular Program (Percy and Zhitkova 2023), we identified stars which had catalog periods of several hundred days, whereas pulsation periods 5 to 10 times shorter could be seen in light curves from ASAS-SN or AAVSO photometry. These include RW Boo, BM Eri, PV Peg, CI Phe, RY UMa, VW UMa, and GO Vel. These stars are therefore "LSP variables," and their catalog periods are LSPs. Catalog users should be aware that the catalog periods of LPVs are not always the pulsation periods.

The ratios of LSP to PP are consistent with previous results, and with the idea that lower-luminosity red giants are more likely to pulsate in the first overtone. In this sense, our sample is similar to other samples of pulsating red giants.

Figure 7 is perhaps the most interesting result of this study, though it is far from definitive. The LSP amplitude is a measure of the eclipse coverage by the dust-enshrouded companion. This presumably depends on the relative sizes of the star and companion (or, more precisely, the effective size of its dusty

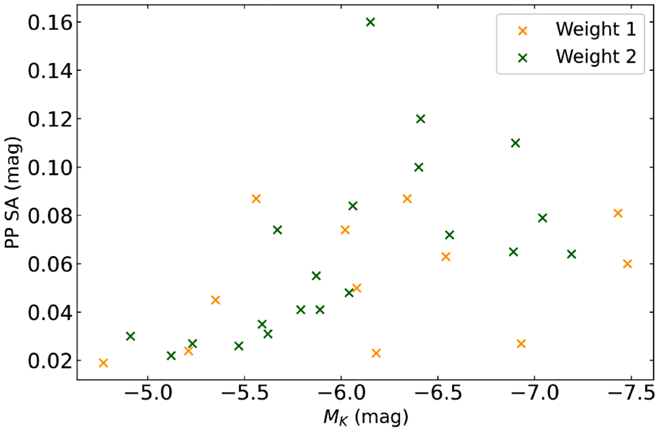

Figure 5. The relation between the pulsation amplitude and the luminosity M_K. There is a positive trend, as expected, but the choice of "LSP variables" from the ASAS-SN catalog undoubtedly introduces a bias in favor of small pulsation amplitudes.

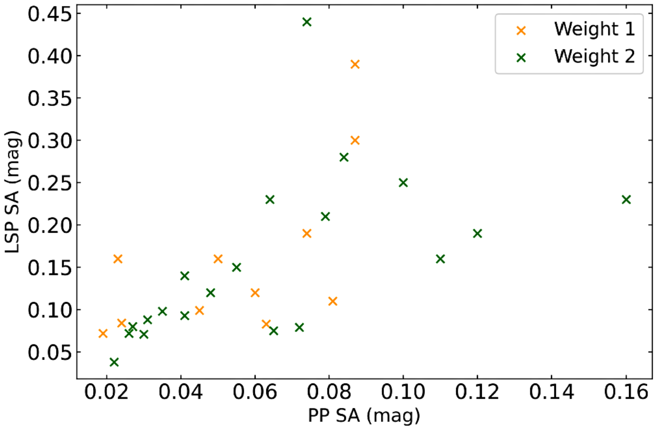

Figure 6. The relation between LSP amplitude and pulsation amplitude. There is a distinct positive trend, as would be expected, since both are positively correlated with the luminosity.

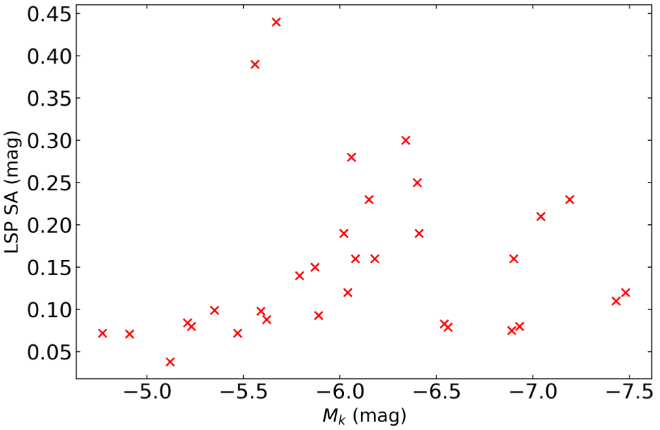

Figure 7.The relation between LSP amplitude and luminosity M_K. The LSP amplitude is smaller for low- and high-luminosity stars, especially when the results for Mira stars are included.

envelope), and on the inclination of the companion's orbit. If the size of the companion was independent of luminosity, we would expect the LSP amplitude to decrease with increasing luminosity and size of the star, which it does. But the LSP amplitude also becomes smaller in lower-luminosity, smaller stars. This suggests that the effective size of the companion and its envelope is *smaller* in smaller, lower-luminosity stars. This could be because such stars have weaker winds, and have not been able to transfer as much dust to their companion.

Derekas *et al.* (2006) measured LSP amplitudes in a much larger sample of stars, and found the same pattern as we did, namely that the distribution of LSP amplitudes peaked in moderate-luminosity stars and, at every luminosity, there was a range of amplitudes. However, in those authors' opinion, the results "...argue for pulsation rather than binarity as the cause of the LSP phenomenon."

It would obviously be desirable to have more information on the relationship between the LSP amplitude and the luminosity of the star. That was the motivation for studying the LSPs in the sample of Mira stars in Table 2. We also examined LSP amplitudes in two overlapping samples: 37 LPVs with LSPs (Percy 2022) and listed in Houk (1963), and several dozen red variables in the AAVSO Binocular Program (Percy and Zhitkova 2023). For stars with short LSPs (400–800 days), and therefore assumed to be smaller stars, the LSP amplitudes were less than 0.15 and averaged less than 0.10. For stars with moderate LSPs (800–1400 days), the LSP amplitudes averaged over 0.20 and ranged up to 0.40. For stars with larger LSP values than 1400 days, the LSP amplitudes averaged about 0.15, consistent with the values in Table 2.

There is still much to learn about the LSP phenomenon and, because it is a long-term phenomenon, AAVSO visual observations can be especially useful. Is the LSP constant in time? If it is a binary period, it should be. Does the LSP amplitude, and the LSP phase curve vary with time? This can provide information about variability in the amount and distribution of the dust around the companion. A decade or two ago, systematic radial velocities of red giants with LSPs were carried out. Comparing these with contemporaneous AAVSO photometry can ensure that the relative phase of the radial velocities and the photometry are consistent with the Soszyński *et al.* (2021) binary model. There is certainly a place for AAVSO observers in all of these projects.

The origin of LSP stars is still a bit of a mystery. Their short pulsation periods, and small pulsation amplitudes suggest that they are low-luminosity giants, which would have weak winds. In that case, however, how do they transfer enough matter to the companion for it to grow into a brown dwarf or low-mass star, and produce a significant LSP phenomenon?

5. Conclusions

We have presented and discussed the period and amplitude analysis of a random sample of 35 so-called LSP stars, in which the LSP variability is significantly larger than the pulsational variability. The pulsation period and amplitude increase with luminosity, as expected, and the LSP also increases with the luminosity as would be expected if the LSP were the orbital period of a close, dust-enshrouded companion. The LSP amplitude, which is related to the eclipse depth, is low in low-luminosity stars, perhaps because the effective size of the dust-enshrouded companion is smaller. The LSP amplitude is also low in high-luminosity stars, perhaps because the size of the stellar disc is large compared to the effective size of the companion. The LSP amplitude is largest, on average, for stars of moderate luminosity. The amplitude will also depend on the inclination of the companion's orbit to the line of sight, so at any M_K, there will be a range of LSP amplitudes.

6. Acknowledgements

We thank the ASAS-SN project for making their data publicly available, and the creators and maintainers of the AAVSO VStar package for making it user-friendly and publicly available. We also thank the University of Toronto Work-Study Program and the Dunlap Institute for financial support. The Dunlap Institute is funded through an endowment created by the David Dunlap Family and the University of Toronto.

References

Benn, D. 2013, VStar data analysis software (https://www.aavso.org/vstar-overview).

Derekas, A., Kiss, L. L., Bedding, T. R., Kjeldsen, H., Lah, P., and Szabó, Gy. M. 2006, *Astrophys. J., Lett.*, **650**, L55.

Houk, N. 1963, *Astron. J.*, **68**, 253.

Jayasinghe, T. *et al.* 2018, *Mon. Not. Roy. Astron. Soc.*, **477**, 3145.

Jayasinghe, T. *et al.* 2019, *Mon. Not. Roy. Astron. Soc.*, **486**, 1907.

Kim, J.V.E., and Percy, J. R. 2022, *J. Amer. Assoc. Var. Star Obs.*, **50**, 178.

Kochanek, C. S., *et al.* 2017, *Publ. Astron. Soc. Pacific*, **129**, 104502.

Lebzelter, T., and Wood, P. R. 2005, *Astron. Astrophys.*, **441**, 1117.

O'Connell, D. J. K. 1933, *Bull. Harvard Coll. Obs.*, No. 893, 19.

Pawlak, M. 2023, *Astron. Astrophys.*, **669A**, 60.

Payne-Gaposchkin, C. 1954, *Ann. Harvard Coll. Obs.*, **113**, 189.

Percy, J. R. 2022, University of Toronto, TSpace Repository (https://tspace.library.utoronto.ca/handle/1807/124406).

Percy, J. R., and Deibert, E. 2016, *J. Amer. Assoc. Var. Star Obs.*, **44**, 94.

Percy, J. R., and Gupta, P. 2021, *J. Amer. Assoc. Var. Star Obs.*, **49**, 209.

Percy, J. R., Landis, H. J., and Milton, R. E. 1989, *Publ. Astron. Soc. Pacific*, **101**, 893.

Percy, J. R., Wilson, J. B., and Henry, G. W. 2001, *Publ. Astron. Soc. Pacific*, **113**, 983.

Percy, J. R., and Zhitkova, S. 2023, *J. Amer. Assoc. Var. Star Obs.*, **51** (app.aavso.org/jaavso/article/3906/).

Samus, N. N., Kazarovets, E. V., Durlevich, O. V., Kireeva, N. N., and Pastukhova, E. N. 2017, *Astron. Rep.*, **61**, 80.

Shappee, B. J., *et al.* 2014, *Astrophys. J.*, **788**, 48 (https://asas-sn.osu.edu/).

Soszyński, I., *et al.* 2021, *Astrophys. J., Lett.*, **911**, L22.

Udalski, A., Szymański, M. K., and Szymański, G. 2015, *Acta Astron.*, **65**, 1.

Wood, P. R. 2000, *Publ. Astron. Soc. Australia*, **17**, 18.

Wood, P. R., Olivier, A. E., and Kawaler, S. D. 2004, in *Variable Stars in the Local Group*, eds. D. W. Kurtz, K. R. Pollard, ASP Conf. Proc. 310, 322.

An Orbital Solution for WASP-12 b: Updated Ephemeris and Evidence for Decay Leveraging Citizen Science Data

Avinash S. Nediyedath
Department of Physics, Kristu Jayanti College, Bangalore, India, and Exoplanet Watch; avinash123salgunan@gmail.com

Martin J. Fowler
Anthony Norris
Exoplanet Watch

Shivaraj R. Maidur
Department of Physics, Kristu Jayanti College, Bangalore, India

Kyle A. Pearson
Jet Propulsion Laboratory, California Institute of Technology, 4800 Oak Grove Drive, Pasadena, CA 91109, and Exoplanet Watch

Scott Dixon **Andre O. Kovacs** **Ken Davis** **Prithwis Das** **Douglas Lalla**
Pablo Lewin **Alessandro Odasso** **Michael Primm** **Bryan E. Martin**
Exoplanet Watch

Received August 14, 2023; revised September 29, 2023; accepted October 2, 2023

Abstract NASA Citizen Scientists have used Exoplanet Transit Interpretation Code (EXOTIC) to reduce 40 sets of time-series images of WASP-12 taken by privately owned telescopes and a 6-inch telescope operated by the Center for Astrophysics | Harvard & Smithsonian MicroObservatory (MOBs). Of these sets, 24 result in clean transit light curves of WASP-12 b which are included in the NASA Exoplanet Watch website. We use priors from the NASA Exoplanet Archive to calculate the ephemeris of the planet and combine it with ETD (Exoplanet Transit Database), ExoClock, and TESS (Transiting Exoplanet Survey Satellite) observations. Combining these datasets gives an updated ephemeris for the WASP-12 b system of 2454508.97923 ± 0.000051 BJDTDB with an orbital period of 1.09141935 ± 2.16e–08 days, which can be used to inform the efficient scheduling of future space telescope observations. The orbital decay of the planet was found to be –6.89e–10 ± 4.01e–11 days/epoch. These results show the benefits of long-term observations by amateur astronomers that citizen scientists can analyze to augment the field of exoplanet research.

1. Introduction

WASP-12 b was discovered by Hebb *et al.* (2009) and found to be 1.41 times the mass of Jupiter, 1.79 times the radius of Jupiter, and orbiting its F9V host star every 1.09 days. The extreme gravity of the host star is stretching the hot gas giant into an ovoid body, all the while slowly cannibalizing the planet and resulting in a decrease in its orbital period (Yee *et al.* 2020; Wong *et al.* 2022).

The transit method is an important tool for the investigation of Exoplanet systems (Perryman 2018). This method tracks the brightness of the combined system (exoplanet and host star) over time and looks for changes caused when an exoplanet passes in front of its star, which can block some light from reaching the Earth. This technique tells us about the size of the exoplanets and the angle at which they orbit the host star relative to our line of sight. From the observation of multiple transits, it provides information on the orbital period to update the ephemeris. It has become a reliable way of obtaining the mid-transit times of exoplanet orbits. The transit method is within the reach of amateurs with small telescopes, as has been shown by Zellem *et al.* (2020) and Hewitt *et al.* (2023).

In the 14 years since the discovery of WASP-12 b, new tools to investigate exoplanets have been developed, such as the James Webb Space Telescope (JWST). It is being used to study the planets' atmospheric chemistry (Seidel *et al.* 2023). This leads to the need to update the ephemerides of exoplanets to make maximum use of expensive space telescope time to characterize their atmospheres. As of July 2023, we have seen a total of 526 transit observations of WASP-12 b by professional and amateur astronomers in the datasets of ETD (Exoplanet Transit Database, Poddaný *et al.* 2010), ExoClock (Kokori *et al.* 2022), TESS (Ricker *et al.* 2015), and Exoplanet Watch.

In this paper we study 24 transits of WASP-12 b from NASA's Exoplanet Watch, a citizen science project (https://Exoplanets.nasa.gov). Exoplanet Watch enables members around the world to use their time and effort to observe and reduce their own data to produce light curves. We have combined those with observations from the ETD, ExoClock, and TESS databases to update the ephemeris of the exoplanet.

2. Observations

Thirty-one observations were made with 60-second, unfiltered exposures with 3-minute cadence collected by a 6-inch aperture MicroObservatory telescope located at Mount Hopkins (latitude 31.675°, longitude –110.952°, 1,268m altitude

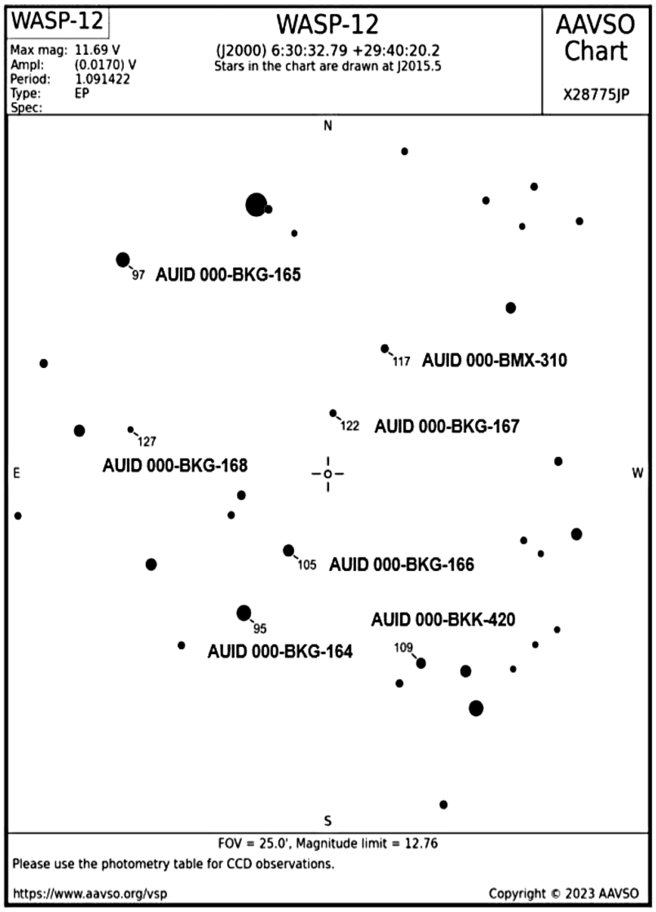

Figure 1. AAVSO VSP view of the WASP-12 star field.

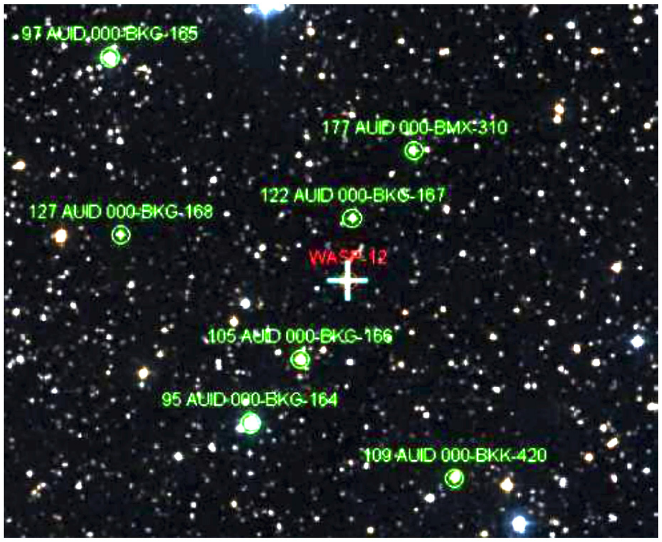

Figure 2. WASP-12 labeled star field in AstroImageJ. Green annotations are used to indicate comparison stars and red annotation is used to indicate the target star. Image by Anthony Norris.

above sea level) in Arizona. This telescope uses a KAF-1403 ME CCD camera with a pixel scale of 5.2" per pixel and 2 × 2 binning to reduce noise. In addition, nine observations were taken from privately owned telescopes by citizen scientists, yielding a total of 40 observation sets from 03 January 2015 to 06 March 2023. All of the data were analyzed using Exoplanet Transit Interpretation Code (EXOTIC), which is a Python-based tool developed by the Jet Propulsion Laboratory's Exoplanet Watch program for reducing exoplanet transit data. This software can run locally as well as on the cloud via Google's online "Colaboratory" tool (Zellem *et al.* 2020). Prior parameters for WASP-12 b used for nested sampling fitting by EXOTIC are automatically scraped from the NASA Exoplanet Archive (Akeson *et al.* 2013). EXOTIC generates estimates of mid-transit times along with 1σ uncertainties based on the resulting posterior distributions.

Observations of WASP-12 for reduction were provided by Exoplanet Watch from the MicroObservatory archive for citizen scientists who did not have their own telescope. Using the AAVSO (American Association of Variable Star Observers) finder chart for WASP-12 (see Figure 1), we identified up to seven non-variable comparison stars: AUID 000-BKG-164, AUID 000-BKG-165, AUID 000-BKG-166, AUID 000-BKK-420, AUID 000-BMX-310, AUID 000-BKG-167, and AUID 000-BKG-168. They were selected based on the AAVSO Variable Star Plotter (VSP; AAVSO 2021) and were used for EXOTIC's reduction of the light curves. EXOTIC aligns the images and determines the optimal inner and outer photometric apertures (see Figure 2). The inner aperture encompasses the star's point spread function (PSF) without including the sky background, which fills the space between the outer and inner apertures.

EXOTIC determines the optimal aperture sizes by fitting to a Gaussian PSF model (Mizrachi *et al.* 2021). To account for changes in sky brightness affecting the measured flux, EXOTIC subtracts the background photon count from the star's flux. Finally, the change in flux of the target star is compared to the light emitted by each of the selected comparison stars, and a "quick fit" is performed to identify the best comparison to be used. Nested sampling is used to fit the modeled transit to the observations and produces a triangle plot showing the distribution of posteriors to see whether they were Gaussian (see Figure 3). It is a technique commonly used for posterior exploration and parameter estimation in both ephemeris and light-curve fitting, because of its ability to handle complex parameter spaces and efficiently explore regions of high likelihood. From the sampling, estimates of the full posterior distribution of the parameters are calculated, which is valuable for understanding the uncertainties and correlations between the estimate quantities.

EXOTIC's output included a light curve for each series along with the scatter in the residuals, the midpoint time, transit depth, transit duration, semi-major axis relative to the stellar radius, and planetary versus stellar radius. Example light curves are shown (see Figure 4).

Results from the EXOTIC reductions were uploaded to the AAVSO Exoplanet Database then processed by JPL using the CITISENS (Citizen Initiated Transit Information Survey Enabling NASA Science) pipeline to give the results that are

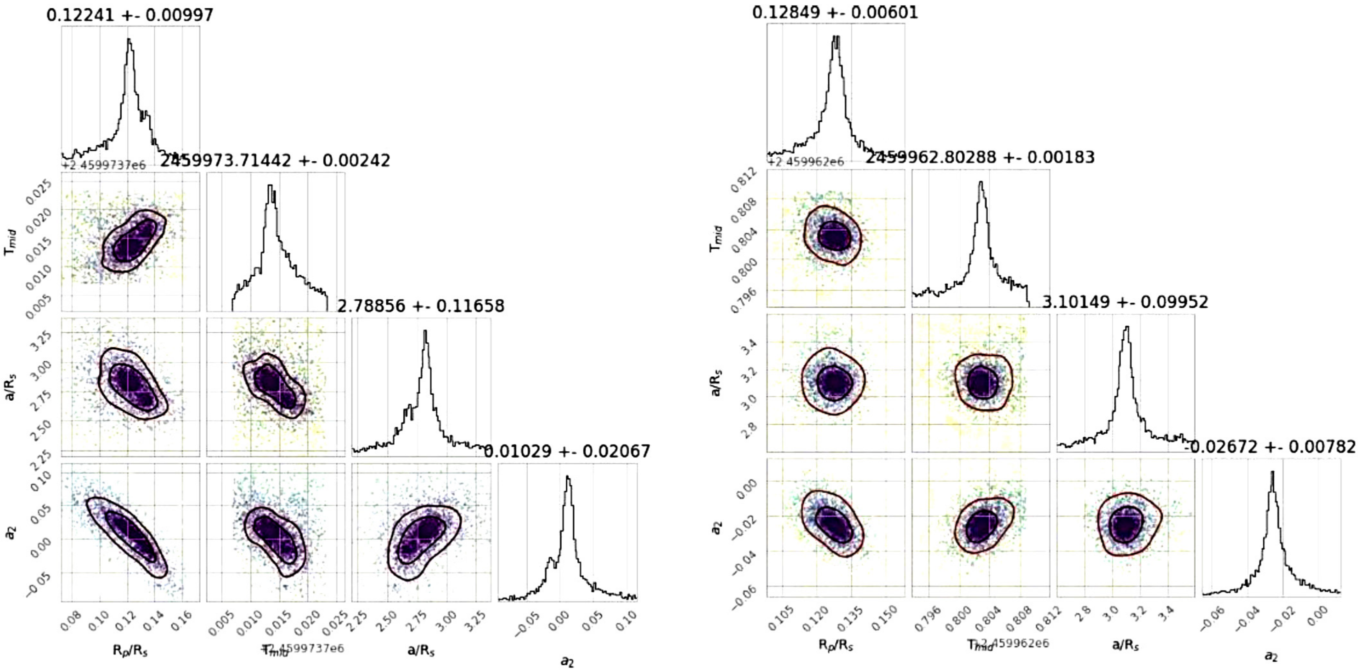

Figure 3. Nested sampling posterior triangle plots using EXOTIC. The data points are color-coded to the likelihood of each fit, with darker colors indicating a higher likelihood. Not all posteriors are shown for reasons of space.

Table 1. Assumed priors by NASA's exoplanet archive for Exoplanet Watch.

Parameter	*Value*	*Uncertainty*	*Units*	*Reference*
R.A. 97.624645			Decimal	
Dec. 29.6722662			Decimal	
Host Star Metallicity	0.3	0.05		Öztürk and Erdem (2019)
Host Star log(g)	4.17	0.03	Log10(cgs)	Öztürk and Erdem (2019)
Host Star Radius	1.57	0.07	Sol	Kokori *et al.* (2022)
Host Star Effective Temperature	6300.0	200.0	K	Kokori *et al.* (2022)
a/R_s	3.0	0.016		Chakrabarty and Sengupta (2019)
Eccentricity	0.0	0.01		Öztürk and Erdem (2019)
Inclination	83.52	0.03	Deg	Chakrabarty and Sengupta (2019)
Omega	272.7	2.4	Deg	Knutson *et al.* (2014)
Orbital Period	1.09141911	6e–08	Day	Ivshina and Winn (2022)
R_p	21.71	0.63	R_Earth	Chakrabarty and Sengupta (2019)
R_p / R_s	0.1170	0.0002		Chakrabarty and Sengupta (2019)
Ephemeris	2457010.512173	7e–05	BJDTDB	Ivshina and Winn (2022)

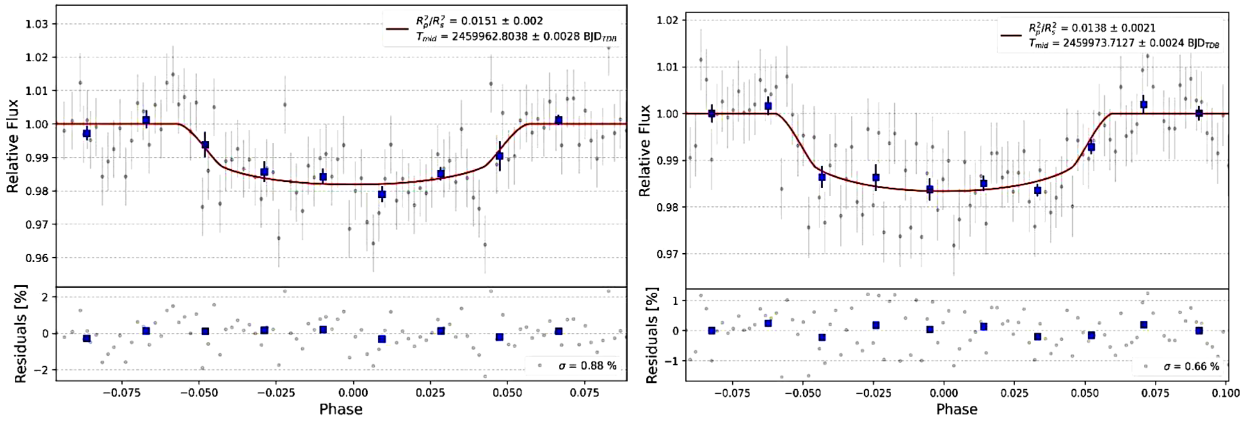

Figure 4. Example transit light curves of WASP-12 b. The gray points represent data from each image in the data set. The blue points represent the average of a set of binned data points, used to guide the eye. The red lines show the EXOTIC model fit for each transit. Not all transits are shown for reasons of space; all the light curves can be seen at: Exoplanet Watch results—Exoplanet Exploration: Planets Beyond our Solar System (nasa.gov).

shown on the Exoplanet Watch website and which were used in this study.

3. Data

There were 14 priors from previously published papers that were used for transit fitting by EXOTIC and CITISENS (see Table 1). EXOTIC's reduction process produced 40 new light curves of WASP-12 b transits (see examples in Figure 4). Of these, seven were duplicate transits taken on the same night by MicroObservatory but which were reduced by different people. There were nine transits that were consistently showing null detection. Adopting the conservative, empirically-derived functions of (Zellem *et al.* 2020) for small telescopes, we consider a transit to have 3-σ detection if $(Rp/Rs)^2$ as a percentage divided by $(R_p / R_s)^2$ uncertainty as a percentage is greater than or equal to 3:

$$\text{(Transit Depth)} / \text{(Transit Depth Uncertainty)} \geq 3 \qquad (1)$$

Therefore, a total of 24 observations were taken into account for the Observed-Calculated (O–C) plot (see Table 2). Each point on the plot in Figure 5 shows the observed mid-transit time minus the calculated mid-transit time from the ephemeris along with the combined 1σ uncertainty.

The literature value of 1.657 ± 0.046 solar radii (11.527 × 105 km) for WASP-12 (Chakrabarty and Sengupta 2019) is used for R_s to calculate the radius of the planet in Jupiter radii (7.149×10^4 km):

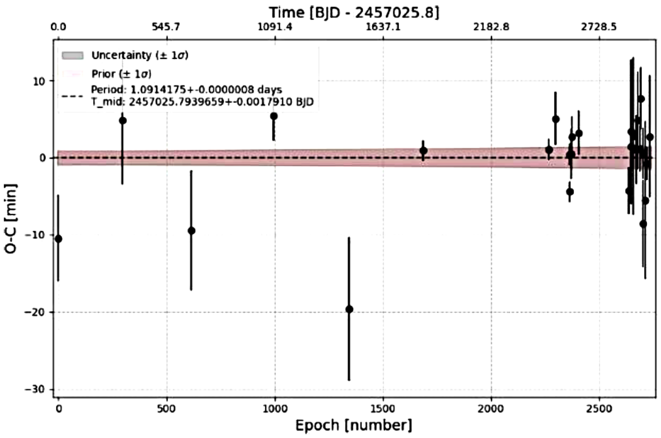

Figure 5. O–C plot of WASP-12 b by Exoplanet Watch.

$$r_j = R_s \times (R_p / R_s) / R_j \qquad (2)$$

Here, the planetary size is calculated to be 1.937 ± 0.056 Jupiter radii. Using the MicroObservatory image sets of WASP-12 b transits, we were able to update the ephemeris using the following equation:

$$t_f = n \times P + T_m \qquad (3)$$

where t_f is a future mid-transit time, P is the period, n is the orbital epoch, and T_m is a reference mid-transit time. The

Table 2. Exoplanet Watch results for T_{mid} after reduction.

Transit Number	*Date (UTC)*	*Mid-transit (BJDTDB)*	*Mid-transit Uncertainty (days)*	*Observer*	*Observer Code*
1	2015-01-03	2457025.7867	0.0038	Ken Davis	DKEB
2	2015-11-21	2457347.7655	0.0058	Finn Russom	RFCA
3	2016-11-02	2457694.8263	0.0054	Prithwis Das	DPRA
4	2017-12-25	2458112.8501	0.0022	Martin J. Fowler	FMAA
5	2019-01-09	2458492.6454	0.0065	Martin J. Fowler	FGIC
6	**2021-11-14**	**2459532.7834**	**0.0024**	**Douglas Lalla**	**LDJC**
7	**2022-01-25**	**2459604.81036**	**0.00091**	**Mike Chasin**	**CMIA**
8	**2022-01-25**	**2459604.81379**	**0.00096**	**Douglas Lalla**	**LDJC**
9	**2022-02-04**	**2459614.6365**	**0.0022**	**Bryan E. Martin**	**MBEB**
10	**2022-02-06**	**2459616.8209**	**0.0018**	**Scott Dixon**	**DSCC**
11	**2022-03-13**	**2459651.7466**	**0.002**	**Pablo Lewin**	**LPAC**
12	**2022-11-20**	**2459903.8588**	**0.0021**	**Anthony Norris**	**NANF**
13	2022-12-01	2459914.7782	0.0066	Muazzez Kumrucu-Lohmiller	KMUA
14	2022-12-02	2459915.8686	0.0037	Nathan Kurth	KNAC
15	2022-12-02	2459925.6921	0.0071	Andre Kovacs	KADB
16	2022-12-26	2459939.8793	0.0031	Muazzez Kumrucu-Lohmiller	KMUA
17	2022-12-26	2459949.7043	0.0042	Alessandro Odasso	OAS
18	**2023-01-14**	**2459959.5249**	**0.0021**	**Andrew Smith**	**SAJB**
19	2023-01-18	2459962.8037	0.0028	Martin J. Fowler	FMAA
20	2023-01-29	2459973.7129	0.0023	Martin J. Fowler	FMAA
21	2023-01-30	2459974.798	0.0039	Martin J. Fowler	FMAA
22	2023-02-11	2459986.8057	0.0071	Alessandro Odasso	OAS
23	2023-02-18	2459994.4482	0.0014	Andrew Smith	SAJB
24	**2023-03-06**	**2460009.731**	**0.0056**	**Michael Primm**	**PMIF**

Note: Transits in bold indicate that they did not use MicroObservatory for observations. All transits were used for the O–C plot.

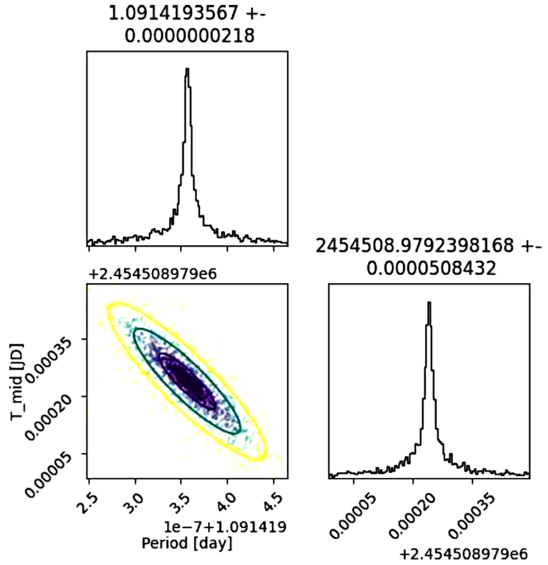

Figure 6. Nested posterior triangle plot using UltraNest for the updated ephemeris. The data points are color- coded to the likelihood of each fit, with darker colors indicating a higher likelihood.

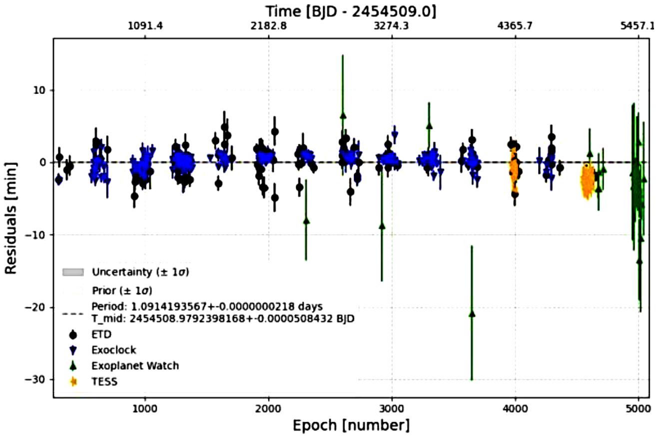

Figure 7. Combined O–C plot data with ExoClock, ETD, TESS, and Exoplanet Watch datasets.

linear ephemeris is optimized using nested sampling to derive posterior distributions for the mid-time and period.

NASA Exoplanet Watch's observations gave a T_{mid} = 2460009.73115 ± 0.00011 BJDTDB with an orbital period of 1.09141889 ± 3.8e–08 days. This is a clear indication of how advanced and easily accessible it has become to reduce transit data from the perspective of a citizen scientist.

Updating the ephemeris of WASP-12 b using amateur observations from Exoplanet Watch can ensure the maximum use is made of expensive non-terrestrial assets such as JWST and ARIEL (Zellem *et al.* 2020, Edwards *et al.* 2019). The ExoClock observations from 12 February 2008 to 20 December 2020 give a T_{mid} = 2457024.706177 ± 5.5e–05 BJDTDB with an orbital period of 1.091419179 ± 4.3e–08 days (Kokori *et al.* 2022). Likewise, ETD observations from 12 February 2008 to 27 December 2021 gave a T_{mid} = 2456594.6766 with an orbital period of 1.09141964 days (Poddaný *et al.* 2010). The ephemerides of the ExoClock and ETD datasets were then forward-propagated using the formula:

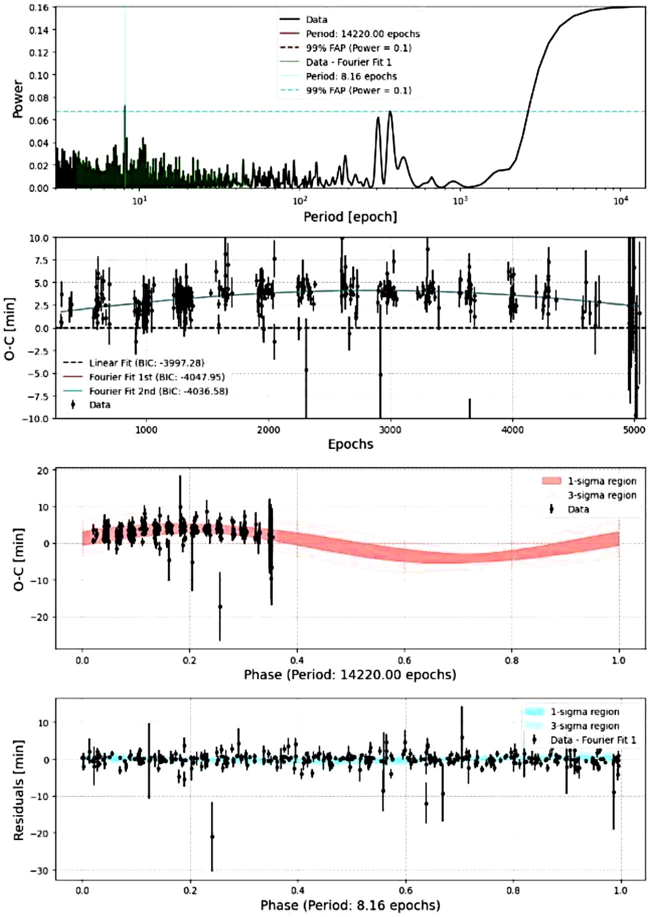

Figure 8. Lomb-Scargle periodogram fitting on the ephemeris to look for period signals.

$$\Delta T_f = (n^2 \cdot \Delta P^2 + 2n \cdot \Delta P \Delta T_m + m^2)^{1/2} \qquad (4)$$

where T_f is a future mid-transit time, n is the orbital epoch, P is the period, and T_m is a reference mid-transit time (Zellem *et al.* 2020).

The 26 TESS observations from 26 December 2019 to 1 December 2021 were then added to the ephemeris. This was done to match the same epoch as Exoplanet Watch to combine the updated ephemerides. Posteriors were then derived for the updated ephemeris of the combined data using nested sampling (see Figure 6) (Pearson *et al.* 2022).

4. Results

Combining the Exoplanet Watch, ETD, ExoClock, and TESS datasets gives an updated ephemeris for the WASP-12 b system of 2454508.97923 ± 0.000051 BJDTDB with an orbital period of 1.09141935 ± 2.16e–08 days. This is 0.619-minute different from the original ExoClock dataset, implying that there is a twofold improvement in the precision of the period (see Figure 7). It is clear that the Exoplanet Watch O–C differs from those of ExoClock and ETD in that it appears to have a linear, rather than a non-linear, spread of data points. This is possibly because of the shorter time frame that is covered by the majority of the Exoplanet Watch observations. They extend back only around 500 epochs, compared with the ExoClock and

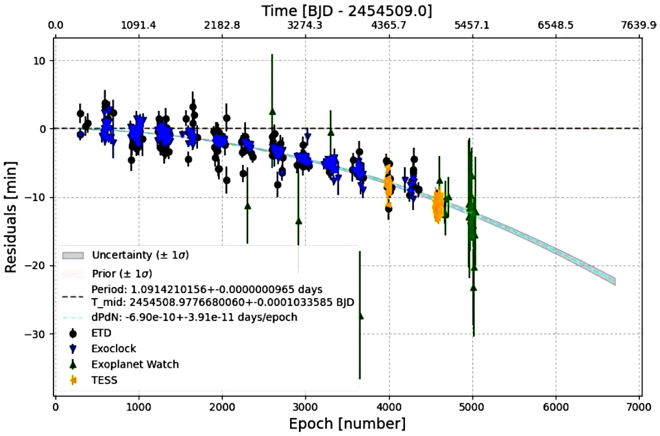

Figure 9. Orbital decay model over the timing residuals of WASP-12 b with future projections around 1σ confidence interval.

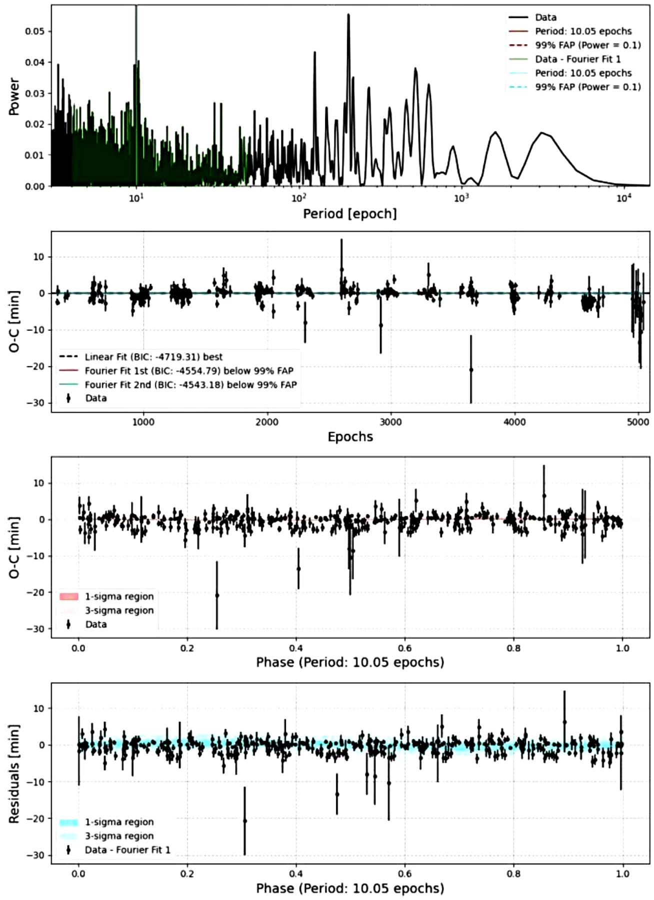

Figure 10. Lomb-Scargle periodogram fitting on the orbital decay model to look for period signals.

ETD data which cover a longer period of observations (i.e., over 4000 epochs). Whilst this is a linear ephemeris that does not take into account the observed changes over the past 5000 epochs, it may nevertheless be considered sufficiently accurate to inform the efficient scheduling of future space telescope observations.

This ephemeris was then analyzed with the Lomb-Scargle periodogram to search for periodic signals since the data were irregular with uniform sampling intervals (see Figure 8). Lomb-Scargle is commonly used in astronomy to find periodic signals in light curves generated by variable stars and exoplanets.

The periodogram shows that there is a known system of orbital change which suggests an orbital decay, and which is in agreement with Yee *et al.* (2020), Hagey *et al.* (2022), and Wong *et al.* (2022). The sinusoids are fitted as a linear system of equations to the residuals of the O–C plot. After identifying the signal, it was possible to predict the planet's future behavior after phase-folding it and extending it to twice the period along 1σ and 3σ confidence intervals to a certain extent. It is not possible to completely predict the future behavior since this is not the same as modeling the orbital decay of the planet. In order to overcome this, we modeled the orbital decay of the exoplanet using the equation:

$$t_f = n \times P + T_m + \tfrac{1}{2} \times d_P / d_n \times n2 \qquad (5)$$

where t_f is a future mid-transit time, P is the period, n is the orbital epoch, and T_m is a reference mid-transit time (Yee *et al.* 2020).

The orbital decay of WASP-12 b was found to be –6.89e–10 ± 4.01e–11 days/epoch. After modeling the orbital decay, we added that model to the linear ephemeris model which can be seen in the new O–C plot (see Figure 9). Using this model it was possible to clearly see the orbital decay and predict the planet's future behavior. Using the new orbital decay model, the Lomb-Scargle periodogram was run again to see if any other periodic signals existed (see Figure 10). No such signals above the 99% FAP (false alarm probability) were found, which indicates that the orbital decay could be the only factor contributing to the change in the orbital period from the previous periodogram.

5. Conclusions

This paper presents 24 new mid-transit values and light curves from citizen scientists of Exoplanet Watch for WASP-12 b using MicroObservatory and individual observations. This confirmed parameters for the planet's size and orbit, supporting its classification as a hot Jupiter-type exoplanet. It demonstrates the functionality of EXOTIC and CITISENS and accessibility of its advanced capabilities for use by citizen scientists. We combined Exoplanet Watch, ETD (Poddaný *et al.* 2010), ExoClock (Kokori *et al.* 2022) and TESS datasets to give an updated ephemeris for the WASP-12 b system of 2454508.97923 ± 0.000051 BJDTDB with an orbital period of 1.09141935 ± 2.16e–08 days, which can be used to inform the efficient scheduling of future terrestrial and non-terrestrial observations. The orbital decay of WASP-12 b was found to be –6.89e-10 ± 4.01e-11 days/epoch, which is consistent with other estimates (Yee *et al.* 2020; Wong *et al.* 2022). Further observations can be used to refine this technique and may be used to more precisely determine causes of variations of exoplanet orbits.

6. Acknowledgements

Data used here come from the MicroObservatory telescope archives maintained by Frank Sienkiewicz, who also provides information on weather and delta temperature measurements.

MicroObservatory is maintained and operated as an educational service by the Center for Astrophysics | Harvard & Smithsonian and is a project of NASA's Universe of Learning, supported by NASA Award NNX16AC65A. Additional MicroObservatory sponsors include the National Science Foundation, NASA, the Arthur Vining Davis Foundations, Harvard University, and the Smithsonian Institution.

This research has made use of the NASA Exoplanet Archive, which is operated by the California Institute of Technology, under contract with the National Aeronautics and Space Administration under the Exoplanet Exploration Program. This publication makes use of the EXOTIC data reduction package from Exoplanet Watch, a citizen science project managed by NASA's Jet Propulsion Laboratory on behalf of NASA's Universe of Learning. This work is supported by NASA under award number NNX16AC65A to the Space Telescope Science Institute.

This paper includes data collected with the TESS mission, obtained from the MAST data archive at the Space Telescope Science Institute (STScI). Funding for the TESS mission is provided by the NASA Explorer Program. STScI is operated by the Association of Universities for Research in Astronomy, Inc., under NASA contract NAS5–26555.

References

AAVSO. 2021, Variable Star Plotter (VSP; https://www.aavso.org/apps/vsp/).

Akeson, R. L., *et al.* 2013, *Publ. Astron. Soc. Pacific*, **125**, 989.

Chakrabarty, A., and Sengupta, S. 2019, *Astron. J.*, **158**, 39.

Edwards, B., Mugnai, L.; Tinetti, G.; Pascale, E.; and Sarkar, S. 2019, *Astron. J.*, **157**, 242.

Hagey, S. R., Edwards, B., and Boley, A. C. 2022, *Astron. J.*, **164**, 220.

Hebb, L., *et al.* 2009, *Astrophys. J.*, **693**, 1920.

Hewitt, H. B., *et al.* 2023, *J. Amer. Assoc. Var. Star Obs.*, **51**, 68.

Ivshina, E. S., and Winn, J. N. 2022, *Astrophys. J., Suppl. Ser.*, **259**, 62.

Kokori, A., *et al.* 2022, *Astrophys. J., Suppl. Ser.*, **258**, 40.

Knutson H. A., *et al.* 2014, *Astrophys. J.*, **785**, 126.

Mizrachi, R., Ly, D., Bewersdorff, L., and Tock, K. 2021, *J. Amer. Assoc. Var. Star Obs.*, **49**, 1.

Öztürk, O., and Erdem, A. 2019, *Mon. Not. Roy. Astron. Soc.*, **486**, 2290.

Pearson, K. A., *et al.* 2022, *Astron. J.*, **164**, 178.

Perryman, M. 2018, *The Exoplanet Handbook*, 2nd ed., Cambridge University Press, Cambridge, UK, 153.

Poddaný, S., Brát, L., and Pejcha, O. 2010, *New Astron.*, **15**, 297.

Ricker, G. R., *et al.* 2015, *J. Astron. Telesc. Instrum. Syst.*, **1**, 014003.

Seidel, J. V., Nielsen, L. D., and Sarkar, S. 2023, *Nature*, **614**, 632.

Wong, I. Shporer, A., Vissapragada, S., Greklek-McKeon, M., Knutson, H. A., Winn, J. N., and Benneke, B., 2022, *Astron. J.*, **163**, 175.

Yee, S. W., *et al.* 2020, *Astrophys. J., Lett.*, **888**, L5.

Zellem, R. T., *et al.* 2020, *Publ. Astron. Soc. Pacific*, **132**, 054401.

Recent Minima of 229 Eclipsing Binary Stars

Gerard Samolyk
P.O. Box 20677, Greenfield, WI 53220; gsamolyk@wi.rr.com

Received August 22, 2023; accepted August 22, 2023

Abstract This paper continues the publication of times of minima for eclipsing binary stars. Times of minima for 299 variable stars were determined from observations received by the American Association of Variable Star Observers (AAVSO) Eclipsing Binaries Section from February 2023 through July 2023.

1. Recent observations

The accompanying list (Table 1) contains times of minima calculated for 229 variable stars calculated from recent CCD observations made by participants in the AAVSO's eclipsing binary program. These observations were reduced by the observers or the writer using the method of Kwee and van Worden (1956).

The linear elements in the *General Catalogue of Variable Stars* (GCVS; Kholopov *et al.* 1985) were used to compute the O–C values for most stars. For a few exceptions where the GCVS elements are missing or are in significant error, light elements from another source are used: CD Cam (Baldwin and Samolyk 2007), AC CMi (Samolyk 2008), DV Cep (Frank and Lichtenknecker 1987), Z Dra (Danielkiewicz-Krosńiak *et al.* 1996), DF Hya (Samolyk 1992), DK Hya (Samolyk 1990), EF Ori (Baldwin and Samolyk 2005), and GU Ori (Samolyk 1985).

The light elements used for EH Cnc, CX CMa, TY CMi, CZ CMi, LR Com, AS CrB, V728 Cyg, V796 Cyg, V1918 Cyg, V2364 Cyg, LS Del, GW Gem, IT Her, V728 Her, WZ Leo, DE Lyn, CU Tau, and KM UMa are from (Kreiner 2004).

The light elements used for V1687 Aql, V1713 Aql, DN Boo, GW Boo, MU Cnc, FV CVn, AW CrB, BD CrB, V700 Cyg, V2181 Cyg, V2477 Cyg, V1057 Her, CE Leo, GU Leo, HI Leo, FI Lyn, V740 Per, RZ Pyx, V1332 Tau, V1370 Tau, BU Tri, QT UMa, and IR Vir are from (Paschke 2014).

The light elements used for V459 Aur, LQ Dra, and V871 Per are from (Nelson 2014).

The light elements used for DG CMi, V417 Gem, EU Hya, V740 Lyr, and V958 Mon are from (Watson *et al.* 2014).

The standard error is included when available. Column F indicates the filter used. A "C" indicates a clear filter.

This list will be web-archived and made available through the AAVSO ftp site at:

ftp://ftp.aavso.org/public/datasets/gsamj512eb229.txt.

This list, along with the eclipsing binary data from earlier AAVSO publications, is also included in the Lichtenknecker Database administrated by the Bundesdeutsche Arbeitsgemeinschaft für Veränderliche Sterne e. V. BAV; Walter *et al.* 2015).[1]

References

Baldwin, M. E., and Samolyk, G. 2005, *Observed Minima Timings of Eclipsing Binaries No. 10*, AAVSO, Cambridge, MA.
Baldwin, M. E., and Samolyk, G. 2007, *Observed Minima Timings of Eclipsing Binaries No. 12*, AAVSO, Cambridge, MA.
Danielkiewicz-Krośniak, E, Kurpińska-Winiarska, M., eds. 1996, *Rocznik Astron.* (SAC 68), **68**, 1.
Frank, P., and Lichtenknecker, D. 1987, *BAV Mitt.*, No. 47, 1.
Kholopov, P. N., *et al.* 1985, *General Catalogue of Variable Stars*, 4th ed., Moscow.
Kreiner, J. M. 2004, *Acta Astron.*, **54**, 207 (http://www.as.up.krakow.pl/ephem/).
Kwee, K. K., and van Woerden, H. 1956, *Bull. Astron. Inst. Netherlands*, **12**, 327.
Nelson, R. 2014, Eclipsing Binary O–C Files (http://www.aavso.org/bob-nelsons-o-c-files).
Paschke, A. 2014, "O–C Gateway" (http://var.astro.cz/ocgate/).
Samolyk, G. 1985, *J. Amer. Assoc. Var. Star Obs.*, **14**, 12.
Samolyk, G. 1990, *J. Amer. Assoc. Var. Star Obs.*, **19**, 5.
Samolyk, G. 1992, *J. Amer. Assoc. Var. Star Obs.*, **21**, 111.
Samolyk, G. 2008, *J. Amer. Assoc. Var. Star Obs.*, **36**, 171.
Walter, F., Hübscher, J., and Grimm, W. 2015, *Lichtenknecker-Database of the BAV: Collection of Times of Minima of Eclipsing Binaries*, Bundesdeutsche Arbeitsgemeinschaft für Veränderliche Sterne e.V. (BAV), Berlin.[1]
Watson, C., Henden, A. A., and Price, C. A. 2014, AAVSO International Variable Star Index VSX (Watson+, 2006–2014; http://www.aavso.org/vsx).

---

[1] Walter *et al.* (2015), https://www.bav-astro.eu/index.php/veroeffentlichungen/service-for-scientists/lkdb-engl

Table 1. Recent times of minima of stars in the AAVSO eclipsing binary program.

Star	*JD (min) Hel. 2400000 +*	*Cycle*	*O–C (day)*	*F*	*Observer*	*Standard Error (day)*
XZ And	59987.3502	26531	0.2161	V	T. Arranz	0.0001
AB And	60158.7595	72461	–0.0569	V	K. Menzies	0.0001
KO Aql	60105.8317	6361	0.1054	V	G. Samolyk	0.0002
KO Aql	60154.5205	6378	0.1053	V	T. Arranz	0.0001
OO Aql	60130.5337	42458	0.0862	V	T. Arranz	0.0001
OO Aql	60149.5385	42495.5	0.0864	V	T. Arranz	0.0001
OO Aql	60152.5796	42501.5	0.0868	V	T. Arranz	0.0001
OO Aql	60153.5932	42503.5	0.0868	V	T. Arranz	0.0001
OO Aql	60154.6066	42505.5	0.0867	V	T. Arranz	0.0004
V342 Aql	60155.4913	6145	–0.0596	V	T. Arranz	0.0003
V343 Aql	60146.5635	17187	–0.0453	V	T. Arranz	0.0002
V1687 Aql	60047.8494	12901	0.0192	V	L. Hazel	0.0003
V1713 Aql	60153.4490	14428	–0.0482	V	T. Arranz	0.0004
RY Aur	60016.3927	7972	0.0126	V	T. Arranz	0.0001
SX Aur	60000.4160	16394	0.0257	V	T. Arranz	0.0002
WW Aur	60008.6979	10718	0.0026	V	G. Samolyk	0.0004
AP Aur	60023.3712	30875.5	1.9541	V	T. Arranz	0.0002
AR Aur	60001.6808	5224	–0.1491	V	G. Samolyk	0.0004
CL Aur	59987.5784	21714	0.1856	V	G. Samolyk	0.0001
CL Aur	60022.4206	21742	0.1856	V	T. Arranz	0.0001
EM Aur	59994.4843	15918.5	–1.1409	V	T. Arranz	0.0006
EP Aur	60001.5910	57008	0.0249	V	G. Samolyk	0.0002
EP Aur	60042.3686	57077	0.0230	V	T. Arranz	0.0001
HP Aur	59992.3818	12114	0.0752	V	T. Arranz	0.0001
IM Aur	60014.3755	15633	–0.1494	V	T. Arranz	0.0001
V404 Aur	60000.4540	9942	–0.0016	V	T. Arranz	0.0004
V459 Aur	60008.6674	2791.5	0.0112	V	G. Samolyk	0.0008
SU Boo	60110.4295	25005	0.0262	V	T. Arranz	0.0002
TU Boo	60043.8102	83190.5	–0.1748	V	G. Samolyk	0.0002
TY Boo	60044.8021	80607	0.0524	V	K. Menzies	0.0001
TY Boo	60101.5707	80786	0.0516	V	T. Arranz	0.0001
TY Boo	60124.4053	80858	0.0516	V	T. Arranz	0.0001
TY Boo	60124.5654	80858.5	0.0531	V	T. Arranz	0.0003
TZ Boo	60048.6632	68702.5	0.0491	V	G. Samolyk	0.0003
TZ Boo	60048.8140	68703	0.0513	V	G. Samolyk	0.0001
TZ Boo	60103.6391	68887.5	0.0500	V	G. Samolyk	0.0003
TZ Boo	60119.3894	68940.5	0.0507	V	T. Arranz	0.0001
TZ Boo	60119.5386	68941	0.0514	V	T. Arranz	0.0001
UW Boo	60097.6667	17610	–0.0035	V	G. Samolyk	0.0002
VW Boo	60047.6937	84348.5	–0.3379	V	G. Samolyk	0.0001
VW Boo	60047.8684	84349	–0.3343	V	G. Samolyk	0.0001
VW Boo	60074.7367	84427.5	–0.3386	V	K. Menzies	0.0001
VW Boo	60126.4257	84578.5	–0.3407	V	T. Arranz	0.0002
AD Boo	60112.6753	18057	0.0412	V	G. Samolyk	0.0001
DN Boo	60084.4470	11584	0.0118	V	T. Arranz	0.0003
EQ Boo	60112.4227	2241	–0.0131	V	T. Arranz	0.0002
GW Boo	60045.8622	13653.5	–0.0112	V	K. Menzies	0.0005
V376 Boo	60112.4772	24989	–0.0066	V	T. Arranz	0.0007
AO Cam	59991.3246	22707.5	–0.0369	V	T. Arranz	0.0001
AO Cam	59991.4879	22708	–0.0385	V	T. Arranz	0.0001
CD Cam	60044.5855	9529	–0.0250	V	K. Menzies	0.0005
FN Cam	60012.7516	11094.5	0.0198	V	L. Hazel	0.0003
SW Cnc	60002.6020	2849	–0.0049	V	L. Hazel	0.0006
TW Cnc	60017.4507	105	–0.1393	V	T. Arranz	0.0008
TX Cnc	60039.3784	57532	0.0469	V	L. Corp	0.0006
XZ Cnc	60025.3851	9656	0.0254	V	T. Arranz	0.0001
YY Cnc	60054.3999	5377	–0.0038	V	T. Arranz	0.0003
EH Cnc	60018.3970	17984.5	–0.0128	V	T. Arranz	0.0002
MU Cnc	60002.6753	22254	0.0040	V	L. Hazel	0.0003
MU Cnc	60030.6039	22350	–0.0047	V	L. Hazel	0.0003
FV CVn	59710.5417	21134.5	–0.0119	V	T. Arranz	0.0002
SX CMa	60041.3577	19668	0.0439	V	T. Arranz	0.0002
TU CMa	59991.6391	29273	–0.0153	V	L. Hazel	0.0003
UU CMa	60006.4027	7112	–0.0449	V	T. Arranz	0.0001
UU CMa	60008.5669	7113	–0.0472	V	L. Hazel	0.0003
CX CMa	59987.6641	7843	0.0068	V	L. Hazel	0.0006
TY CMi	60016.4009	5785	–0.0314	V	T. Arranz	0.0003
XZ CMi	60030.3769	30383	0.0062	V	T. Arranz	0.0002
AC CMi	60053.4105	9311	0.0055	V	T. Arranz	0.0002
AK CMi	60001.6092	29864	–0.0257	V	G. Samolyk	0.0001
AK CMi	60055.3697	29959	–0.0255	V	T. Arranz	0.0001
CZ CMi	60018.3745	17632	–0.0199	V	T. Arranz	0.0001
DG CMi	60044.6188	6975	0.0611	V	L. Hazel	0.0003
TW Cas	59982.4481	12584	0.0316	V	T. Arranz	0.0002
WZ Cep	60143.6555	76904	–0.2523	V	G. Samolyk	0.0002
WZ Cep	60143.8635	76904.5	–0.2530	V	G. Samolyk	0.0002
XX Cep	60144.6626	6548	0.0458	V	G. Samolyk	0.0002
ZZ Cep	60091.8418	15017	–0.0198	V	G. Samolyk	0.0001
DK Cep	60152.8796	26942	0.0264	V	G. Samolyk	0.0002
DV Cep	60116.7617	11492	–0.0057	V	G. Samolyk	0.0002
RW Com	59993.7913	84144.5	0.0229	V	G. Samolyk	0.0002
RW Com	60053.6029	84396.5	0.0234	V	G. Samolyk	0.0002
RW Com	60053.7225	84397	0.0243	V	G. Samolyk	0.0002
RW Com	60076.6260	84493.5	0.0239	V	L. Hazel	0.0003
RZ Com	60022.6710	74401	0.0633	V	G. Samolyk	0.0001
RZ Com	60022.8404	74401.5	0.0635	V	G. Samolyk	0.0001
RZ Com	60061.7684	74516.5	0.0633	V	G. Samolyk	0.0001
RZ Com	60088.6803	74596	0.0639	V	G. Samolyk	0.0002
SS Com	60047.7405	84895.5	1.0558	V	G. Samolyk	0.0002
SS Com	60089.6419	84997	1.0588	V	L. Hazel	0.0006
CC Com	60029.6654	92874.5	–0.0455	V	G. Samolyk	0.0002
CC Com	60029.7743	92875	–0.0470	V	G. Samolyk	0.0001
CC Com	60029.8860	92875.5	–0.0456	V	G. Samolyk	0.0002
CC Com	60089.5831	93146	–0.0441	V	L. Hazel	0.0003
LR Com	60002.7888	8370	0.0319	V	L. Hazel	0.0003
U CrB	60076.7049	12551	0.1542	V	L. Hazel	0.0006
RW CrB	60094.6126	26628	–0.0004	V	L. Hazel	0.0006
TW CrB	60103.6656	37708	0.0642	V	G. Samolyk	0.0001
AS CrB	60146.4154	20087	0.0227	V	T. Arranz	0.0002
AW CrB	60137.4227	24203	–0.0231	V	T. Arranz	0.0003
BD CrB	60070.4264	24802	0.0224	V	T. Arranz	0.0005
BD CrB	60075.4227	24816	0.0225	V	T. Arranz	0.0005
W Crv	60086.6402	52666.5	0.0152	V	G. Samolyk	0.0002
RV Crv	60088.6739	25506	–0.1222	V	G. Samolyk	0.0008
V Crt	60061.6670	26586	0.0029	V	G. Samolyk	0.0002
SW Cyg	60118.7902	3991	–0.4053	V	G. Samolyk	0.0001
WW Cyg	60118.7836	5950	0.1721	V	G. Samolyk	0.0002
AE Cyg	60104.8494	16012	–0.0047	V	G. Samolyk	0.0002
BR Cyg	60048.7830	13890	0.0016	V	L. Hazel	0.0003
BR Cyg	60132.7347	13953	0.0017	V	G. Samolyk	0.0001
BR Cyg	60151.3907	13967	0.0018	V	T. Arranz	0.0001
CG Cyg	60076.7726	32721	0.0858	V	L. Hazel	0.0003
DK Cyg	60152.7851	47065	0.1506	V	G. Samolyk	0.0002
MR Cyg	60094.7687	15920	–0.0134	V	L. Hazel	0.0006
V387 Cyg	60094.7328	50124	0.0178	V	L. Hazel	0.0003
V388 Cyg	60152.7404	21186	–0.1590	V	G. Samolyk	0.0001
V401 Cyg	60082.8194	27882	0.1056	V	L. Hazel	0.0003
V401 Cyg	60150.4151	27998	0.1055	V	T. Arranz	0.0003
V466 Cyg	60097.8582	22509.5	0.0078	V	G. Samolyk	0.0002
V466 Cyg	60159.7834	22554	0.0083	V	K. Menzies	0.0001
V477 Cyg	60097.8216	6778.5	–0.5181	V	G. Samolyk	0.0002
V700 Cyg	60145.5875	96744	–0.0393	V	T. Arranz	0.0002
V700 Cyg	60146.6041	96747.5	–0.0399	V	T. Arranz	0.0001
V700 Cyg	60156.6311	96782	–0.0396	V	T. Arranz	0.0001
V728 Cyg	60090.7408	3684	0.0649	V	L. Hazel	0.0003
V753 Cyg	60142.4589	55310	0.0859	V	T. Arranz	0.0001
V796 Cyg	60094.6680	5128	–0.0183	V	L. Hazel	0.0006
V995 Cyg	60162.4527	9507	0.6963	V	T. Arranz	0.0001
V1918 Cyg	60044.8724	18260	–0.0071	V	L. Hazel	0.0003
V1918 Cyg	60047.7669	18267	–0.0049	V	L. Hazel	0.0003
V2181 Cyg	59812.5001	15791.5	–0.0113	V	T. Arranz	0.0005
V2364 Cyg	60082.7328	12805.5	0.0113	V	L. Hazel	0.0009
V2477 Cyg	60145.5880	27800	0.0030	V	T. Arranz	0.0001
TY Del	60130.8260	14416	0.0958	V	G. Samolyk	0.0001

Table continued on following pages

Table 1. Recent times of minima of stars in the AAVSO eclipsing binary program, cont.

Star	JD (min) Hel. 2400000 +	Cycle	O–C (day)	F	Observer	Standard Error (day)
LS Del	60139.5688	20996	–0.0114	V	L. Corp	0.0007
Z Dra	60053.6745	7521	–0.0004	V	G. Samolyk	0.0002
Z Dra	60091.6816	7549	–0.0015	V	L. Hazel	0.0003
Z Dra	60091.6825	7549	–0.0006	V	G. Samolyk	0.0001
RZ Dra	60085.7668	28878	0.0777	V	G. Samolyk	0.0001
RZ Dra	60116.6156	28934	0.0776	V	G. Samolyk	0.0002
TW Dra	60098.7352	5687	–0.0987	V	G. Samolyk	0.0001
TW Dra	60101.5419	5688	–0.0988	V	T. Arranz	0.0001
UZ Dra	60115.6820	5686.5	0.0029	V	G. Samolyk	0.0001
AI Dra	60048.7006	13978	0.0431	V	L. Hazel	0.0003
AI Dra	60090.6611	14013	0.0451	V	G. Samolyk	0.0003
BH Dra	60105.7319	11053	–0.0042	V	G. Samolyk	0.0003
BH Dra	60147.5288	11076	–0.0038	V	T. Arranz	0.0001
BV Dra	60125.4973	44709	0.0203	V	T. Arranz	0.0001
BW Dra	60125.4930	60079	–0.1522	V	T. Arranz	0.0001
LQ Dra	60044.7766	2120	0.0353	V	L. Hazel	0.0003
YY Eri	59969.6550	57195	0.1731	V	L. Hazel	0.0003
RW Gem	59995.6426	14550	0.0033	V	L. Hazel	0.0006
TX Gem	60031.3677	14351	–0.0452	V	T. Arranz	0.0001
TX Gem	60045.3676	14356	–0.0454	V	T. Arranz	0.0001
WW Gem	60047.6175	27519	0.0396	V	G. Samolyk	0.0002
AC Gem	59960.6222	12950	–0.3544	V	L. Hazel	0.0006
AF Gem	60014.3622	26419	–0.0657	V	T. Arranz	0.0001
AL Gem	60018.6065	24217	0.1153	V	G. Samolyk	0.0001
CX Gem	59987.5751	14699	–0.0493	V	L. Hazel	0.0006
FG Gem	59934.7134	40082	–0.0192	V	L. Hazel	0.0006
FG Gem	60049.3860	40222	–0.0246	V	T. Arranz	0.0001
GW Gem	60022.4323	11407	0.0003	V	T. Arranz	0.0002
V417 Gem	60007.4722	21306.5	–0.1249	V	T. Arranz	0.0008
SZ Her	60090.6777	22279	–0.0391	V	G. Samolyk	0.0001
SZ Her	60136.4910	22335	–0.0393	V	T. Arranz	0.0001
TT Her	60048.8426	21986	0.0435	V	G. Samolyk	0.0001
TT Her	60135.4893	22081	0.0431	V	T. Arranz	0.0001
TU Her	60079.8048	7066	–0.2827	V	L. Hazel	0.0006
TU Her	60104.7450	7077	–0.2795	V	G. Samolyk	0.0001
TU Her	60136.4839	7091	–0.2786	V	T. Arranz	0.0001
UX Her	60081.7392	13177	0.1919	V	G. Samolyk	0.0001
AK Her	60042.7966	42361.5	0.0320	V	L. Hazel	0.0003
CC Her	60105.7305	11786	0.3961	V	G. Samolyk	0.0001
CT Her	60129.4530	9856	0.0110	V	T. Arranz	0.0002
DI Her	60147.5300	1698	–0.0029	V	T. Arranz	0.0001
IT Her	60148.5127	22535.5	–0.0173	V	L. Corp	0.0014
LT Her	60104.7235	17849	–0.1694	V	G. Samolyk	0.0003
V450 Her	60134.4746	37741	–0.3956	V	T. Arranz	0.0003
V728 Her	60148.4011	16228	0.0389	V	T. Arranz	0.0001
V1057 Her	60157.4295	9392	–0.0122	V	T. Arranz	0.0003
WY Hya	60018.4748	27161	0.0468	V	T. Arranz	0.0001
AV Hya	60043.6918	34197	–0.1260	V	G. Samolyk	0.0003
DF Hya	59987.7103	52025.5	0.0319	V	G. Samolyk	0.0001
DF Hya	59987.8759	52026	0.0322	V	G. Samolyk	0.0001
DF Hya	60024.4077	52136.5	0.0321	V	T. Arranz	0.0001
DF Hya	60040.6079	52185.5	0.0327	V	G. Samolyk	0.0001
DI Hya	59989.7127	46844	–0.0434	V	G. Samolyk	0.0002
DK Hya	59987.7665	32848	–0.0027	V	G. Samolyk	0.0002
EU Hya	60041.4296	33301	–0.0266	V	T. Arranz	0.0002
Y Leo	60017.7645	8648	–0.0966	V	G. Samolyk	0.0001
Y Leo	60061.6029	8674	–0.0968	V	G. Samolyk	0.0001
Y Leo	60073.4057	8681	–0.0968	V	T. Arranz	0.0001
UU Leo	60041.6902	8718	0.2530	V	G. Samolyk	0.0002
UV Leo	60001.8242	35930	0.0517	V	G. Samolyk	0.0001
VZ Leo	60032.6180	26487	–0.0382	V	G. Samolyk	0.0003
VZ Leo	60044.6084	26498	–0.0368	V	K. Menzies	0.0002
VZ Leo	60066.4058	26518	–0.0375	V	T. Arranz	0.0003
WZ Leo	59987.8507	5317	–0.0006	V	G. Samolyk	0.0002
WZ Leo	60079.3835	5382	0.0005	V	T. Arranz	0.0002
XY Leo	60022.7284	52616	0.1953	V	K. Menzies	0.0002
XY Leo	60039.4900	52675	0.1952	V	L. Corp	0.0007
XY Leo	60084.3779	52833	0.1958	V	T. Arranz	0.0002
AP Leo	60061.4216	47692.5	0.0497	V	T. Arranz	0.0002
CE Leo	60066.5436	40823	–0.0122	V	T. Arranz	0.0001
GU Leo	60065.3713	21690	0.0055	V	T. Arranz	0.0001
HI Leo	60072.4172	23530	0.0480	V	T. Arranz	0.0001
T LMi	60040.6479	4849	–0.1425	V	G. Samolyk	0.0002
SS Lib	60118.7378	13187	0.1942	V	G. Samolyk	0.0004
SS Lib	60137.4321	13200	0.1945	V	T. Arranz	0.0003
RY Lyn	60022.6018	11941	–0.0329	V	K. Menzies	0.0001
UV Lyn	60060.4151	47686	0.1337	V	T. Arranz	0.0001
DE Lyn	60042.4542	18449	–0.0455	V	T. Arranz	0.0005
FI Lyn	60043.4363	22677.5	–0.0020	V	T. Arranz	0.0002
RV Lyr	60145.4608	4062	–0.3117	V	T. Arranz	0.0002
UZ Lyr	60151.5191	8704	–0.0600	V	T. Arranz	0.0001
BV Lyr	60148.5153	14903	0.0405	V	T. Arranz	0.0001
EW Lyr	60103.7995	17244	0.3231	V	G. Samolyk	0.0002
EW Lyr	60154.4672	17270	0.3240	V	T. Arranz	0.0001
FL Lyr	60142.4970	10064	–0.0014	V	T. Arranz	0.0001
FL Lyr	60144.6742	10065	–0.0023	V	G. Samolyk	0.0002
V740 Lyr	60129.5986	22134.5	0.0283	V	T. Arranz	0.0001
V740 Lyr	60130.4191	22137	0.0270	V	T. Arranz	0.0001
V740 Lyr	60130.5847	22137.5	0.0283	V	T. Arranz	0.0001
RU Mon	59960.7285	5082	–0.1606	V	L. Hazel	0.0006
RU Mon	60050.3319	5107	–0.1759	V	T. Arranz	0.0003
RW Mon	60001.6053	13809	–0.0965	V	G. Samolyk	0.0001
RW Mon	60047.3508	13833	–0.0973	V	T. Arranz	0.0001
AT Mon	60019.3814	16467	0.0091	V	T. Arranz	0.0003
BB Mon	60008.3631	45485	–0.0046	V	T. Arranz	0.0002
BO Mon	60025.4042	7423	0.0043	V	T. Arranz	0.0001
V958 Mon	59993.4368	28385.5	0.0570	V	T. Arranz	0.0001
SX Oph	60129.6587	12955	0.0010	V	G. Samolyk	0.0004
V501 Oph	60103.8018	30159	–0.0093	V	G. Samolyk	0.0002
V508 Oph	60132.6943	43650	–0.0251	V	G. Samolyk	0.0002
V839 Oph	60115.7238	48086	0.3619	V	G. Samolyk	0.0001
V839 Oph	60148.4440	48166	0.3625	V	T. Arranz	0.0001
V1010 Oph	60113.7445	32016	–0.2435	V	G. Samolyk	0.0003
V1010 Oph	60116.7227	32020.5	–0.2417	V	G. Samolyk	0.0004
EF Ori	60007.3505	4728	0.0112	V	T. Arranz	0.0002
ER Ori	60007.3783	43412.5	0.1672	V	T. Arranz	0.0001
FH Ori	59993.6345	15849	–0.4873	V	G. Samolyk	0.0003
FL Ori	59993.3224	9443	0.0392	V	T. Arranz	0.0001
FT Ori	59986.5646	5916	0.0265	V	G. Samolyk	0.0001
GU Ori	59992.4560	35953.5	–0.0763	V	T. Arranz	0.0002
GU Ori	59994.3386	35957.5	–0.0765	V	T. Arranz	0.0002
U Peg	60132.8350	63027	–0.1830	V	G. Samolyk	0.0002
DM Peg	59841.7663	13128	0.0211	V	L. Hazel	0.0006
ST Per	60008.4041	6635	0.3261	V	T. Arranz	0.0001
WY Per	59979.3809	4201	–0.3846	V	T. Arranz	0.0001
XZ Per	59980.3663	14304	–0.0856	V	T. Arranz	0.0001
AY Per	59985.3893	2788	–0.1330	V	T. Arranz	0.0005
V740 Per	60002.3936	23065.5	–0.0017	V	T. Arranz	0.0001
V871 Per	59619.3579	886	–0.1706	V	T. Arranz	0.0002
V871 Per	60000.3416	1012	–0.1977	V	T. Arranz	0.0004
V873 Per	59984.3888	29208	–0.0393	V	T. Arranz	0.0001
Beta Per	59989.6630	5004	0.1588	V	G. Samolyk	0.0003
UZ Pup	60031.4133	19397	–0.0137	V	T. Arranz	0.0001
XZ Pup	60012.6560	8028	0.1704	V	L. Hazel	0.0002
RZ Pyx	59918.8657	32741.5	0.0064	V	L. Hazel	0.0003
RZ Pyx	59991.7085	32852.5	0.0027	V	L. Hazel	0.0006
U Sge	60145.4521	12724	0.0403	V	T. Arranz	0.0001
RS Ser	60086.8262	42072	0.0266	V	G. Samolyk	0.0002
RS Ser	60130.4901	42145	0.0262	V	T. Arranz	0.0001
AO Ser	60047.8264	29470	–0.0070	V	G. Samolyk	0.0001
CC Ser	60043.8841	43722.5	1.2330	V	G. Samolyk	0.0003
Y Sex	60043.6557	43536	–0.0377	V	G. Samolyk	0.0004
Y Sex	60047.6472	43545.5	–0.0345	V	L. Hazel	0.0003
RZ Tau	59981.3659	53659	0.1102	V	T. Arranz	0.0001

Table continued on next page

Table 1. Recent times of minima of stars in the AAVSO eclipsing binary program, cont.

Star	*JD (min) Hel. 2400000 +*	*Cycle*	*O–C (day)*	*F*	*Observer*	*Standard Error (day)*
TY Tau	59993.6386	36015	0.2853	V	G. Samolyk	0.0002
AC Tau	59989.3572	7024	0.2347	V	T. Arranz	0.0001
AM Tau	60006.3879	7218	–0.0870	V	T. Arranz	0.0001
AQ Tau	59988.4483	24947	0.5172	V	T. Arranz	0.0002
AQ Tau	59989.6638	24948	0.5168	V	G. Samolyk	0.0002
CT Tau	59990.5280	21874	–0.0770	V	K. Menzies	0.0002
CT Tau	59990.5289	21874	–0.0761	I	K. Menzies	0.0007
CU Tau	59993.4218	18164.5	–0.0815	V	T. Arranz	0.0002
EQ Tau	59978.3680	57903	–0.0580	V	T. Arranz	0.0001
EQ Tau	59987.5844	57930	–0.0580	V	G. Samolyk	0.0001
V781 Tau	59990.3074	46723.5	–0.0489	V	T. Arranz	0.0001
V781 Tau	59990.4799	46724	–0.0489	V	T. Arranz	0.0001
V1332 Tau	59981.3687	23157	0.0292	V	T. Arranz	0.0001
V1370 Tau	59991.3264	28842	0.0141	V	T. Arranz	0.0002
V1370 Tau	59991.4737	28842.5	0.0136	V	T. Arranz	0.0002
X Tri	59985.3801	17995	–0.1168	V	T. Arranz	0.0001
X Tri	59986.3519	17996	–0.1166	V	T. Arranz	0.0001
RV Tri	59978.3467	18503	–0.0522	V	T. Arranz	0.0001
BU Tri	59611.3768	18987.5	–0.0976	V	T. Arranz	0.0007
BU Tri	59978.3138	20229	–0.1058	V	T. Arranz	0.0006
W UMa	60048.6197	42810	–0.1397	V	G. Samolyk	0.0003
W UMa	60048.7879	42810.5	–0.1384	V	G. Samolyk	0.0002
TX UMa	60075.7060	4922	0.3001	V	G. Samolyk	0.0004
TY UMa	60033.6603	57823.5	0.5011	V	G. Samolyk	0.0001
TY UMa	60033.8377	57824	0.5012	V	G. Samolyk	0.0002
UX UMa	60040.5760	114952	–0.0014	V	G. Samolyk	0.0003
VV UMa	60053.6257	20714	–0.1001	V	G. Samolyk	0.0001
KM UMa	60076.4330	21532	–0.0264	V	T. Arranz	0.0002
QT UMa	60078.4202	17980	0.0130	V	T. Arranz	0.0001
RU UMi	60104.6941	35259	–0.0146	V	G. Samolyk	0.0001
VV Vir	60017.8904	64547	–0.0531	V	G. Samolyk	0.0002
VV Vir	60125.4093	64788	–0.0530	V	T. Arranz	0.0002
AG Vir	60036.6298	22725	–0.0231	V	G. Samolyk	0.0003
AH Vir	60001.7322	34813	0.3186	V	G. Samolyk	0.0001
AK Vir	60075.7026	14661	–0.0471	V	G. Samolyk	0.0001
AW Vir	59984.8923	42266.5	0.0352	V	K. Menzies	0.0001
AW Vir	60097.6400	42585	0.0349	V	G. Samolyk	0.0001
AW Vir	60111.4455	42624	0.0345	V	T. Arranz	0.0002
AX Vir	60044.7520	46225	0.0344	V	K. Menzies	0.0001
AZ Vir	60033.8455	45922	–0.0157	V	G. Samolyk	0.0001
AZ Vir	60105.7018	46127.5	–0.0156	V	G. Samolyk	0.0002
AZ Vir	60111.4703	46144	–0.0165	V	T. Arranz	0.0002
BH Vir	60091.6396	20641	–0.0163	V	G. Samolyk	0.0001
BH Vir	60110.4273	20664	–0.0166	V	T. Arranz	0.0001
IR Vir	60082.4385	27767.5	–0.0146	V	T. Arranz	0.0001
Z Vul	60156.5455	7010	–0.0195	V	T. Arranz	0.0007
BE Vul	60132.8501	12900	0.1015	V	G. Samolyk	0.0004
BO Vul	60141.5676	12412	0.0106	V	T. Arranz	0.0001
BS Vul	60112.8364	35383	–0.0401	V	G. Samolyk	0.0001
BT Vul	60130.8500	21669	0.0072	V	G. Samolyk	0.0003
BU Vul	60130.7038	46744	0.0120	V	G. Samolyk	0.0001
CD Vul	60130.6616	20230	–0.0048	V	G. Samolyk	0.0002

Index to Volume 51

Author

Subject

NOTES